UNIVERSITY OF OKLAHOMA

GRADUATE COLLEGE

DIAGNOSIS OF SEVERE WIND PROCESSES IN TWO NOCTURNAL MCSS OBSERVED DURING PECAN

A DISSERTATION

SUBMITTED TO THE GRADUATE FACULTY

in partial fulfillment of the requirements for the

Degree of

DOCTOR OF PHILOSOPHY

By

RACHEL LEIGH MILLER
Norman, Oklahoma
2023

DIAGNOSIS OF SEVERE WIND PROCESSES IN TWO NOCTURNAL MCSS OBSERVED DURING PECAN

A DISSERTATION APPROVED FOR THE
SCHOOL OF METEOROLOGY

BY THE COMMITTEE CONSISTING OF

Dr. Michael Biggerstaff, Chair

Dr. Michael Coniglio, Co-Chair

Dr. Boris Apanasov

Dr. Edward Mansell

Dr. David Schvartzman Cohenca

Dr. Xuguang Wang

Dr. Guifu Zhang

Dr. Conrad Zielger

Table of Contents

Acknowledgements

I never would have thought that 12 years ago, standing in front of the National Weather Center during a tour of The School of Meteorology and the University of Oklahoma, my academic journey would cumulate in a Ph.D. The School of Meteorology has afforded me opportunity after opportunity to challenge myself and grow as a scientist through classes, field work, and the wonderful people I've met along the way.

First, I want to thank my family for always encouraging me in school, buying me books on every topic that piqued my interest, and reaffirming that I could achieve anything. In particular, I would like to acknowledge my grandmother, Shirley Shanholtz, who bought me my first weather book and sparked an interest and curiosity that has driven me to this day. I also would not be here without the unwavering support of my parents, Mike and Jill, who reinforced the importance of education and have believed in me since day one. And thank you to my brothers, Josh and Seth, for being a constant source of annoyance and fun.

I also have to thank all of my amazing teachers at Century High School including but not limited to Mr. Ferrin, Mr. Beard, Mrs. Cohen, Ms. Frey, Mr. Michael, and Ms. Adelman for fostering my love of math and science and encouraging critical thinking. I would not be here without all of the wonderful professors at the School of Meteorology including but not limited to Drs. Kevin Kloesel, Evgeni Fedorovich, Petra Klein, Alan Shapiro, Elinor Martin, Jeff Basara, Cameron Homeyer, and Xuguang Wang. Thank you to my committee members Drs. Michael Biggerstaff, Michael Coniglio, Boris Apanasov, Ted Mansell, Conrad Ziegler, Guifu Zhang, Xuguang Wang, and David Schvartzman Cohenca for enduring the record largest SoM Ph.D. committee. In particular, I have to thank my chair Michael Biggerstaff and my advisor Michael Coniglio for your support, guidance, and encouragement during the final push to finish my dissertation. I would also like to thank Jens Redemann for being a great SoM director and always advocating for students.

This journey to get my PhD would not have been nearly as fun without my wonderful friends Dr. Liz DiGangi, Emily Jugle, Alanna Leipold, and Jennifer Forsythe who have loved and supported me no matter how many miles apart we are. I must also acknowledge the friends that have become chosen family for their constant love and support including Dr. Kenzie Krocak, Dr. Matt Flournoy, Kate and BJ Schafstall, Dr. Andy Wade, Heather Wade, Andrew Rickels, Kristen Perez-Rickels, Dr. Tony Lyza, and Michael Smith. You all make living in Oklahoma worth it.

Finally, I have to thank my husband, best friend, and biggest supporter Dr. Addison Alford who has been by my side for most of my graduate school career. You have lifted me up and celebrated my every high, and supported and encouraged me through my every low. You have always believed in me even when I didn't believe in myself. So many refer to having a partner in the same field as the "two-body problem", but you have been my greatest asset on this journey. Finding such a kind person with the bonus of being a brilliant scientist has many every struggle in grad school more than worth it. Thank you for choosing to do life and science with me.

This dissertation is supported thanks to the National Science Foundation via NSF grant AGS-1359726.

Abstract

Severe wind processes in nocturnal mesoscale convective systems (MCSs) are not well understood since historically it has been assumed that these systems are elevated due to a stable surface layer. However, recent studies utilizing data from the Plains Elevated Convection at Night (PECAN) field project have shown that nocturnal MCSs behave like their afternoon counterparts once a surface-based cold pool is established. Many processes producing severe surface winds in MCSs have been observed and modeled such as mesovortices, microbursts, and the descent of the rear inflow jet. To further investigate these processes, two MCSs from the PECAN field project were selected for analysis due to their different evolution to cover a broad range of severe wind processes: the 25-26 June 2015 Kansas MCS and the 5-6 July 2015 South Dakota MCS. One radar analysis documented severe wind will be shown for the 25-26 June MCS. All other results will be presented from WRF simulations with three nested grids utilizing a vertically-integrated ice data assimilation scheme which produced simulated reflectivity that best resembled the observed reflectivity during the severe phases of the MCSs.

To investigate severe wind processes, backwards trajectories were calculated using WRF output from the inner-most nest with 333-m grid spacing every 5 seconds. This WRF output was first run through a pressure decomposition code to compute the pressure perturbation contribution from buoyancy pressure (p_b') and both the linear and nonlinear dynamic pressure (p_d'). This allowed for gradients in the horizontal and vertical to be calculated along the trajectories for acceleration from p_b' and p_d'. Other variables analyzed along the trajectories include convective momentum transport (CMT), diabatic temperature tendency, vorticity, thermal buoyancy, and typical WRF output variables. Selected trajectories were analyzed every

30 minutes for both cases to cover three categories: sub-severe winds (20-26 m s^{-1}), severe winds (> 26 m s^{-1}), and significant severe winds (> 33.5 m s^{-1}). While most of the typical WRF output variables were unable to discern between the three categories, the integrated acceleration from the horizontal buoyancy and dynamic forcing showed that within the last 5 and/or 2 minutes of the trajectory the increase in wind speed due to the dynamic forcing became larger than impacts from buoyancy. Over the entire trajectory time period, buoyancy forcing is the largest forcing term and explains increases in horizontal and vertical wind speed. This suggests that while all surface-based MCSs with an established cold pool will have buoyancy contributing the most to the wind speed, an extra contribution from some dynamic process is necessary for those winds to exceed the severe or significant threshold. For a more strongly forced system such as the 5-6 July MCS, the enhanced dynamic push came from leading line mesovortices. For a more marginal MCS such as the 25-26 June MCS, an updraft/downdraft couplet associated with horizontal vorticity would enhance the horizontal acceleration.

Chapter 1: Introduction

Processes contributing to the initiation and maintenance of nocturnal mesoscale convective systems (MCS) and their attendant hazards are not as well known as their diurnal counterparts. In particular, nocturnal MCSs' propensity to produce severe winds at the surface is not well understood. While recent studies (Miller et al. 2020; Hitchcock et al. 2019; Parker 2008; Parker et al. 2020; Parker 2021; Billings and Parker 2012) have shown that most nocturnal MCSs do eventually develop a surface-based cold pool and ingest surface-based parcels, historically nocturnal MCSs were assumed to be elevated due to the statically-stable nocturnal near-surface layer and therefore, were less likely to produce severe winds at the ground. In response to a lack of literature on nocturnal MCS dynamics and understanding, the Plains Elevated Convection at Night (PECAN) experiment in 2015 obtained a variety of observations critical to understanding nocturnal MCS processes and evolution (Geerts et al. 2017). Results of this field program showed that nocturnal MCSs often behave like their afternoon counterparts once a surface-based cold pool is established (Hitchcock et al. 2019; Parker et al. 2020; Parker 2021; Miller et al. 2020). However, few of these studies have investigated the details of severe wind production in nocturnal MCSs and how these processes may evolve through an evolving nocturnal boundary layer.

Quasi-linear convective systems (QLCSs), a subset of MCSs, are estimated to be responsible for 28% of severe wind reports (wind speed > 58 mph) in the central and eastern United States (Ashley et al. 2019). In particular, over 79% of QLCSs in the Ashley et al. (2019) dataset produced at least one severe wind report with over 30 % of events producing more than 20 severe wind reports. While Ashley et al. (2019) (and others) show that tornadoes are not uncommon with QLCSs, they show that severe winds are the dominant hazard in QLCSs/MCSs, particularly in the warm season. Indeed, many past studies into QLCS/MCS hazards have mainly focused on mesovortices and their connection to tornadoes to aid in QLCS/MCS hazard forecasting [eg. Trapp et al. 2005, Flournoy and Coniglio 2019, Trapp et al. 1999, Atkins et al. 2005, Atkins and St. Laurent 2009a, 2009b], or have focused on severe wind mechanisms in the daytime higher instability environments in the spring and summer months [eg. Atkins et al. 2005, Forbes and Wakimoto 1983, Funk et al. 1999, Atkins et al. 2004, Wakimoto et al. 2006b, Newman and Heinselman 2012, Mahale et al. 2012, Weisman 1992, 1993]. However, the spectrum of mechanisms that produce MCS severe winds within a stable, nocturnal environment remains both unclear and difficult to forecast.

In addition to tornadoes, MCS severe winds have been connected to mesovortices, which, more specifically, are defined as meso-gamma-scale (2-20 km) vorticity maxima along the leading edge of the convective line (Orlanski 1975). Mesovortices tend to be short-lived (< 60 min), only extend up to 3 km above ground level (AGL), and are strongest near the surface (Flournoy and Coniglio 2019; Trapp et al. 1999) with tornadic mesovortices typically stronger and longer-lived than their nontornadic counterparts (Atkins et al. 2005, Davis and Parker 2014). MCS mesovortices are often not associated with a midlevel mesocyclone, indicating that their source of rotation can be different from that of a supercell (Wakimoto et al. 2006b). Mesovortices have been observed (Forbes and Wakimoto 1983; Funk et al. 1999; Przybylinski et al. 2000; Atkins et al. 2004, 2005; Wakimoto et al. 2006b; McDonald and Weiss 2021; Newman and Heinselman 2012; Mahale et al. 2012) and modeled (Wheatley and Trapp 2008; Weisman and Trapp 2003; Trapp and Weisman 2003; Flournoy and Coniglio 2019; Atkins and St. Laurent 2009a,b; Snook et al. 2011; Parker et al. 2020; Schenkman et al. 2011a,b, 2012; Xu et al. 2015) in many past studies of MCSs. They have been shown to enhance straight-line wind damage in areas where the linear superposition of the vortex flow and MCS propagation caused an additive effect on ground relative winds (Flournoy and Coniglio 2019; Atkins and St. Laurent 2019a,b; Trapp and Weisman 2003; Wakimoto et al. 2006a,b, Weisman 1993). To show this, Atkins and St. Laurent (2009a) used stream functions to separate the vortex flow from the background flow. While the vortex flow was generally no greater than 17 m s^{-1}, the rear inflow jet (RIJ) driven background flow was not strong enough on its own to drive severe winds at the surface despite always being larger than the vortex flow. Severe straight-line winds could only occur with the two flows combined. Observational studies of damage from bow echoes have noted areas of straight-line wind damage just south of tornadoes indicating that the mesovortex responsible for the tornado could have also enhanced the flow to its south (Forbes and Wakimoto 1983; Fujita 1978, 1979, 1981; Funk et al. 1999, Wakimoto et al. 2006a).

Microbursts are also associated with severe winds in MCSs with many of Dr. Ted Fujita’s damage surveys attributing severe surface winds to microbursts (Fujita 1978, 1979, 1981). Microbursts are downdrafts on scales < 4 km and are thought to be forced primarily by localized maxima in diabatic cooling (Fujita 1978, 1979, 1981; Fujita and Wakimoto 1981; Biggerstaff and Houze 1993; Richter et al. 2014), although some have been shown to be aided dynamically by local vorticity maxima (e.g., Bernardet and Cotton 1998, Richter et al. 2014). Both have been associated with straight-line wind damage in MCSs and bow echoes since their top intensity can reach F3 strength (Fujita 1978). Newman and Heinselman (2012) observed a microburst preceding a tornado in a MCS when a hail-laden core (> 65 dBZ) descended to the surface causing estimated winds of 30 m s^{-1}. This locally strengthened the outflow leading to a bowing segment and an increase in azimuthal shear, which increased the likelihood of mesovortex formation. Microbursts leading to severe surface winds were also noted in many

MCSs sampled in the Bow Echo and MCV Experiment (BAMEX) (Atkins et al. 2005, Newman and Heinselman 2012, Biggerstaff and Houze 1991a). Miller et al. (2020) documented radar-derived surface winds approaching 29 ms^{-1} ahead of precipitation-cooled downdraft air resembling a traveling microburst described by Fujita (1981) in the 26 June 2015 PECAN MCS well after dark.

The rear inflow or rear inflow jet (RIJ) has been shown in simulations and observations to be an important component of MCS dynamics by advecting drier air from the rear of the system to enhance diabatic cooling via melting, evaporation, and sublimation (Smull and Houze 1985, 1987; Houze et al. 1989; Zipser 1977; Rutledge et al. 1988; Jorgensen and Smull 1993; Fovell and Ogure 1988; Biggerstaff and Houze 1991a,b). Rear inflow first develops behind high-reflectivity cores, and as these cores mature, intensifies and expands rearward (Miller et al. 2020; Rutledge et al. 1988; Klimowski 1994). This process is enhanced once a stratiform precipitation region develops and the diabatic heating in the mesoscale updraft creates a mesolow which further accelerates the rear inflow. When strong RIJs descend to the surface, they bolster the outflow causing the convective line to bow and priming the environment for mesovortices to form (Wheatley et al. 2006; Trapp and Weisman 2003; Przybylinski and DeClaire 1985; Jorgensen and Smull 1993; Jorgensen et al. 1997; Klimowski et al. 2000; Przybylinski 1995; Schaumann and Przybylinski 2012). The descent of the RIJ to the surface is thought to be a main driver of severe straight-line winds in MCSs either by descending directly to the surface through favorable mesoscale pressure gradients or by providing a source of strong horizontal momentum that is then transferred to the surface via vertical advection in convective downdrafts (Smull and Houze 1987; Mahoney et al. 2009). One bow echo apex observed during BAMEX confirmed this hypothesis with descending rear inflow producing F-0 intensity wind damage (Wheatley et al.

2006). More recently it has been shown that the RIJ is the main driver of bowing segments that make the environment more favorable for mesovortex development with many observed and modeled mesovortices having an enhanced RIJ in the bow apex just south of them (Flournoy and Coniglio 2019; Trapp and Weisman 2003; Atkins and St. Laurent 2019a; Wakimoto et al. 2006b; Atkins et al. 2005; Schaumann and Przybylinski 2012; Newman and Heinselman 2012; Xu et al. 2015). Overall, the RIJ is not only an important component of MCS dynamics but also a large factor in the development of severe winds via bow echoes and mesovortices.

Besides the focus of Rotunno et al. (1988) and many later studies on the balance between cold pool vorticity and ambient shear vorticity for controlling the structure of squall lines, the direct impact of cold pool properties on severe winds has not been studied in much detail, other than a recognition that strong negative buoyancy tends to be associated with stronger downdrafts, colder cold pools, and stronger near-surface outflow winds related to the enhanced mesoscale high pressure near the surface (Fujita 1981). Analyses from supercell-related studies and simulations showed that warmer cold pools tend to favor tornadogenesis since the reduced magnitude of negative buoyancy of the cold pool air parcels would be less likely to resist the dynamically-forced vertical stretching that contributes to the low-level mesocyclone and main rotating updraft (Markowski et al. 2002; Shabbott and Markowski 2006; Markowski and Richardson 2014). For MCSs, in addition to an association with stronger outflow winds, colder cold pools can reinforce the solenoidal circulation along the leading line gust front which increases low-level forcing and causes stronger leading line updrafts when the low-level shear is sufficiently strong to counter the cold pool circulation. Therefore, the cold pool characteristics that increase tornadogenesis likelihood in a supercell may not apply to a cold pool-driven MCS. Atkins and St. Laurent (2009a) noted that warmer cold pools decrease the likelihood of mesovortex formation due to weaker ground-relative winds and low-level circulation. However, despite multiple studies on mesovortices finding that the vorticity is initially baroclinically generated in the cold pool, the relationship between the magnitude of the baroclinic vorticity and the strength of the cold pool is not clear (Atkins and St. Laurent 2009b; Trapp and Weisman 2003; Wakimoto 2006b; Flournoy and Coniglio 2019). Using StickNet data (Weiss and Schroeder 2008), McDonald and Weiss (2021) found that potential temperature deficits nearest tornadic mesovortices were much larger than any other region within the MCS. Engerer et al. (2008) utilized Oklahoma mesonet data to analyze cold pool properties from 39 MCSs but mainly focused on the mean potential temperature deficit and surface pressure rises over the MCS life cycle. They noted that mean wind gusts are above 15 m s^{-1} for the complete life cycle with the strongest winds from individual MCSs increasing with convective system age. However, the overall relationship between cold pool deficits and severe straight-line winds has received little attention.

As introduced earlier through discussion of the impacts of the RIJ, another crucial factor in severe wind production is convective momentum transport (CMT), the transport of higher momentum air downward via convectively driven downdrafts, which has been discussed in more generic terms in multiple studies as being important to the forcing of severe near-surface winds (Foster 1958; Johns and Doswell 1992; Wesiman 1992; Geerts 2001; Kuchera and Parker 2006). CMT can be broken down into three main components: the pressure gradient acceleration in mid-level flow, the vertical transport of the horizontal environmental wind, and the vertical transport of the storm perturbation horizontal wind (Mahoney et al. 2009, Mahoney and Lackmann 2011). Looking at CMT from an Eulerian and Lagrangian framework, Mahoney et al. (2009) showed that MCS motion is largely impacted by the vertical transport of horizontal storm perturbation and environmental wind. In fact, the descent of a RIJ into an intensifying mesovortex would be a prime example of the aforementioned terms leading to severe surface winds. While CMT does not necessarily explain the exact feature that causes the severe winds (i.e. mesovortex vs microburst), it describes an integral process inherent in the overall MCS structure. Furthermore, CMT can be tied to both leading line severe winds with vertical advection driven by strong, convectively generated downdrafts and severe winds farther rearward mostly by vertical advection of the RIJ momentum (Mahoney and Lackmann 2011).

Most of the physical processes described above are primarily driven by dynamic pressure perturbations (e.g., from mesovortices) or by buoyancy pressure perturbations (e.g., from cold pools) which can be decomposed from the total pressure perturbation as described in Rotunno and Klemp (1985). Trapp and Weisman (2003) used this decomposition technique to diagnose the forcing for the horizontal acceleration of wind trajectories in idealized severe MCSs by separating the perturbation pressure into the buoyancy and dynamic components, with the latter further decomposed into a vorticity component. They found that while the buoyancy forcing was associated with most of the parcel's acceleration over the entire period, the contribution from vorticity especially towards the end of the trajectory was three times that of the buoyancy forcing. This showed that mesovortices were responsible for the strongest low-level winds. Pressure decomposition can also be used to explain changes in the vertical velocity of trajectories as shown in equation (9) of Doswell and Markowski (2004). They showed that by combining the thermal buoyancy with the perturbation pressure buoyancy, the total buoyancy can be determined independent of the base state. Any change in the selection of the base state on the thermal buoyancy component will be offset by the buoyancy pressure perturbation so that the sum remains the same regardless of base state selection. By looking at the buoyancy and dynamic terms in the vertical and horizontal in this manner, a more complete picture of trajectory accelerations will be presented here.

One of the main factors for nocturnal MCS severe wind production is the extent to which the system is surface-based. Surface-based in this study is defined as MCSs that have a surface-based cold pool as the primary lifting mechanism so that convective line updrafts are ingesting surface-based parcels (eg. Miller et al. 2020). Observations from multiple PECAN cases (Flournoy and Coniglio 2019; Miller et al. 2020; Parker et al. 2020; Parker 2021) and modeling simulations of MCSs in environments with near-surface stable layers (Parker 2008; Bryan and Weisman 2006, Parker 2021) all show severe wind production occurring after a transition from elevated to surface-based or a cessation in severe wind production once an MCS becomes elevated. Once these nocturnal MCSs become surface-based, processes similar to their diurnal counterparts can occur and lead to severe winds at the surface. For example, all PECAN cases simulated in Parker (2021) produced some severe surface winds. Note that most of the few studies involving nocturnal MCSs from PECAN (Parker 2020; Flournoy and Coniglio 2019) have focused on the contribution of mesovortices to the observed severe winds. However, the Miller et al. (2020) analysis of the 26 June MCS using radar analyses showed no evidence of a mesovortex and attributed the severe winds to a traveling microburst.

Two PECAN MCS cases have been selected to cover many possible mechanisms of severe wind production from isolated, sporadic severe winds to extensive swaths: the 26 June MCS over Kansas and the 6 July MCS over South Dakota. While both of these MCSs produced severe winds, their overall evolution from convective initiation to maturation was very different. The 26 June MCS initiated well after dark from isolated, elevated convective cells. As these cells grew upscale, a surface-based cold pool developed, and convective line updrafts began ingesting surface-based parcels. This MCS continued to intensify and eventually produced multiple wind LSRs across northern KS into MO. On the other hand, the 6 July MCS over South Dakota initiated in the afternoon and was initially a severe, surface-based bowing line. Around 0000 UTC, another convective line formed along a cold front and grew upscale after dark. The bowing and linear MCSs merged and weakened before entering the PECAN domain. It is unknown what impact overall morphology of nocturnal MCSs has on surface severe wind production. For the 6 July MCS, it is hypothesized that mesovortices will have a larger impact on severe wind production compared to the 26 June case. The only other documented severe winds from a nocturnal MCS during PECAN was the traveling microburst in the 26 June case. Due to the lack of observations of the MCS in the greater Kansas City area, it is unknown if the severe wind processes changed as the system intensified and wind LSRs increased in number and density. The goal of this study is to utilize data from deterministic WRF simulations of two severe MCSs during PECAN to diagnose severe wind processes in nocturnal MCSs.

Chapter 2: Methods

2.1 WRF Model Set-up

The Advanced Research core of the Weather Research and Forecasting (WRF) Model (the WRF-ARW; Klemp et al. 2007, Skamarock and Klemp 2008, Skamarock et al. 2008) version 3.9 was used to produce simulations of two MCSs observed during PECAN with three nested grids. The outermost nest (D01) with 3 km horizontal grid spacing covered an area surrounding the MCSs and their regional environment with output every hour. D01 surrounded a smaller nest (D02) with 1-km grid spacing that fully encompassed convective initiation (CI) and MCS maturation with output every 10 minutes. Finally, a third domain with 333-m grid spacing (D03) was nested inside D02 to focus on the main area of severe winds within the MCSs with output every 5 seconds. The configuration of the WRF simulations is summarized in Table 1.

2.2 Vertically-Integrated Ice (VII) Nudging

Control runs of both MCSs without any supplemental data assimilation beyond the standard WRF initialization (i.e., "cold starts" from the NAM initial condition at various times) were conducted but neither were able to properly capture CI and subsequent MCS development and maturation. Therefore, steps were required to increase the accuracy of the initialization of convection in the simulations. This study explores – and improves upon – a technique that introduces convection into numerical simulations through modifying the vertical distribution of ice hydrometeor mixing ratio, or the vertically-integrated ice (VII). The method of assimilating vertically integrated ice (VII) was based on the lightning data assimilation (LDA) technique described in Fierro et al. (2012, 2014, 2016, 2019). This method assumes that in areas where lightning is active, updrafts with a mixed-phased region must also be present for inductive charging. In the Fierro method, data from Earth Networks Total Lightning Network (ENTLN) is mapped to the WRF grid, and wherever lightning exists in a grid cell, the water vapor mixing ratio is increased in a column between 0 and -20°C. The amount of water vapor added to the column is based on a hyperbolic tangent function with stronger nudging for higher magnitudes of lightning flashes. While this method is effective for generating convection without resorting to more complicated DA techniques, it is not able to account for the initial convective stage where cells are developing and maturing before lightning is produced. Also, lightning is not always exactly colocated with convective updrafts, e.g., extensive areas of lightning have been observed in the stratiform region of mesoscale convective systems. VII was selected over lightning since it is highly correlated with convective updrafts and is indicative of updrafts strong enough to penetrate above the freezing level. Columns of VII will generally precede lightning due to lightning formation being dependent not only on the presence of a mixed phase region but also on ample time for charge separation and electric potential to develop.

Although direct observations of VII do not exist, proxies can be derived from radar observations. The VII fields used in this study were generated from the multi-radar multi-sensor (MRMS) product which uses gridded RAP output to sum VII between 0 and -20°C and produces output fields approximately every 2 minutes. Like the methods described for lightning data in the Fierro papers, VII from multiple radar volumes is summed over a 10-minute period that corresponds to the assimilation window used in this study. Since VII is more representative of an updraft, the incremental increase in q_v is applied to a different portion of the column than the mixed phase region used in the original LDA method. The lifted condensation level (LCL) and level of free convection (LFC) were defined for both cases using built-in functions within the WRF python package along with in-situ soundings launched during the PECAN field campaign to determine an approximate temperature level for the cloud base. Based on those values, nudging was applied to the 15-5°C layer to more accurately reflect where updrafts would be initiating. While the original LDA method nudged over a 20°C depth, a smaller window was chosen to limit updraft magnitudes in both cases to more representative values because the nudging is done at higher temperatures and thus produces higher CAPE parcels. Finally, the overall window for nudging as detailed in Table 2 was selected subjectively based on trial and error. The windows and times selected for VII assimilation for each case produced simulated reflectivity that subjectively best resembled the observed reflectivity during the severe phases of the MCSs while also allowing the 333 m nest to be initialized from the 1 km nest without requiring any additional nudging. This ensures that the nudging is not interfering with any processes related to severe wind production on the 333 m grid.

2.3 Trajectory Calculations

To explore the airflow within the simulated MCSs, output from D03 was saved every 5 seconds and then interpolated to a set height field that reflects the original WRF stretched vertical levels. These files were then used to calculate backward trajectories following an iterative method described by Seibert (1993) and Flournoy and Coniglio (2019). Variables such as vorticity and buoyancy were calculated along these trajectories while other variables computed directly in the WRF code were interpolated from the WRF grid to the trajectory point every 5 s. Prior to backward trajectories being computed, the WRF output was run through a pressure decomposition code developed by George Bryan based on methods described in Rotunno and Klemp (1982) and Weisman and Rotunno (2000) which computes the perturbation contribution from buoyancy pressure (p_b') and both the linear and nonlinear dynamic pressure (p_d'). Combining the WRF output and the pressure decomposition output allows for gradients of p_b' and p_d' to be calculated along the trajectory to diagnose the severe wind processes. A component of the full buoyancy forcing is thermal buoyancy, which requires the definition of a base state. Various times and locations were tested for a base state and overall the patterns in the buoyancy and dynamic fields were not sensitive to base state choice. The base state for both cases was defined using a 200 x 200 km box in the outer domain (3 km horizontal resolution) at 0400 UTC that covered the inflow environment and by averaging relevant variables over this box at every vertical level. The thermal buoyancy calculated from this base state was added to the vertical acceleration due to p_b' to get the full buoyancy forcing that is independent of the base state as described in Doswell and Markowski (2004). The horizontal gradient of p_b' and p_d' was calculated locally along the trajectory so that changes in the horizontal wind speed due to buoyancy and dynamics separately could be calculated as in Trapp and Weisman (2003). The aforementioned base state was also utilized to calculate CMT which breaks down the downward transportation of the environmental wind (CMT_0) and the perturbation wind induced by the MCS (CMT') (Mahoney and Lackmann 2011, equation 1).

2.4 Diabatic Lagrangian Analysis (DLA)

To complement the severe wind analysis from the 25-26 June simulation, thermodynamic variables of the surface severe wind event captured in the radar analysis were needed. Fig. 9 of Miller et al. (2020) was only able to show the kinematic and reflectivity fields due to the limitations of the radar analysis. Thermodynamic information such as potential temperature can be very useful for analyzing cold pool properties such as deficit, depth, and buoyancy but cannot be derived from a 3-D wind field. To address this gap, a model-like thermodynamic retrieval was conducted. The Diabatic Lagrangian Analysis (DLA) is a kinematic thermal-microphysical continuity retrieval of heat and water substance based on integration along Lagrangian trajectories that proceeds from a series of input time-varying 3-D wind-reflectivity analyses

(Ziegler 2013a,b; DiGangi 2016). Output fields include predicted potential temperature (Θ), water vapor mixing ratio (q_v) cloud water (q_c), and cloud ice (q_i), as well as derived temperature, virtual potential temperature, and other variables. A DLA grid domain is nested within the portion of the radar analysis domain containing the best overall multi-Doppler radar coverage from the radar analysis presented by Miller et al. (2020). Backward 3-D trajectories are then computed with a 20 s time step from all DLA gridpoints into the MCS inflow environment, and inflow-environmental point values of pressure, temperature, and relative humidity are initialized from a selected sounding. Due to the large number of soundings launched during the IOP, there are three separate soundings to represent the environments both ahead of and behind the developing MCS.

Following trajectory initialization, a system of heat and water substance-conserving ordinary differential equations is integrated forward in time along each trajectory path. Using airflow and dBZ values, these calculations diagnose snow, graupel/hail, and rain mixing ratios as well as parameterized rates of collection/riming, freezing/melting, and deposition/sublimation at every Lagrangian point along the DLA trajectories. Forward integration along all trajectories back to their gridpoints of origin, combined with a final gathering operation, yields the 3-D analysis fields at a particular analysis time. The DLA domain used in this study is 90 km x 90 km by 15 km, with 500 m grid spacing that is periodically moved to follow MCS motion.

Chapter 3: Case Overview

3.1 25-26 June 2015 (IOP 16)

The PECAN domain in northeastern Kansas was located in a Storm Prediction Center (SPC) Slight risk area corresponding to a predicted probability of damaging winds and damaging hail of 15% within 25 mi of a point. The 2000 UTC convective outlook noted that for northern Kansas into northern Missouri "OTHER STORMS ARE EXPECTED TO DEVELOP ALONG AND JUST NORTH OF E-W BOUNDARY WHERE STEEP LAPSE RATES WILL EXIST AND THE ATMOSPHERE WILL BECOME MODERATELY TO STRONGLY UNSTABLE. GENERALLY WEAK SHEAR WILL SUPPORT MULTICELL STORM MODES WITH ISOLATED DAMAGING WIND AND LARGE HAIL THE MAIN THREATS". While SPC forecasters highlighted the PECAN domain in the outlook, there was not any discussion of upscale growth into an MCS to continue the severe wind threat into the nighttime hours. Isolated cells initiated on the cool side of the aforementioned E-W boundary around 0230 UTC in northeastern Kansas and slowly grew upscale into an elevated convective line. This line then matured and entered the PECAN observational domain. Between 0400 and 0430 UTC, the line developed a surface-based cold pool and began ingesting surface parcels into convective line updrafts (Miller et al. 2020). After the elevated to surface-based transition, the MCS developed a bowing segment to the southwest of the original line and produced its first local storm report (LSR) for severe winds at 0521 UTC. While this severe wind event was observed within the PECAN domain, the MCS continued to intensify and produce multiple bowing segments after it exited the PECAN domain. This is where the majority of LSRs for winds occurred and will be the focus of this modeling study. An interesting note is that this MCS outperformed expectations as the extent and severity were not anticipated by the PECAN investigators. A detailed description of the radar and in situ PECAN observations from the 26 June 2015 Kansas MCS can be found in Miller et al. (2020). Further information about the 26 June 2015 PECAN MCS can be found in Degelia et al. (2019), Parker et al. (2020), and Parker et al. (2021).

3.2 5-6 July 20165 (IOP 20)

The PECAN domain in Southeastern South Dakota was located in a SPC Enhanced Risk area corresponding to the predicted probability of damaging winds and damaging hail being 30% and the probability of a tornado being 5% within 25 mi of a point. The t2000 UTC convective outlook noted that "MORE INTENSE DEVELOPMENT SHOULD OCCUR ALONG THE COLD FRONT FROM CNTRL AND ERN SD INTO MN LATER...COINCIDENT WITH AN INCREASE IN DEEP-LAYER FLOW AND FORCING. EXPECT INITIAL STORMS TO POSE SOME CHANCE FOR A TORNADO OR TWO AS WELL AS LARGE HAIL BEFORE TRANSITIONING INTO QUASI-LINEAR SYSTEM WITH GREATEST CHANCE FOR DAMAGING WINDS CONTINUING INTO THE NIGHT ACROSS PORTIONS OF ERN SD AND MN". Unlike the 26 June PECAN MCS, the 5-6 July MCS was expected to produce prolific severe winds by both SPC and PECAN forecasters. A bowing MCS developed around 2100 UTC on 5 July in south central South Dakota and propagated eastward. This bowing MCS produced multiple wind reports west of the PECAN observational domain during the late afternoon and early evening hours. Farther east, a linear MCS developed along a cold front draped across South Dakota and Minnesota from initially isolated convective cells. This line grew upscale and slowly propagated south ahead of the severe MCS approaching from the west. These two MCSs collided and merged between 0300 and 0400 UTC leading to a disorganized convective system by 0400 UTC with the bowing segment weakening and convection initiating in the inflow of the linear system. The MCS reorganized between 0500 and 0600 UTC and produced a brief EF0 tornado near the intersection of the two original MCSs. Severe wind reports followed after this reorganization period and will be the focus of this study. Unlike the 26 June MCS, this case underperformed PECAN investigator expectations and did not produce the extensive severe winds throughout the later evening and early nighttime hours expected by forecasts. Other detailed analyses of the 5-6 July MCS can be found in Flournoy and Coniglio (2019), Bodine and Rasmussen (2017), Chipilski et al. (2020), and Parker (2021).

Chapter 4: Observational Results

4.1 Ground Verification of DLA

Results from the DLA are first presented to provide an observation-based analysis of the 25-26 June 2015 MCS to supplement the analysis of the same event presented in Miller et al. (2020). These observation-based analyses are used to assess the realism of the WRF simulations of this event. Between 0300 and 0600 UTC, multiple mobile mesonets (MM) and mobile sounding platforms (MGs) were within the radar analysis domain and provide observations to compare to the DLA. For comparison, surface Θ and q_v were chosen since Θ is a conserved temperature variable and surface water vapor is an important parameter both for cold pool development via evaporation and for updrafts that feed on warm, moist inflow air. Some platforms such as the NOAA X-band polarimetric radar (NOXP) scout vehicle and two of the radiosonde platforms were stationary throughout the period. However, two mesonets were mobile during the period and sampled multiple portions of the MCS inflow and outflow.

An overall comparison of the various MM surface measurements of Θ and q_v subtracted from the DLA values is shown in Fig. 1. Overall, the DLA has a warm bias in Θ and a moist bias in water vapor mixing ratio, however, the magnitude varies between the platforms. There also is no clear delineation in the average differences between stationary platforms (NOXP, MG1, and MG2) and mobile platforms (MM1 and MM2). For example, NOXP has the highest average difference in Θ at 2.58 K but the lowest average q_v difference of 0.37 g kg^{-1}. NOXP sampled the northern portion of the domain more than any platform so the high average Θ difference may reflect on the DLA overestimating surface temperatures not associated with a strong cold pool. Most of the average differences in Θ are between +1 and +1.5 K. There is also a trend in the Θ differences being a bit higher at the beginning of the observation period and decreasing with time for MM2, MG1, and MG2. Despite MG1 and MG2 being co-located, MG2 has a larger average difference in Θ than MG1 but the reverse is true for q_v. Any differences between MG1 and MG2 show variability between the two platforms rather than differences in DLA values due to them being located in the same DLA gridpoint and provide an estimation of observational uncertainty inherent in this particular analysis. MM1 had the highest average Θ difference (excluding NOXP) whereas MM2 had the lowest average Θ difference along with MG1. While both of these platforms were mobile, MM1 stayed farther north in the domain compared to MM2 which further supports the idea that the DLA struggled the most with surface Θ farther north in the domain. On the other hand, the q_v average difference between the platforms does not follow the same pattern as average Θ differences since NOXP has the lowest average difference and MM2 has the highest. The water vapor mixing ratio also shows more variability in the differences with more time periods having a negative difference (DLA is drier than observations) compared to Θ. Overall, the relatively small average differences in Θ between 1 and 1.5 K and in q_v between +0.4 and +1.1 g kg^{-1} lend credibility to utilizing the DLA for thermodynamic information in MCSs.

Focusing on individual platforms, Fig. 2 shows the Θ and q_v values for the DLA and MM1 throughout the time period. DLA values for Θ and q_v are consistently above MM1 observed values until 0400 UTC (28 hours (fph), 24 + however many hours since 0000 UTC). Before 0400 UTC, MM1 was driving north in the pre-MCS inflow environment indicating that the DLA overestimated the temperature within the inflow environment. After 0400 UTC, the DLA is still generally warmer and moister than the MM1 measurements but there is much more variability in the magnitude of the difference. The other mobile platform, MM2, shows a similar increase in the variability of the magnitude after the passage of the cold pool around 0430 UTC

(28.5 fph) (Fig. 3). The slope of the temperature drop after 0430 UTC is similar for both the DLA and MM2 despite the DLA having generally warmer Θ values. After 0500 UTC (29 fph), the difference between DLA and MM2 Θ becomes quite small. This shows that the DLA performs better in the cold pool than in the inflow environment. The water vapor mixing ratio does not show the same pattern as Θ for MM2 and is consistently too moist the entire time period, especially during the initial cold pool passage.

NOXP experienced cold pool passage between 0440 and 0445 UTC (28.67 to 28.75 fph) as shown in the Θ decrease (Fig. 4a). While the DLA was much warmer than NOXP for the majority of the time period, around 0500 UTC (29 fph) the Θ values are biased less than 1 K. For q_v, the DLA has a moistening trend whereas NOXP observations show a drying trend before cold pool passage (Fig. 4b). After cold pool passage, the overall difference in magnitude between the DLA and NOXP observations decreases once again showing that the DLA performs better post outflow passage. A similar trend is apparent in the other two stationary platforms, MG1 and MG2. DLA Θ values for both MG1 and MG2 are consistently 1.5 K higher than observations until cold pool passage after 0500 UTC (29 fph) (Fig. 5a, 6a). Trends in q_v are improved compared to NOXP with the DLA q_v approximately constant while MG1 and MG2 show a drying in the inflow environment (Fig. 5b, 6b). Post cold pool passage, the difference between the DLA and both MGs is below 1 g kg^{-1}. While the DLA has a warm and moist bias overall, post cold pool DLA Θ and q_v values are close to the observed values by the various in situ platforms. All further discussion of DLA output will consider this bias and lend more credence to post cold pool values.

4.2 Severe Winds at 0510 UTC

0510 UTC was the earliest radar analysis that showed winds over severe limits at the surface. These severe radar-analyzed winds are only 11 minutes off from an LSR at 0521 UTC. Fig. 7 shows negative Θ_v' covering most of the area behind the outflow boundary with values down to -6°C. The southernmost pocket of cold air is associated with the strengthening bowing segment driven by a large swath of anticyclonic flow. Within this flow, there is an associated maximum in negative vertical vorticity about 10 km to the west of one of the Doppler-on-Wheels (DOW) radars (labeled DOW8 in Fig. 7b) that seems to extend south along the edge of the outflow boundary (Fig. 7b). While there are localized maxima in positive vertical vorticity along the leading edge of the outflow, none of them are strong enough or last long enough to be considered as a mesovortex and they appear to remain mostly in the inflow region. Since there is no consensus on criteria for a mesovortex, the mesovortex criteria in this study is based on a vertical vorticity threshold around 0.013 s^{-1}. This was determined by assuming an axis-symmetric vortex with a ΔV of 10 m s^{-1} over a 2-3 km width (Tony Lyza, personal communication, 2023). Fig. 8 shows the wind speed at the surface and the severe winds to the west of DOW8. Four trajectories flowing into the region of maximum winds come from heights between the surface and over 2.5 km, however, they all follow a similar path. All the trajectories show a sharp turn to the southwest when they encounter the MCS outflow followed by a turn to the southeast as they follow the northwesterly, anticyclonic flow of the near-ground wind field. Finally, there is a gradual descent towards the end of the trajectories as they flow into the wind speed maximum.

To better understand how the severe winds at 0510 UTC developed, a trajectory that ends near the center of the wind maximum is analyzed in time and space. Fig. 9 shows a trajectory with its approximate location at five-minute intervals that align with radar analysis times. Similar to the trajectories shown in the spaghetti plot, this trajectory initially turns to the southwest as it interacts with the MCS outflow around 0430 UTC and begins its turns to the southeast at 0445 UTC. At 0445 UTC, the trajectory reaches its peak height (1.2 km) and begins its descent until the final analysis time. Fig. 10 shows the trajectory's location at 0450 UTC with a northwest-to-southeast oriented cross-section. Fig. 10a shows the parcel on the back edge of a reflectivity core around 50 dBZ within a weak downdraft. Windspeed (Fig. 10c) shows a local maximum of 16 m s^{-1} at the surface downstream of the weak downdraft. Θ_e shows that the downdraft toward the rear of the line contains air descending from higher altitudes unlike the weak downdraft the parcel is in and Θ_v' shows the negative buoyancy of the parcel (Fig. 10b, 10d). The bottom two panels show trajectory cumulative cooling due to rain evaporation and graupel melting (Fig. 10e, 10f). Unlike the other fields which are instantaneous values of the analysis, the cumulative plots show the total cooling that has occurred along the trajectory (and the surrounding grid points) up until the shown analysis time. For example, the parcel has experienced 3°C of cooling from rain evaporation and 1°C of cooling from graupel melting for a total of 4°C of diabatic cooling. Notice that the weak downdraft is superimposed between a region of higher values of rain evaporative cooling and graupel melting.

Five minutes later at 0455 UTC, the parcel is directly downstream of a much stronger downdraft at the back edge of a reflectivity core and at the leading edge of higher wind speeds just downstream (Fig. 11a, 11c). Compared to 5 minutes prior, this downdraft at 0455 UTC appears to be associated with a significant depression in the Θ_e values and is in a larger area of cooler Θ_v' values (Fig. 11b, 11d). While rain evaporative cooling values have not increased for the parcel itself, the cooling rates at the bottom of the downdraft are much larger and suggest that this increase in downdraft magnitude is being driven by diabatic cooling (Fig. 11e). Unlike rain evaporative cooling, graupel melt cooling has increased to 2°C implying a 1°C change in a 5 minute period (Fig. 11f). Similar to rain evaporative cooling values being maximized at the bottom of the downdraft, graupel melt cooling is maximized in the core of the downdraft which further points to diabatic cooling processes.

At 0500 UTC, the parcel is in a downdraft of -2 m s^{-1} below 1 km AGL within the convective line (Fig. 12a). Θ_e values have decreased for the parcel by about 3°C and Θ_v' values have decreased by over a degree compared to five minutes prior (Fig. 12b, 12d). This seems to be primarily driven by rain evaporative cooling on the order of 2°C in the past 5 minutes whereas there was no change in the cumulative graupel melt cooling (Fig. 12e, 12f). This is most likely due to the parcel being below 1 km AGL where rain evaporation processes dominate. However, the overall magnitude of rain evaporative cooling has increased in the vicinity of the parcel as well as graupel melt cooling in the core of the downdraft in the last 5 minutes. There are also higher wind speeds associated with the downdraft as in previous times as well as a localized maximum at the surface downwind of the weak downdraft in which the parcel resides (Fig. 12c).

At 0505 UTC, approximately 5 minutes before the severe winds at the surface, the parcel is about 5 km ahead of a downdraft behind a reflectivity core (Fig. 13a). Associated with this downdraft, is a large area of winds around 22 m s^{-1} extending from 500 m above ground to just under 3 km (Fig. 13c). Θ_e is depressed under the downdraft and in general Θ_v' values are similar to the previous analysis (Fig. 13b, 13d). Looking at the cumulative graupel melt cooling, the maximum magnitude of cooling has increased to 8°C just downstream of the downdraft but within the higher wind speed core (Fig. 13f). The graupel melting cooling on the parcel itself has not changed in the past 5 minutes. However, the cumulative cooling due to rain evaporation for the parcel has increased by 1°C since the previous analysis (Fig. 13e).

At the severe wind analysis time, the maximum in severe winds at the surface is directly downstream of a strong downdraft with a leading line updraft just upstream of the severe winds at the surface (Fig. 14c). This positioning implies a dynamically induced acceleration between a localized high-pressure perturbation at the base of the downdraft and a localized low-pressure perturbation at the base of the updraft. When this dynamic acceleration is added to the background rear-to-front flow and the downward accelerations induced by the negative buoyancy due to cumulative rain evaporative cooling, winds at the surface are enhanced and exceed severe levels. The cumulative rain cooling magnitude is 7°C at the parcel at the time of the severe winds with 4°C of the cooling occurring in the past 15 minutes of the parcel's trajectory (Fig. 14e). Furthermore, the graupel melt cooling contributing to the main downdraft behind the wind maximum has also increased its cooling maximum by another 1°C in the past five minutes further contributing to the negative buoyancy driven by diabatic cooling (Fig. 14f). Θ_v' continues to be maximized within these downdraft cores (Fig. 14d). The differences in the diabatically cooled air versus the warmer air in the updraft is clearly shown in Θ_e with the air of maximum winds straddling the two air masses (Fig. 14b).

4.3 Sub-Severe Winds at 0520 UTC

At 0521 UTC, a LSR was noted for wind just south of DOW8, labeled W (Fig. 15). The radar analysis does not show wind speeds above severe limits at this time; however, the DLA in the area in which this LSR occurred does show similar characteristics to the analysis 10 minutes prior described above. The surface Θ_v' shows a large area of -6°C perturbation just upwind of the LSR. Just south of the LSR, the kinematic boundary of the southerly outflow was ahead of the thermodynamic boundary at the edge of the cold pool with the LSR located just on the cool side of the largest temperature gradient. Overall, the magnitudes of the temperature decrease are similar to those at 0510 UTC (Fig. 7), however, the area of the coldest perturbations has increased. Looking at vertical vorticity at the surface, there are a few vorticity maxima along the leading edge of the kinematic outflow (Fig. 15b). However, the LSR is embedded in an area of negative vertical vorticity, though it is weaker in magnitude than at 0510 UTC (Fig. 7b).

The largest surface wind speed at 0520 UTC is 22 m s^{-1} just south of DOW8 and about 10 km to the north of the location of the LSR (Fig. 16). Unlike at 0510 UTC there are two areas with wind speeds higher than 20 m s^{-1}, one along the leading edge of the outflow and another about 10 km to the northwest. The spaghetti plot of trajectories in these wind maximums shows the air comes from two distinct regions. The leading line winds mainly come from the inflow below 1 km and follow a similar path to the trajectories at 0510 UTC. A selected trajectory details the exact path of a parcel in the leading wind maximum with this trajectory in the inflow moving to the northwest until 0500 UTC (Fig. 17). After 0500 UTC, the parcel descends as it flows to the southeast with the largest accelerations in the last 5 minutes of the trajectory. The other trajectories going into the leading wind maximum are similar in their history. On the other hand, the trajectory in the rearward wind maximum starts around 1.2 km well to the rear of the convective line, ascends to 2.3 km around 0450 UTC, and descends in the rear-to-front (RTF) flow over the next 30 minutes (Fig. 18).

While the two trajectories described above both end with sub-severe wind speeds, their different evolution implies a different missing ingredient for severe winds at the surface. Looking at a cross-section through the leading line trajectory, the parcel within the RTF flow terminates at 0520 UTC right below a weak downdraft located within a local reflectivity core around 45 dBZ (Fig. 19a). Wind speeds near the surface are between 20 and 22 m s^{-1} just below the downdraft and the maximum is localized below 1 km (Fig. 19c). Θ_v' is larger in the base of the updraft than the surrounding cold pool air (though still negative overall) and this warming is reflected in Θ_e as well, which implies that compressional warming is countering the diabatic cooling to limit the magnitude of the Θ_v perturbations (Fig. 19b, 19d). The trajectory's cumulative cooling from rain evaporation is only 2°C with no cooling due to graupel melting which illustrates the overall lack of diabatic cooling for this trajectory (Fig. 19e, 19f). Compared to the severe wind trajectory at 0510 UTC, the leading line trajectory at 0520 UTC is lacking strong diabatic cooling despite the kinematic impacts of a downdraft reaching below 1 km.

While the more rearward trajectory has a different evolution than the leading line trajectory, the wind speed maximum magnitude and reflectivity values of the parcel are approximately the same as those within the leading line (Fig. 20a, 20c). However, unlike for the leading line trajectory, Θ_e values in the wind speed maximum are cooler compared to the surrounding cold pool environment and Θ_v' shows the parcel trajectory terminating just above very cold air at the surface within an overall colder environment (Fig. 20b, 20d). The diabatic cooling for this trajectory was much more similar to the severe wind trajectory at 0510 UTC than the leading line trajectory at 0520 UTC with cumulative cooling of 5°C from rain evaporation and 4°C from graupel melt (Fig. 20e, 20f). So in this trajectory, while having ample amounts of diabatic cooling, the lack of kinematic support from a downdraft keeps the wind speed sub-severe near the surface.

Chapter 5: Simulation Results

5.1 Comparison of WRF Simulation to Observations

For the initial comparison of the 26 June case, the composite reflectivity from MRMS from 0400 to 0700 UTC and composite reflectivity derived from D02 of the WRF simulation at the model time equivalent are shown side by side (Fig. 21). VII DA allowed the portion of the simulated MCS over north central Kansas and far southeast Nebraska to be in approximately the correct location (on scales of a few tens of kilometers) at 0400 UTC (when DA nudging was stopped) and also have upscale growth into a quasi-linear convective system with a structure and shape similar to the observed system. While the convection to the east over Missouri is stronger in the simulation than observations, inflow into the MCS mainly originates from the unstable airmass over east Kansas and therefore the spurious convection over Missouri should not greatly impact the portion of the MCS that is of interest here. By 0500 UTC, the bowing segment on the southwest part of the QLCS over northeast Kansas is shown in MRMS reflectivity and is represented as a developing N-S line segment on the far western edge of the simulated QLCS. Furthermore, the convective cells along the back edge of the observed system over north-central Kansas are captured in the simulations though their intensity coverage and intensity is not quite as high. By 0600 UTC the eastern portions of the QLCSs over far northeast Kansas in both the simulated and observed MCS have rotated to be less SW-to-NE and more E-to-W oriented. While the simulated system is slightly farther north than in observations, the overall structure is quite similar. At 0700 UTC, the overall structure with a weakening N-to-S oriented bow appendage on the western portion of the QLCS and more E-to-W oriented widespread convection within the eastern portion of the line is well captured, although the storm-scale details of the individual convective cells show some differences. Overall, the VII nudging allowed for an MCS to develop and intensify in the same region as the observed MCS and follow a very similar progression throughout its most intense period.

The 5-6 July case was a bit more difficult to simulate due to the complex situation of two merging MCSs prior to the period of scattered severe winds and an EF0 tornado. At 0000 UTC, a compact SW-to-NE oriented MCS with small-scale bowing segments developed in south-central SD, which is represented well in the simulation (Fig. 22). However, spurious convection occurs in many places throughout the simulation surrounding the MCS of interest. By 0200 UTC, the bowing MCS and a cold front-forced linear MCS have merged in the simulation while they are still separate in observations. However, aided by the VII DA over the previous 4 h, the simulation by 0400 UTC shows a convective system with a general orientation and footprint similar to the observed MCS, although the exact placement of the individual convective cells within and surrounding the main convective line differ, along with a lag in the development of a new convective line ahead of the main line in observations. The 3 h period after 0400 UTC is when most of the scattered severe winds and an EF0 tornado were observed and is the period selected for detailed analysis. At 0600 UTC, the broad structure of the simulation – in terms of a large, elongated convective system oriented from SW-to-NE with a more N-to-S oriented portion on its western end – resembles the observations in SE SD where the PECAN array was located and where the nested grid is located. Overall, while the 5-6 July simulation did not resemble the true MCS evolution as well as the 25-26 June simulation, the simulation post-MCS merger (after ~0400 UTC) appears sufficiently close to observations and produces scattered severe surface winds within the N-to-S oriented portion of the line in the period after 0400 UTC similar to the observed patterns.

5.2 June 25-26 Bulk Trajectory Analysis

Before delving into individual severe wind trajectories, a bulk analysis of sub-severe winds (20-26 m s^{-1}), severe winds (> 26 m s^{-1}), and significant severe winds (> 33.5 m s^{-1}) was performed by finding and compiling WRF grid points in each of the three categories at z = 80 m in the D03 2 minute output. For reference, the number of points meeting the criteria was 2,033,856 for sub-severe, 653,841 for severe, and 21,663 for significant severe for 25-26 June and 4,157,545 for sub-severe, 1,452,902 for severe, and 171,165 for significant severe for 5-6 July. Due to the sheer number of trajectories, a random sample of 500 trajectories from each category was selected for further analysis. From there, 30-minute backwards trajectories from each trajectory endpoint in the random sample were calculated and the 10th, 25th, 50th (median), 75th, and 90th percentiles of relevant variables were computed every 5 s along each trajectory.

First, the x and y locations of the trajectories are compared in a normalized coordinate system with the end point of the trajectory at the origin (Fig. 23) . The overall trajectory length in space is shortest for the sub-severe trajectories with increasing length for severe and the longest for significant severe, as expected. However, what wasn't necessarily expected is that, as the wind speed category increases, a greater percentage of the long-distance trajectories come from the northeast relative to the convective line. Furthermore, the vast majority of trajectories are coming from the rear inflow of the MCS with very few exceptions in the sub-severe and significant severe categories.

The quartiles for height (z) show a trend of gradual descent with time for all 3 categories with sub-severe trajectories having the smallest Δz in the median (Fig. 24). Overall, the distributions for the sub-severe and severe categories appear very similar showing that Δz is not a sufficient statistical discriminator between the two categories. Likewise, the significant severe median Δz has a similar value to the other two categories; however, the upper quartiles show parcels that are substantially different in that they descend from over a kilometer with the strongest descent in the last 600 s of the trajectory. This indicates a separate process is occurring that induces descent on the order of -1 m s^{-1} for the significantly severe parcels that are not present for the other categories. The 10th quartile for vertical velocity shows w values down to -2 m s^{-1} for significant severe trajectories which correlates to the aforementioned trend in height (Fig. 25). Even the median dips below zero for the final 600 s of the time series aside from a brief increase right as the trajectory reaches 80 m. While the median value of w for all three categories is near zero, the distribution of the 25th and 75th percentiles for severe and significant severe winds favors negative w values implying more trajectories are descending, as expected.

Quartiles for Θ reflect a similar pattern seen in Δz and w with only the significant severe category 75th and 90th quartiles being distinct from the sub and severe trajectories (Fig. 26). Overall, all trajectories gradually cool over the 30-minute period with the significant severe showing the most cooling. This also correlates with the drop in Z and negative w values. An interesting finding is that most trajectories that terminate with > 20 m s^{-1} wind speeds cool to about the same Θ value (~296-298 K) indicating a lack of heterogeneity within the portions of the cold pool responsible for the stronger wind speeds.

To support later analyses that explore the potential impact of mesovortices on severe surface winds, the bulk values of vertical vorticity (ζ) along the trajectories were also analyzed (Fig. 27). While some individual trajectories may show positive or negative ζ, the distribution is centered on a median value near zero, and no differences in any of the percentiles among the categories are apparent. This confirms the observational analysis showing no evidence of consistent mesovortices near the strongest radar-observed winds in this case (eg. Fig. 7 & 15).

The total diabatic temperature tendency was also analyzed and showed similar trends in the medians compared to all other variables (Fig. 28). The severe trajectories show somewhat larger negative values of cooling for the 25th and 10th percentiles compared to the sub-severe trajectories. The distribution for the significant severe category once again differs the most from the other two categories and shows the largest magnitude of overall cooling, especially in the last 600 s. This indicates that the drop in Θ and height with the increased downdraft magnitude is correlated with increasing diabatic cooling which is dominated by rain evaporation (not shown). With the exception of the 90th percentile of significant winds showing some diabatic warming around 1200 s, all other trajectories show a negative temperature tendency throughout the 30-minute period. The aforementioned diabatic cooling dominated by rain evaporation is augmented by large downward vertical velocities attributed to hydrometeor loading with 25th and 10th quartiles extending to -3 m s^{-1} and -10 m s^{-1}, respectively, in the final 5 min of the trajectory (Fig. 29). Not surprisingly, the hydrometeor loading terms are dominated by rain loading, similar to the diabatic terms being dominated by rain evaporation.

5.3 Bulk July 5-6 Trajectories

Unlike the 25-26 June bulk trajectories, the 5-6 July trajectories acquired a more westerly component as the wind speed increased relative to the convective line (Fig. 30). Sub-severe trajectories are generally shorter and have a larger spread across the x-direction. Severe wind trajectories have an increased length in the y-direction indicating stronger northerly outflow and less spread in the x-direction compared to sub-severe. The significant severe trajectories appear to have a more compact region where a large portion of the trajectories originate (x: -30,000 to -12,000 m; y: -45,000 to -60,000 m), are the longest out of all 3 categories, and have the least amount of spread in the x-direction. There is a trend of increasing ΔZ over the 1800 s of the trajectory as wind speed increases across all of the percentiles (Fig. 31). Based on the median values alone, ΔZ increases from approximately 40 m for sub-severe, 140 m for severe, and 220 m for significant severe. Unlike the 25-26 June trajectories, there is a consistent decrease in Z with time across all percentiles and all 3 categories. However, both cases show trajectories descending from generally under 1 km indicating that strong convective downdrafts are not the primary reason for the majority of the strong near-surface winds in the 5-6 July case (at least in the 30 min preceding the trajectory end point). This result is also reflected in the w quartiles for all three categories with a median around zero (Fig. 32). The sub-severe category has the smallest spread of w values indicating very little vertical motion is characteristic of these trajectories. The severe trajectories are more weighted towards weak descent with the 25th percentile staying just under -0.5 m s^{-1} and the 10th percentile just over 1 m s^{-1} towards the beginning of the trajectory. The largest spread is apparent in the significant severe wind trajectories with a slight bias towards weak descent.

The distributions for Θ show more distinction between the three categories than for w with the median of the sub-severe category showing a slight warming with time as opposed to the cooling evident in the median for the severe and significant severe categories (Fig. 33). The severe trajectory median cools a little more than 1 K over 30 minutes whereas the significant severe trajectory cools about 2.5 K. However, all three categories' medians converge to the same value, around 299 K, with relatively small interquartile ranges (~1.5 K) at the termination of the trajectories, similar to the 25-26 June case.

The ζ distributions between the three categories are also similar to the 25-26 June case with all medians around zero the entire trajectory and the spread of values increasing with increasing wind speeds at the end of the trajectory (Fig. 34). The spread in ζ is larger for the 5-6

July case compared to the 25-26 June case, which could relate to the increased likelihood of mesovortices in this case (as shown later and in Flournoy and Coniglio 2019). However, the near symmetric distribution in ζ about zero indicates no clear tendency for the strength of the surface winds to relate to the ζ along the trajectories.

The total diabatic temperature tendency, which was dominated by evaporative cooling, shows increasing amounts of evaporative cooling as wind speeds increase but the instantaneous cooling tends to decrease with time along the trajectory (Fig. 35). The median values of diabatic cooling are similar for both the severe and significant-severe categories, starting around -1×10^{-3} K s^{-1}, with the sub-severe category being much smaller, less than -0.5×10^{-3} K s^{-1}. An expected trend of increasing hydrometeor loading with increases in wind speed is also observed (Fig. 36). Similar to the diabatic temperature tendency, the largest median values of hydrometeor loading are at the beginning of the trajectory and decrease in time for the sub-severe and severe category. The distribution for the significant severe category shows an increase in downward acceleration induced by hydrometeor loading through about 1200 s followed by a decrease in acceleration (although still with downward acceleration overall). However, there is a substantial difference between the sub-severe category and both severe wind categories indicating that stronger downward accelerations induced by hydrometeor loading appears to be a common occurrence along the severe and significant-severe wind trajectories.

5.4 Selected 25-26 June Trajectories

While looking at bulk trajectories can help identify general characteristics of trajectories in the three categories, it is not able to identify the individual processes causing some trajectories to accelerate above the severe threshold as opposed to others in the same vicinity. When looking at bulk trajectories, processes that force only a handful of trajectories may be lost in the median and not even show up in the 90th percentiles. The bulk trajectory analysis is also unable to show changes in characteristics in time. To address these limitations, a selection of trajectories in all 3 categories was analyzed every 30 minutes to focus on individual processes and examine how the aforementioned characteristics evolve with time.

5.4.1 0500 UTC

At 0500 UTC, the 25-26 June MCS is in the upper lefthand corner of the inner 333 m domain, limiting the region where trajectory analysis can be performed. Severe winds were sparse and concentrated in two areas where square points are shown at the end of the trajectories shown in Fig. 37b. Sub-severe trajectories, ending in circle points, were selected subjectively surrounding the severe winds to examine the forcing differences in the two trajectory types. One region of trajectories is located in a small convective core with reflectivity over 40 dBZ and the other region is within reflectivity under 30 dBZ (Fig. 37a). Near-surface Θ_v' shows all trajectories terminate within the cold pool region and with most having a negative Θ_v', up to -4 K, with the exception of one sub-severe trajectory that terminates with a positive Θ_v' (Fig. 37c). Vertical vorticity shows a lack of mesovortices at this time and indicates that other forcing mechanisms are likely causing severe winds at 80 m (Fig. 37d).

For this portion of the analysis, plots similar to those shown for the bulk trajectories will be presented and discussed for each time period but for a much more limited set of trajectories. This set includes 17 sub-severe trajectories and 4 severe trajectories. Both sub-severe and severe trajectories show general descent in the mean with all individual severe trajectories descending the entire ~15-min trackable time period (Fig. 38a). However, only a few trajectories descend from around 1 km with most descending from 800 - 400 m. This is also evident in the time series of w with most trajectories having negative w values the entire time period with the exception of a few sub-severe trajectories (Fig. 38b). In general, the magnitude of the descent is larger for the severe trajectories than the sub-severe. There is not much distinction between the sub-severe and severe trajectories in either CMT component, though CMT′ is much larger, with the severe having larger values from 1350 - 1600 s and the sub-severe having larger values from 1600 s on (Fig. 38c, 38d).

The full time period, last 5 minutes, and last 2 minutes of acceleration along the trajectories expressed as the wind speed added due to the buoyancy and dynamic pressure perturbations in both the horizontal and vertical at 0500 UTC is shown in Fig. 39. Integrated over the entire trajectory, the buoyancy-induced pressure gradient contributes the most to increases in horizontal wind speed for both sub-severe and severe winds (Fig. 39a). Note that the sub-severe trajectories' distributions in added wind speed have a larger spread due to the larger number of trajectories compared to severe wind trajectories (17 vs 4). The median value of integrated wind speed increase for buoyancy forcing for the sub-severe and severe categories is +3 m s^{-1} and +5 m s^{-1}, respectively, and the median value of integrated wind speed increase for dynamic forcing for the sub-severe and severe categories is around +1 m s^{-1} and +3 m s^{-1}, respectively. Overall, the severe trajectories have larger magnitudes of added horizontal wind speed from both buoyancy and dynamic pressure accelerations compared to the sub-severe trajectories with the buoyancy forcing being the main contributor for both categories when integrating over the entire trajectory. Buoyancy remains the primary forcing in the horizontal for the last 5 minutes of the trajectories (Fig. 39b). However, an interesting result is that this pattern changes in the last two minutes of the trajectories with the medians of sub-severe buoyancy forcing, sub-severe dynamic forcing, and severe buoyancy forcing all around zero (Fig. 39c). Unlike previous time periods, the dynamic forcing term for the severe trajectories is the largest contributor with a median around

+3 m s^{-1}. This indicates that while stronger buoyancy and dynamic forcing over the entire trajectory time period give the severe trajectories an overall increase in wind speed, dynamic pressure perturbations in the last few minutes force the severe wind trajectories to cross the 26 m s^{-1} threshold.

The full integrated acceleration of the vertical component of wind along the trajectory is shown in Fig. 39d with buoyancy being the dominant forcing for the descending motion of the parcels. The dynamic contribution to the descending motion opposes the buoyancy forcing for both the sub-severe and severe trajectories and is small with medians just above zero. This pattern is repeated for the last 5 minute and 2 minute portion of the trajectories with smaller overall magnitudes in the contribution with the exception of the severe dynamic forcing term becoming more positive and indicating an upward acceleration (Fig. 39e, 39f).

A trajectory from each category, svr0 and sub9, has been selected to illustrate the aforementioned evolution in forcing along individual trajectories identified in the bulk statistics. The sub9 trajectory descends from 600 m to 80 m and shows an increase in horizontal wind speed about halfway through this descent with a maximum of 25 m s^{-1} right at the end of the trajectory (Fig. 40a). The increase in wind speed just before 1600 s is coincident with an increase in the overall hPGA, CMT′, and CMT_0 with the perturbation CMT being larger than the environmental contribution (Fig. 40b). This increase in the hPGA around 1600 s is first driven by buoyancy (Fig. 40c), which contributes the most to the increase in wind speed over the whole trajectory, and then followed by a rapid increase in the dynamic forcing going from -0.03 m s^{-2} to almost 0.05 m s^{-2} in the last minute (Fig. 40c). In the vertical, the downdraft driving the positive CMT′ is forced by negative buoyancy that is not entirely offset by a gradually increasing dynamic forcing (Fig. 40d). While this trajectory remained under the severe wind threshold, the dramatic increase in dynamic forcing aided in continuing to accelerate the trajectory as it approached the surface. However, this dynamic forcing was either not large enough in magnitude and/or not acting long enough on the trajectory to surpass the severe threshold. A cross-section of reflectivity shows sub9 just ahead of a 35 dBZ core that is descending in the lower portions of a downdraft with a peak magnitude of -4 m s^{-1} (Fig. 40e). This trajectory is just behind a small area of severe winds that is underneath an updraft and appears to be experiencing the combined horizontal acceleration of an updraft/downdraft pair. A cross-section of Θ_v' shows the sub9 trajectory in cold outflow air and beneath a downward intrusion of positive Θ_v' values within the downdraft which points to a lack of diabatic cooling strong enough to offset compressional warming (Fig. 40f).

Similar to the sub9 trajectory, the svr0 trajectory experienced a decrease in wind speed as it descended from 600 to 200 m with a sharp increase in wind speed for the rest of the trajectory (Fig. 41a). The sharp increase in wind speed is associated with a large increase in the hPGA and contributions from CMT' and CMT_0 followed by a brief plateau in wind speed just after 1600 s while all aforementioned terms decrease (Fig. 41b). While CMT remains small the rest of the trajectory, the hPGA increasing leads to another increase in wind speed. The horizontal forcing shows the initial increase in wind speed is associated with positive horizontal buoyancy forcing and CMT, while the second acceleration after 1600 s is associated with a sharp increase in positive dynamic forcing (Fig. 41c). This final push by the dynamic forcing accelerates the wind from 23 to 27 m s^{-1} and above the severe threshold. The vertical wind speed is negative for most of the trajectory due to overall descent, with buoyancy as the main driver similar to sub9 (Fig. 41d), but the CMT contributions are small compared to the horizontal dynamic forcing in the final three minutes. The svr0 trajectory is within a lull of reflectivity and in the center of a small severe wind area that is in between an updraft/downdraft pairing (Fig. 41e). While the overall magnitude of negative Θ_v is almost identical over the svr0 and sub9 trajectory end point, the air descending from the upstream downdrafts does not have any positive Θ_v perturbation (Fig. 41e).

In this early time period before the MCS has fully matured, trajectories are accelerated initially overall by positive buoyancy forcing in the horizontal and negative buoyancy driving downdrafts for some CMT. The main difference between the sub9 and svr0 trajectory is the integrated horizontal acceleration from the dynamic forcing is larger in svr0, along with somewhat more diabatic cooling that offsets the compressional warming in the upstream downdrafts. The hydrometeor loading does not contribute much to the downward acceleration in these early times.

5.4.2 0530 UTC

By 0530 UTC, more of the main MCS convective line has moved into the inner domain and the coverage of severe wind has increased to the leading edge of the convective cores (Fig. 42a, 42b). This time also has the first instance of a significant severe wind at 80 m, located at a minimum in reflectivity around x=62, y=111 in Fig. 42b. Furthermore, the severe wind endpoints do not appear to be located within the coldest Θ_v values, which are located farther back in the convection, but rather are close to the Θ_v gradient near the leading edge of the cold pool (Fig. 42c). Finally, ζ again shows the lack of mesovortices associated with any severe or significant severe wind indicating other processes leading to severe surface winds (Fig. 42d).

This analysis contains 30 sub-severe trajectories, 9 severe trajectories, and one significant severe trajectory. With the exception of one sub-severe trajectory that begins around 3 km, all of the 30-min trajectories originate below 1 km, as they did at 0500 UTC (Fig. 43a). In the median, the sub-severe trajectories do not experience any appreciable descent whereas the severe trajectories experience weak descent throughout the time period. The only significant severe trajectory in this period weakly ascends throughout most of the time period and then descends from 400 m in the final two minutes. The median w for the sub-severe and severe trajectories is close to zero for most of the time period due to trajectories going through different periods of weak ascent and descent (Fig. 43b). As shown in the Z plot (Fig. 43a), w for the significant severe trajectory is weakly positive, but no more than 1 m s^{-1}, until the last two minutes when w abruptly becomes negative to its minimum of -2 m s^{-1}. Along with the minimum in w is a rapid increase in CMT from both the environment and the perturbation wind component, with a maximum downward acceleration of +0.035 m s^{-2} from the environment and just under +0.06 m s^{-2} from the perturbation component (Fig. 43c, 43d). While the median values of both CMT components for sub-severe and severe trajectories do not have a clear distinction for most of the time period, they are both weakly positive throughout the period, and the last two minutes show higher values for the severe trajectories compared to the sub-severe trajectories.

The integrated horizontal acceleration from the buoyancy and dynamic forcing over the entire time period shows significant overlap in the interquartile ranges, although the median value for buoyancy forcing is larger than the dynamic forcing for all three categories (Fig. 44a) similar to the trajectories that terminate at 0500 UTC. There's also an increase in the median value of the buoyancy and dynamic forcing contributions as the wind speed increases similar to 0500 UTC. This general overlap of the interquartile ranges continues for the last five minutes of the trajectory for the sub-severe and severe categories (Fig. 44b). However, the significant severe trajectory breaks the pattern of buoyancy being the larger of the two forces for horizontal acceleration with the dynamic acceleration adding +4 m s^{-1} of horizontal wind compared to less than +2 m s^{-1} for buoyancy. The median for both sub-severe forcings is near zero with the median for severe trajectories adding +2 m s^{-1} from buoyancy and just under +2 m s^{-1} from the dynamic forcing.

The pattern in the last two minutes of the 0530 UTC trajectories is similar to that of 0500 UTC with the dynamic contribution being larger than buoyancy for the severe and significant severe trajectories (Fig. 44c). Similar to the five minute integration, the median wind speed addition is zero for the sub-severe trajectories indicating that one distinction between severe and non-severe winds is continued positive acceleration as the trajectories approach the surface in the final two minutes. While the median of around +1 m s^{-1} in additional wind speed for buoyancy is the same for the severe and significant severe, the dynamic term contribution for the significant severe trajectory is double that of the median for the severe trajectories.

Integrated over the entire trajectory, the added vertical wind speed shows buoyancy being the main driver of descent, similar to the 0500 UTC trajectories, with the dynamic forcing contribution generally near zero for the sub-severe and severe categories (Fig. 44d). The median value of descent from buoyancy forcing increases with increasing wind speeds. The last five minutes continue the trend of strong downward forcing from buoyancy increasing as wind speed increases but the significant severe trajectory has a dynamic forcing that more strongly opposes the downward buoyancy forcing (Fig. 44e). This dynamic forcing somewhat offsets the buoyancy forcing in the last two minutes of the significant severe trajectory, unlike for the sub-severe and severe trajectories. However, the net vertical acceleration continues to be downward through the end of the trajectory (Fig. 44f).

The time series of height vs wind speed for the one significant severe trajectory at 0530 UTC (sig0) clearly shows the rapid increase in horizontal wind speed as the trajectory descends in the last 200 s (Fig. 45a). This rapid speed increase is associated with an increase in the hPGA with increased values of CMT′ and CMT_0 (Fig. 45b). As at 0500 UTC, the contribution from CMT′ is larger than CMT_0 and is correlated with a -2 m s^{-1} buoyancy driven downdraft in the final 100 s of the trajectory (Fig. 45b, 45d). As in the svr trajectory at 0500 UTC, the increase in horizontal wind speed occurs first from positive horizontal buoyancy accelerations (Fig. 45c). This is followed by a sharp increase in the horizontal dynamic acceleration that becomes larger in magnitude than the horizontal buoyancy forcing, which accelerates the trajectory above the significant severe threshold. A cross-section of reflectivity shows the sig0 trajectory terminates directly in between another downdraft/updraft pairing (Fig. 45e). The very small horizontal distance between this pairing may be causing the strong dynamic forcing that caused sig0 to rapidly accelerate at the end of the trajectory. Sig0 is also located in a much colder Θ_v′ region of the cold pool compared to the trajectories at 0500 UTC (Fig. 45f), likely a consequence of the strong integrated negative buoyancy forcing along this parcel.

5.4.3 0600 UTC

By 0600 UTC, the MCS has matured further with stronger convective reflectivity cores, a larger area of severe winds, and a faster system motion (Fig. 46a, 46b). This is coincident with an expanding cold pool and a warming inflow environment as shown with Θ_v′ (Fig. 46c). Unlike previous times, there is evidence of a mesovortex associated with significant severe winds on the leading edge of a reflectivity appendage (Fig. 46d). The 0600 UTC analysis period contains 24 sub-severe, 20 severe, and 3 significant severe trajectories. The height of the selected trajectories in time shows that the significant severe trajectories and many of the severe trajectories analyzed here oscillate between positive and negative w at various times before descending at the end of the time period (Fig. 47a). The w for the two significant severe trajectories show this oscillatory behavior, but then show a peak descent rate over -3 m s^{-1} following a period of strong ascent toward the end of the period (Fig. 47b). These peaks in descent in the significant severe trajectories also coincide with peaks in CMT from both the background flow and the perturbation component (Fig. 47c, 47d). The severe trajectories also show an increase in CMT from both components at the end of the time periods but not to the same magnitude as the significant severe trajectories.

Like at 0500 and 0530 UTC, the horizontal buoyancy acceleration accounts for most of the increase in horizontal wind speed integrated over the entire period, while the dynamic forcing has a negative median for the sub-severe and severe trajectories (Fig. 48a). However, there is not much discrimination in the buoyancy forcing magnitude between the three wind speed categories. This trend changes in the last five minutes with increasing buoyancy forcing as wind speed increases and separation between the interquartile values of severe and significant severe (Fig. 48b). Also note that the dynamic forcing for the significant severe trajectories is all positive as opposed to the severe category that has a median around 0 and the sub severe values being mostly negative. In the last two minutes, the differences between the severe and significant severe categories are small as both have positive medians for horizontal buoyancy and dynamic forcing, with the dynamic forcing being slightly larger (Fig. 48c). However, the overall trend of the horizontal dynamic forcing often becoming as large or larger than the horizontal buoyancy forcing in the last two minutes continues to be apparent. The median value for both forcing terms for the sub-severe category is zero indicating that most severe wind trajectories accelerate as they approach the surface whereas sub-severe trajectories maintain their speed or decelerate.

The total added vertical wind speed integrated over the entire trajectory shows buoyancy being the dominant downward forcing with all dynamic terms much smaller (Fig. 48d), similar to the 0500 and 0530 UTC analysis. However, unlike other times, severe trajectories have the largest negative buoyancy values followed by sub-severe trajectories and then significant severe trajectories. This pattern does not hold in the last five minutes, however, with the median buoyancy forcing being the most negative for the significant severe trajectories at -15 m s^{-1}, followed by severe at -12.5 m s^{-1}, and sub-severe much smaller at -3 m s^{-1} (Fig. 48e). This pattern continues to hold in the last two minutes with the exception of the dynamic term becoming increasingly positive for increasing wind speed which counters, but does not offset, the increasingly larger magnitude negative buoyancy forcing over the same period (Fig. 48f).

The trajectory going into the mesovortex (near x=60, y=64 in Fig. 46d), sig0, starts near the ground and experiences rapid ascent from 1300 to 1500 s along with an increase in wind speed to just above the severe threshold (Fig. 49a). It then goes through a rapid descent as wind speed increases again to significant severe levels. During this final descent, the hPGA term initially drops before becoming very positive again at the very end of the trajectory, but both the CMT′ and CMT_0 are strongly positive and compensate for the decrease in the hPGA (Fig. 49b). This decrease in the hPGA is due to the buoyancy forcing decreasing and becoming negative during a period of negative dynamic forcing (Fig. 49c). However the dynamic term increases in the last 100 s of the trajectory which accounts for the final increase in hPGA. In the vertical, the dynamic term has a larger impact on w compared to previous times but ultimately negative buoyancy forcing drives the final descent and CMT (Fig. 49d). The reflectivity cross-section over sig0 shows the wind speed maximum in between an updraft/downdraft couplet like that seen at some previous times; however this couplet is in extremely low reflectivity compared to any other couplets (Fig. 49e). This trajectory ends at the leading edge of the cold pool (Fig. 49f).

The svr8 trajectory experiences multiple periods of ascent and descent with the final increase in wind speed above the severe threshold during its final descent from 800 m (Fig. 50a).

This final wind speed increase is associated with a positive hPGA and equal contributions from both CMT terms (Fig. 50b). This increase in the hPGA is first associated with a maximum in buoyancy forcing followed by a peak in the dynamic forcing like other severe trajectories (Fig. 50c). Despite positive dynamic forcing in the vertical, negative buoyancy forcing, now with some non-negligible contributions from hydrometeor loading, causes this trajectory to have maximum descent over -4 m s^{-1} aiding the CMT (Fig. 50d). The reflectivity cross-section shows the trajectory ending ahead of a reflectivity core with a -6 m s^{-1} downdraft upstream and a 6 m s^{-1} updraft downstream for another updraft/downdraft couplet (Fig. 50e). Unlike other severe trajectories, svr8 is in a region of warmer Θ_v air in between the updraft/downdraft couplet (Fig. 50f).

A sub-severe trajectory to the north of the mesovortex, sub22, shows a gradual increase in wind speed through the time period with large changes in height with descent from 900 to 80 m in the last 6 minutes (Fig. 51a). This gradual increase in horizontal wind speed is timed with an increase in the hPGA with small contributions from CMT (Fig. 51b). While buoyancy forcing gradually increases over the time period, the dynamic forcing changes rapidly with a final positive increase during the trajectories main wind speed increase at 1600 s (Fig. 51c). In the vertical, the buoyancy term is the main driver of descent with the dynamic forcing occasionally offsetting it (Fig. 51d). The sub22 trajectory ends in low reflectivity at the leading line of the MCS and just upstream of an area of severe winds being accelerated by a leading line updraft (Fig. 51e). Trajectory sub22 is also in a warmer portion of the cold pool compared to the downstream severe winds (Fig. 51f).

Without any assistance from horizontal dynamic forcing, the sub22 trajectory stayed sub-severe indicating that enhanced dynamic forcing was necessary in the final 200 s in order to reach the severe threshold. Both sig0 and svr8 experienced a rapid increase in the horizontal dynamic forcing as the buoyancy forcing decreased. This aligns with the integrated acceleration distributions showing the importance of the dynamic term in the last two minutes of the trajectories. The sig0 and svr8 trajectories were also directly in between an updraft/downdraft couplet which likely led to the last minute enhancement of the dynamic forcing. Furthermore, the analysis of the individual trajectories at 0600 UTC shows an increasing contribution from CMT compared to 0500 and 0530 UTC and points to an increasing contribution from negative buoyancy throughout the night. This is interesting because this is occurring during a period when the near-surface environment typically cools and one would expect a concurrent decrease in contributions from negative buoyancy with time. As discussed later, this is an indication that the 25-26 June MCS is well within what is considered to be "surface-based" and is becoming more surface-based with time, as previously discussed for this event in Parker et al. (2021) and Miller et al. (2020).

5.4.4 0630 UTC

At 0630 UTC, there is a concentrated area of significant severe and severe winds in the E-W oriented portion of the line with more scattered areas of severe winds elsewhere (Fig. 52a, 52b). Note that the environment ahead of the line has continued to warm relative to 0400 UTC with Θ_v values of +3 to 4 K just south of the NS-oriented segment (Fig. 52c). Unlike the previous time, there is no evidence of any mesovortices along the leading convective line associated with severe or significant severe winds (Fig. 52d). This analysis time has 21 sub-severe, 23 severe, and 3 significant severe trajectories. Similar to previous times, most trajectories selected for further analysis descend from below 1000 m (Fig. 53a). Due to the differing time periods of ascent and descent for each trajectory, the median only shows weak descent (Fig. 53b). This is also reflected in the w time series with a median around zero for all three categories despite instances of strong ascent and descent for individual trajectories (Fig. 53b). Unlike previous times, the CMT contribution from the environment and perturbation components do not distinguish between the three categories with the exception of the CMT′ for significant severe being smaller than for the severe and sub-severe trajectories (Fig. 53c, 53d). However, the overall magnitudes of the CMT, particularly for CMT′, have become quite large compared to earlier times.

For the full time period, the additional horizontal wind speed is once again dominated by the buoyancy forcing with the median of the dynamic forcing term being below zero for all three categories (Fig. 54a). In the final five minutes of the trajectories, buoyancy forcing continues to be larger than the dynamic forcing for all three categories. The median of the buoyancy forcing for the sub-severe trajectories is actually near zero, indicating no contributions to acceleration, but the median of the buoyancy forcing for severe trajectories is around +1.25 m s^{-1}, and is around +3 m s^{-1} for the significant severe trajectories (Fig. 54b). Though most dynamic contributions are centered around zero, the entire interquartile range of the significant severe category is negative in contrast to previous times. Within the last two minutes of the trajectories, the median of both forcing terms for the sub-severe trajectories continues to be near zero with both forcing terms for the severe and significant categories being positive (Fig. 54c). The last two minutes follow the typical trend of the dynamic forcing for the significant severe trajectories being positive, and more comparable to the magnitude of the positive buoyancy forcing, right at the end of the trajectory. Likewise, the full vertical acceleration follows previous patterns of buoyancy being the main downward force with the median of the dynamic terms around zero

(Fig. 54d). This pattern holds for the final five minutes and final two minutes with the exception of the significant severe dynamic term contributing 1 m s^{-1} of upward motion (Fig. 54e, 54f).

The svr6 trajectory follows a more typical route of horizontal wind speed gradually increasing with the largest acceleration at the end during descent (Fig. 55a). This increase is associated with a small peak in positive hPGA at the very end but very strong CMT′ forcing (Fig. 55b). While buoyancy forcing is increasingly positive for the end of the trajectory, this trajectory is somewhat unlike the others in that the dynamic term becomes very negative explaining the decreased overall hPGA (Fig. 55c). In the vertical, hydrometeor loading and negative buoyancy forcing account for the descent and offset upward dynamic forcing that helps contribute to the strong CMT forcing for this trajectory (Fig. 55d). The svr6 trajectory is located on the leading edge of a reflectivity gradient and also just downstream of a low-level downdraft (Fig. 55e). The area of severe winds only reaches the surface just downstream of this low-level downdraft and otherwise remains above the surface. This is one of the few severe trajectories not showing an acceleration due to dynamic forcing at the very end, but a very large CMT′ bringing severe winds towards the surface within a small, localized downdraft.

Shifting to a sub-severe trajectory, sub0 has a brief period of severe winds associated with weak descent from 400 to 700 s but otherwise remains under the severe wind threshold (Fig. 56a). This initial period of severe winds is associated with a large, positive hPGA acceleration that decreases and oscillates around zero for the remainder of the trajectory. (Fig. 56b). There also is very little CMT at the end of the trajectory. The lack of strong horizontal buoyancy and dynamic forcing align with a very small hPGA (Fig. 56c). Though the vertical forcing shows relatively large hydrometeor loading acceleration in the middle of the trajectory time period, it weakens after 1000 s and only has a slight increase in the last 200 s (Fig. 56d).

The hydrometeor loading was not strong enough to sustain a downdraft needed for CMT. The sub0 trajectory is located behind a reflectivity core and upstream of severe winds at the surface (Fig. 56e). The Θ_v does not show much discrimination between this area and the severe winds downstream except cooler values above 100 m (Fig. 56f).

5.4.5 0700 UTC

At this time, the MCS has severe and significantly severe winds concentrated in the western portion of the convective system near where the two segments previously connected and more sporadically within stronger cores of the NE portion of the line (Fig. 57a, 57b). The western portion of the line has the strongest Θ_v gradient between the inflow environment and the cold pool and a zone of large horizontal shear along the gust front accelerating the flow along the leading edge (Fig. 57c, 57d). This analysis time has 23 sub-severe, 19 severe, and 2 significant severe trajectories. The change in Z over time for the trajectories is similar to previous times with most descending from less than 1 km and an oscillating w pattern due to the trajectories ascending and descending at different points in the time period (Fig. 58a, 58b). Unlike the previous time where CMT did not discriminate between the categories, at 0700 UTC the two significant severe trajectories have much higher CMT from the environment throughout the time period and much higher CMT′ from 0 to 1200 s (Fig. 58c, 58d).

Like all other times, the horizontal acceleration is dominated by buoyancy forcing integrated over the full time period for all three categories (Fig. 59a). Buoyancy forcing still dominates for the sub-severe and severe categories in the last five minutes, but the dynamic category for the significant severe category becomes slightly larger (Fig. 59b). Interestingly, in the last two minutes, the median for both terms in the significantly severe category is less than zero which has not been observed at any other time period (although there are still plenty of severe and significantly severe trajectories that have positive dynamic forcing) (Fig. 59c). Also note that the buoyancy term's median is always larger for the sub-severe and severe categories.

The pattern of buoyancy driving downward motion at all previous times continues for 0700 UTC for all three categories over the entire time period with the buoyancy forcing for the significantly severe category larger than the other two categories (Fig. 59d). Within the last five minutes, the difference in downward buoyancy forcing becomes even larger with the median of the sub-severe category around –5 m s^{-1}, and around -4 m s^{-1} and -12 m s^{-1} for the severe and significantly severe categories, respectively (Fig. 59e). The median for the sub-severe and severe dynamic terms is zero with only significant severe becoming slightly positive. This pattern continues for the last two minutes of the trajectories (Fig. 59f). It seems that the buoyancy forcing in the horizontal is more important for the severe trajectories and buoyancy forcing in the vertical is more important for the significant severe trajectories.

5.4.6 0730 UTC

The final time period for analysis has the largest areal coverage of significant severe winds, especially in the vicinity of a very strong convective cell in the most NE portion of the line with a strong Θ_v gradient and mesovortices at the leading edge (Fig. 60a, 60b, 60c, 60d). This analysis time has 29 sub-severe, 26 severe, and 10 significant severe trajectories. Unlike previous times, the height of the trajectories shows some ascending over 4 km before descending with quite a few significant severe trajectories descending from between 1 and 2 km (Fig. 61a). This corresponds to much larger w values over time with multiple significant trajectories in descent after 1000 s, with one significant severe trajectory, in particular, descending at a rate greater than -15 m s^{-1} (Fig. 61b). This is correlated with the significant severe trajectories having larger environmental CMT than the other two categories, especially in the last 1400 s (Fig. 61c). The difference is not as clear when looking at the perturbation contribution to CMT (Fig. 61d).

The integrated horizontal acceleration over the entire period for the three categories once again has buoyancy as the main forcing with all the interquartile ranges being positive and all medians of the dynamic term being less than zero (Fig. 62a). There is a trend of increasing buoyancy forcing with wind speed as in previous times. The final five minutes of the trajectories show the forcing for the sub-severe category around zero with the severe and significant severe categories having positive buoyancy forcing (Fig. 62b). This trend is also observed in the final two minutes but at a smaller magnitude (Fig. 62c). While the sub-severe and severe categories follow previous trends of most buoyancy forcing leading to downward motion, the median for significant severe winds in buoyancy and dynamic forcing is positive indicating integrated upward acceleration (Fig. 62d). For the final five and two minutes, all buoyancy forcing interquartile ranges are indicative of downward motion and the dynamic medians are very close to zero (Fig. 62e, 62d).

For the sig7 trajectory, the horizontal wind speed does not increase from severe to significant severe until after descent from over 1500 m to 80 m due to strong acceleration from the hPGA and the CMT′ term during very strong descent (Fig. 63a, 63b, 63d). This descent was driven by hydrometeor loading causing a downdraft of almost -7 m s^{-1} (Fig. 63d). The sig7 trajectory is located at the leading edge of a reflectivity core with a downdraft extending down to 250 m upstream (Fig. 63e). It is within a deep area of significant severe winds (up to 1000 m) within an even deeper area of severe winds. The Θ_v cross-section shows this significant severe area containing extremely cold air with the trajectory in one of the colder sections which is unlike previous times (Fig. 63f).

The svr16 trajectory peaks in wind speed during its descent from 1000 to 80 m in the last 300 s of the trajectory (Fig. 64a). This is associated with an increasing hPGA which reaches a maximum at the end of the trajectory due to increasing horizontal dynamic forcing (Fig. 64b, 64c). However, a large component of the forcing once again appears to be hydrometeor loading causing strong descent that allows for large CMT' and CMT_0 with CMT' being the larger contributor (Fig. 64b, 64d). The svr16 trajectory is within a very strongly forced flow ahead of an over -8 m s^{-1} downdraft associated with 65 dBZ descending to the surface (Fig. 64e). Once again a leading line updraft/downdraft couplet is present with the 2 m s^{-1} updraft contour down to less than 100 m. However, it appears that most of the horizontal wind speed increase is due to hydrometeor laden cores allowing CMT to drag down higher wind speed air from the rear inflow to the surface. The Θ_v' field shows a tilt toward the ground associated with multiple weak downdrafts behind the main downdraft core (Fig. 64f).

The sub20 trajectory has an initial descent from 1750 to 850 m with an increase in horizontal wind speed followed by a more rapid descent from 1000 to 80 m in the last 400 s (Fig. 65a). The horizontal forcing is increasingly negative due to an increasingly negative dynamic forcing term throughout the trajectory (Fig. 65b, 65c). The slight increase in wind speed at the end of the trajectory is associated with increasing CMT' and CMT_0 caused by hydrometeor loading driven descent (Fig. 65b, 65d). Sub20 is just behind an area of severe winds forced by a 60+ dBZ core with a -6 m s^{-1} downdraft (Fig. 65e). The downdraft is once again bringing down severe winds from above 1000 m to the surface but only in an extremely small horizontal area. The Θ_v' field shows colder Θ_v' air spreading out horizontally at the base of the downdraft with a "U" shape to the coldest air and a core of warmer Θ_v' air in the downdraft center (Fig. 65f).

It appears that the main forcing for severe winds in the 26 June MCS was due initially to favorable updraft/downdraft couplet locations for enhanced dynamic horizontal forcing. However, once the MCS intensified and a strong cold pool was established, CMT from strong downdrafts due to hydrometeor loading in high reflectivity cores brought down higher wind speeds to the surface. This was sometimes further augmented by updraft/downdraft couplets and those trajectories showed the previously noted increase in horizontal dynamic forcing at the end of the trajectory. But at this time, updraft/downdraft couplets are not necessary for severe wind production. This transition from mainly pockets of enhanced dynamic forcing in the horizontal to an increase in CMT due to negatively buoyant downdrafts and finally to hydrometeor drag accelerating CMT shows that the MCS was becoming more surface-based despite continuing well after midnight. Furthermore, the intensity and coverage of both severe and significant severe winds increased with each time period.

5.5 Selected 5-6 July Trajectories

5.5.1 0430 UTC

At 0430 UTC, multiple areas of convection are associated with severe and significant severe winds including the remnants of the bowing and linear MCS that was responsible for widespread severe winds earlier in the evening farther west (Fig. 66a, 66b). The intersection of the bowing and linear MCS is the location of the coldest Θ_v air (-4 to -5 K) with much warmer Θ_v air (+7 to +8 K) in the inflow region (Fig. 66c). Along the leading line of the remnant bowing segment is where some mesovortices are associated with severe and significant severe winds (Fig. 66d), similar to those observed with this event around this time (Flournoy and Coniglio 2019). However, other areas without mesovortices also have severe and significant severe winds indicating multiple forcing mechanisms likely contributed to the severe winds, as in the 25-26 June MCS.

This analysis time has 18 sub-severe, 21 severe, and 14 significant severe trajectories. While one sub-severe trajectory descends from 3.5 km, most descend from around 1 km similar to the 25-26 June case (Fig. 67a). However, many of these individual trajectories appear to have gradual descent rather than most of the descent happening at the end of the time period, as was seen in many trajectories in the 25-26 June case. This trend is also shown in the w of the trajectories over time with the median around zero and only a few trajectories showing large upward or downward motion (Fig. 67b). Neither CMT from the environment nor the perturbation component show much distinction between the three wind categories (Fig. 67c, 67d), although values are often quite large at various times throughout the trajectories.

Looking at the added horizontal wind speed from integrating the forcing terms, the buoyancy term is contributing more than the dynamic term for all three categories with the median value of added wind speed increasing for each category (Fig. 68a), similar to what was seen in the 25-26 June case. This trend continues for the final five minutes of the trajectory with the dynamic term around zero in all three categories and increasing magnitudes of buoyancy contribution for increasing wind speed (Fig. 68b). However, in the final two minutes, the dynamic term for the significant severe winds becomes positive with contribution to horizontal wind speed comparable to the contributions from the buoyancy forcing (Fig. 68c). This follows trends seen at many times for the 25-26 June MCS.

In the vertical, buoyancy once again is the main downward forcing term with the dynamic term median around zero (Fig. 68d). This pattern continues for the final five minutes of the trajectory with buoyancy forcing being the strongest for the severe and significant severe categories (Fig. 68e). In the final two minutes, the vertical forcing for the sub-severe and severe categories is very similar in median magnitude with buoyancy still contributing the most (Fig. 68f). However, the significant severe term has much stronger downward buoyancy forcing and a smaller, offsetting dynamic forcing term.

The sig10 trajectory experiences its last push above the significant severe threshold during the last 200 s of descent (Fig. 69a). While increases in CMT and the hPGA are both associated with 2 earlier peaks in wind speed, the final increase is mainly due to a rapid increase in the hPGA (Fig. 69b). This rapid increase in the hPGA at the end of the trajectory was initially due to a large positive buoyancy acceleration which was followed by an increase in the dynamic forcing (Fig. 69c) (although the individual magnitude of these two terms appears to be relatively small compared to the large overall hPGA increase in the final few minutes, indicating that sub-grid-scale forcings not accounted for in this horizontal acceleration budget may be important here).

The vertical forcing shows large changes in the dynamic term throughout the time period and a peak downdraft of -4 m s^{-1} (Fig. 69d). During the wind speed increase at the very end of the trajectory, hydrometeor forcing becomes strongly negative despite only forcing a -1 m s^{-1} downdraft. The sig10 trajectory is within a 60 to 65 dBZ reflectivity core associated with a maximum -8 m s^{-1} downdraft aloft, with a magnitude around -2 m s^{-1} below 200 m (Fig. 69e). An area of significant severe winds begins on the -2 m s^{-1} contour and extends downstream with the flow. The sig10 trajectory and the surrounding pocket of significant severe winds are located in very cold Θ_v air (Fig. 69f). This trajectory appears similar to the significant severe trajectories analyzed later in the 25-26 June case with a negatively buoyant downdraft accelerating from hydrometeor drag causing rapid acceleration of the significant severe winds as it encounters the surface, despite relatively small downward motion. The hPGA acceleration was likely enhanced by ‘splat’ deformation at the surface allowing for the final acceleration above the significant severe threshold.

5.5.2 0500 UTC

Like 0430 UTC, the strongest convection and largest coverage of severe winds is located near the intersection point of the N-S oriented bowing segment and the more E-W oriented linear portion of the MCS (Fig. 70a, 70b). However, the inflow environment is not quite as warm as the previous time and the cold pool is a bit warmer (Fig. 70c). There are multiple vortices located along the leading edge of the former bowing segment that are associated with significant severe winds with the strongest vortex being just south of where cells are developing in the inflow (Fig. 70d). This depiction is strikingly similar to the observed evolution of the vortices in this portion of the convective system (see Flournoy and Coniglio 2019 for more details).

The 0500 UTC analysis has 20 sub-severe, 19 severe, and 14 significant severe trajectories. In both the median and the individual trajectories, the significant severe trajectories experience the most ascent with stronger descent towards the end of the time period (Figs. 71a, 71b). The significant severe trajectories have a larger contribution of CMT from the environment compared to the severe and sub-severe trajectories, especially in the first 1000 s (Fig. 71c). The differences in CMT’ among the three categories are not as clear with only a few large values from individual trajectories with median values for the sub-severe, severe, and significant severe categories not showing any significant separation in their distributions (Fig. 71d). The integrated horizontal forcing acceleration terms show buoyancy being the largest contributor over the full time period, as seen in the 25-26 June case, but there is not much distinction in buoyancy forcing between the severe and significant severe categories (Fig. 72a). The full, integrated dynamic contribution becomes increasingly negative as horizontal wind speed increases. This pattern holds for the final five and two minutes as well but the forcing for the severe trajectories is larger than that of the significant severe category for the final two minutes (Fig. 72b, 72c). One distinction at this time from the 25-26 June case is that there is also no longer evidence of an increase in dynamic forcing at the end of the time period. In the vertical forcing integrated over the full trajectory, buoyancy is once again the main driver of downward acceleration with the dynamic forcing median around zero for all three categories (Fig. 72d). This trend continues for the final five and two minutes of the time period with increasingly negative buoyancy forcing for increasing wind speed category (Fig. 72e, 72f). Once again, there is no shift to positive dynamic forcing at the end of the time period like previously observed, which indicates less of an offsetting upward acceleration in these trajectories.

The sub18 trajectory remains just below the severe threshold for most of the time period with a decrease followed by an increase in wind speed during its final descent (Fig. 73a). This decrease in wind speeds is due to a sharp decrease in the hPGA driven by a decrease in the dynamic forcing (Fig. 73b, 73c). Interestingly, CMT increases during this period with a larger contribution from CMT_0 compared to CMT′. The sub18 trajectory experiences a slight increase in hydrometeor loading within an overall negative buoyancy-driven weak downdraft at the end (Fig. 73d). The sub18 trajectory is just upstream of an area of severe winds driven by a descending reflectivity core with a -4 m s^{-1} downdraft (Fig. 73e). In Θ_v a downward slope of cold air is associated with the aforementioned downdrafts (Fig. 73f). The sub18 trajectory did not have positive hPGA and the CMT_0 was not enough to accelerate it above the severe threshold. It is clear in the cross-sections over sub18 that CMT is playing a role in the severe winds just downstream of sub18.

5.5.3 0530 UTC

At 0530 UTC a line of convection has developed in the inflow perpendicular to the remnant bowing MCS with the area of most of the significant and severe winds to the west and south of this intersection point (Fig. 74a, 74b). While there are pockets of warmer Θ_V air below the convection in the inflow, the overall inflow air is about a degree cooler than at 0500 UTC (Fig. 74c). There are multiple mesovortices at and south of the intersection point, like at 0500 UTC, leading to significant and severe wind at the leading edge of the remnant bowing segment (Fig. 74d). This analysis time has 17 sub-severe, 27 severe, and 9 significant severe trajectories. Looking at the height over time of the selected trajectories, the significant severe trajectories show more descent in the median compared to the severe and sub-categories median values (Fig. 75a). This can also be seen in vertical velocity where the significant severe trajectories generally have more variable and larger w magnitudes (Fig. 75b). Larger vertical velocities also lead to larger CMT_0 values for significant severe however this is not reflected in the CMT′ field (Fig. 75c, 75d). For the overall added wind speed due to horizontal forcing, buoyancy as usual is the dominant forcing with the median values for severe and significant both around 3 m s^{-1} (Fig. 76a). The dynamic term median is around zero for all three categories. This pattern continues in the last 5 minutes of the trajectories however the median for the significant severe dynamic forcing is now positive (Fig. 76b). In the last 2 minutes, the buoyancy forcing is larger for both the sub and severe categories but the dynamic term is larger for the significant severe (Fig. 76c). Overall the buoyancy forcing increases with increasing wind speed but the increase in dynamic forcing likely leads to the occurrence of significant severe winds.

In the vertical, buoyancy is the dominant downward acceleration force for the full trajectory time period (Fig. 76d). This continues in the last 5 minutes with negative buoyancy forcing increasing with increasing wind speed, but the dynamic forcing becomes increasingly positive with increasing wind speed (Fig. 76e). Finally in the last 2 minutes, the median of both forcing terms for sub-severe is zero, the median of buoyancy for severe and significant severe are both negative with significant severe being larger, and the median for dynamic forcing is positive for severe and significant severe with significant severe again being larger (Fig. 76f).

The sig1 trajectory descends from about 950 m while horizontal wind speed increases and ends with a brief period of ascent followed by a descent and a sharp increase in wind speed (Fig. 77a). This increase at the end of the trajectory appears to be due to increases in the hPGA driven by the dynamic forcing term, which should increase in the presence of a mesovortex (Fig. 77b, 77c). In the vertical, the negative buoyancy and positive dynamic term tend to balance each other until the very end when a weak downdraft is induced (Fig. 77d). Unlike other trajectories, there is no increase in hydrometeor loading at the end. Looking at a cross-section of reflectivity over sig1, it is in a pocket of significant severe winds beneath a couplet consisting of a 10 m s^{-1} updraft and -4 m s^{-1} downdraft and just behind a small 2 m s^{-1} updraft which extends below 250 m (Fig. 77e). It is also at the leading edge of a Θ_v gradient (Fig. 77f). This trajectory resembles earlier June trajectories where an increase in the dynamic forcing due to an updraft/downdraft couplet accelerated the flow.

The sub1 trajectory rises to 400 m around 1400 s and then descends while maintaining wind speeds just below the severe threshold (Fig. 78a). The hPGA is mainly negative due to mostly negative dynamic forcing and only becomes positive at the very end of the trajectory due to an increase in buoyancy forcing (Fig. 78b, 78c). There are two peaks in both components of CMT during the trajectory's last increase in wind speed but this goes to zero as the vertical acceleration weakens. This is despite the hydrometeor loading term becoming very negative at the end (Fig. 78d). The reflectivity cross-section shows sub1 within a large reflectivity core associated with a downdraft up to -6 m s^{-1}, but it is just upstream of the strongest downdraft forcing and the severe winds (Fig. 78e). The area of severe winds is in a much colder portion of the cold pool compared to sub1 (Fig. 78f).

While sub1 was in a much stronger portion of the MCS in terms of reflectivity and leading line updrafts, a small hPGA forced by buoyancy was not enough to surpass the severe threshold despite large hydrometeor loading. The sig1 trajectory was able to rapidly accelerate past the significant severe threshold due to a last minute acceleration from dynamic forcing and CMT. The sig1 trajectory was in the vicinity of a mesovortex which likely was responsible for some of the dynamic forcing increase.

5.5.4 0600 UTC

At 0600 UTC, there are less significant severe trajectories as the MCS has weakened in the former bowing segment region (Fig. 79a, 79b). Interestingly, a majority of the significant severe trajectories are within the lower reflectivity area south of where the inflow convection intersects the former bowing segment. There is only one region where the coldest cold pool air (-4 to -5 K) reaches the warmer inflow air (3 to 4 K) beneath the strongest convective cell just south of the connection point (Fig. 79c). Finally, the coherent mesovortex structure noted in 0500 and 0530 UTC is no longer visible along the leading line of the former bowing segment (Fig. 79d). This analysis time has 20 sub-severe, 27 severe, and 6 significant severe trajectories. Most trajectories analyzed descend from less than 2 km with a select few descending from as high as 4 km (Fig. 80a). In general, the significant severe trajectories have a larger ΔZ than the severe or sub-severe trajectories. This is reflected in the W over time with the median value of the significant severe trajectories reaching -2 m s^{-1} whereas the median for sub and severe hovers around zero due to the different timing of ascent and descent (Fig. 80b). This larger W value in the significant severe trajectories is reflected in larger values of both CMT_0 and CMT′, especially in the second half of the trajectory (Fig. 80c, 80d).

The added horizontal wind speed from the buoyancy and dynamic terms over the entire time period again shows buoyancy being the largest contributor and its magnitude increasing with wind speed (Fig. 81a). Both sub and significant severe have dynamic terms with medians below zero and the severe dynamic term has a median just above zero. In the last 5 minutes, buoyancy is still the main forcing however the severe category is the only one with both the buoyancy and dynamic median greater than zero (Fig. 81b). The buoyancy forcing median for significant severe is barely above zero with the dynamic term around -3 m s^{-1} indicating the overall horizontal wind speed decreases in the last 5 minutes. In the last 2 minutes, the buoyancy terms for sub and severe have medians barely above zero with negative medians for the dynamic forcing (Fig. 81c). However, the opposite is true for the significant severe with a negative median for buoyancy forcing and a slightly positive median for dynamic forcing.

In the total time period, the vertical velocity added is largest in buoyancy for sub-severe trajectories followed by buoyancy for severe trajectories (Fig. 81d). All three categories have positive contributions (upward motion) from the dynamic term and the significant severe also has a positive contribution from buoyancy which has not been noted in any other time period. In the last 5 minutes of the trajectory, all three categories have a negative contribution from buoyancy with medians around the same magnitude and a positive contribution from dynamic forcing with magnitude increasing with wind speed (Fig. 81e). This pattern occurs in the last 2 minutes as well however the median of buoyancy for severe is the largest of the three categories (Fig. 81f).

The sig3 trajectory descends from well over 1 km but does not begin its final wind speed increase until its descent from 800 m around 1200 s (Fig. 82a). Generally the hPGA is positive for the entire trajectory with periodic acceleration from both CMT terms with CMT_0 tending to be slightly larger. (Fig. 82b). Most of the hPGA is due to positive buoyancy with the exception of the last 100 s when the dynamic term becomes positive right as the horizontal wind speed reaches its peak at the end of the trajectory (Fig. 82c). The sig3 vertical forcing shows hydrometeor loading largest at the beginning of the trajectory and during its strong descent from 800 m (Fig. 82d). Looking at the reflectivity cross-section, the sig3 trajectory is in a small area of significant severe winds underneath a weak updraft/downdraft couplet with more forcing from the downdraft (Fig. 82e). In Θ_v the trajectory shows up in the leading edge of a very shallow layer of colder Θ_v air running into the +2 K Θ_v inflow air (Fig. 82f). Both of these cross-sections show an overall weaker system dynamically and thermodynamically with corresponding smaller areas of severe and significant severe winds.

The trajectory sub12 experiences rapid descent from over 1 km down to 80 m in the last 400 s (Fig. 83a). Like the svr24 trajectory, most of the positive hPGA is due to a positive buoyancy term with the dynamic forcing becoming positive at the very end (Fig. 83b, 83c). The final acceleration is also due to CMT forcing mainly from the CMT_0 term. In the vertical, it is clear that hydrometeor loading combined with negative dynamic forcing caused the very strong descent at the end of the trajectory (Fig. 83d). The reflectivity cross-section shows this rapid descent within a 50 to 55 dBZ core descending from a -6 m s^{-1} downdraft (Fig. 83e). In the Θ_v cross-section it becomes apparent that cold pool is not as cold as it was previously with the coldest air associated with the two downdraft areas (Fig. 83f). Overall the decrease in the coverage of significant severe and severe winds is associated with the MCS weakening in both the dynamic and thermodynamics. This is also reflected in the forcing for individual trajectories with smaller magnitudes of CMT and dynamic forcing at the end of trajectories. Similar processes as earlier times leading to severe and significant severe wind are still occurring, but the more chaotic environment reflected in reflectivity and Θ_v imply that these processes are occurring less often and/or are weaker than before.

5.5.5 0630 UTC

In the final analysis time, the MCS has weakened dramatically with no contiguous line of convection, a much smaller area of severe winds, no mesovortices, a cooler inflow, and a much warmer cold pool (Fig. 84a, 84b, 84c, 84d). This analysis time has 11 sub-severe, 14 severe, and 3 significant severe trajectories. Only one trajectory descends from above 1 km with the vast majority descending from below 500 m, though a few trajectories do show the typical rapid descent at the end of the trajectory (Fig. 85a). The overall magnitudes for W have decreased with no large difference between any of the three categories (Fig. 85b). There is also no distinction between the three categories in either the environmental or prime CMT with overall values being lower than the previous time (Fig. 85c, 85d).

Interestingly, all 3 categories have positive medians for both horizontal forcing terms with the buoyancy forcing once again being the main accelerating force (Fig. 86a). The significant severe category has a median added wind speed from buoyancy of 13 m s^{-1} which is substantially larger than the severe median (6.5 m s^{-1}) or the sub median (3 m s^{-1}). Within the last 5 minutes, the median of dynamic forcing for sig severe and sub-severe is below zero with the severe category being barely positive (Fig. 86b). Once again the significant severe buoyancy is much larger than the other two categories with a median near 5 m s^{-1}. This trend continues in the last 2 minutes as well making this one of the only time periods where the buoyancy term is the main forcing the entire time period for all 3 categories (86c). In the vertical at all three time periods analyzed, the buoyancy overall dominates the downward motion with magnitude increasing with increasing wind speed (Fig. 86d, 86e, 86f).

The 5-6 July trajectories initially start out very similar to the 25-26 June trajectories in later times with an extra push from horizontal dynamic forcing and CMT at the very end of the analyzed trajectories. This continued as the remnant bowing MCS segment contained multiple mesovortices along the leading edge which continued to provide enhanced dynamic forcing. However, by 0600 UTC mesovortices along the leading line are no longer visible and the MCS has visibly weakened. This correlates to a lower number of severe and significant severe trajectories and less aerial coverage of severe winds. By the last analysis period, there is no more dynamic push in the horizontal for the severe and significant severe trajectories with only buoyancy dominating both horizontal and vertical forcing. Despite the 5-6 July MCS starting out as a surface-based, prolific severe wind-producing system and producing significant severe winds from leading line mesovortices after dark, overall forcing in the MCS decreased with a cooling inflow environment and subsequent warming of the cold pool.

5.6 Updraft and Buoyancy Analysis

To try to determine the reasoning for the 25-26 June MCS intensifying over time and the 5-6 July MCS weakening over time, the initial height of updraft inflow trajectories was analyzed. The criteria for defining an updraft are the same as in Miller et al. (2020) of $w > 5$ m s^{-1}, reflectivity greater than 35 dBZ, and a height between 2.5 and 5 km to capture mature MCS convective line updrafts. These criteria were evaluated on the D03 WRF grid every 30 minutes to coincide with the selected trajectory analysis times. Once a list of all points meeting the aforementioned criteria at a given time was determined, a sample of 50 was selected for calculating the backward trajectories. In order to save computation time, a time step of 30 s was used for this analysis since the general location was prioritized over forcing calculations. Violin plots for each analysis time in both cases are shown in Fig. 87. For the 26 June case, the median initial height of updraft inflow trajectories is around 2.5 km for 0500, 0600, and 0630 UTC, 2 km for 0630 UTC, 2.7 km for 0700 UTC, and 1.5 km for 0730 UTC (Fig. 87a). While these values may seem high for surface-based MCS, note that the interquartile range tends to descend overtime and that the violin plot is widest at the lower heights. This supports results from Miller et al. (2020) showing that while the majority of updraft inflow trajectories originated from the surface, the MCS updrafts were ingesting trajectories with a wide range of initial heights. For the 5-6 July case, the median initial height of updraft inflow trajectories is around 3 km for 0430, 2 km for 0500, 0530, and 0600 UTC, and 2.25 km for 0630 UTC (Fig. 87b). Like the 25-26 June case, the interquartile values descend with height and the widest portion of the violin is generally at or below 1 km. This indicates that both MCSs remained surface-based throughout the analysis period and that a surface-based to elevated transition does not explain why the 5-6 July MCS weakened over time.

Next, a buoyancy analysis over the lowest 5 km of the cold pool was conducted similar to the sounding analysis of Hitchcock et al. (2019). A box that encompassed a large portion of the cold pool and the selected trajectories was used to calculate the median buoyancy value at every height from the surface to 5 km every 30 minutes. The buoyancy profiles for 26 June show negative buoyancy in the lowest 2.5 km at 0500 UTC, however, this height increases for each subsequent time period indicating a deepening cold pool (Fig. 88a). One interesting thing to note is that the minimum in buoyancy is not at the surface but slightly elevated and may be due to the remnant stable layer in the environment. Also, the buoyancy for the lowest kilometer does not change much with time but the layer between 2 and 4 km shows buoyancy becoming more negative with time. The buoyancy profiles for July do not have as much spread with time compared to June, but a similar pattern of the level of zero buoyancy increasing with height in time is apparent from 0500 UTC on (Fig. 88b). Also note that there is no low-level inversion layer with the maximum negative buoyancy at the surface for all time periods. While the general trend is for buoyancy to become more negative in time, the final analysis at 0630 UTC shows a reversal below 3.25 km. This is especially prominent below 1 km and may explain part of why the 6 July MCS weakened over time. From the overall Θ_v values at 80 m every 30 minutes, it appeared that the gradient from the inflow to the outflow was becoming stronger over time for the 26 June case and weaker over time for the 6 July case. Perhaps the internal storm dynamics weakened over time due to less available positive buoyancy in the inflow and this started to impact the outflow after 0600 UTC.

Chapter 6: Comparison to Previous Studies

While no previous study has looked into the forcings for nocturnal MCS severe winds utilizing dynamic and buoyant pressure perturbations, the Parker et al. (2020) and Parker (2021) papers briefly delved into PECAN MCS severe wind production. Parker et al. (2020) attributed the 0521 UTC wind report to a mesovortex due to surging outflow evident in KTLX radial velocity shown in Fig. 16a. However, the analysis from Miller et al. (2020) and the current study show no evidence of a mesovortex influencing the surge of outflow just west of DOW8 as shown in Fig. 7. The cause of the severe wind at 0521 UTC appears to be favorable dynamic forcing between an updraft/downdraft couplet with enhanced horizontal vorticity and a minimum in dynamic perturbation pressure. While there is evidence at 0600 UTC of a mesovortex inducing significant severe surface winds (Fig. 49), this is not a common or necessary mechanism for severe winds in the 25-26 June MCS. In fact, the dynamic enhancement from horizontal vorticity was also acting on the mesovortex trajectory. While Parker (2021) did not go into specific mechanisms for severe winds, they noted that all 4 MCSs analyzed from PECAN produced severe surface winds and had a surface-based cold pool supporting the findings from the current simulations.

Though Trapp and Weisman (2003) (hereafter TW03) focused on a typical QLCS observed during BAMEX rather than nocturnal systems, their analysis of a trajectory (Fig. 19) into a wind speed maximum has similitude to many of the aforementioned severe and significant severe trajectories. Like the analyzed trajectories in this study, the TW03 trajectory remains at an altitude generally less than 1 km and its rate of descent never exceeds -2 m s^{-1} implying locally intense microbursts are not responsible for wind speed maximums. Furthermore, the TW03 trajectory experiences its largest wind speed increase below 200 m within the last 200 s of the period like most severe wind trajectories analyzed here. Buoyancy is responsible for the majority of the parcel acceleration until the final few minutes where the dynamic and vorticity components increase to drive the final acceleration due to the mesovortex. Despite using a different NWP model to simulate a QLCS, the same trend in buoyant and dynamic forcing occurs for the TW03 trajectory and many of the analyzed trajectories in both the 25-26 June and 5-6 July MCS.

Chapter 7: Conclusions

The primary goal of this study was to analyze the forcings behind severe surface winds in two PECAN MCS cases. This was approached from both an observational analysis of the 25-26 June MCS and a simulation of both the 25-26 June and 5-6 July MCS. In order for the simulation to more closely resemble the observed systems, a new variation on the Fierro lightning DA method was utilized. Various tests of assimilating VII into WRF simulations showed that this method has utility during research simulations to help with overall MCS timing and morphology. Not only were the two PECAN cases in roughly the same location as observed, the morphology was very close to the observed system, and details such as the timing and location of mesovortices in the 5-6 July case were captured. This ensured confidence that the simulations were capturing similar severe wind dynamics to that of the observed systems.

The DLA analysis of the severe wind observed by the radar analysis showed that a combination of buoyancy forcing from rain evaporative cooling and a favorable position downstream of a downdraft and upstream of an updraft led to winds over 32 m s^{-1} at the surface (Fig. 14). While only one severe wind event from the 26 June case was observed with the PECAN assets, the overall morphology is very similar to many severe and significant severe trajectories analyzed in both MCS cases. In fact, the updraft/downdraft couplet orientation was observed in a large portion of the analyzed trajectories for both cases. Overall, the buoyancy forcing was the largest forcing over the entire time period to explain increases in horizontal and vertical wind speed. However, during the last 5 and/or 2 minutes of the analyzed trajectories, the increase in wind speed due to the dynamic forcings became larger than the impacts from buoyancy. This suggests that while all surface-based MCS with an established cold pool will have buoyancy contributing the most to the wind speed, an extra contribution from some dynamic process is necessary for those winds to exceed the severe or significant severe threshold. The extra dynamic push can come from different processes such as the updraft/downdraft couplet, a mesovortex, and/or deformation. Overall the dynamic push was stronger for the significant severe winds than the severe winds such as being in closer proximity to a leading line mesovortex or having a smaller horizontal distance between the updraft/downdraft couplet to further enhance horizontal acceleration which would imply larger horizontal vorticity. For a more strongly forced system such as the 5-6 July case, the enhanced dynamic push came mainly from leading line mesovortices, especially during the most intense period of the MCS, and favorable updraft/downdraft couplets. For a more marginal severe wind MCS such as the 25-26 June case, enhanced negative buoyancy (such as strong hydrometeor loading), CMT, and/or forcing from an updraft/downdraft couplet provided the extra dynamic push. When a mesovortex was visible along the leading line of convection, it was usually associated with severe and significant severe winds, supporting many studies' findings that the vortex flow was needed on top of the cold pool outflow to have wind reach the severe threshold. However, that is not the only path to severe winds. In more marginal cases where leading line mesovortices may not occur due to the overall strength of the system and/or the shear profile, processes related to strong buoyancy forcing will become more important in generating severe winds. Since hydrometeor loading appeared over and over again as the main accelerator of wind speeds, this would explain at times the sporadic nature of severe winds in nocturnal MCSs. Not all descending cores will have enough negative buoyancy to cause severe winds at the surface, and these cores will descend at different times related to the individual convective cells along the leading convective line.

For a more strongly forced nocturnal MCS, the presence of mesovortices along the leading line will be the most robust indicator of the presence of severe winds due to the vortex flow enhancing the outflow motion. These mesovortices will also act to strengthen updrafts due to the enhanced negative pressure perturbation from rotation to loft more hydrometeors vertically. Stronger updrafts will generally lead to stronger compensatory downdrafts and more hydrometeors will increase the downward acceleration due to hydrometeor drag. These factors combined explain why most of the significant and severe winds associated with the 5-6 July MCS were behind the remnant bowing MCS that had leading line mesovortices. For a more marginal case such as the 25-26 June MCS, most severe winds would be located very close to the leading convective line where most of the dynamic forcing occurs without strong mesovortices with substantial vertical vorticity. This is due to the mechanical lifting of the cold pool forcing updrafts near the surface for a relatively constant source of dynamic acceleration. But severe wind speeds are only achieved when that dynamic forcing is enhanced via a strong downdraft. These strong downdrafts are going to be most related to hydrometeor laden cores which will descend more rapidly than the general rear-to-front flow. Unfortunately for severe wind forecasting, these sporadic processes only act to enhance the horizontal wind speeds in the last 2-5 minutes before a trajectory reaches the surface. Further research into nocturnal MCS severe wind processes is needed to amass more cases of severe winds so that a wider range of dynamic forcings can be observed/simulated. In addition, faster-scanning radar technologies such as phased array will be necessary to observe these processes in the 2-5 minutes before they occur. The current 5-minute volume scan of the 88D network and of the research radars during PECAN will not always capture the processes occurring before severe winds are at the surface.

Tables

Setting	WRF Simulations
Initial Conditions	26 June: NAM model analysis 0000 UTC 26 June 2015 5-6 July: NAM model analysis 1800 UTC 5 July 2015
Lateral Boundary Conditions	NAM analyses every 3 hr
Vertical Levels	60
Microphysics	NSSL 2M
PBL	D01, D02: MYJ, D03: none
LW/SW	RRTMG
Surface	Noah LSM

Table 1: WRF Physical Parameters

Settings	26 June 2015	5-6 July 2015
3 km nest times	0000-1200 UTC	2100-1200 UTC
1 km nest times	0330-1200 UTC	0000-1200 UTC
333 m nest times	0430-0730 UTC	0400-0700 UTC
D01 VII nudging	0230-0430 UTC	2100-0200 UTC
D02 VII nudging	0330-0430 UTC	0000-0200 UTC

Table 2: Nest and VII Nudging Details

References

Ashley et al., 2019: A Climatology of Quasi-Linear Convective Systems and Their Hazards in the United States. *Wea. Forecasting*, **34**, -1631,1605.

Atkins, N. T., J. M. Arnott, R. W. Przybylinski, R. A. Wolf, and B. D. Ketchan, 2004: Vortex structure and evolution within bow echoes, Part I: Single-Doppler and damage analysis of the 29 June 1998 derecho. *Mon. Wea. Rev*., **132**, 2224–2242.

Atkins, N. T., C. S. Bouchard, R. W. Przybylinski, R. J. Trapp, and G. Schmocker, 2005: Damaging surface wind mechanism within the 10 June 2003 Saint Louis bow echo during BAMEX. *Mon. Wea. Rev*., **133**, 2275–2296.

Atkins, N. T., and M. St. Laurent, 2009a: Bow echo mesovortices. Part I: Processes that influence their damaging potential. *Mon. Wea. Rev*., **137**, 1497–1513.

Atkins, N. T., and M. St. Laurent, 2009b: Bow echo mesovortices. Part II: Their genesis. *Mon. Wea. Rev*., **137,**1514–1532.

Bernardet, L., and W. R. Cotton, 1998: Multiscale evolution of a derecho-producing mesoscale convective system. *Mon. Wea. Rev.*, **126 ,** 2991–3015.

Biggerstaff, M. I., and R. A. Houze, 1991a: Kinematic and precipitation structure of the 10-11 June 1985 squall line. *Mon. Wea. Rev*., **119**, 3034-3065.

Biggerstaff, M. I., and R. A. Houze, 1991b: Midlevel Vorticity Structure of the 10–11 June 1985 Squall Line. *Mon. Wea. Rev*., **119**, 3066–3079.

Biggerstaff, M. I., and R. A. Houze, 1993: Kinematics and Microphysics of the Transition Zone of the 10–11 June 1985 Squall Line. *J. Atmos. Sci*., **50**, 3091–3110.

Billings, J. M., and M. D. Parker, 2012: Evolution and maintenance of the 22–23 June 2003 nocturnal convection during BAMEX. *Wea. Forecasting*, **27**, 279–300, https://doi.org/10.1175/WAF-D-11-00056.1.

Bodine, D. J., and K. L. Rasmussen, 2017: Evolution of mesoscale convective system organizational structure and convective line propagation. *Mon. Wea. Rev.*, **145**, 3419–3440, https://doi.org/10.1175/MWR-D-16-0406.1.

Bryan, G. H., and M. L. Weisman, 2006: Mechanisms for the production of severe surface winds in a simulation of an elevated convective system. *23rd Conf. on Severe Local Storms*, St. Louis, MO, Amer. Meteor. Soc., 7.5.

Chipilski, H. G., X. Wang, and D. B. Parsons, 2020: Impact of assimilating PECAN profilers on the prediction of bore-driven nocturnal convection: A multiscale forecast evaluation for the 6 July 2015 case study. *Mon. Wea. Rev.*, **148**, 1147–1175, https://doi.org/10.1175/MWR-D-19-0171.1.

Davis, J.M. and Parker, M.D. (2014) Radar Climatology of Tornadic and Nontornadic Vortices in High-Shear, Low-CAPE Environments in the Mid-Atlantic and Southeastern. Weather and Forecasting, 29, 828-853.

Degelia, S. K., X. Wang, and D. J. Stensrud, 2019: An evaluation of the impact of assimilating AERI retrievals, kinematic profilers, rawinsondes, and surface observations on a forecast of a nocturnal convection initiation event during the PECAN field campaign. *Mon. Wea. Rev.*, **147**, 2739–2764, https://doi.org/10.1175/MWR-D-18-0423.1.

DiGangi, E., D. MacGorman, C. Ziegler, D. Betten, M. Biggerstaff, M. Bowlan, and C. Potvin, 2016: An overview of the 29 May 2012 Kingfisher supercell during DC3. *J. Geophys. Res.*, **121**, 14 316–14 343.

Doswell, C. A., III, and P. M. Markowski, 2004: Is buoyancy a relative quantity? *Mon. Wea. Rev.*, **132**, 853–863, https://doi.org/10.1175/1520-0493(2004)132<0853:IBARQ>2.0.CO;2.

Engerer, N. A., D. J. Stensrud, and M. C.Coniglio, 2008: Surface characteristics of observed cold pools. *Mon. Wea. Rev.*, **136**, 4839–4849.

Fierro, A. O., E. R. Mansell, C. L. Ziegler, and D. R. MacGorman, 2012: Application of a lightning data assimilation technique in the WRF-ARW model at cloud-resolving scales for the tornado outbreak of 24 May 2011. *Mon. Wea. Rev.*, **140**, 2609–2627.

Fierro, A. O., J. Gao, C. L. Ziegler, E. R.Mansell, D. R. MacGorman, and S. R.Dembek, 2014: Evaluation of a cloud-scale lightning data assimilation technique and a 3DVAR method for the analysis and short-term forecast of the 29 June 2012 derecho event. *Mon. Wea. Rev.*, **142**, 183–202.

Fierro, A. O., J. Gao, C. L. Ziegler, K. M.Calhoun, E. R. Mansell, and D. R.MacGorman, 2016: Assimilation of flash extent data in the variational framework at convection-allowing scales: Proof-of-concept and evaluation for the short-term forecast of the 24 May 2011 tornado outbreak. *Mon. Wea. Rev.*, **144**, 4373–4393.

Fierro, A. O., Y. Wang, J. Gao, and E. R.Mansell, 2019: Variational assimilation of radar data and GLM lightning-derived water vapor for the short-term forecasts of high-impact convective events. *Mon. Wea. Rev.*, **147**, 4045–4069.

Flournoy, M. D., and M. C. Coniglio, 2019: Origins of Vorticity in a Simulated Tornadic Mesovortex Observed During PECAN on 6 July 2015. *Mon. Wea. Rev.*, **147**(1), 107-134.

Forbes, G. S., and R. M. Wakimoto, 1983: A concentrated outbreak of tornadoes, downbursts and microbursts, and implications regarding vortex classification. *Mon. Wea. Rev.*, **111**, 220–236.

Foster, D. S., 1958: Thunderstorm gusts compared with computed downdraft speeds. *Mon. Wea. Rev.*, **86**, 91–94.

Fovell, R. G., and Y. Ogura, 1988: Numerical simulation of a midlatitude squall line in two Dimensions. *J. Atmos. Sci.*, **45**, 3846-3879.

Fujita, T. T., 1978: Manual of downburst identification for project Nimrod. Satellite and Mesometeorology Research Paper 156, Dept. of Geophysical Sciences, University of Chicago, 104 pp. [NTIS PB-286048.]

Fujita, T. T., 1979: Objectives, operation, and results of project NIMROD. Preprints, *11th Conf. on Severe Local Storms*, Kansas City, MO, Amer. Meteor. Soc. 259-266.

Fujita, T. T., 1981: Tornadoes and downbursts in the context of generalized planetary scales. *J. Atmos. Sci.,* **38,** 1511–1534.

Fujita, T. T., and R. M. Wakimoto 1981: Five scales of airflow associated with a series of downbursts on 16 July 1980. *Mon. Wea. Rev.*, **109**, 1438-1456.

Funk, T. W., K. E. Darmofal, J. D. Kirkpatrick, V. L. DeWald, R. W. Przybylinski, G. K. Schmocker, and Y. J. Lin, 1999: Storm reflectivity and mesocyclone evolution associated with the 15 April 1994 squall line over Kentucky and southern Indiana. *Wea. Forecasting*, **14**, 976–993.

Geerts, B., 2001: Estimating downburst-related maximum surface wind speeds by means of proximity soundings in New South Wales, Australia. *Wea. Forecasting*, **16**, 261–269.

Geerts, B., and Coauthors, 2017: The 2015 Plains Elevated Convection At Night Field Project. *Bull. Amer. Meteor. Soc.*, **98**, 767–786, https://doi.org/10.1175/BAMS-D-15-00257.1.

Hitchcock, S. M., R. S. Schumacher, G. R.Herman, M. C. Coniglio, M. D. Parker, and C. L.Ziegler, 2019: Evolution of pre- and postconvective environment profiles from mesoscale convective systems during PECAN. *Mon. Wea. Rev.*, **147**, 2329–2354.

Houze, R. A., S. A. Rutledge, M. I.Biggerstaff, and B. F. Smull, 1989: Interpretation of Doppler weather radar displays of midlatitude mesoscale convective systems. *Bull. Amer. Meteor. Soc.*, **70**, 608–619.

Johns, R. H., and C. A. Doswell III, 1992: Severe local storms forecasting. *Wea. Forecasting*, **7**, 588–612.

Jorgensen, D. P., and B. F. Smull, 1993: Mesovortex circulations seen by airborne Doppler radar within a bow-echo mesoscale convective system. *Bull. Amer. Meteor. Soc.*, **74**, 2146–2157.

Jorgensen, D. P., and M. A. LeMone, and S. B. Trier, 1997: Structure and evolution of the 22 February 1993 TOGA COARE squall line: Aircraft observations of precipitation, circulation, and surface energy fluxes. *J. Atmos. Sci.*, **54**, 1961-1985.

Klemp, J. B., W. C. Skamarock, and J. Dudhia, 2007: Conservative split-explicit time integration methods for the compressible nonhydrostatic equations. *Mon. Wea. Rev.*, **135**, 2897–2913.

Klimowski, B. A., 1994: Initiation and development of rear inflow within the 28–29 June 1989 North Dakota mesoconvective system. *Mon. Wea. Rev.*, **122**, 765–779.

Klimowski, B. A., , R. Przybylinski, G. Schmocker, and M. R. Hjelmfelt, 2000: Observations of the formation and early evolution of bow echoes. Preprints, *20th Conf. on Severe Local Storms*, Orlando, FL, Amer. Meteor. Soc., 44–47.

Kuchera, E. L., and M. D. Parker, 2006: Severe convective wind environments. *Wea. Forecasting*, **21**, 595–612.

Mahale, V. N., J. A. Brotzge, H. B. Bluestein, 2012: An analysis of vortices embedded within a quasi-linear convective system using X-band polarimetric radar. *Wea. Forecasting*, **27**, 1520–1537.

Mahoney, K. M., G. M. Lackmann, and M. D. Parker, 2009: The role of momentum transport in the motion of a quasi-idealized mesoscale convective system. *Mon. Wea. Rev.*, **137**, 3316-3338.

Mahoney, K. M., and G. M. Lackmann, 2011: The sensitivity of momentum transport and severe surface winds to environmental moisture in idealized simulations of a mesoscale convective system. *Mon. Wea. Rev.*, **139**, 1352–1369.

Markowski, P. M., and Y. P. Richardson, 2014: : The influence of environmental low-level shear and cold pools on tornadogenesis: Insights from idealized simulations. *J. Atmos. Sci.*, **71**, 243-275.

Markowski, P. M., J. M. Straka, and E. N. Rasmussen, 2002: Direct surface thermodynamic observations within the rear-flank downdrafts of nontornadic and tornadic supercells. *Mon. Wea. Rev.*, **130**, 1692-1721.

McDonald, J. M., and C. C. Weiss, 2021: Cold pool characteristics of tornadic quasi-linear convective systems and other convective modes observed during VORTEX-SE. Mon. Wea. Rev., 149, 821-840.

Miller, R. L., C. L. Ziegler, and M. I. Biggerstaff, 2020: Seven-Doppler radar and in situ analysis of the 25-26 June 2015 Kansas MCS during PECAN. *Mon. Wea. Rev.*, **148**, 211-240.

Newman, J. F., and P. L. Heinselman, 2012: Evolution of a quasi- linear convective system sampled by phased array radar. *Mon. Wea. Rev.*, **140**, 3467–3486.

Orlanski, I., 1975: A rational subdivision of scales for atmospheric processes. *Bull. Amer. Meteor. Soc.*, **56**, 527–534.

Parker, M. D., 2008: Response of simulated squall lines to low-level cooling. *J. Atmos. Sci.*, **65**, 1323–1341, https://doi.org/10.1175/2007JAS2507.1.

Parker, M. D., 2021: Self-organization and maintenance of simulated nocturnal mesoscale convective systems from PECAN. *Mon. Wea. Rev.*, **149**, 999–1022, https://doi.org/10.1175/MWR-D-20-0263.1.

Parker, M. D., B. S. Borchardt, R. L. Miller, and C. L. Ziegler, 2020: Simulated Evolution and Severe Wind Production by the 25–26 June 2015 Nocturnal MCS from PECAN. *Mon. Wea. Rev.*, **148**, 183–209.

Przybylinski, R. W., 1995: The bow echo: Observations, numerical simulations, and severe weather detection methods. *Wea. Forecasting*, **10**, 203–218.

Przybylinski, R. W., G. K. Schmocker, and Y. J. Lin, 2000: A study of storm and vortex morphology during the 'intensifying stage' of severe wind mesoscale convective systems. Preprints, 20th Conf. on Severe Local Storms, Orlando, FL, Amer. Meteor. Soc., 6.2.

——, and D. M. DeCaire, 1985: Radar signatures associated with the derecho: One type of mesoscale convective system. Preprints, *14th Conf. on Severe Local Storms*, Indianapolis, IN, Amer. Meteor. Soc., 228–231.

Richter, H., J. Peter, and S. Collis, 2014: Analysis of a destructive wind storm on 16 November 2008 in Brisbane, Australia. *Mon. Wea. Rev*., **142**, 3038–3060.

Rotunno, R., and J. B. Klemp, 1982: The influence of the shear-induced pressure gradient on thunderstorm motion. *Mon. Wea. Rev.*, **110**, 136–151, https://doi.org/10.1175/1520-0493(1982)110<0136:TIOTSI>2.0.CO;2.

Rotunno, R., and J. B. Klemp, 1985: On the rotation and propagation of simulated supercell thunderstorms. *J. Atmos. Sci.*, **42**, 271–292, https://doi.org/10.1175/1520-0469(1985)042<0271:OTRAPO>2.0.CO;2.

Rotunno, R., J. B. Klemp, and M. L. Weisman, 1988: A theory for strong, long-lived squall lines. *J. Atmos. Sci*., **45**, 463–485.

Rutledge, S. A., R. A. Houze, M. I. Biggerstaff, T.Matejka, 1988: The Oklahoma-Kansas mesoscale convective system of 10-11 June 1985: Precipitation structure and single-Doppler radar analysis. *Mon. Wea. Rev*., **116**, 1409-1430.

Schaumann, J. S., and R. W. Przybylinski, 2012: Operational application of 0–3 km bulk shear vectors in assessing quasi-linear convective system mesovortex and tornado potential. *26th Conf. on Severe Local Storms*, Nashville, TN, Amer. Meteor. Soc., 142.

Schenkman, A. D., M. Xue, A. Shapiro, K. Brewster, and J. Gao, 2011a: The analysis and prediction of the 8–9 May 2007 Oklahoma tornadic mesoscale convective system by assimilating WSR-88D and CASA radar data using 3DVAR. *Mon. Wea. Rev*., **139**, 224– 246. 24

——, ——, ——, ——, and ——, 2011b: Impact of CASA radar and Oklahoma Mesonet data assimilation on the analysis and pre- diction of tornadic mesovortices in an MCS. *Mon. Wea. Rev*., **139**, 3422–3445.

——, ——, and ——, 2012: Tornadogenesis in a simulated mesovortex within a mesoscale convective system. *J. Atmos. Sci.*, **69**, 3372–3390.

Seibert, P., 1993: Convergence and accuracy of numerical methods for trajectory calculations. *J. Appl. Meteor.*, **32**, 558–566, https://doi.org/10.1175/1520-0450(1993)032<0558:CAAONM>2.0.CO;2.

Shabbott, C. J., and P. M. Markowski, 2006: Surface and in situ observations within the outflow of forward-flank downdrafts of supercell thunderstorms. *Mon. Wea. Rev.*, **134**, 1422- 1441.

Skamarock, W., and Coauthors, 2008: A description of the Advanced Research WRF version 3. NCAR Tech. Note NCAR/TN-475+STR, 113 pp., https://doi.org/10.5065/D68S4MVH.

Skamarock, W. C., and J. B. Klemp, 2008: A time-split nonhydrostatic atmospheric model for weather research and forecasting applications. *J. Comput. Phys.*, **227**, 3465–3485, https://doi.org/10.1016/j.jcp.2007.01.037.

Smull, B. F., and R. A. Houze, 1985: A Midlatitude Squall Line with a Trailing Region of Stratiform Rain: Radar and Satellite Observations. *Mon. Wea. Rev.*, **113**, 117–133.

——, and ——, 1987: Rear inflow in squall lines with trailing stratiform precipitation. *Mon. Wea. Rev.*, **115**, 2869–2889.

Snook, N., M. Xue, and Y. Jung, 2011: Analysis of a tornadic mesoscale convective vortex based on ensemble Kalman filter assimilation of CASA X-band and WSR-88D radar data. *Mon. Wea. Rev.*, **139**, 3446–3468.

Trapp R. J, E. D. Mitchell, G. A. Tipton, D. W. Effertz, A. I. Watson, D. L. Andra Jr., and M. A. Magsig, 1999: Descending and nondescending tornadic vortex signatures detected by WSR-88Ds. *Wea. Forecasting*, **14**, 625–639.

Trapp, R. J, G. J. Stumph, and K. L. Manross, 2005: A reassessment of the percentage of tornadic mesocyclones. *Wea. Forecasting*, **20**, 680–687.

Trapp, R. J., and M. L. Weisman, 2003: Low-level mesovortices within squall lines and bow echoes. Part II: Their genesis and implications. *Mon. Wea. Rev.*, **131**, 2804–2823.

Wakimoto, R. M., H. V. Murphey, A. Nester, D. P. Jorgensen, and N. T. Atkins, 2006a: High winds generated by bow echoes. Part I: Overview of the Omaha bow echo 5 July 2003 storm during BAMEX. *Mon. Wea. Rev.*, **134**, 2793–2812.

Wakimoto, R. M. C. A. Davis, and N. T. Atkins, 2006b: High winds generated by bow echoes. Part II: The relationship between the mesovortices and damaging straight-line winds. *Mon. Wea. Rev.*, **134**, 2813–2829.

Wheatley, D. M., and R. J. Trapp, 2008: The effect of mesoscale heterogeneity on the genesis and structure of mesovortices within quasi-linear convective systems. Mon. Wea. Rev., 136, 4220–4241.

Wheatley, D. M., R. J. Trapp, and N. T. Atkins, 2006: Radar and damage analysis of severe bow echoes observed during BAMEX. *Mon. Wea. Rev.*, 134, 791–806, https://doi.org/10.1175/MWR3100.1.

Weisman, M. L., 1992: The role of convectively generated rear- inflow jets in the evolution of long-lived mesoconvective systems. *J. Atmos. Sci.*, **49**, 1826–1847.

Weisman, M. L., 1993: The genesis of severe, long-lived bow echoes. *J. Atmos. Sci.*, **50**, 645–670.

Weisman, M. L., and R. Rotunno, 2000: The use of vertical wind shear versus helicity in interpreting supercell dynamics. *J. Atmos. Sci.*, **57** , 1452–1472.

Weisman, M. L., and R. J. Trapp, 2003: Low-level mesovortices within squall lines and bow echoes. Part I: Overview and dependence on environmental shear. *Mon. Wea. Rev*., **131**, 2779–2803.

Weiss, C. C., and J. L. Schroeder, 2008: StickNet: A new portable, rapidly-deployable, surface observing system. *Bull. Amer. Meteor. Soc.*, **89**, 1502–1503.

Xu, X., M. Xue, and Y. Wang, 2015: The genesis of mesovortices within a real-data simulation of a bow echo system. *J. Atmos. Sci*., **72**, 1963–1986.

Ziegler, C. L., 2013a: A diabatic Lagrangian technique for the analysis of convective storms. Part I: Description and validation via an observing system simulation experiment. *J. Atmos. Oceanic Technol.*, **30**, 2248–2265.

Ziegler, C. L., 2013b: A diabatic Lagrangian technique for the analysis of convective storms. Part II: Application to a radar-observed storm. *J. Atmos. Oceanic Technol.*, **30**, 2266–2280.

Zipser, E., 1977: Mesoscale and convective–scale downdrafts as distinct components of squall-line structure. *Mon. Wea. Rev.*, **105**, 1568–1589.

Figures

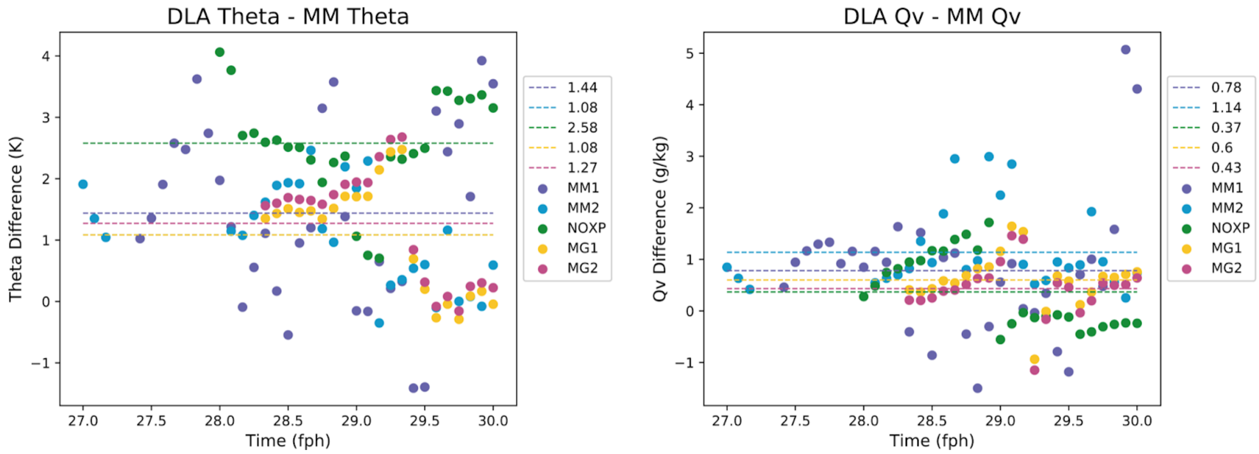

Figure 1. The difference in a) theta and b) water vapor mixing ratio of the DLA grid point value minus the in situ platform measurement every 5 minutes. The dashed line indicates the mean difference value for the 3 hour period.

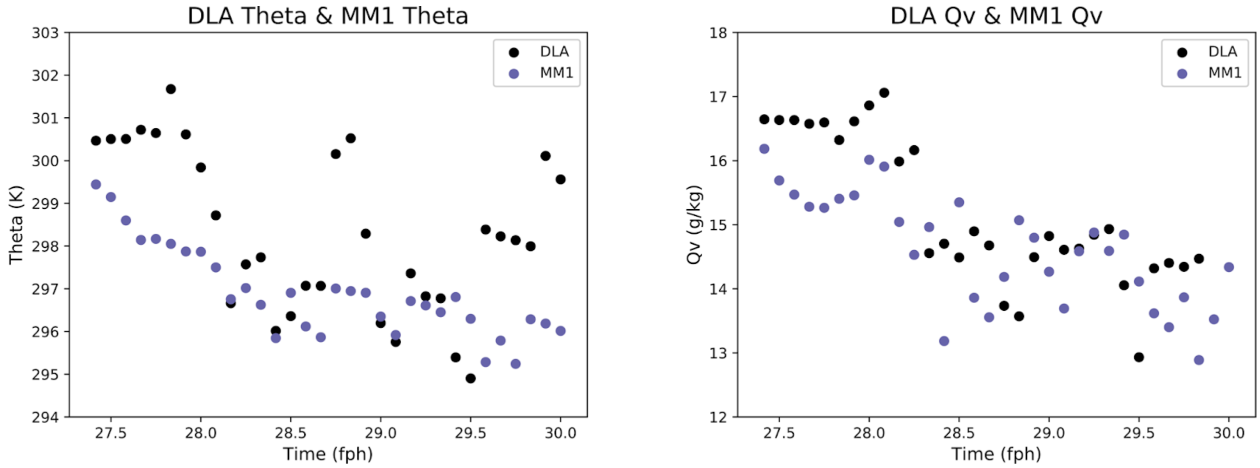

Figure 2. The measured vs calculated value of a) theta and b) water vapor mixing ratio over a three hour period between the DLA and MM1.

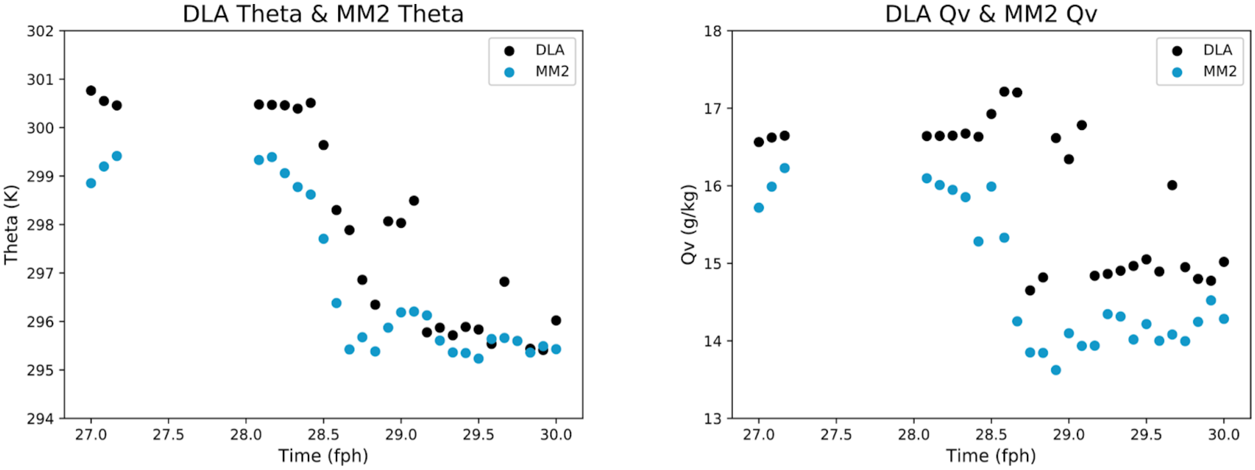

Figure 3. The measured vs calculated value of a) theta and b) water vapor mixing ratio over a three hour period between the DLA and MM2.

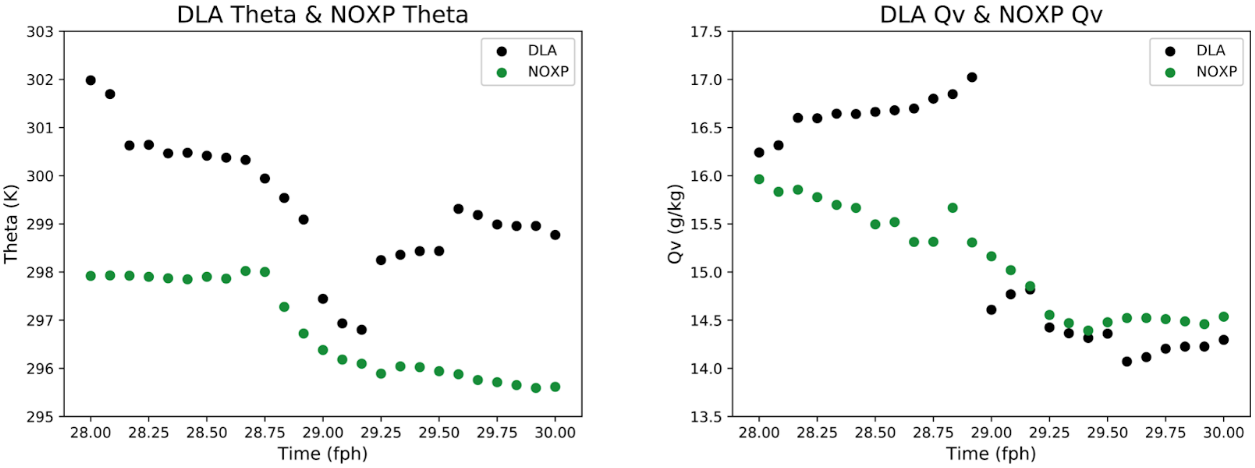

Figure 4. The measured vs calculated value of a) theta and b) water vapor mixing ratio over a three hour period between the DLA and NOXP.

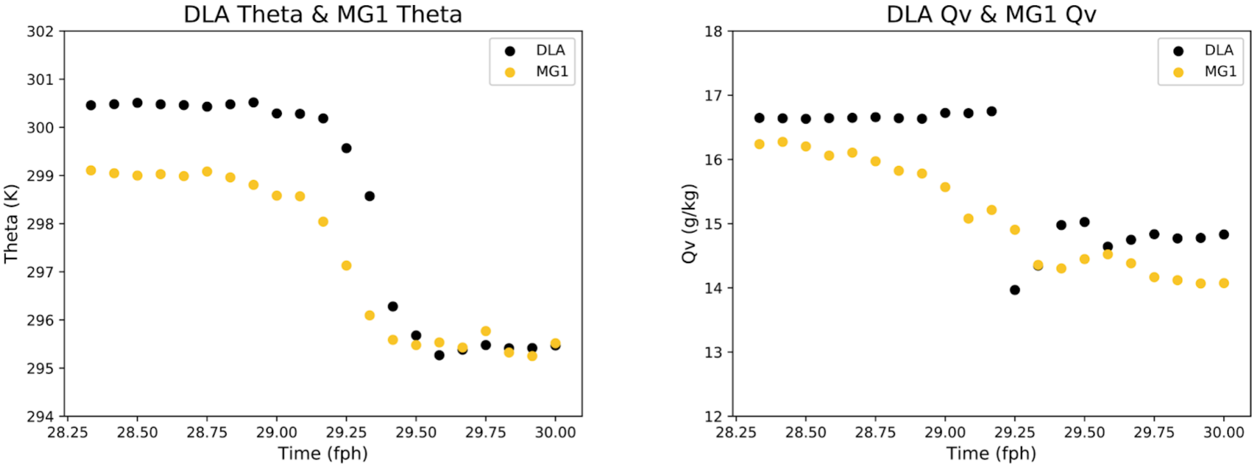

Figure 5. The measured vs calculated value of a) theta and b) water vapor mixing ratio over a three hour period between the DLA and MG1.

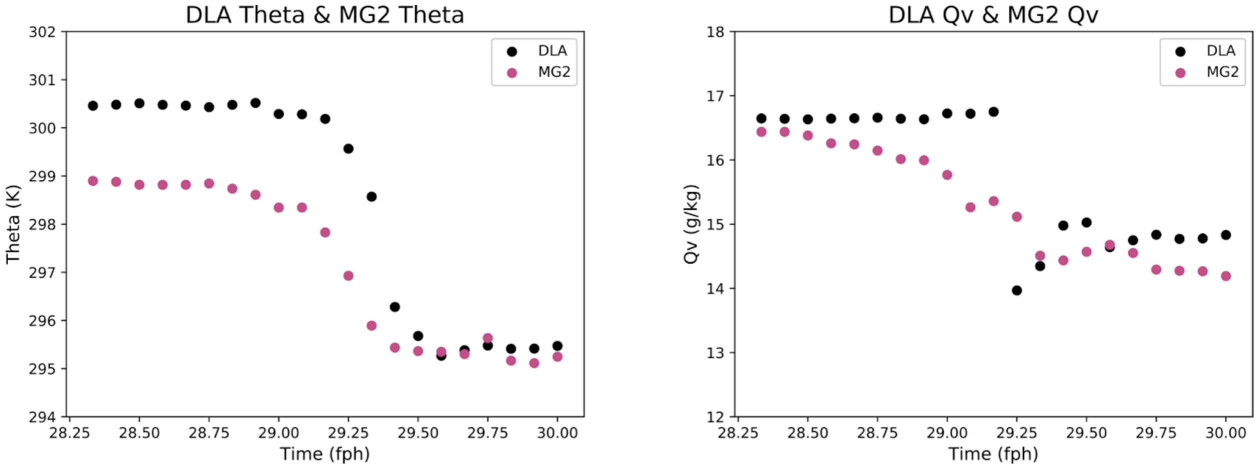

Figure 6.The measured vs calculated value of a) theta and b) water vapor mixing ratio over a three hour period between the DLA and MG1.

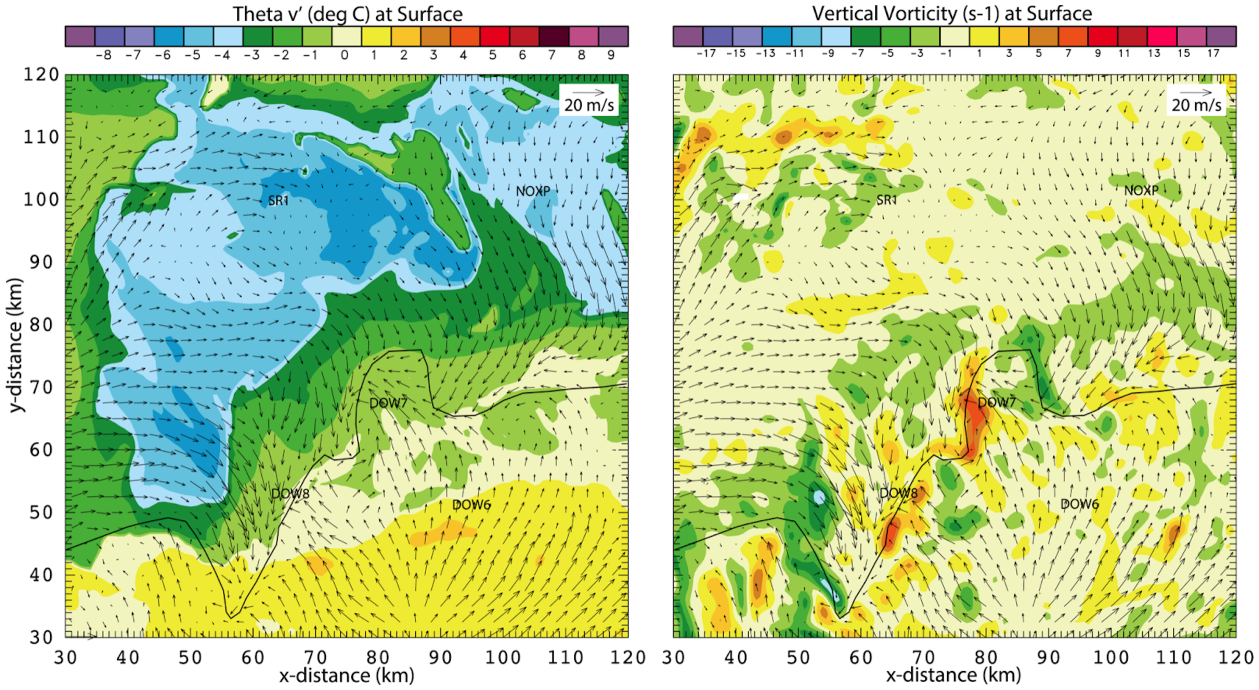

Figure 7. a) DLA derived Θ_v' and b) radar analysis calculated vertical vorticity at the surface at 0510 UTC. Black line denotes the edge of the MCS outflow. The area of severe winds is to the west of DOW8. Vertical vorticity scale has a multiplier factor of 10^{-3}.

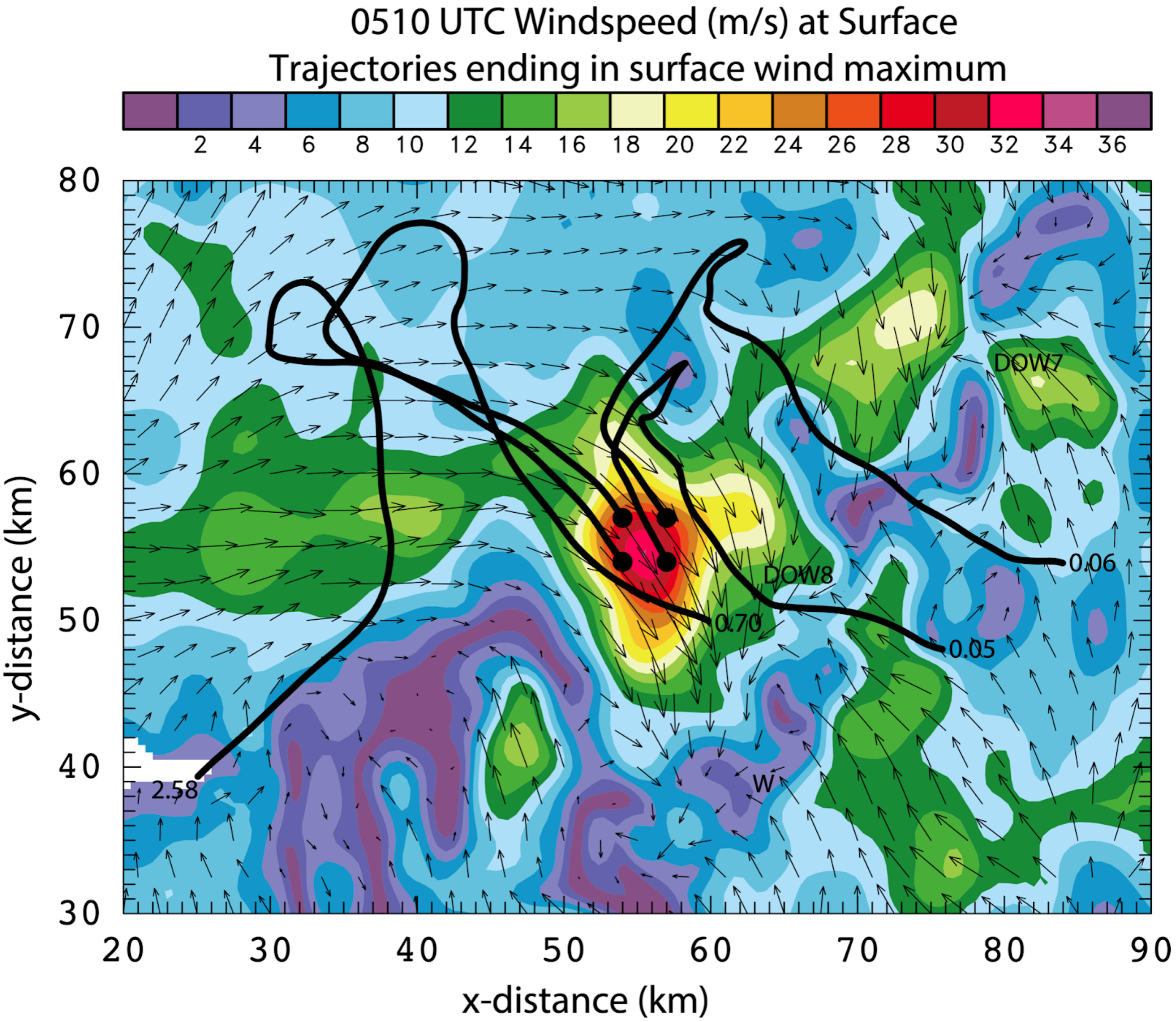

Figure 8. Spaghetti plot of trajectories at 0510 UTC flowing into the wind maximum with their initial trajectory height (in km) listed at the beginning of the trajectory. All trajectories end at 500 m in altitude.

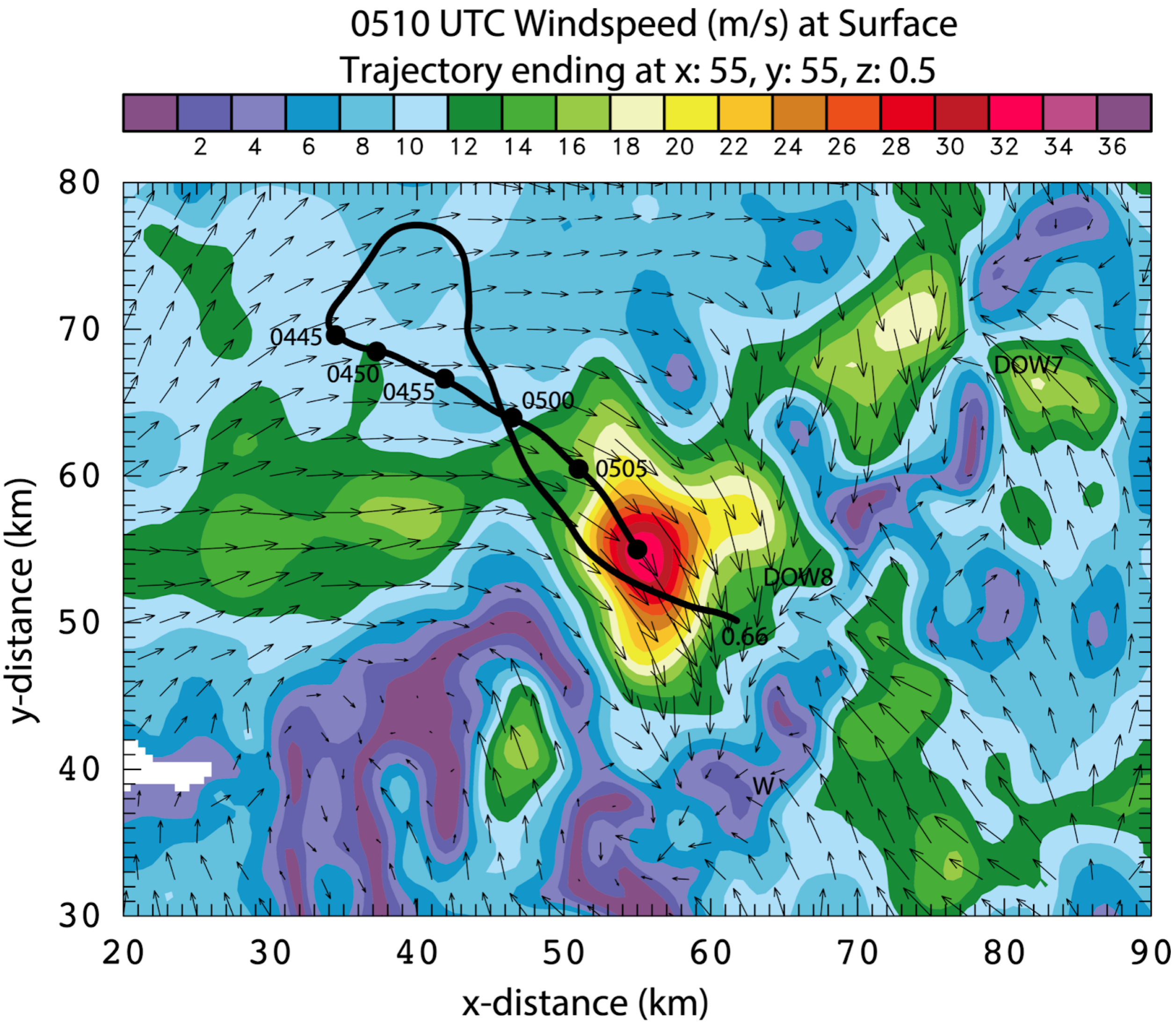

Figure 9. Single trajectory towards the center of wind speed maximum at 0510 UTC. Black dots are labeled with the time to denote the parcel's location along the trajectory.

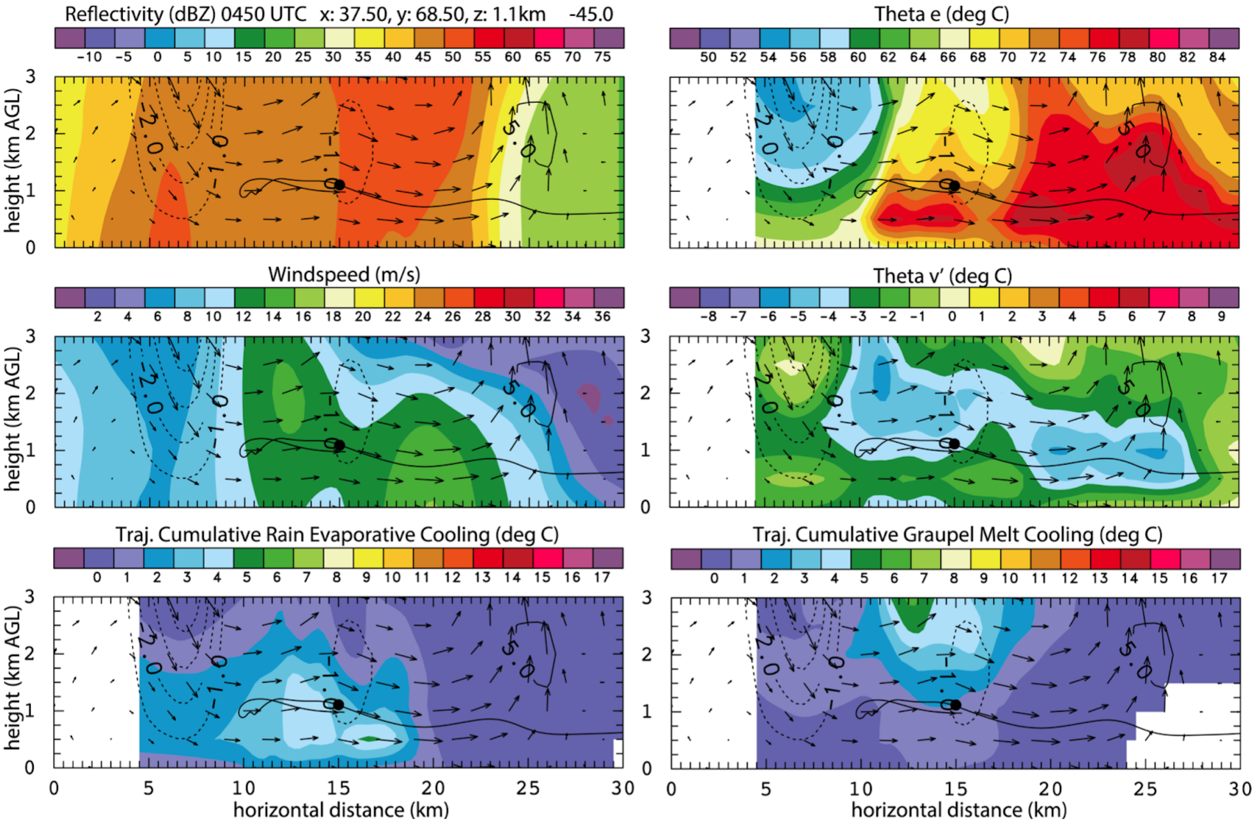

Figure 10. Cross-sections at 0450 UTC of a) reflectivity b) Θ_e c) wind speed d) Θ_v' e) rain evaporative cooling f) graupel/hail melt cooling along the trajectory shown in Fig. 9. Solid (dashed) contours indicate updrafts (downdrafts) every 5 m s^{-1} (-1 m s^{-1}).

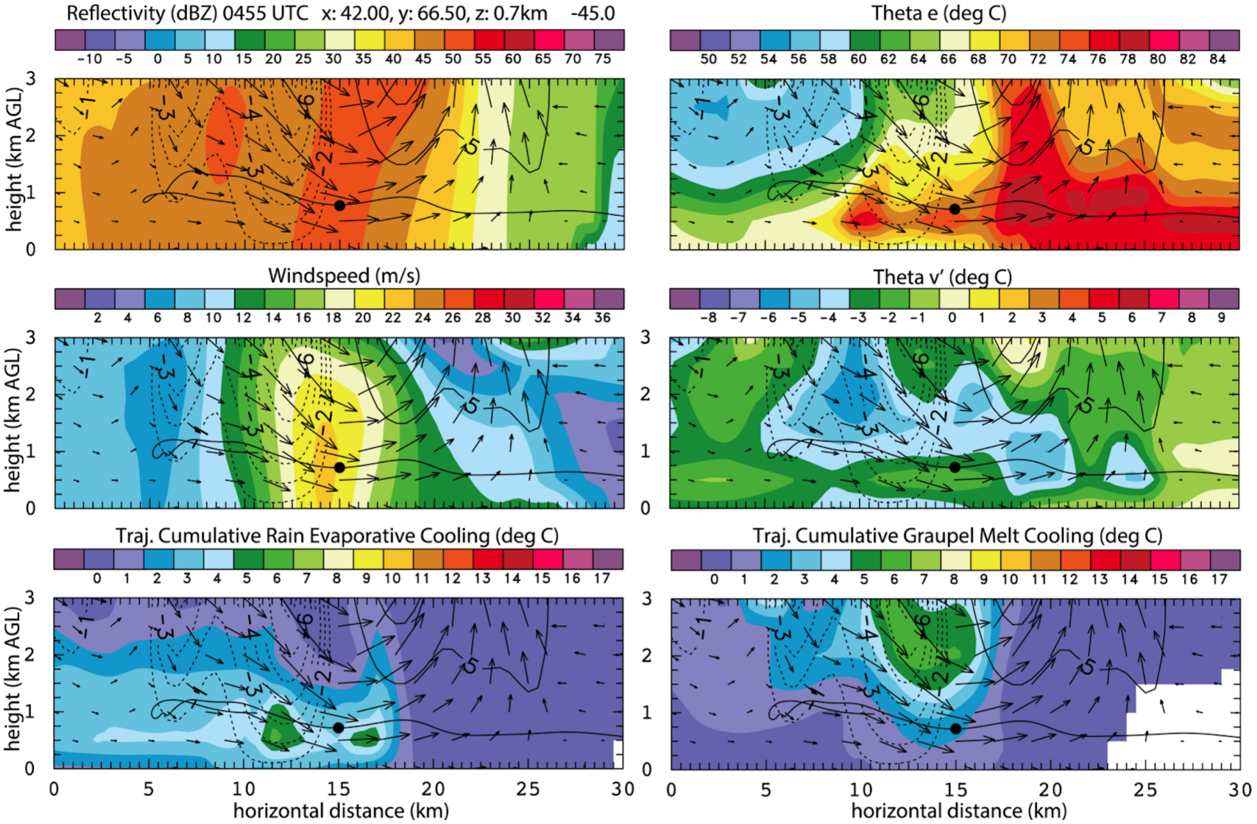

Figure 11. Cross-sections at 0455 UTC of a) reflectivity b) Θ_e c) wind speed d) Θ_v' e) rain evaporative cooling f) graupel/hail melt cooling along the trajectory shown in Fig. 9. Solid (dashed) contours indicate updrafts (downdrafts) every 5 m s^{-1} (-1 m s^{-1}).

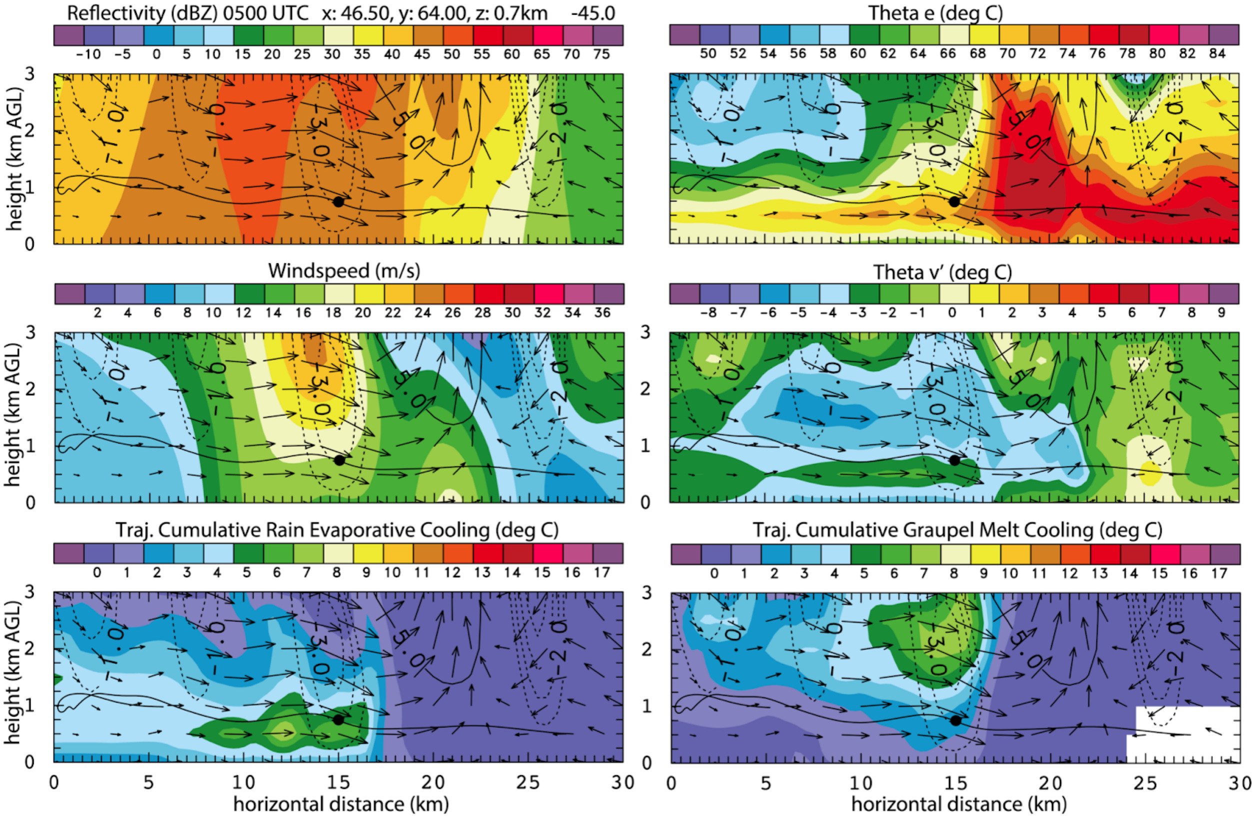

Figure 12. Cross-sections at 0500 UTC of a) reflectivity b) Θ_e c) wind speed d) Θ_v' e) rain evaporative cooling f) graupel/hail melt cooling along the trajectory shown in Fig. 9. Solid (dashed) contours indicate updrafts (downdrafts) every 5 m s^{-1} (-1 m s^{-1}).

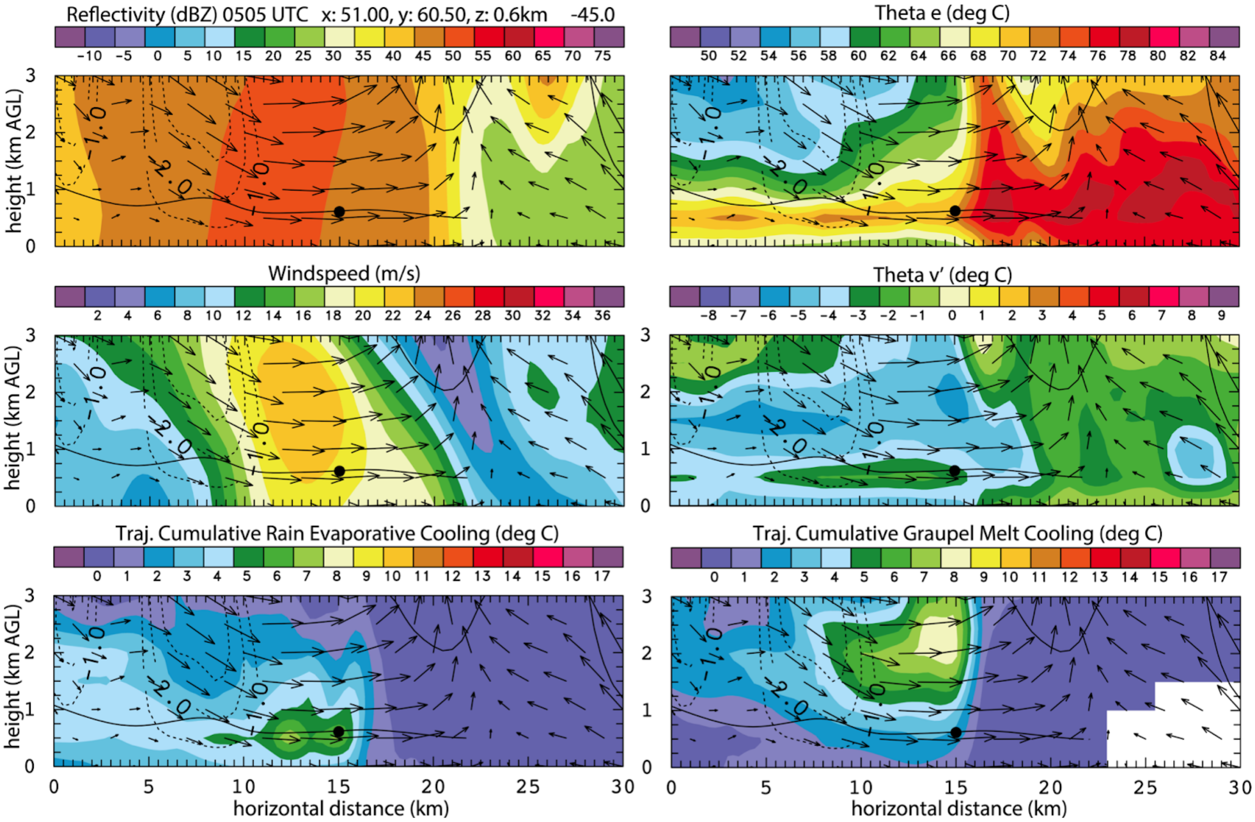

Figure 13. Cross-sections at 0505 UTC of a) reflectivity b) Θ_e c) wind speed d) Θ_v' e) rain evaporative cooling f) graupel/hail melt cooling along the trajectory shown in Fig. 9. Solid (dashed) contours indicate updrafts (downdrafts) every 5 m s^{-1} (-1 m s^{-1}).

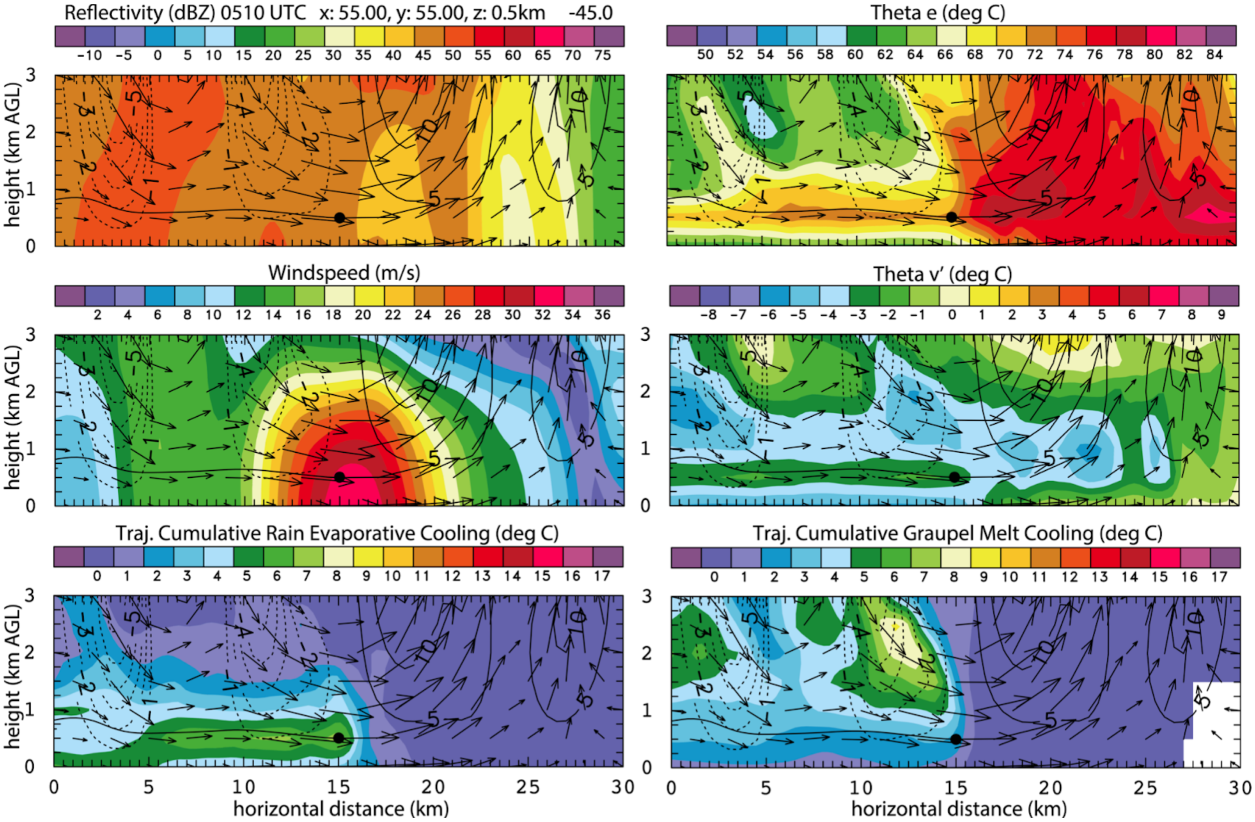

Figure 14. Cross-sections at 0510 UTC of a) reflectivity b) Θ_e c) wind speed d) Θ_v' e) rain evaporative cooling f) graupel/hail melt cooling along the trajectory shown in Fig. 9. Solid (dashed) contours indicate updrafts (downdrafts) every 5 m s^{-1} (-1 m s^{-1}).

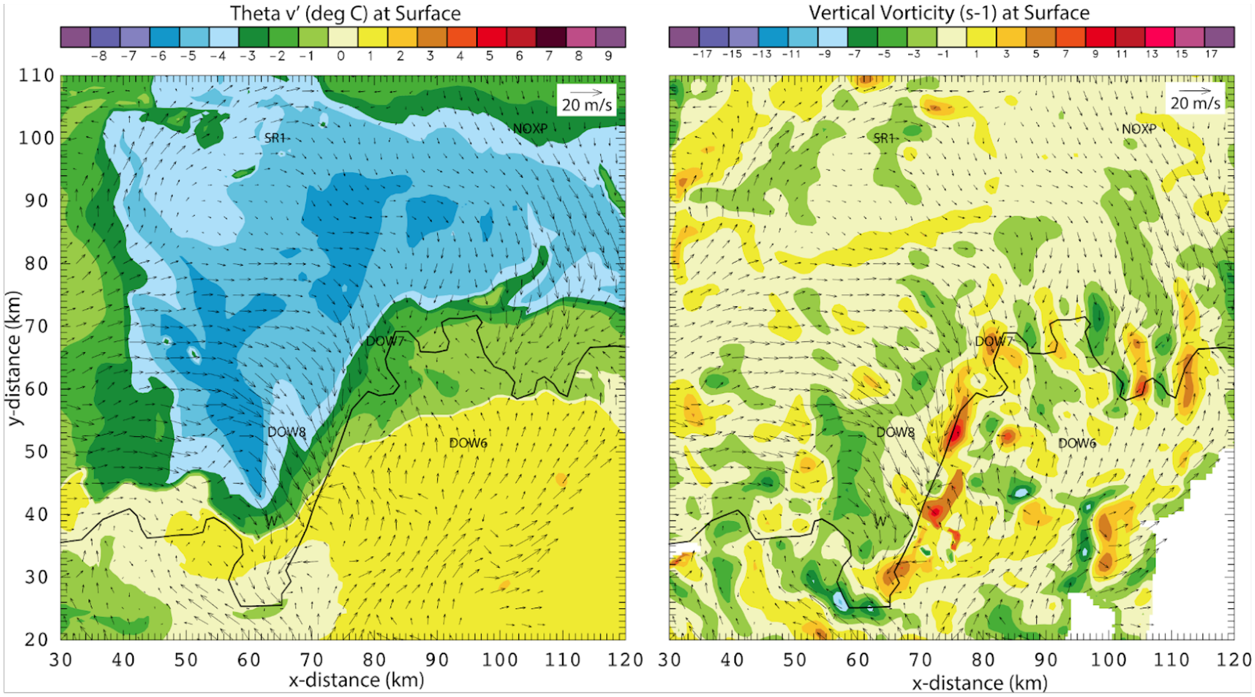

Figure 15. a) DLA derived Θ_v' and b) radar analysis calculated vertical vorticity at the surface at 0510 UTC. Black line denotes the edge of the MCS outflow. The area of severe winds is to the west of DOW8.

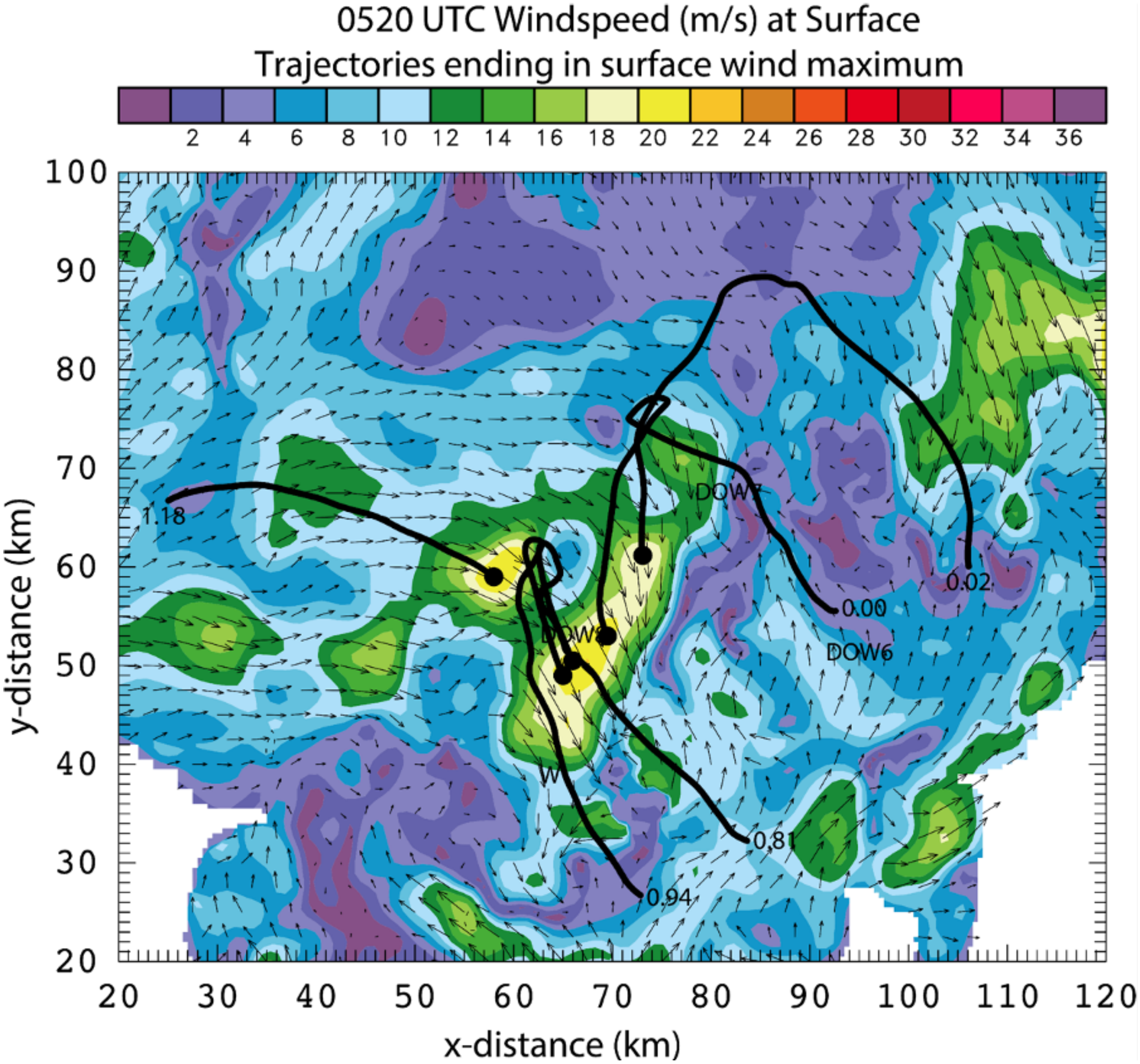

Figure 16. Spaghetti plot of trajectories flowing into the wind maximum at 0520 UTC with their initial trajectory height (in km) listed at the beginning of the trajectory. All trajectories end at 500 m in altitude.

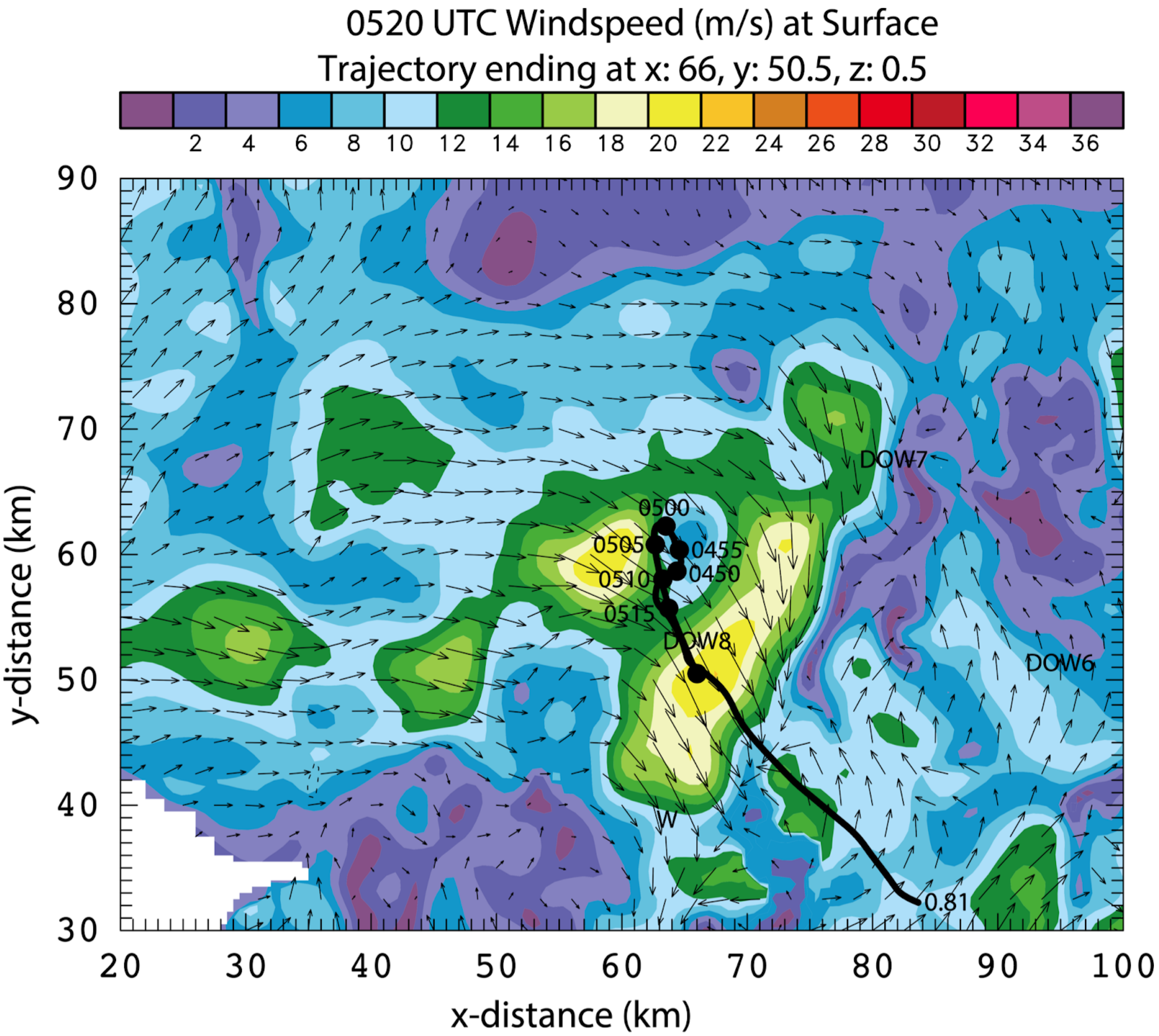

Figure 17. Single trajectory into the leading line wind speed maximum at 0520 UTC. Black dots are labeled with the time to denote the parcel's location along the trajectory.

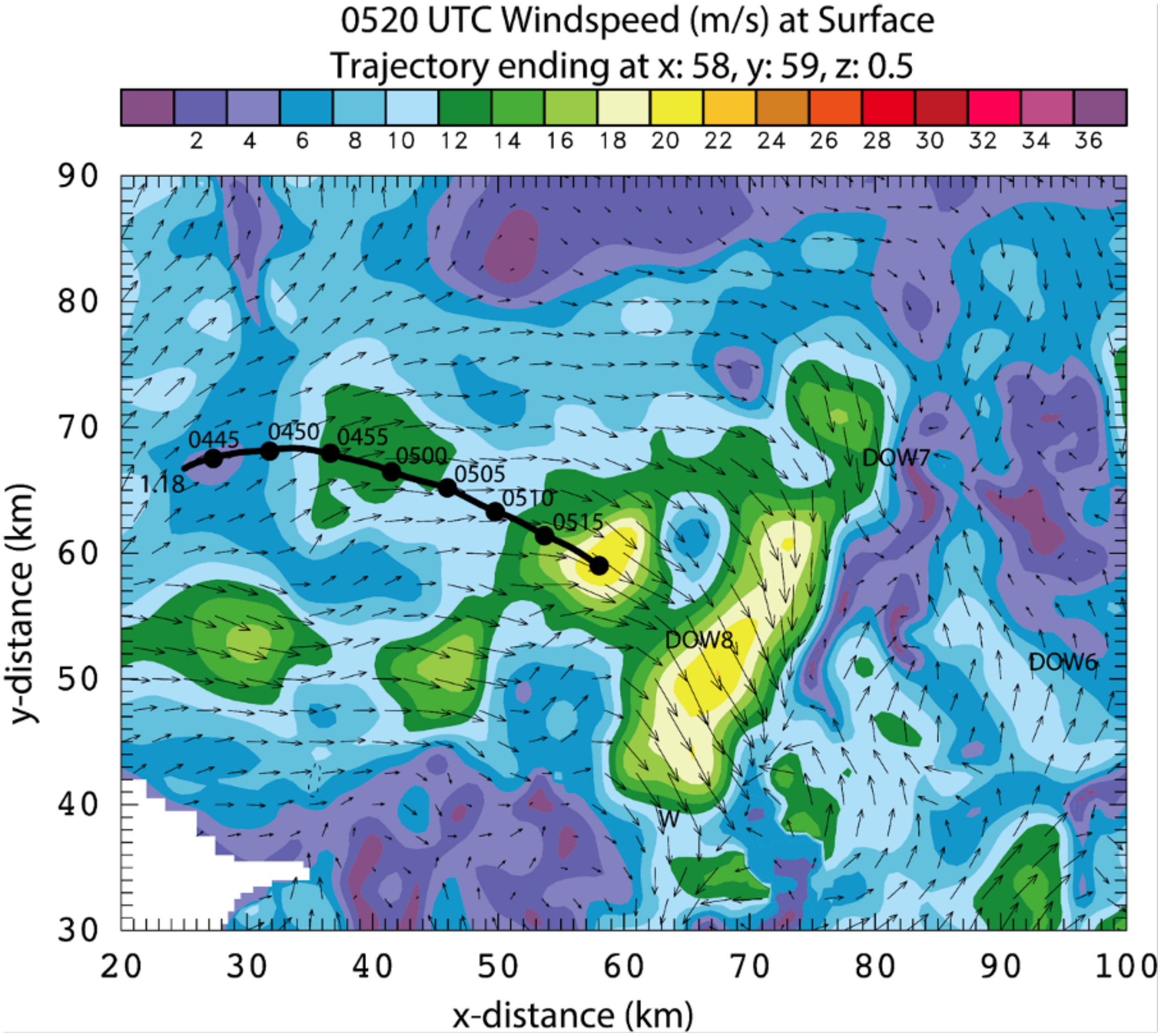

Figure 18. Single trajectory into the more rearward wind speed maximum at 0520 UTC. Black dots are labeled with the time to denote the parcel’s location along the trajectory.

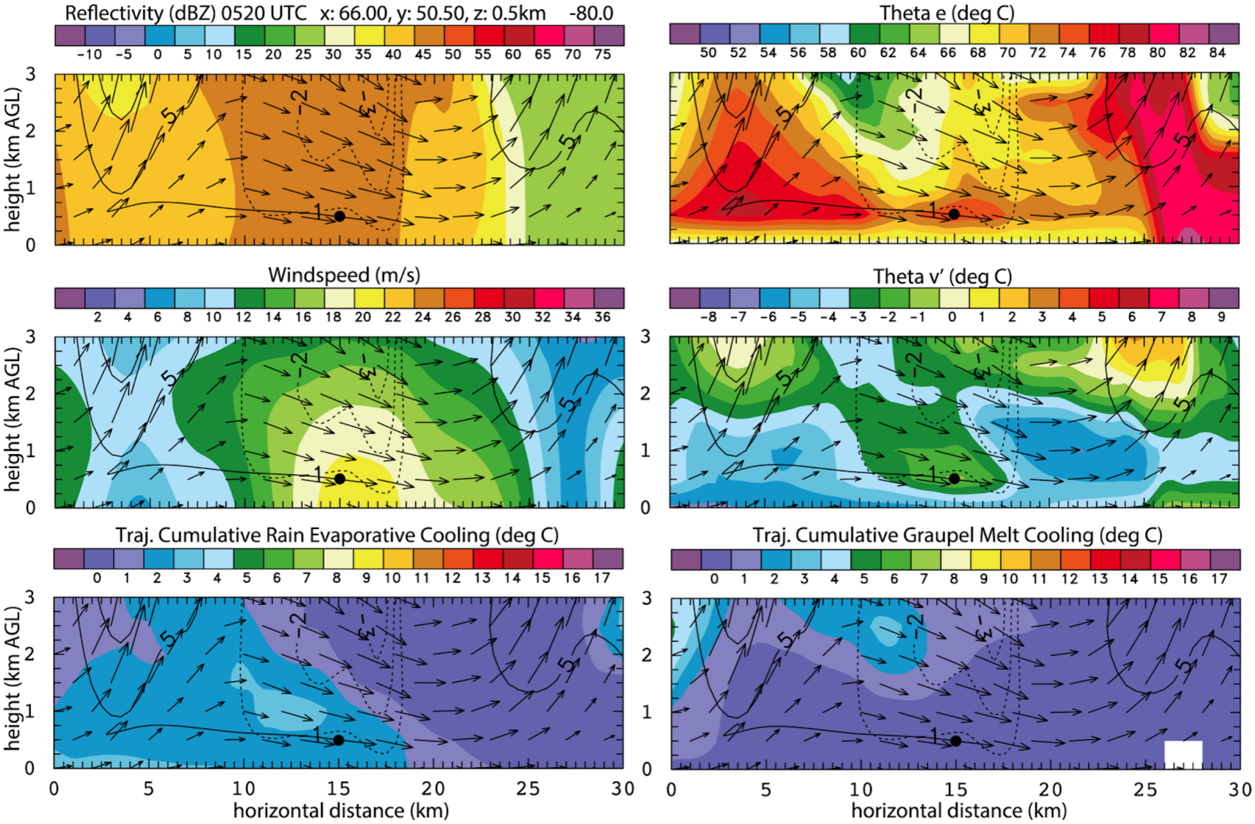

Figure 19. Cross-sections at 0520 UTC of a) reflectivity b) Θ_e c) wind speed d) Θ_v' e) rain evaporative cooling f) graupel/hail melt cooling along the trajectory shown in Fig. 17. Solid (dashed) contours indicate updrafts (downdrafts) every 5 m s^{-1} (-1 m s^{-1}).

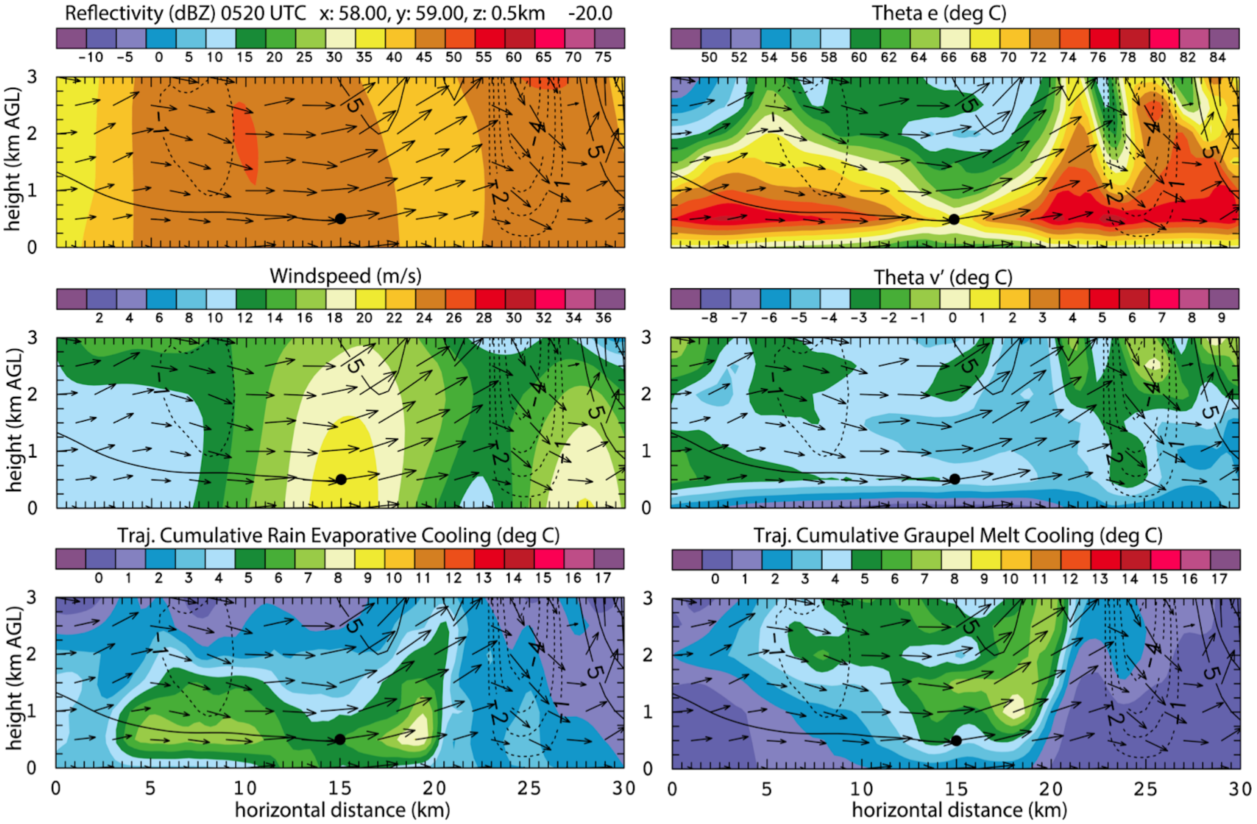

Figure 20. Cross-sections at 0510 UTC of a) reflectivity b) Θ_e c) wind speed d) Θ_v' e) rain evaporative cooling f) graupel/hail melt cooling along the trajectory shown in Fig. 18. Solid (dashed) contours indicate updrafts (downdrafts) every 5 m s^{-1} (-1 m s^{-1}).

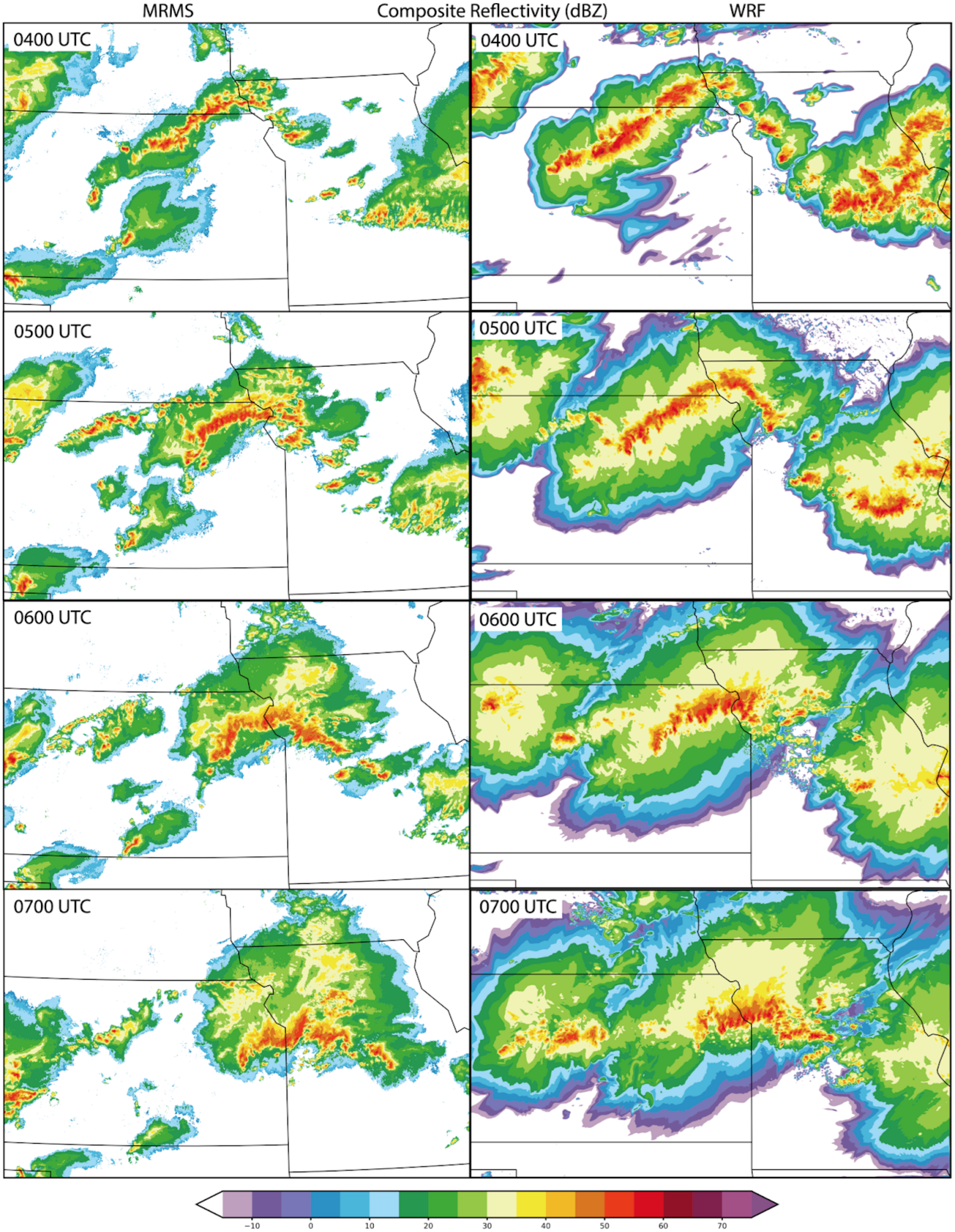

Figure 21. 25-26 June 2015 composite reflectivity from MRMS vs D02 WRF simulation from 0400-0700 UTC.

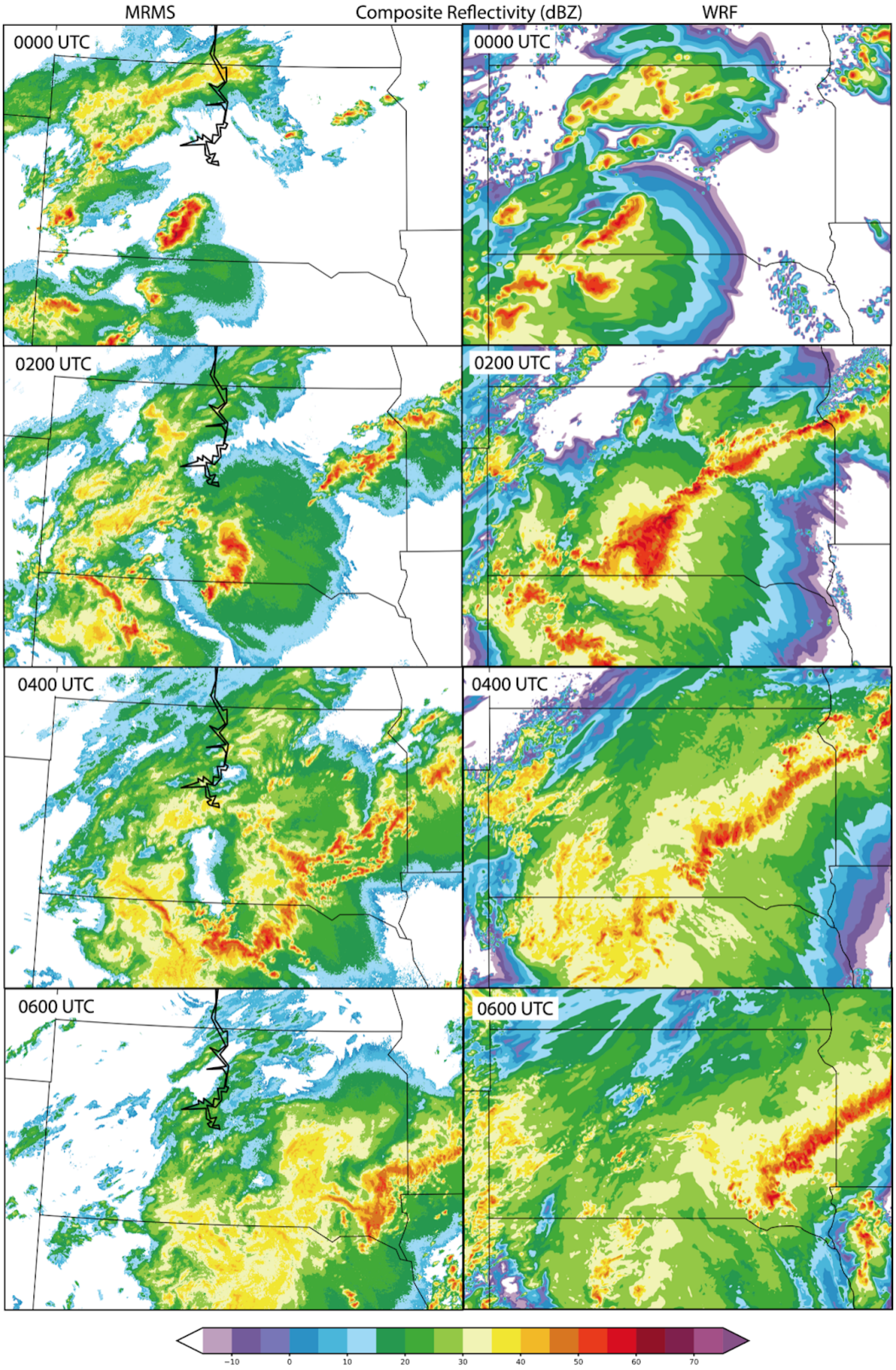
MRMS
Composite Reflectivity (dBZ)
WRF
0000 UTC
0000 UTC
0200 UTC
0200 UTC
0400 UTC
0400 UTC
0600 UTC
0600 UTC
−10
0
10
20
30
40
50
60
70

Figure 22. 5-6 July 2015 composite reflectivity from MRMS vs D02 WRF simulation from 0000-0600 UTC.

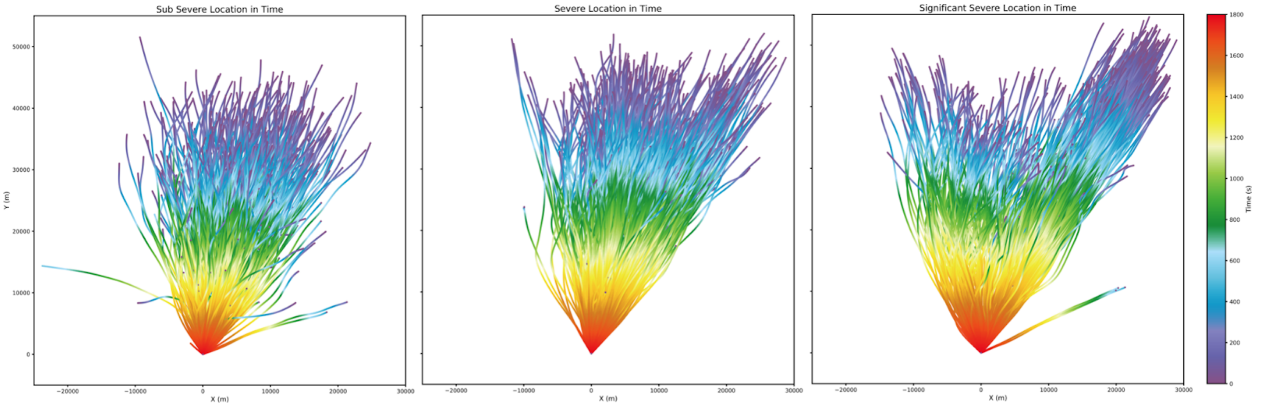

Figure 23. Normalized trajectories over time from a) sub-severe b) severe and c) significant severe categories ending at the origin in the 25-26 June MCS.

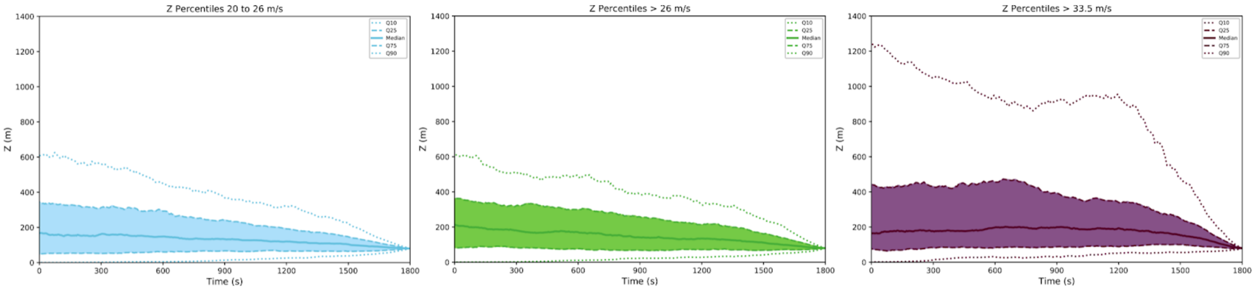

Figure 24. Change in height (z) over time from a) sub-severe b) severe and c) significant severe categories with the 10th, 25th, 50th (median), 75th, and 90th percentiles for the 25-26 June MCS.

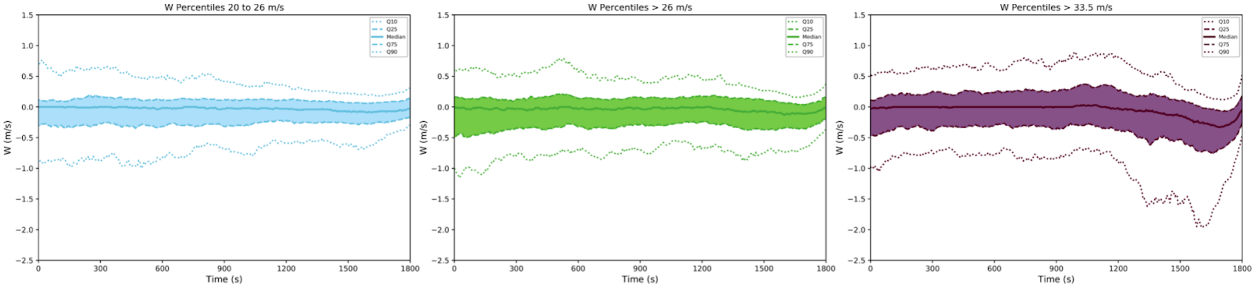

Figure 25. Change in W (m/s) over time from a) sub-severe b) severe and c) significant severe categories with the 10th, 25th, 50th (median), 75th, and 90th percentiles for the 25-26 June MCS.

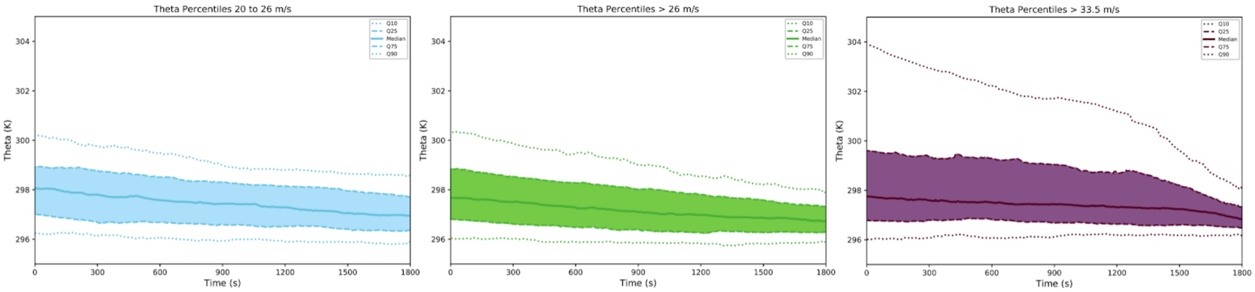

Figure 26. Change in Θ over time from a) sub-severe b) severe and c) significant severe categories with the 10th, 25th, 50th (median), 75th, and 90th percentiles for the 25-26 June MCS.

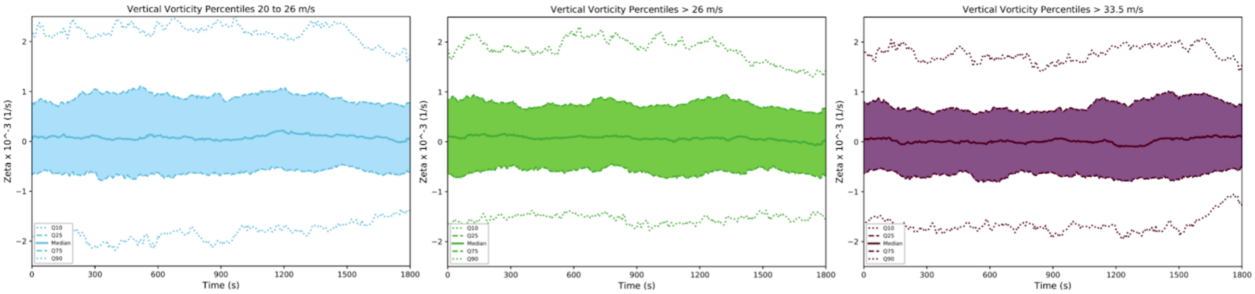

Figure 27. Change in vertical vorticity over time from a) sub-severe b) severe and c) significant severe categories with the 10th, 25th, 50th (median), 75th, and 90th percentiles for the 25-26 June MCS.

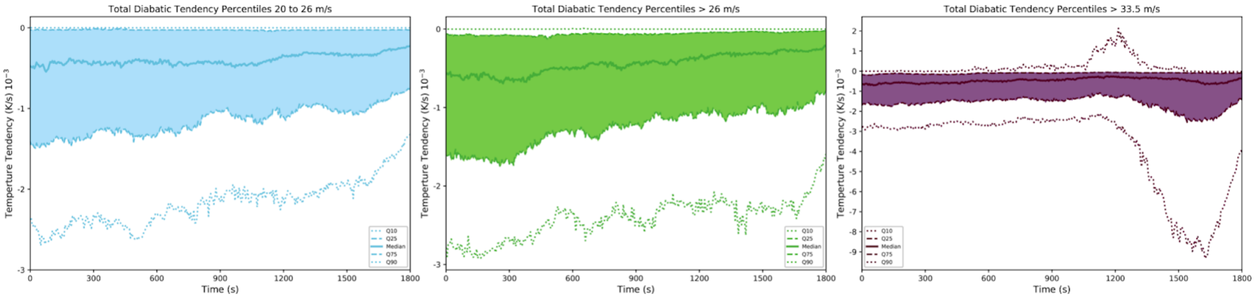

Figure 28. Change in diabatic temperature tendency over time from a) sub-severe b) severe and c) significant severe categories with the 10th, 25th, 50th (median), 75th, and 90th percentiles for the 25-26 June MCS.

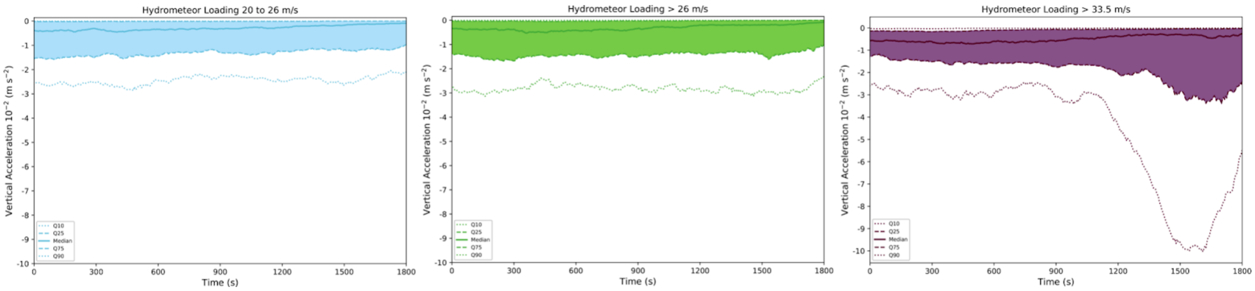

Figure 29. Change in hydrometeor loading drag over time from a) sub-severe b) severe and c) significant severe categories with the 10th, 25th, 50th (median), 75th, and 90th percentiles for the 25-26 June MCS.

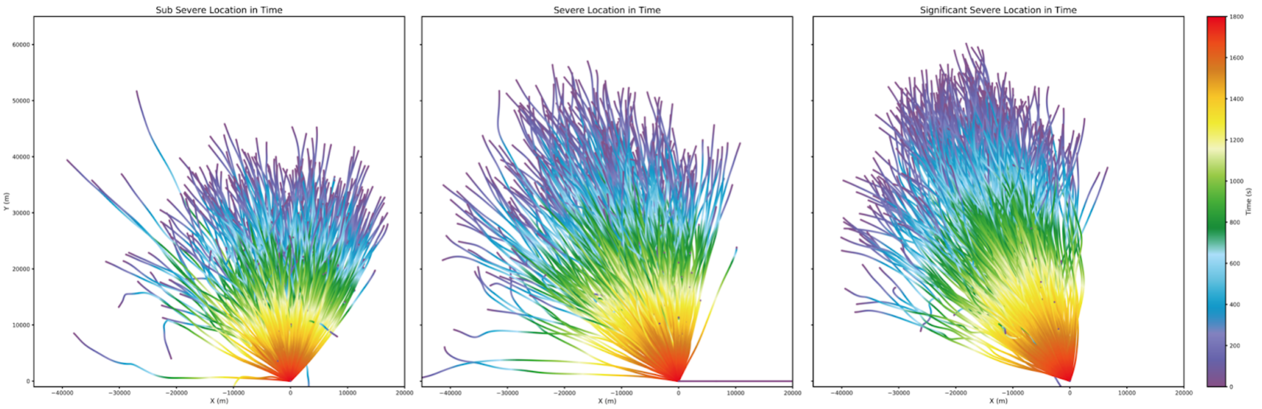

Figure 30. Normalized trajectories over time from a) sub-severe b) severe and c) significant severe categories ending at the origin in the 5-6 July MCS.

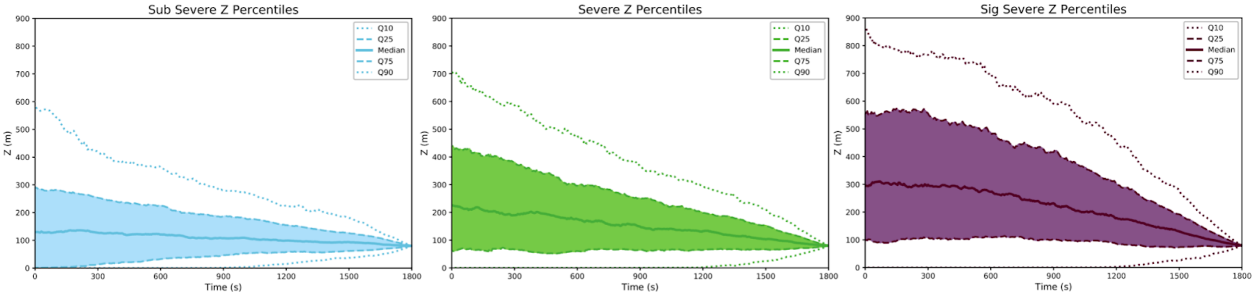

Figure 31. Change in height (z) over time from a) sub-severe b) severe and c) significant severe categories with the 10th, 25th, 50th (median), 75th, and 90th percentiles for the 5-6 July MCS.

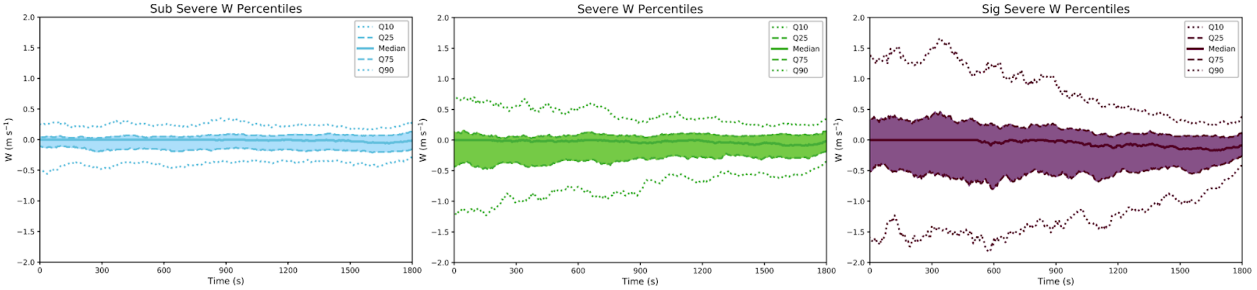

Figure 32. Change in W (m/s) over time from a) sub-severe b) severe and c) significant severe categories with the 10th, 25th, 50th (median), 75th, and 90th percentiles for the 5-6 July MCS.

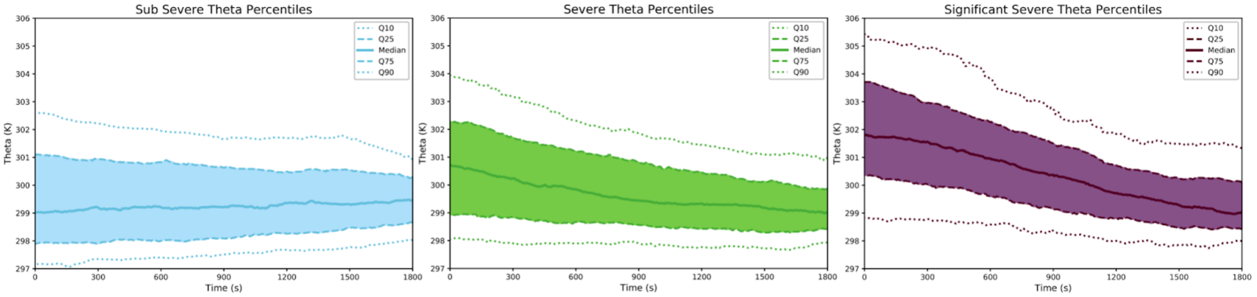

Figure 33. Change in Θ over time from a) sub-severe b) severe and c) significant severe categories with the 10th, 25th, 50th (median), 75th, and 90th percentiles for the 5-6 July MCS.

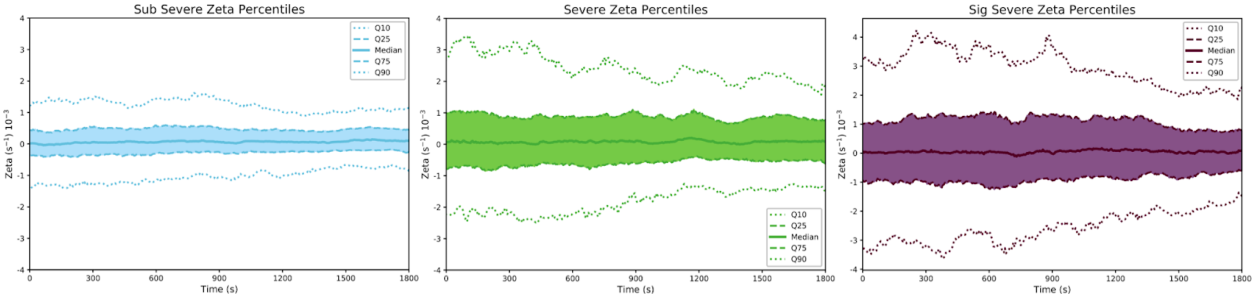

Figure 34. Change in vertical vorticity over time from a) sub-severe b) severe and c) significant severe categories with the 10th, 25th, 50th (median), 75th, and 90th percentiles for the 5-6 July MCS.

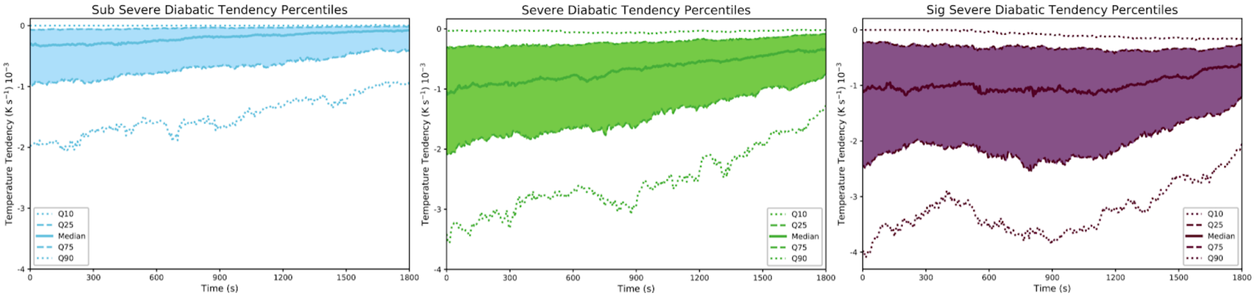

Figure 35. Change in diabatic temperature tendency over time from a) sub-severe b) severe and c) significant severe categories with the 10th, 25th, 50th (median), 75th, and 90th percentiles for the 5-6 July MCS.

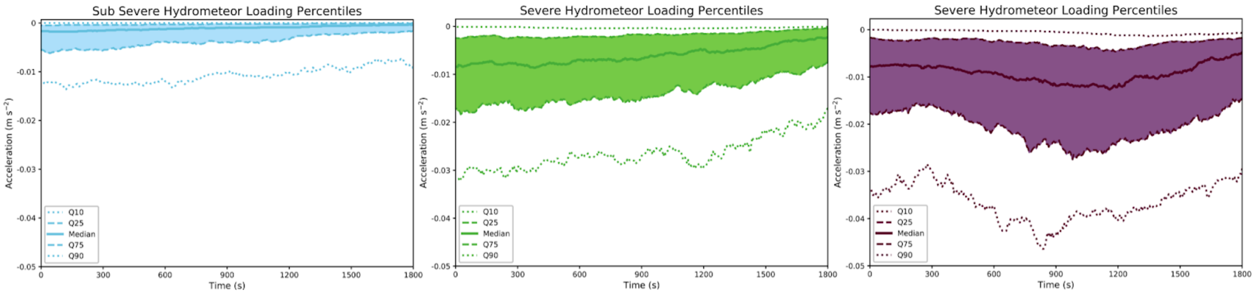

Figure 36. Change in hydrometeor loading drag over time from a) sub-severe b) severe and c) significant severe categories with the 10th, 25th, 50th (median), 75th, and 90th percentiles for the 5-6 July MCS.

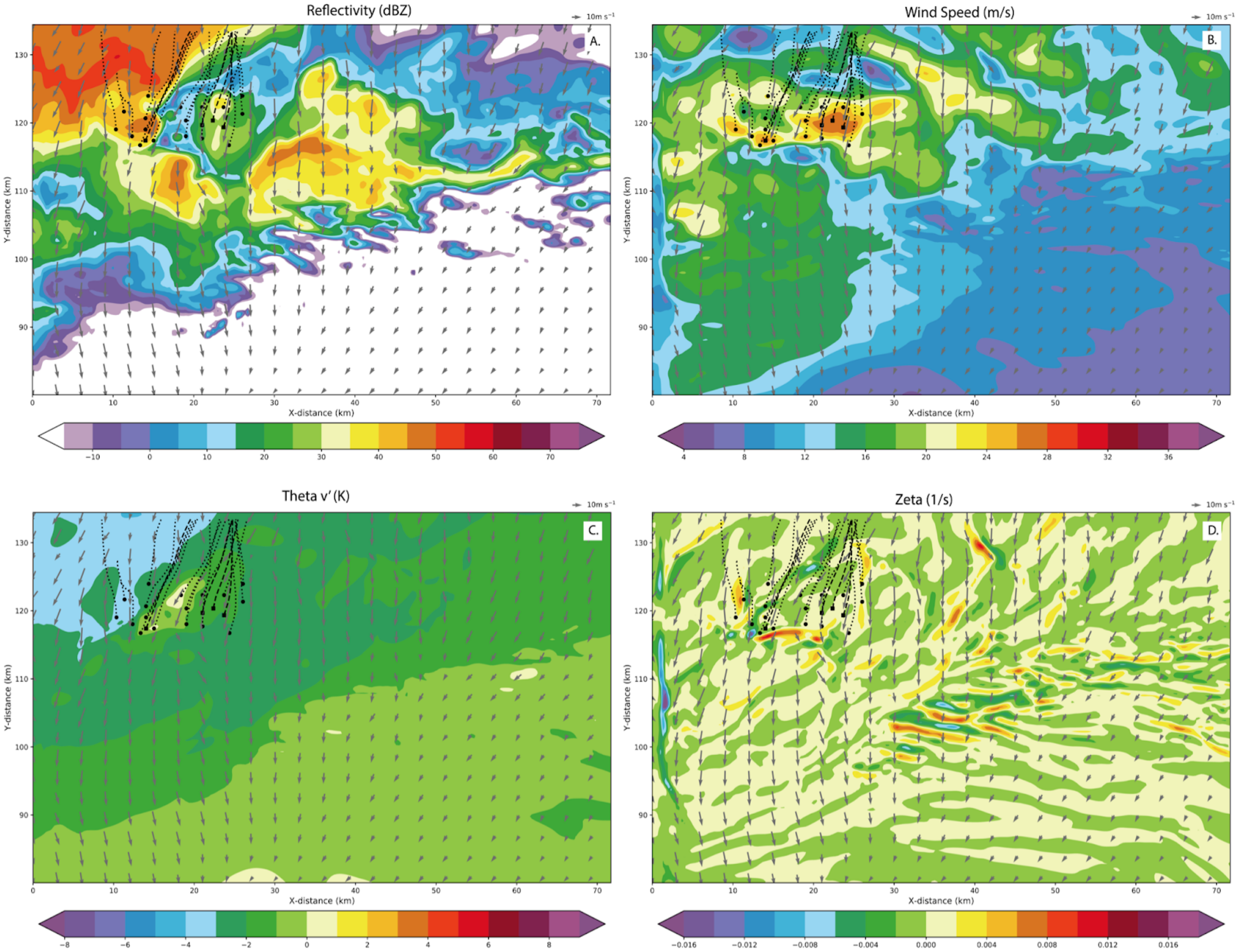

Figure 37. Horizontal plots of the 25-26 June MCS at 80 m at 0500 UTC of a) reflectivity, b) wind speed, c) Θ_v', and d) vertical vorticity with wind vectors. Severe (sub-severe) trajectories are indicated by dashed (dotted) lines and end in square (circle) points.

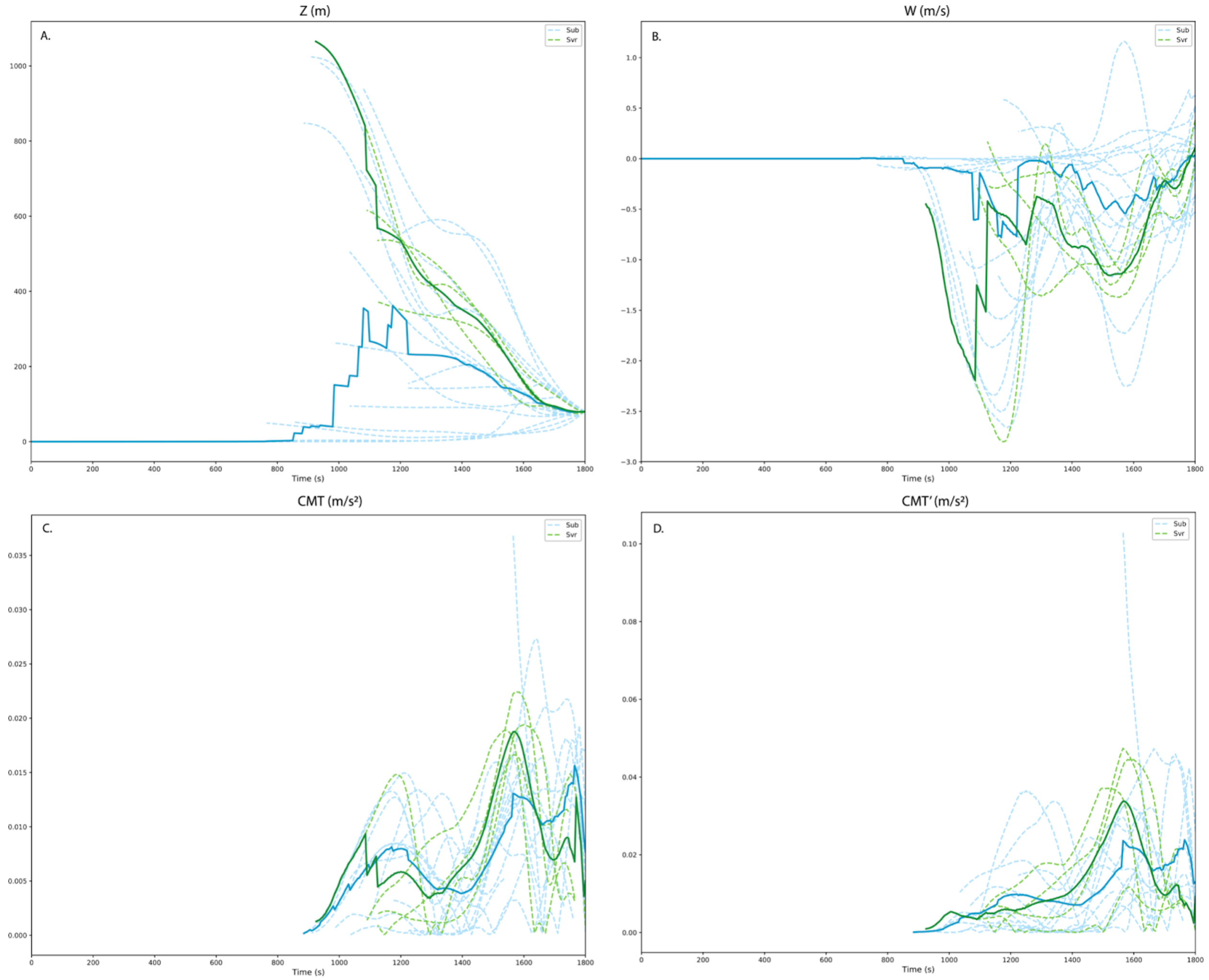

Figure 38. Change in a) height, b) vertical velocity, c) CMT$_0$, and d) CMT$'$ for the 17 sub-severe and 4 severe trajectories at 0500 UTC for the 25-26 June MCS. Dashed lines are individual trajectories and the solid line is the median.

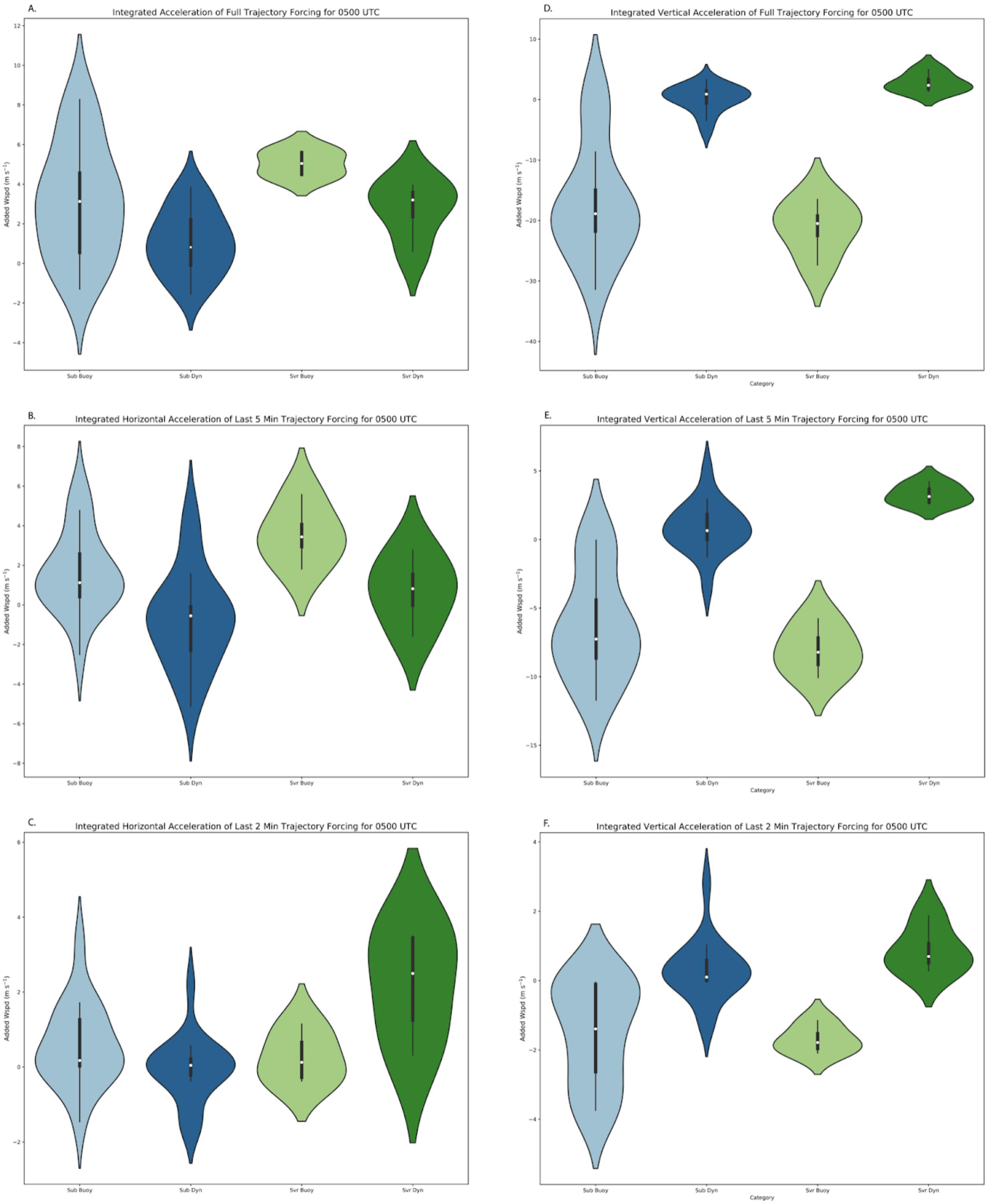

Figure 39. The 0500 UTC integrated acceleration gives total added wind speed from the buoyancy and dynamic forcing for a) the entire trajectory in the horizontal, b) the last 5 minutes of the trajectory in the horizontal, c) the last 2 minutes of the trajectory in the horizontal, d) the entire trajectory in the vertical, e) the last 5 minutes of the trajectory in the vertical, and f) the

last 2 minutes of the trajectory in the vertical. Sub-severe distributions are in blue and severe distributions are in green.

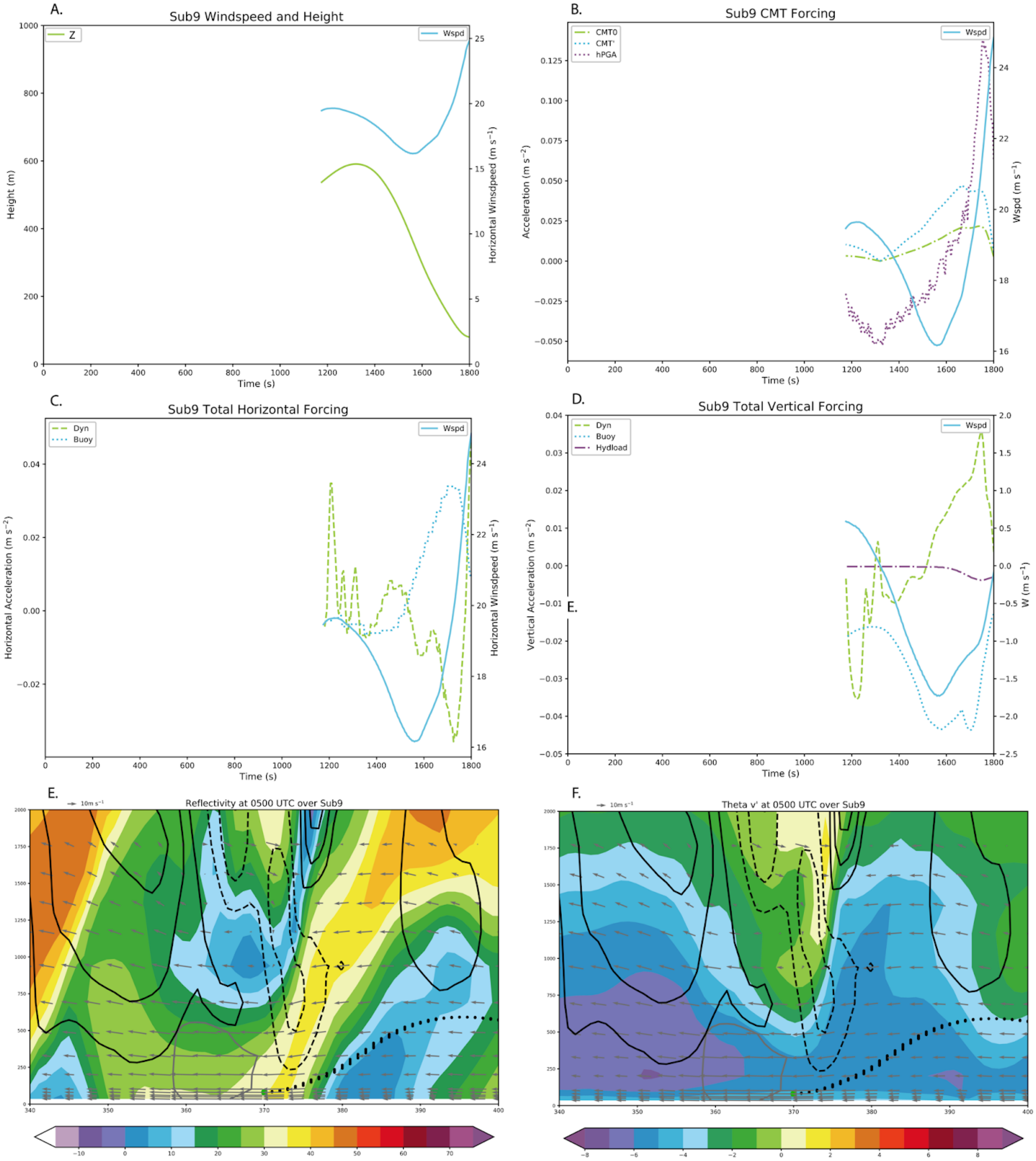

Figure 40. The sub9 trajectory at 0500 UTC a) height and wind speed, b) CMT and hPGA forcing with wind speed, c) horizontal dynamic and buoyancy forcing with wind speed, d) vertical dynamic and buoyancy forcing with w, e) reflectivity cross-section over sub9, and f) Θ_v' cross-section over sub9. Reflectivity and Θ_v' have solid (dashed) contours for updrafts

(downdrafts) every 2 m s^{-1} (-2 m s^{-1}). Solid gray contours are for severe winds and significant severe winds.

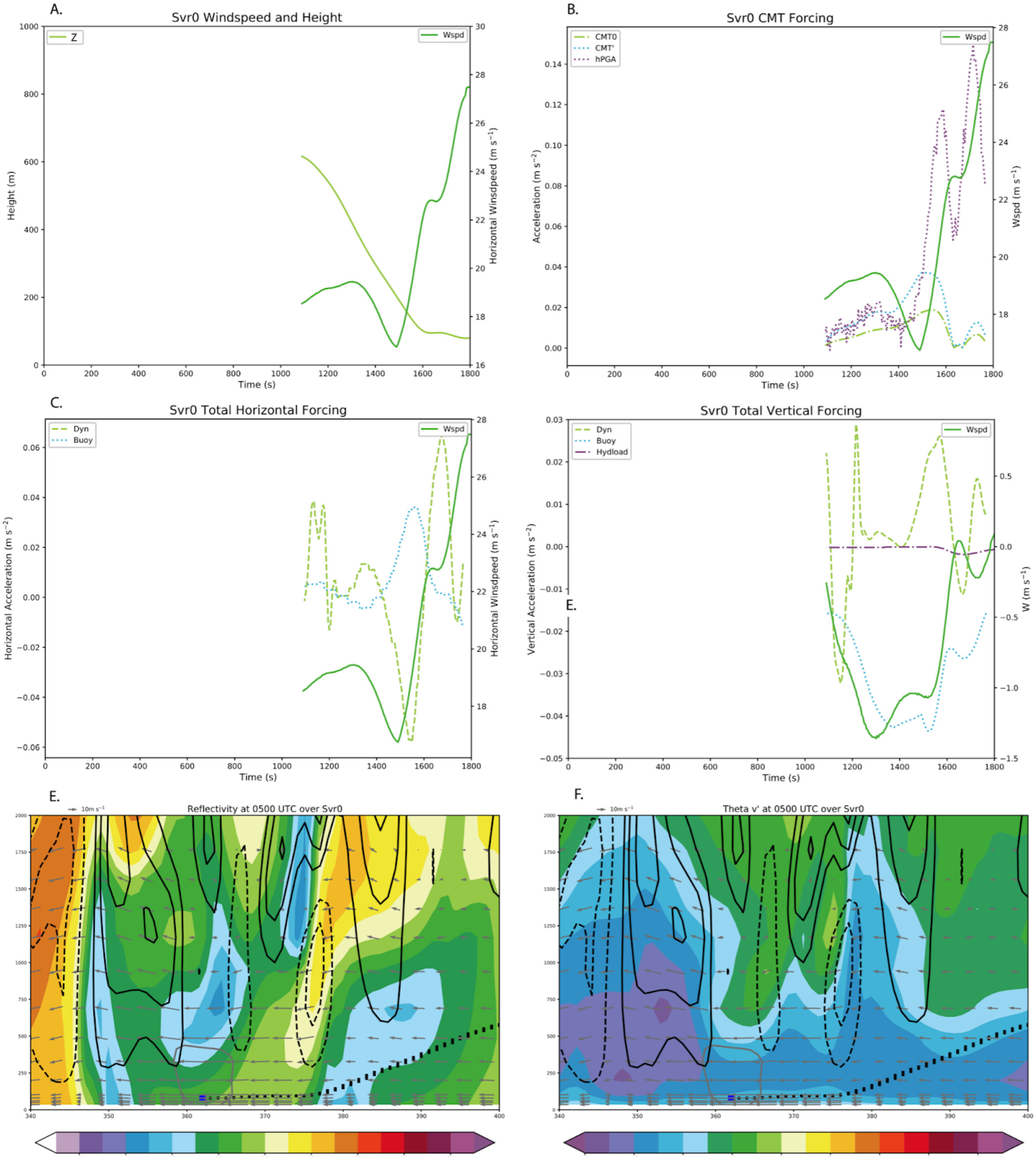

Figure 41. The svr0 trajectory at 0500 UTC a) height and wind speed, b) CMT and hPGA forcing with wind speed, c) horizontal dynamic and buoyancy forcing with wind speed, d) vertical dynamic and buoyancy forcing with w, e) reflectivity cross-section over svr0, and f) Θ_v' cross-section over svr0. Reflectivity and Θ_v' have solid (dashed) contours for updrafts

(downdrafts) every 2 m $\mathrm{s^{-1}}$ (-2 m $\mathrm{s^{-1}}$). Solid gray contours are for severe winds and significant severe winds.

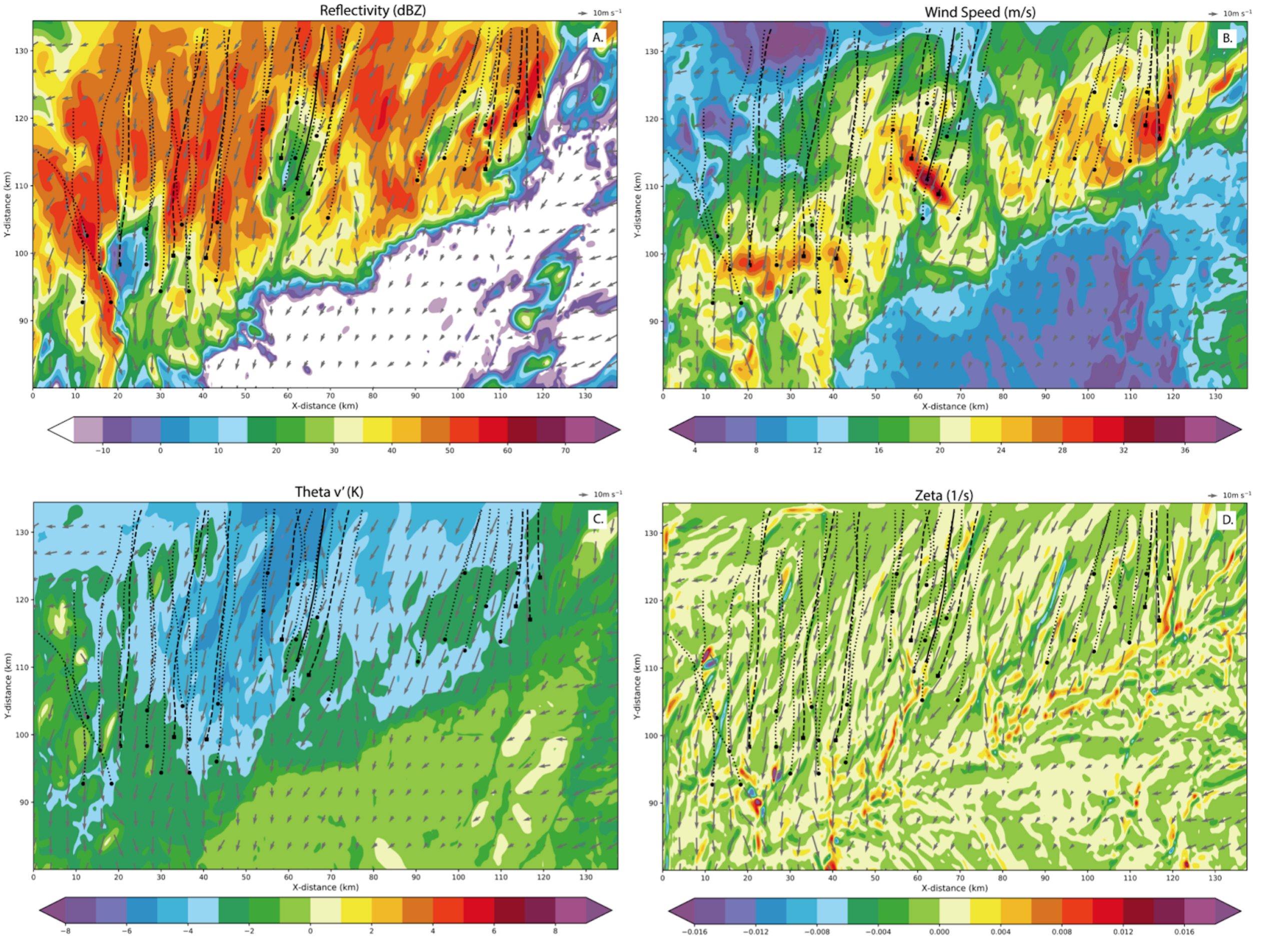

Figure 42. Horizontal plots of the 25-26 June MCS at 80 m at 0530 UTC of a) reflectivity, b) wind speed, c) Θ_v', and d) vertical vorticity with wind vectors. Severe (sub-severe) [significant severe] trajectories are indicated by dashed (dotted) [solid] lines and end in square (circle) [triangle] points.

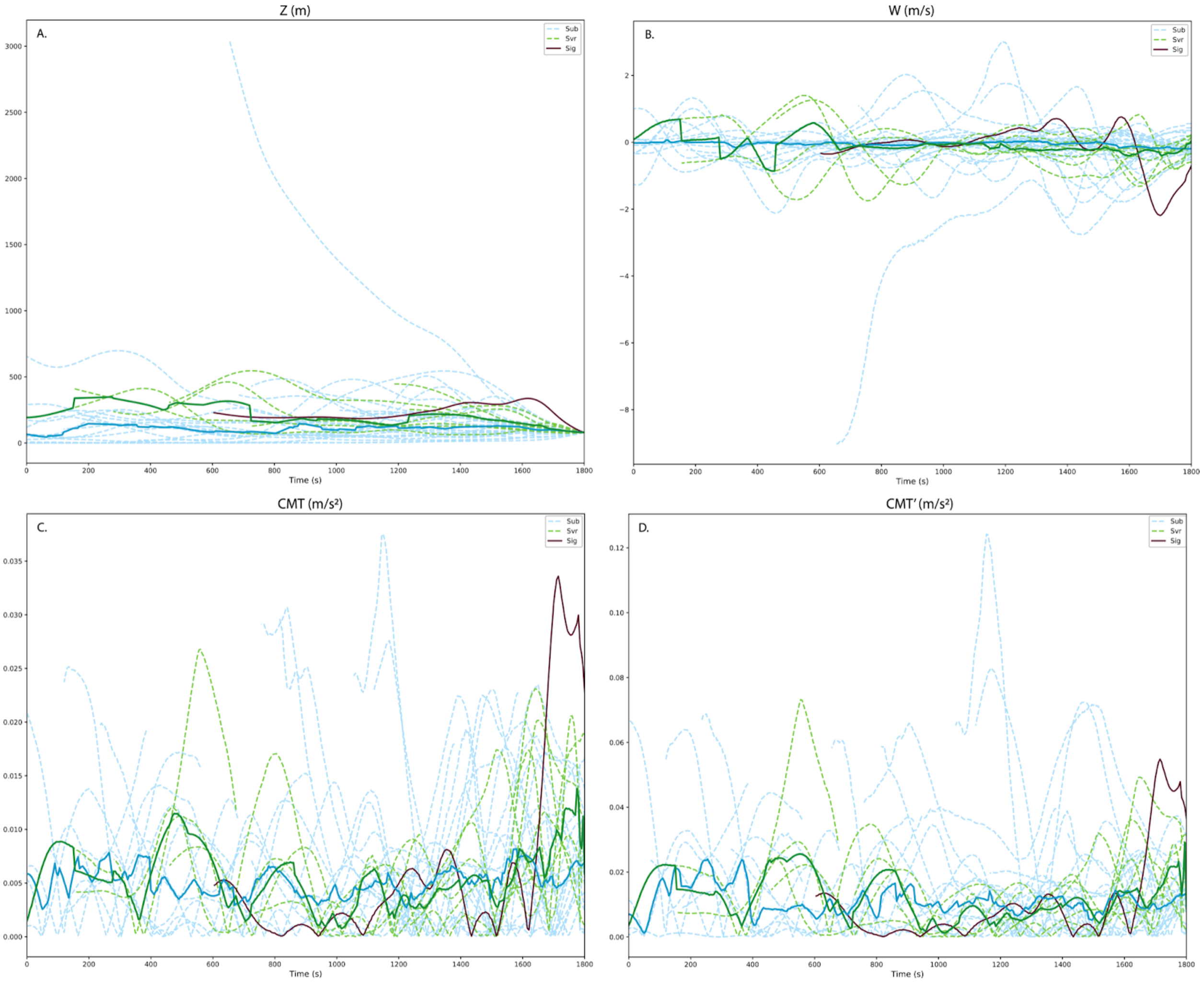

Figure 43. Change in a) height, b) vertical velocity, c) CMT′, and d) CMT$_0$ for the 30 sub-severe, 9 severe, and 1 significant severe trajectories at 0530 UTC for the 25-26 June MCS. Dashed lines are individual trajectories and the solid line is the median.

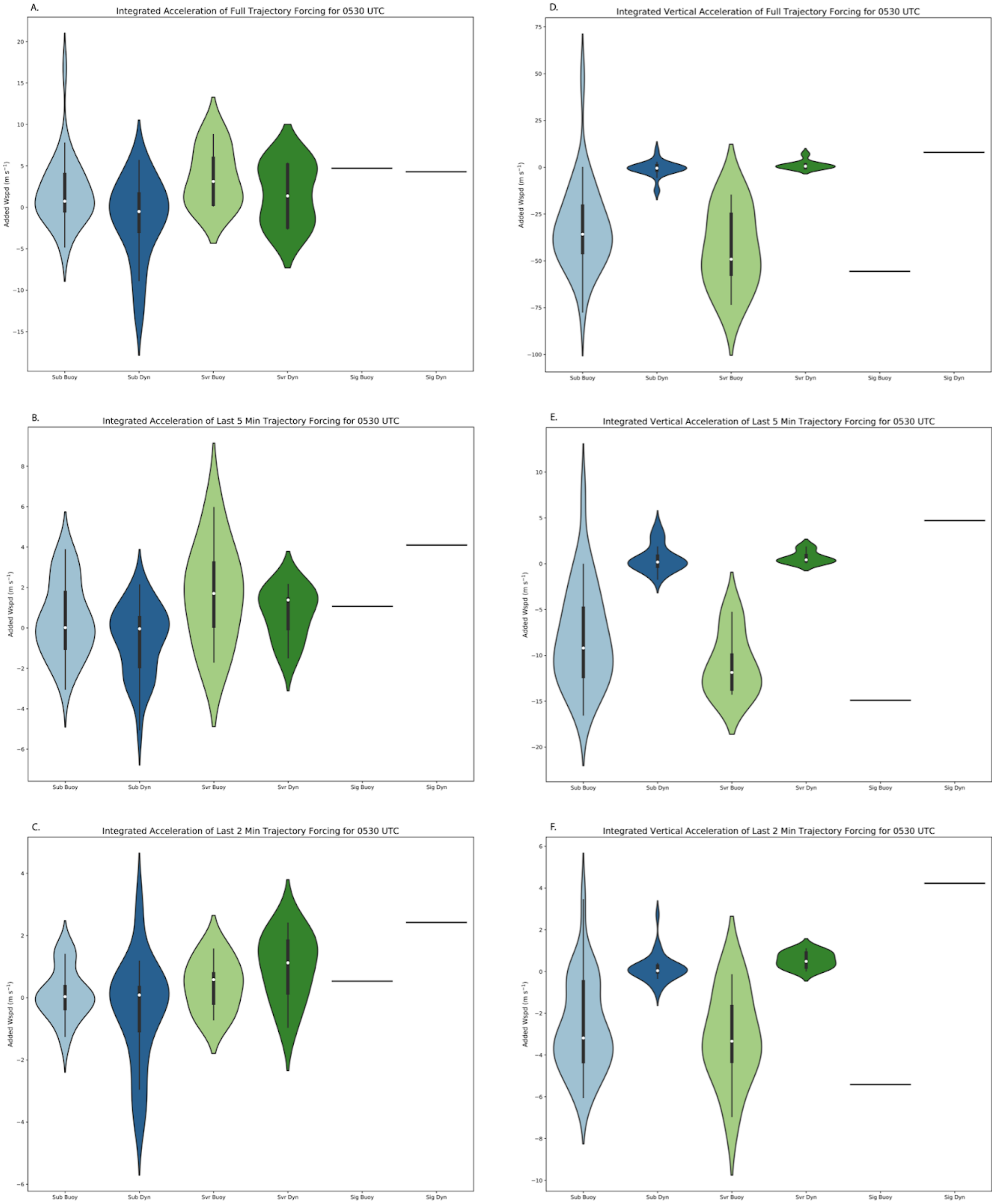

Figure 44. The 0530 UTC integrated acceleration givestotal added wind speed from the buoyancy and dynamic forcing for a) the entire trajectory in the horizontal, b) the last 5 minutes of the trajectory in the horizontal, c) the last 2 minutes of the trajectory in the horizontal, d) the entire trajectory in the vertical, e) the last 5 minutes of the trajectory in the vertical, and f) the

last 2 minutes of the trajectory in the vertical. Sub-severe distributions are in blue and severe distributions are in green. The median of the significant trajectory is a line.

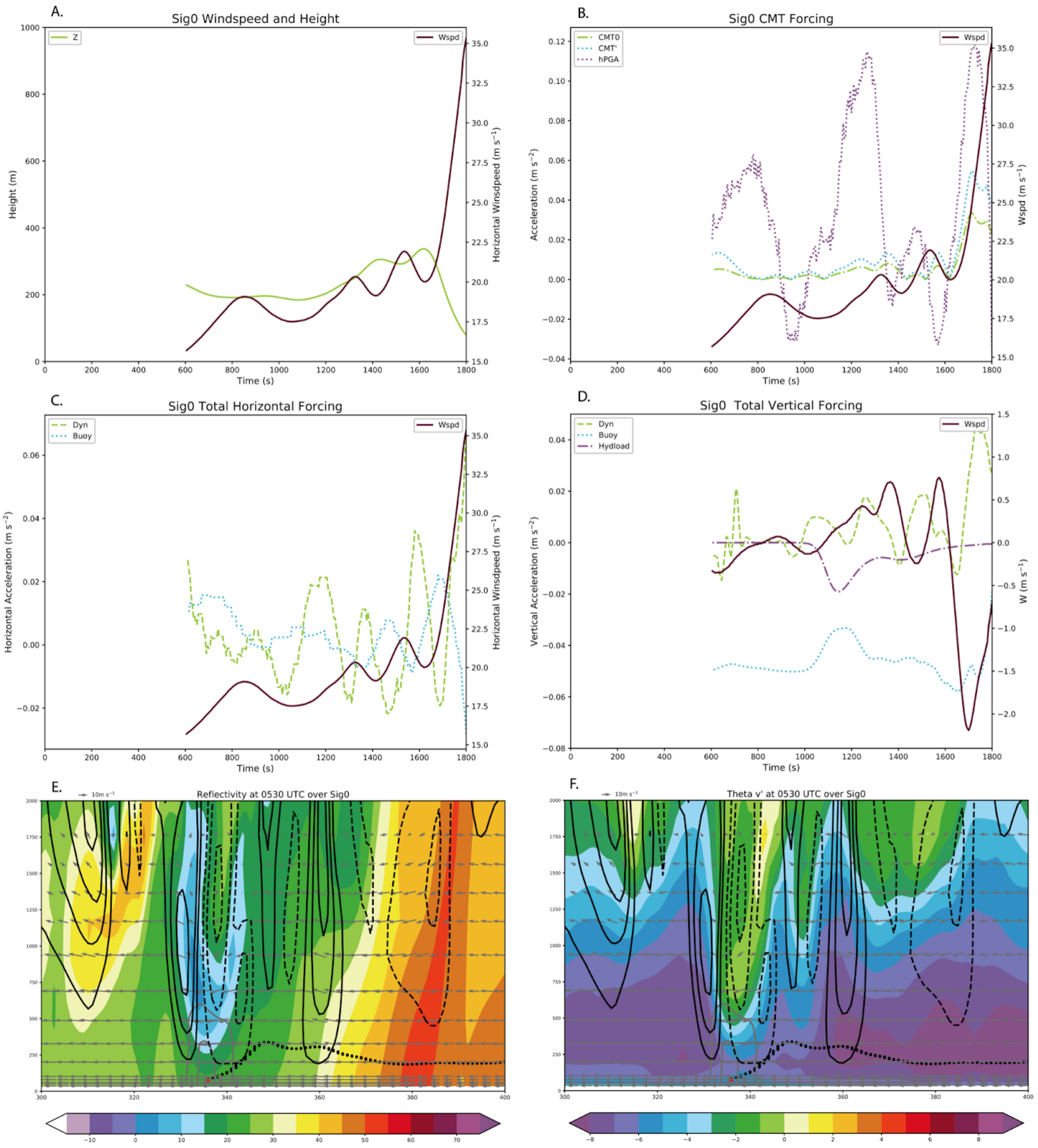

Figure 45. The sig0 trajectory at 0530 UTC a) height and wind speed, b) CMT and hPGA forcing with wind speed, c) horizontal dynamic and buoyancy forcing with wind speed, d) vertical dynamic and buoyancy forcing with w, e) reflectivity cross-section over sig0, and f) Θ_v' cross-section over sig0. Reflectivity and Θ_v' have solid (dashed) contours for updrafts (downdrafts) every 2 $m\ s^{-1}$ ($-2\ m\ s^{-1}$). Solid gray contours are for severe winds and significant severe winds.

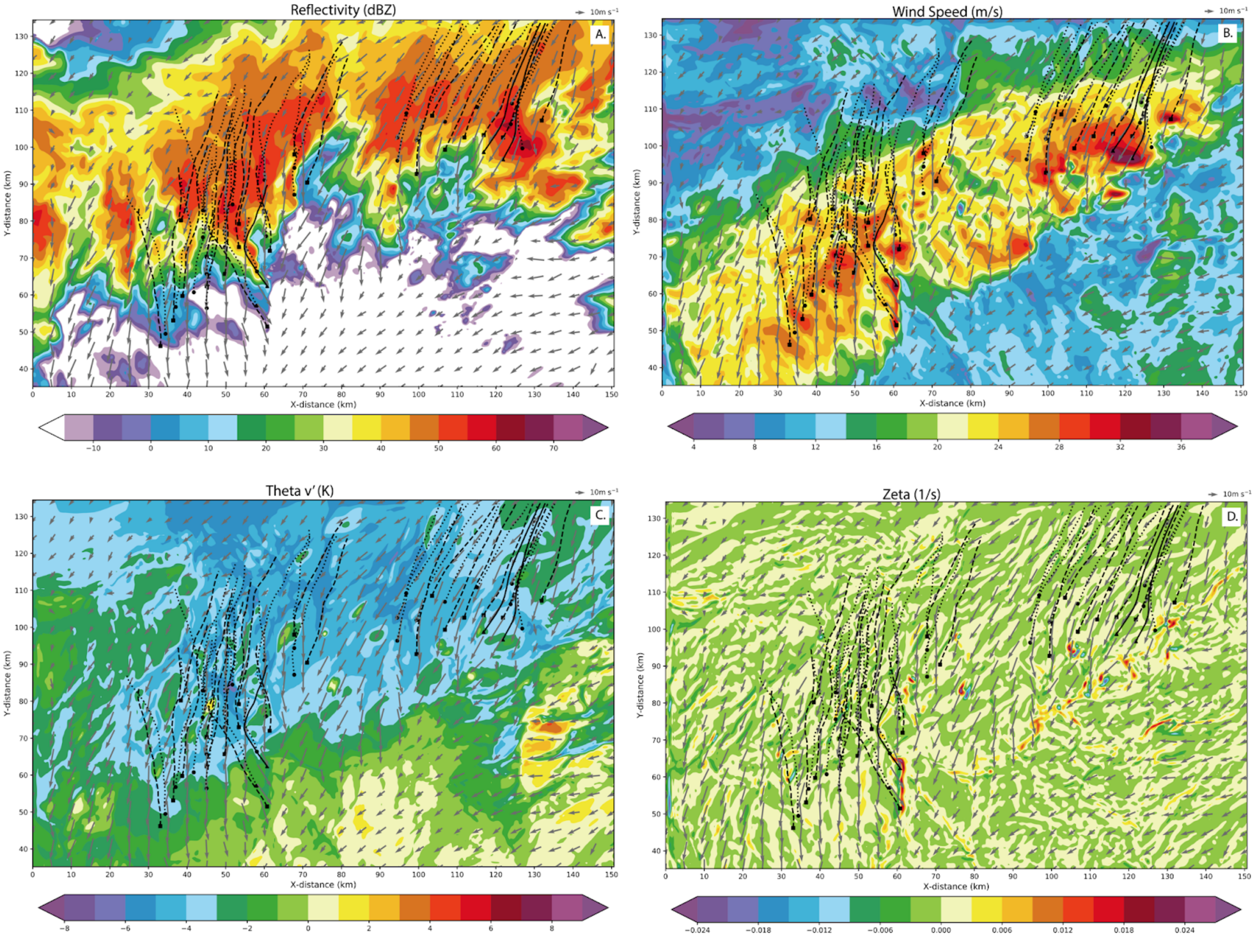

Figure 46. Horizontal plots of the 25-26 June MCS at 80 m at 0600 UTC of a) reflectivity, b) wind speed, c) Θ_v', and d) vertical vorticity with wind vectors. Severe (sub-severe) [significant severe] trajectories are indicated by dashed (dotted) [solid] lines and end in square (circle) [triangle] points.

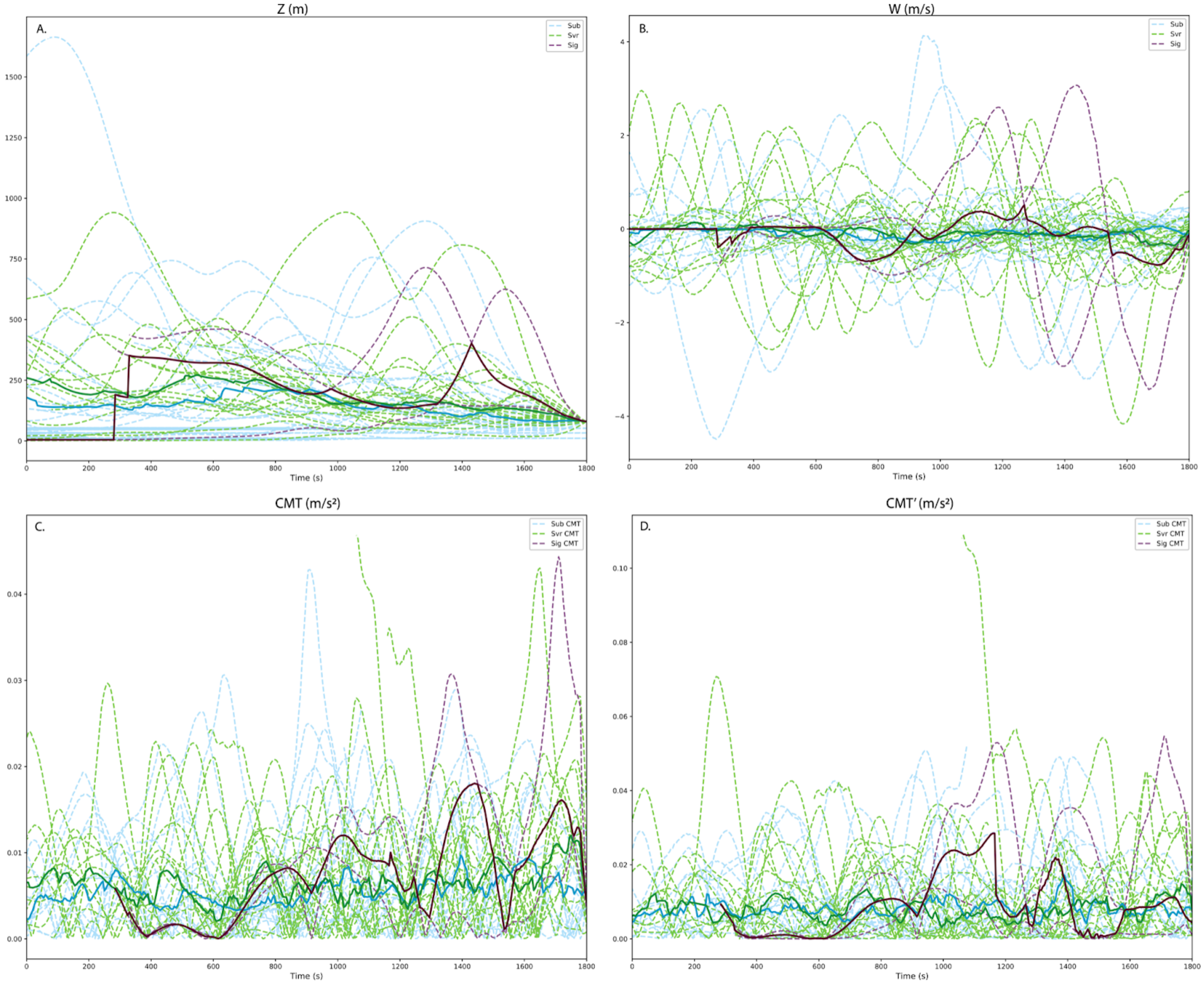

Figure 47. Change in a) height, b) vertical velocity, c) CMT′, and d) CMT_0 for the 24 sub-severe, 20 severe, and 3 significant severe trajectories at 0600 UTC for the 25-26 June MCS. Dashed lines are individual trajectories and the solid line is the median.

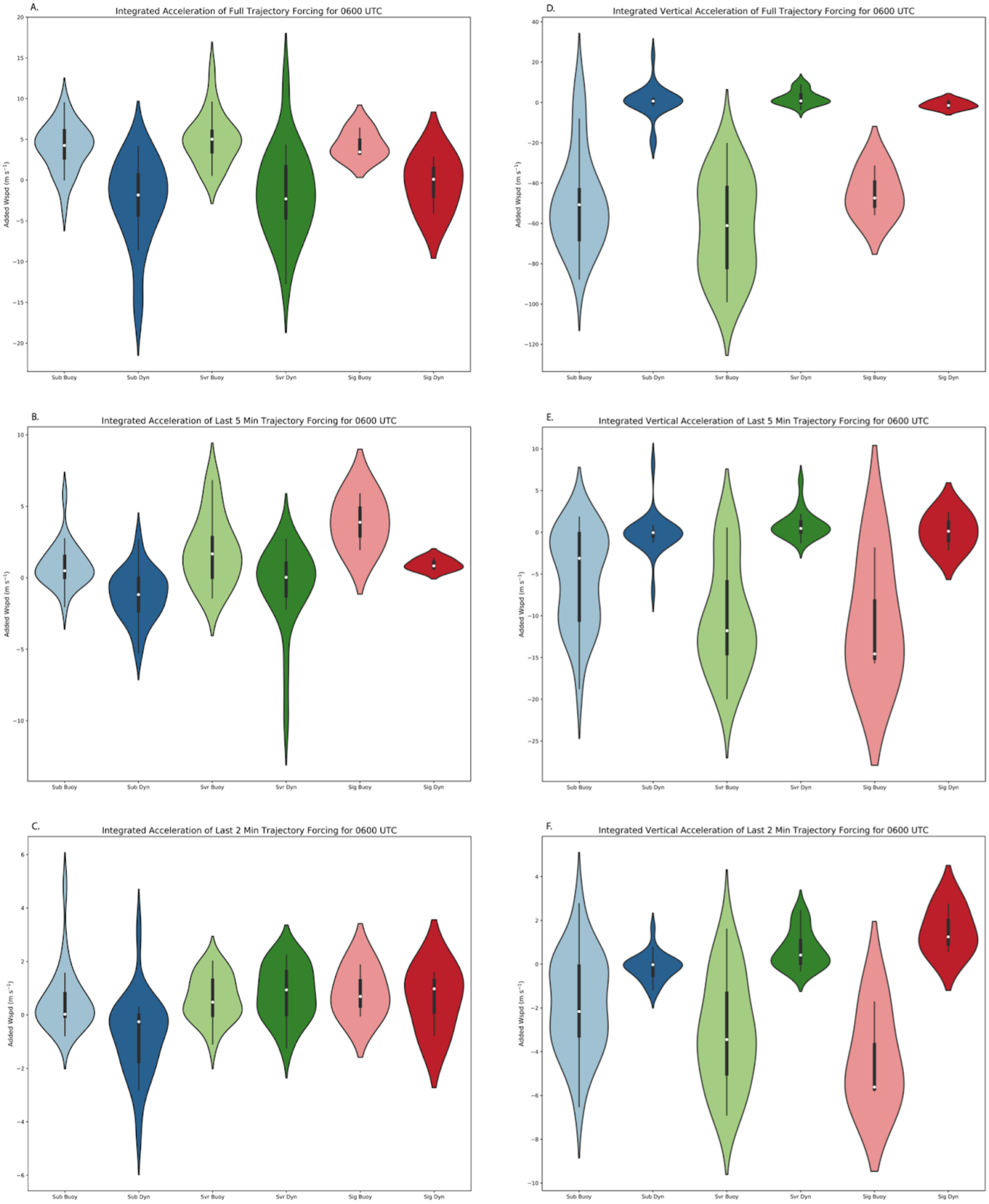

Figure 48. The 0600 UTC integrated acceleration givestotal added wind speed from the buoyancy and dynamic forcing for a) the entire trajectory in the horizontal, b) the last 5 minutes of the trajectory in the horizontal, c) the last 2 minutes of the trajectory in the horizontal, d) the entire trajectory in the vertical, e) the last 5 minutes of the trajectory in the vertical, and f) the

last 2 minutes of the trajectory in the vertical. Sub-severe distributions are in blue, severe in green, and significant severe in red.

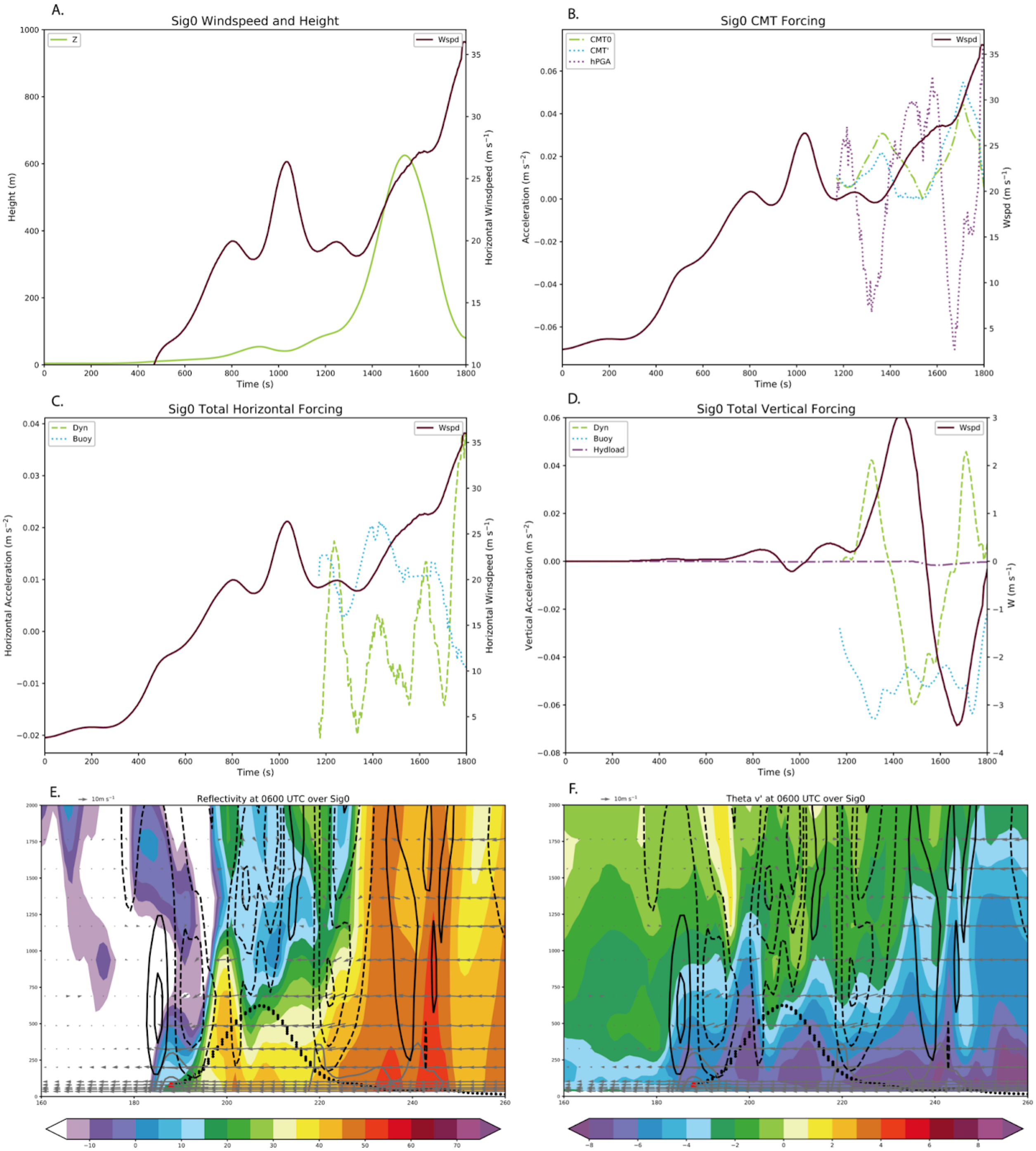

Figure 49. The sig0 trajectory at 0600 UTC a) height and wind speed, b) CMT and hPGA forcing with wind speed, c) horizontal dynamic and buoyancy forcing with wind speed, d) vertical dynamic and buoyancy forcing with w, e) reflectivity cross-section over sig0, and f) Θ_v' cross-section over sig0. Reflectivity and Θ_v' have solid (dashed) contours for updrafts (downdrafts) every 2 m s^{-1} (-2 m s^{-1}). Solid gray contours are for severe winds and significant severe winds.

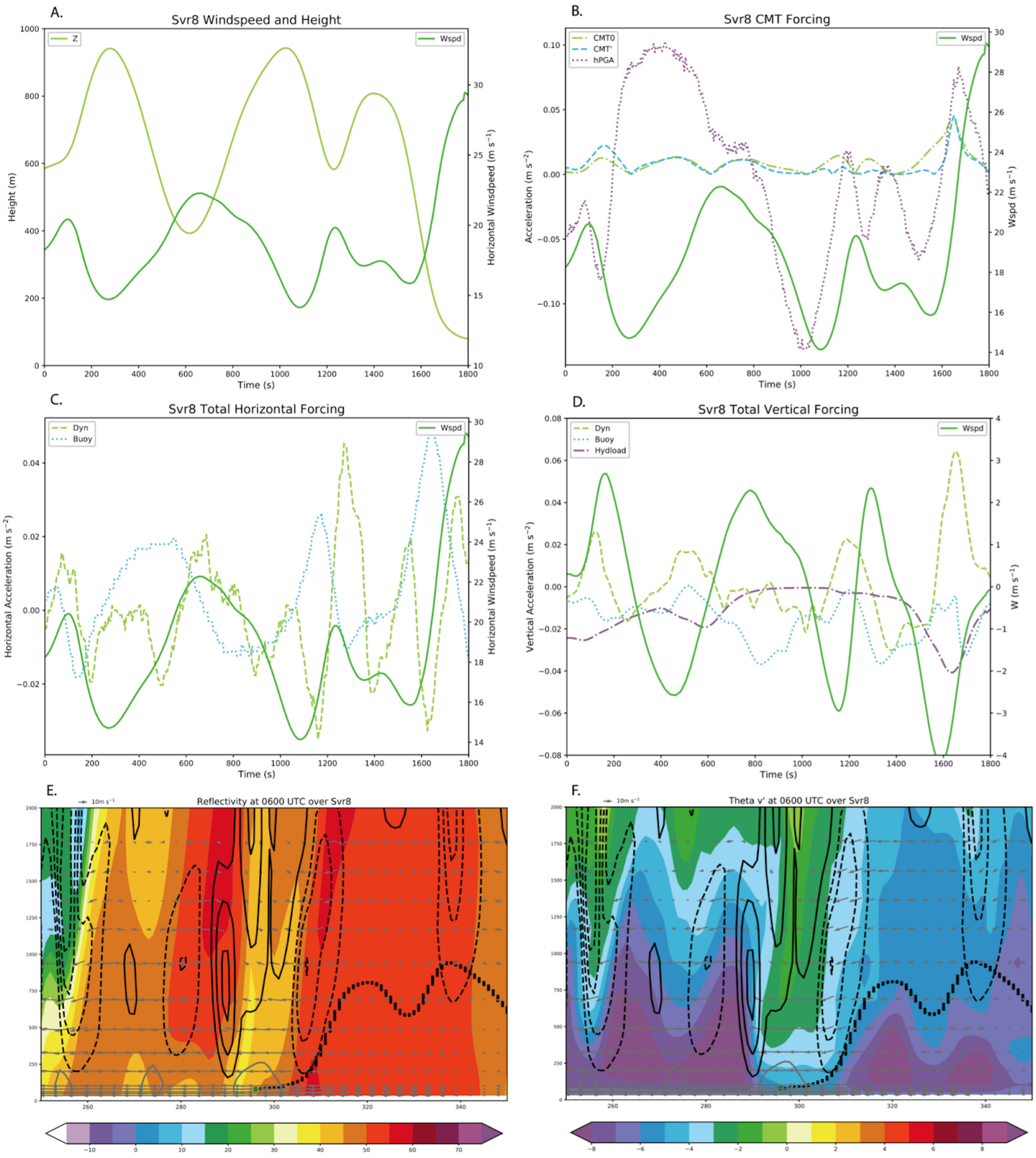

Figure 50. The svr8 trajectory at 0600 UTC a) height and wind speed, b) CMT and hPGA forcing with wind speed, c) horizontal dynamic and buoyancy forcing with wind speed, d) vertical dynamic and buoyancy forcing with w, e) reflectivity cross-section over svr8, and f) Θ_v' cross-section over svr8. Reflectivity and Θ_v' have solid (dashed) contours for updrafts (downdrafts) every 2 m s^{-1} (-2 m s^{-1}). Solid gray contours are for severe winds and significant severe winds.

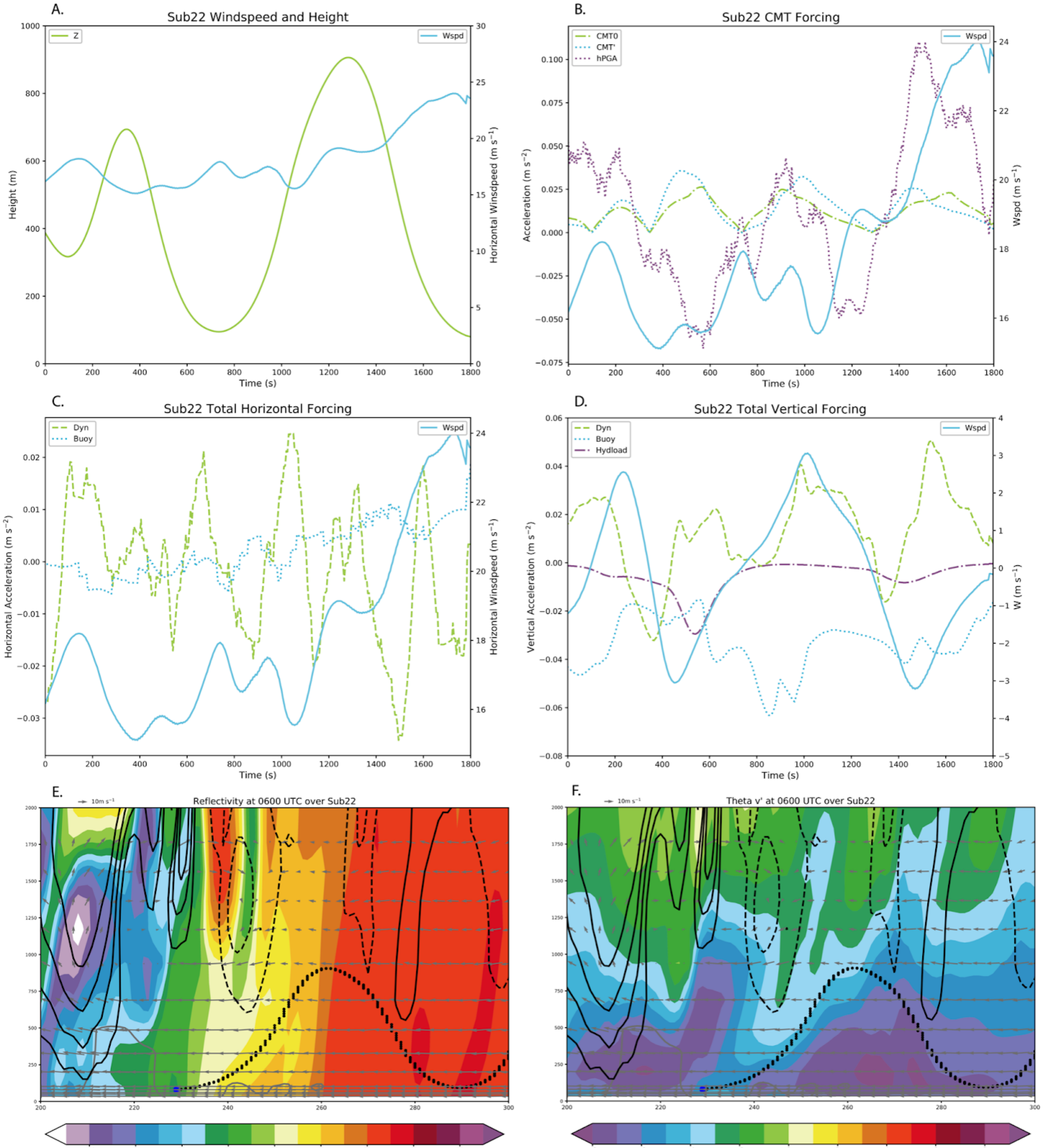

Figure 51. The sub22 trajectory at 0600 UTC a) height and wind speed, b) CMT and hPGA forcing with wind speed, c) horizontal dynamic and buoyancy forcing with wind speed, d) vertical dynamic and buoyancy forcing with w, e) reflectivity cross-section over sub22, and f) Θ_v' cross-section over sub22. Reflectivity and Θ_v' have solid (dashed) contours for updrafts (downdrafts) every 2 $m\ s^{-1}$ (-2 $m\ s^{-1}$). Solid gray contours are for severe winds and significant severe winds.

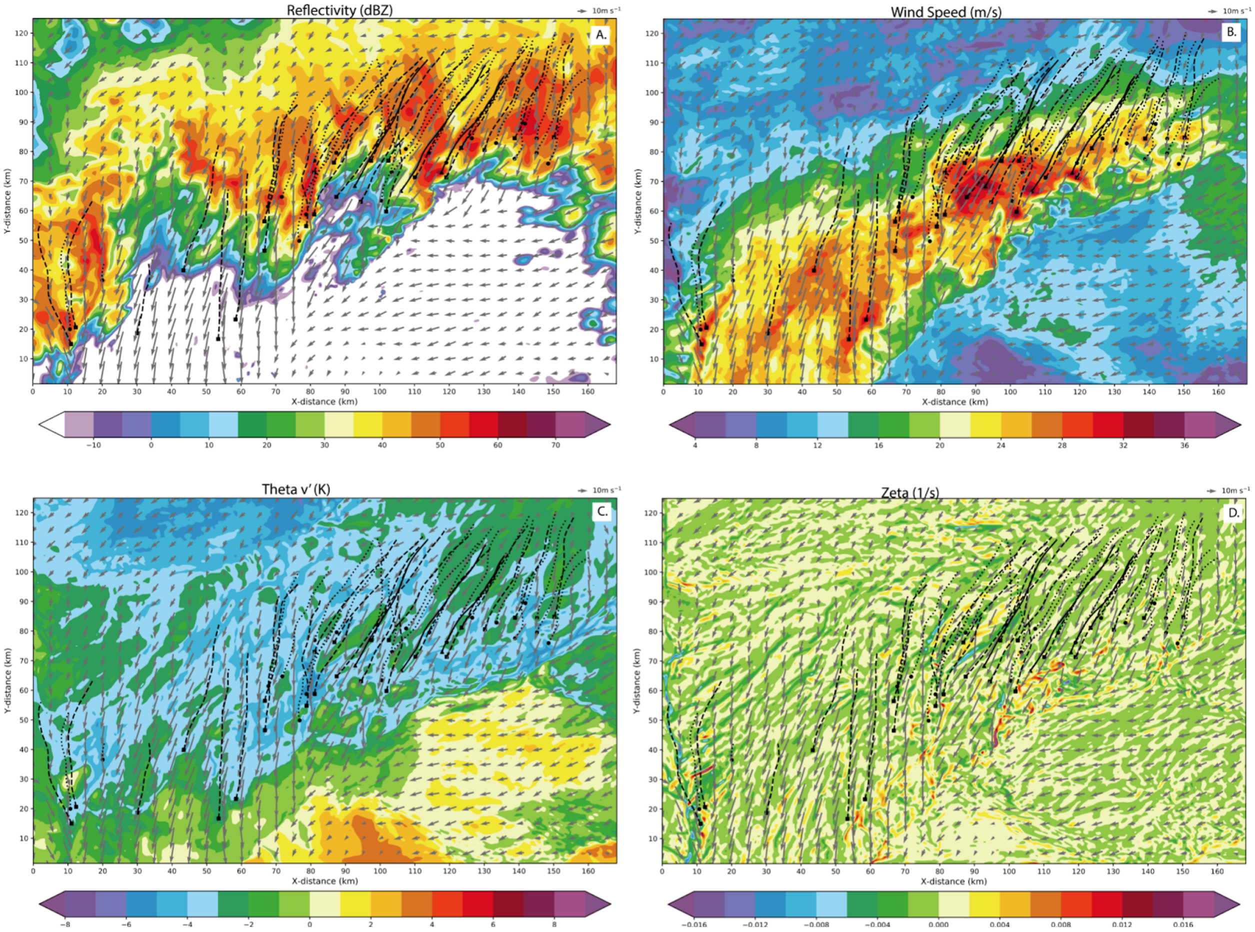

Figure 52. Horizontal plots of the 25-26 June MCS at 80 m at 0630 UTC of a) reflectivity, b) wind speed, c) Θ_v', and d) vertical vorticity with wind vectors. Severe (sub-severe) [significant severe] trajectories are indicated by dashed (dotted) [solid] lines and end in square (circle) [triangle] points.

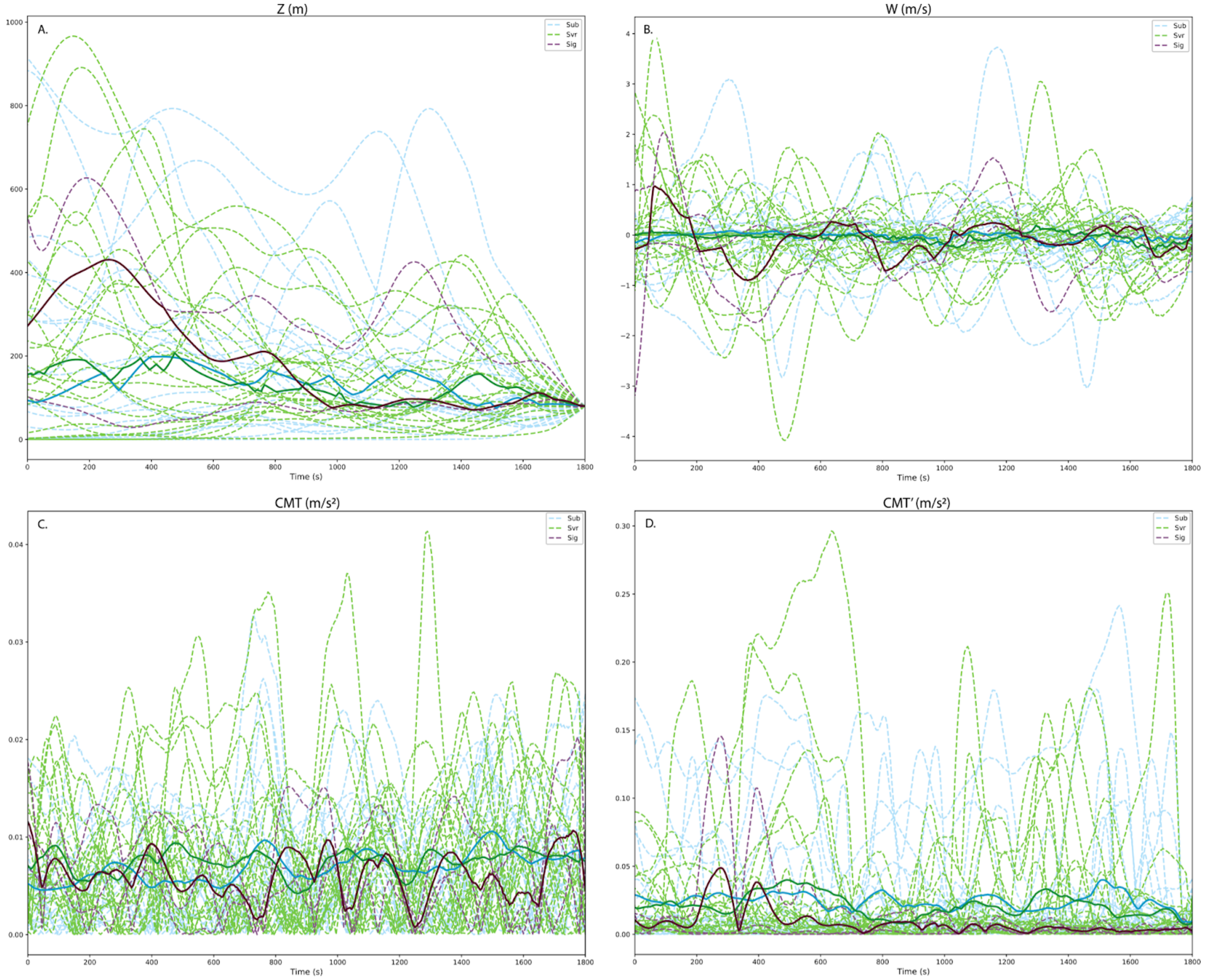

Figure 53. Change in a) height, b) vertical velocity, c) CMT′, and d) CMT_0 for the 21 sub-severe, 23 severe, and 3 significant severe trajectories at 0630 UTC for the 25-26 June MCS. Dashed lines are individual trajectories and the solid line is the median.

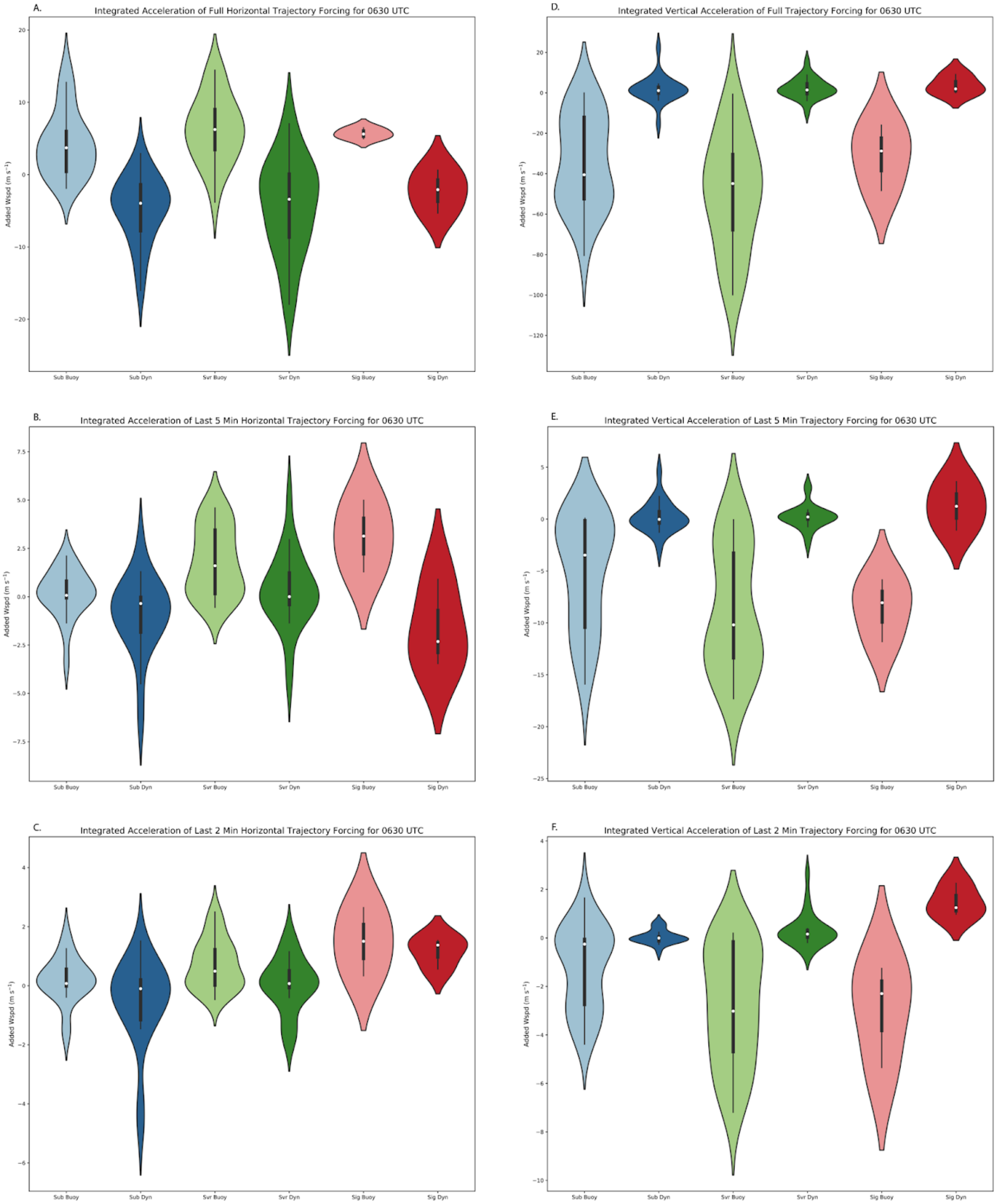

Figure 54. The 0630 UTC integrated acceleration givestotal added wind speed from the buoyancy and dynamic forcing for a) the entire trajectory in the horizontal, b) the last 5 minutes of the trajectory in the horizontal, c) the last 2 minutes of the trajectory in the horizontal, d) the entire trajectory in the vertical, e) the last 5 minutes of the trajectory in the vertical, and f) the last 2 minutes of the trajectory in the vertical. Sub-severe distributions are in blue, severe in green, and significant severe in red.

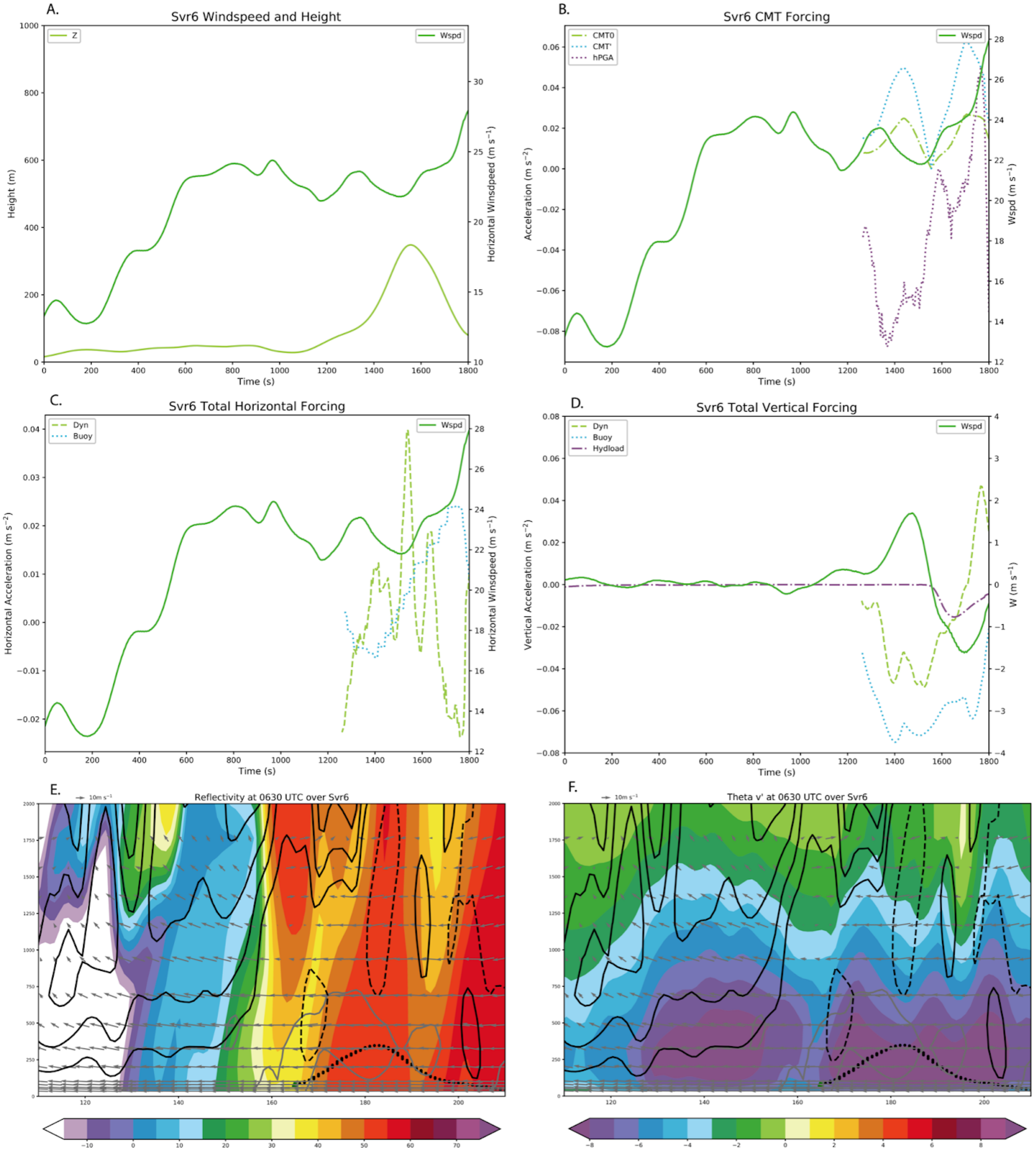

Figure 55. The svr6 trajectory at 0630 UTC a) height and wind speed, b) CMT and hPGA forcing with wind speed, c) horizontal dynamic and buoyancy forcing with wind speed, d) vertical dynamic and buoyancy forcing with w, e) reflectivity cross-section over svr6, and f) Θ_v' cross-section over svr6. Reflectivity and Θ_v' have solid (dashed) contours for updrafts (downdrafts) every 2 m s^{-1} (-2 m s^{-1}). Solid gray contours are for severe winds and significant severe winds.

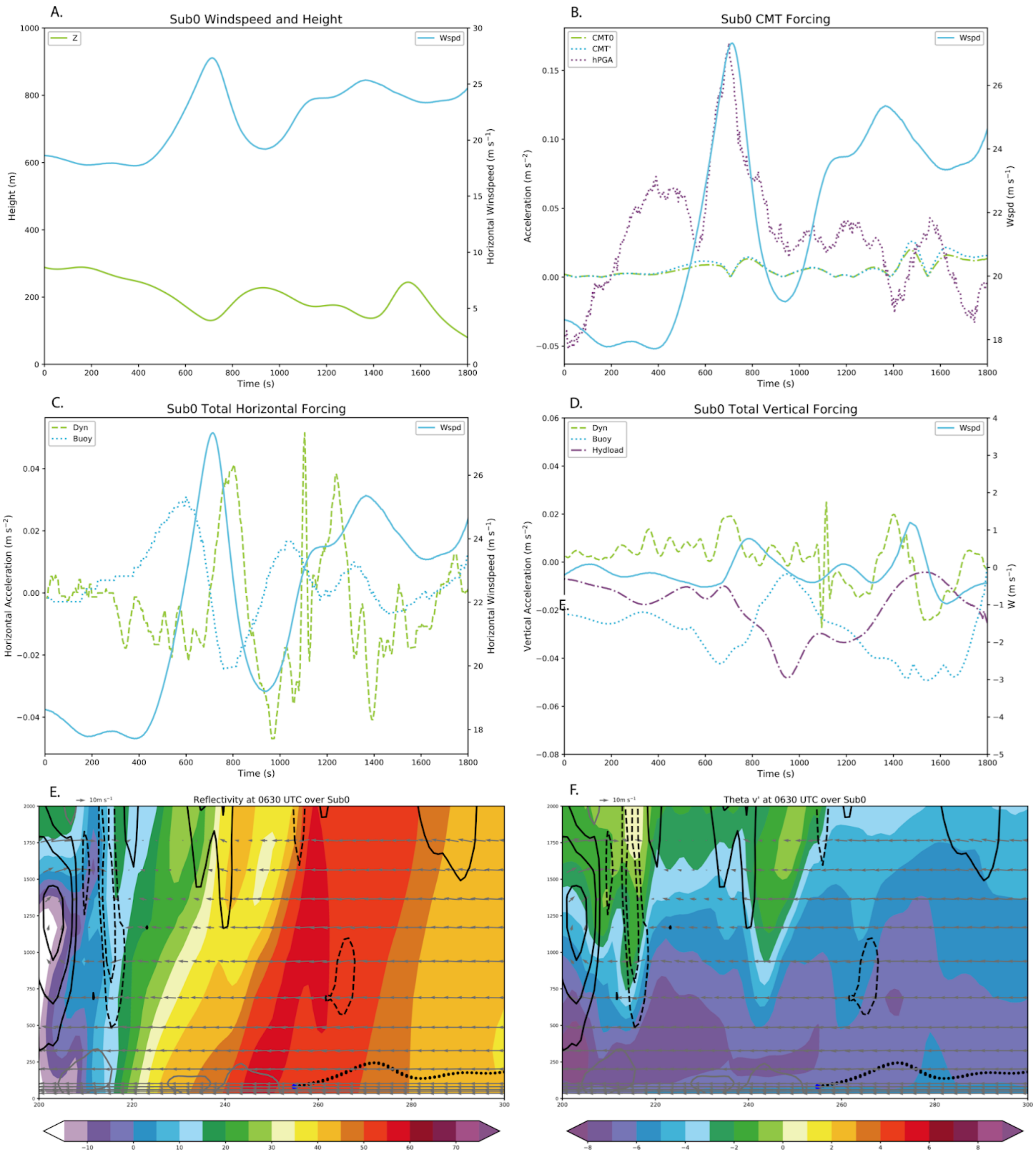

Figure 56. The sub0 trajectory at 0630 UTC a) height and wind speed, b) CMT and hPGA forcing with wind speed, c) horizontal dynamic and buoyancy forcing with wind speed, d) vertical dynamic and buoyancy forcing with w, e) reflectivity cross-section over sub0, and f) Θ_v' cross-section over sub0. Reflectivity and Θ_v' have solid (dashed) contours for updrafts (downdrafts) every 2 m s^{-1} (-2 m s^{-1}). Solid gray contours are for severe winds and significant severe winds.

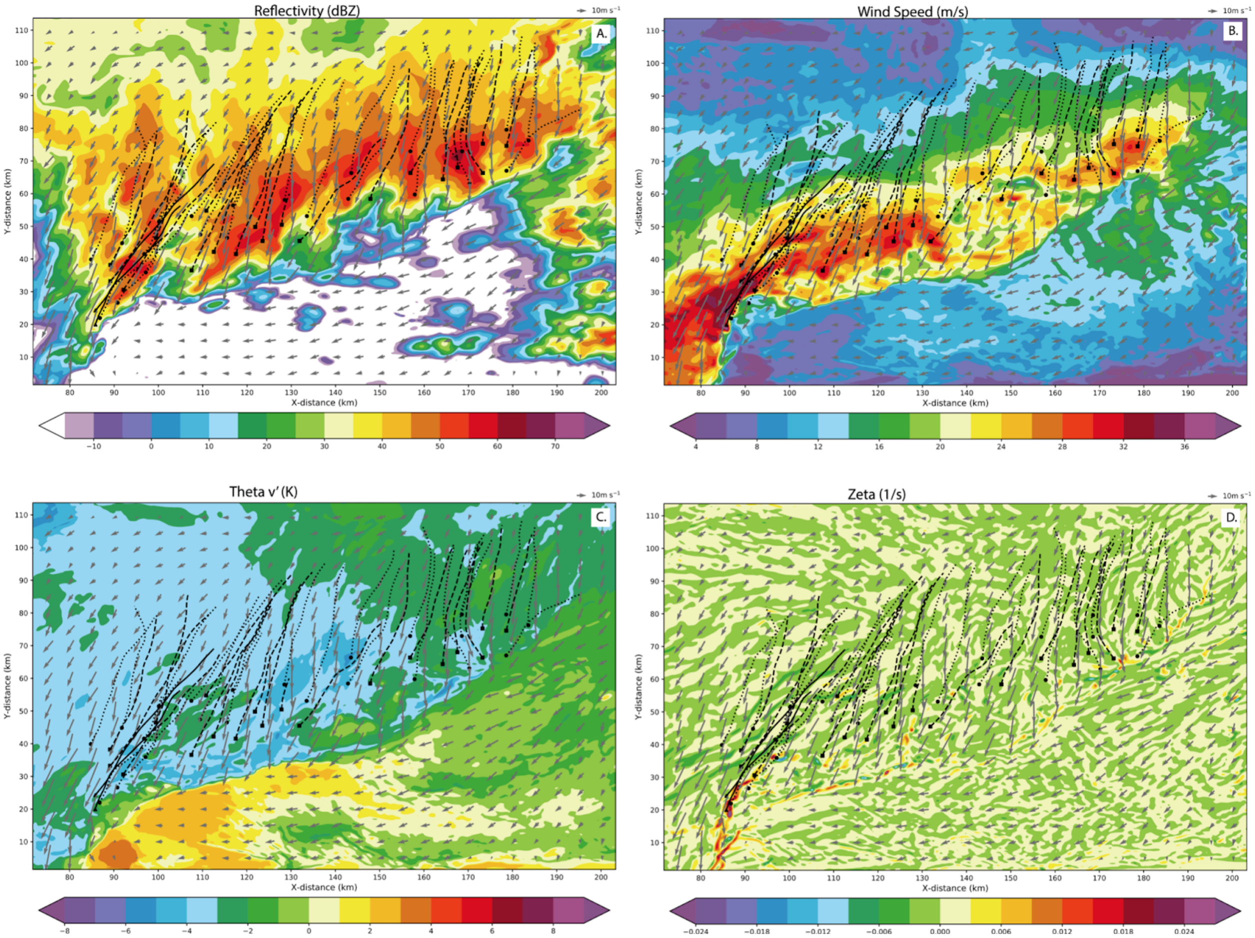

Figure 57. Horizontal plots of the 25-26 June MCS at 80 m at 0700 UTC of a) reflectivity, b) wind speed, c) Θ_v', and d) vertical vorticity with wind vectors. Severe (sub-severe) [significant severe] trajectories are indicated by dashed (dotted) [solid] lines and end in square (circle) [triangle] points.

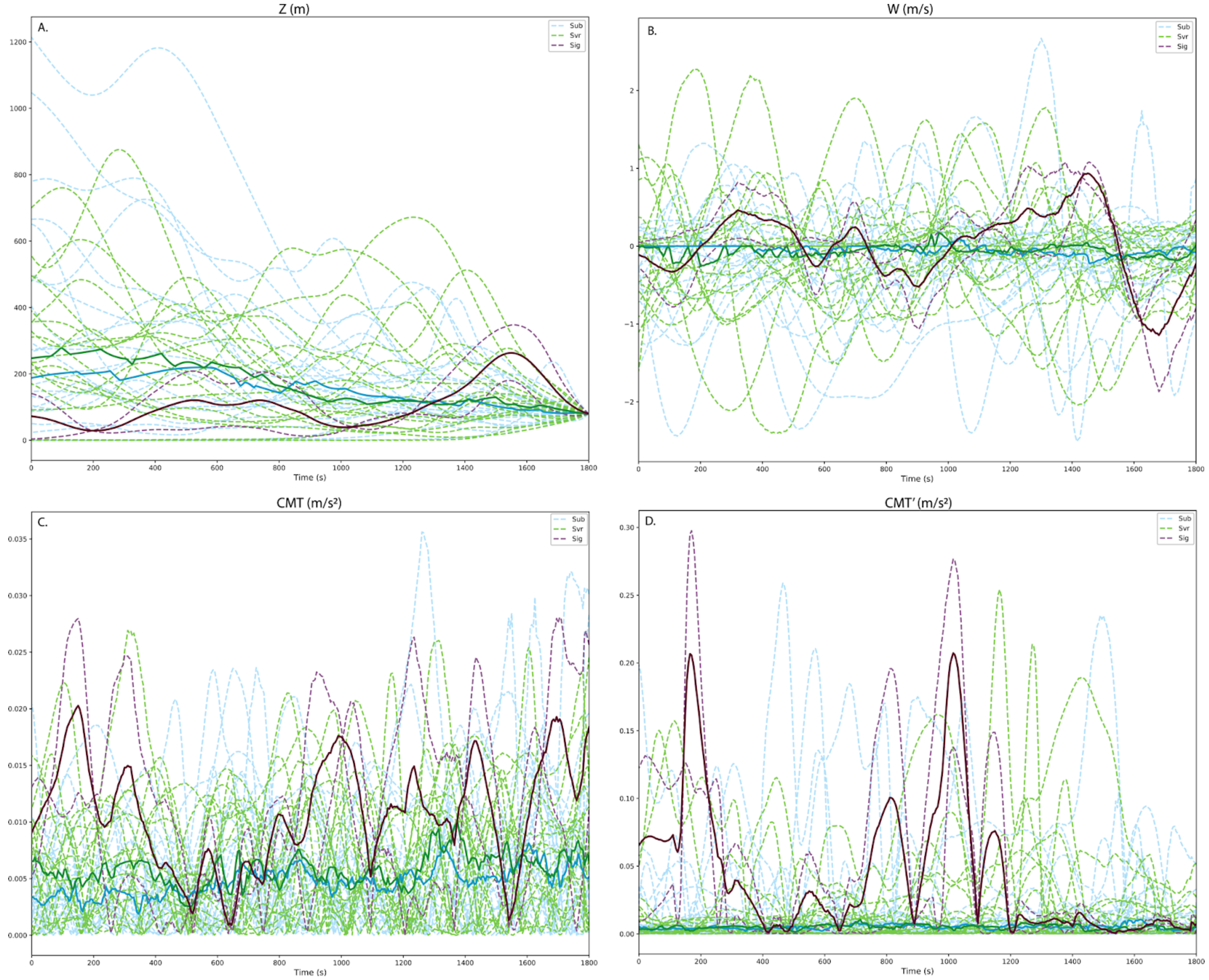

Figure 58. Change in a) height, b) vertical velocity, c) CMT′, and d) CMT_0 for the 23 sub-severe, 19 severe, and 2 significant severe trajectories at 0700 UTC for the 25-26 June MCS. Dashed lines are individual trajectories and the solid line is the median.

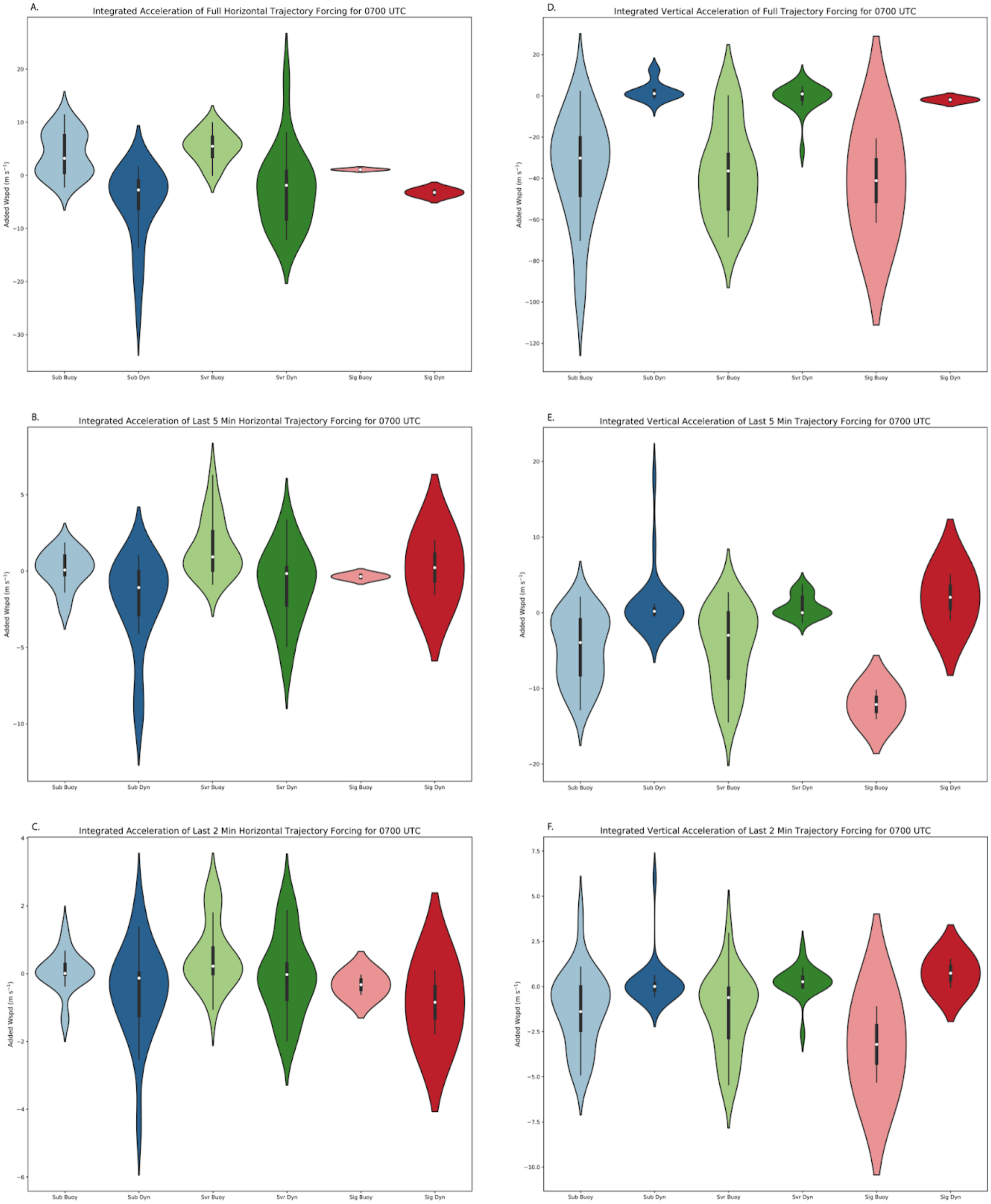

Figure 59. The 0700 UTC integrated acceleration givestotal added wind speed from the buoyancy and dynamic forcing for a) the entire trajectory in the horizontal, b) the last 5 minutes of the trajectory in the horizontal, c) the last 2 minutes of the trajectory in the horizontal, d) the entire trajectory in the vertical, e) the last 5 minutes of the trajectory in the vertical, and f) the

last 2 minutes of the trajectory in the vertical. Sub-severe distributions are in blue, severe in green, and significant severe in red.

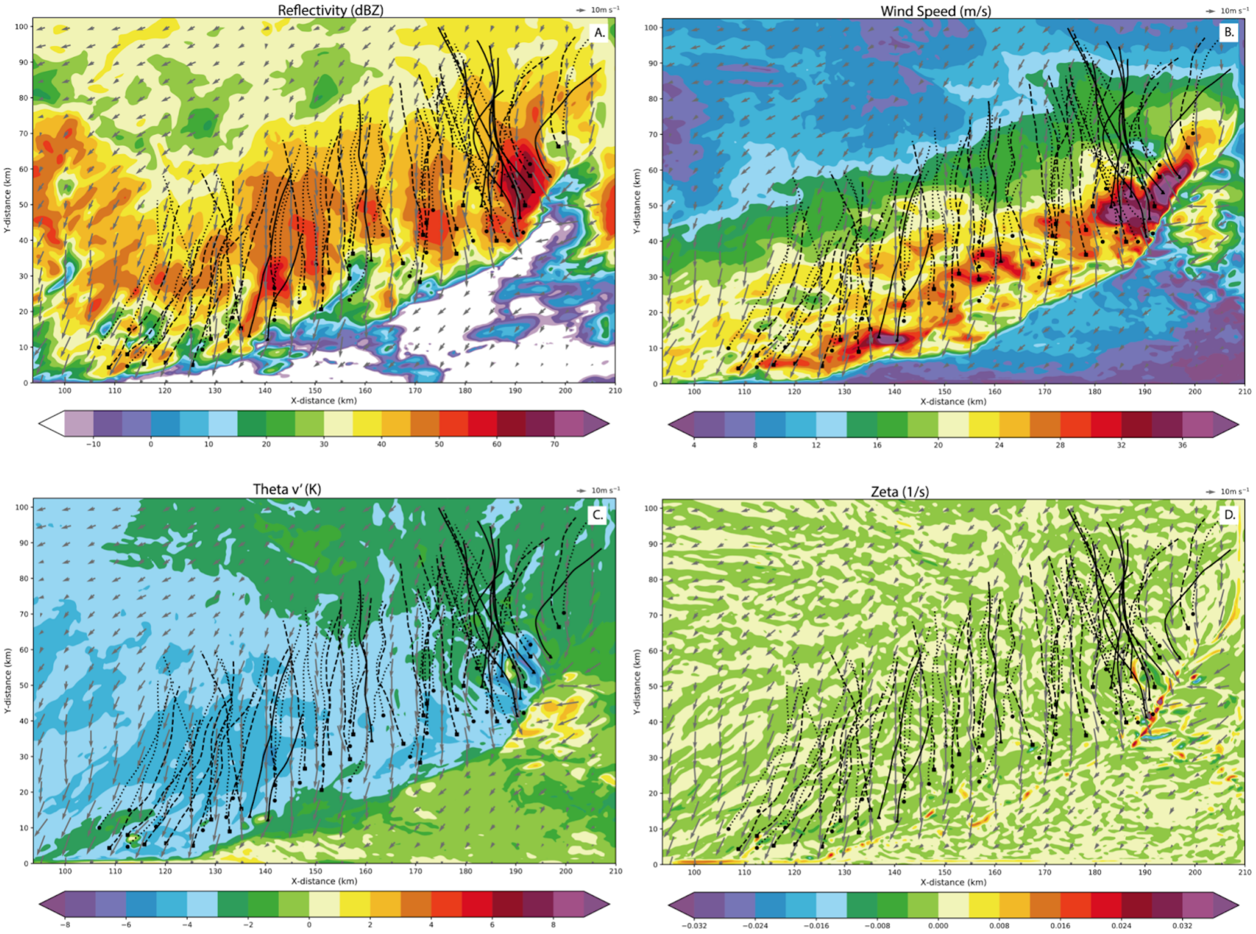

Figure 60. Horizontal plots of the 25-26 June MCS at 80 m at 0730 UTC of a) reflectivity, b) wind speed, c) Θ_v', and d) vertical vorticity with wind vectors. Severe (sub-severe) [significant severe] trajectories are indicated by dashed (dotted) [solid] lines and end in square (circle) [triangle] points.

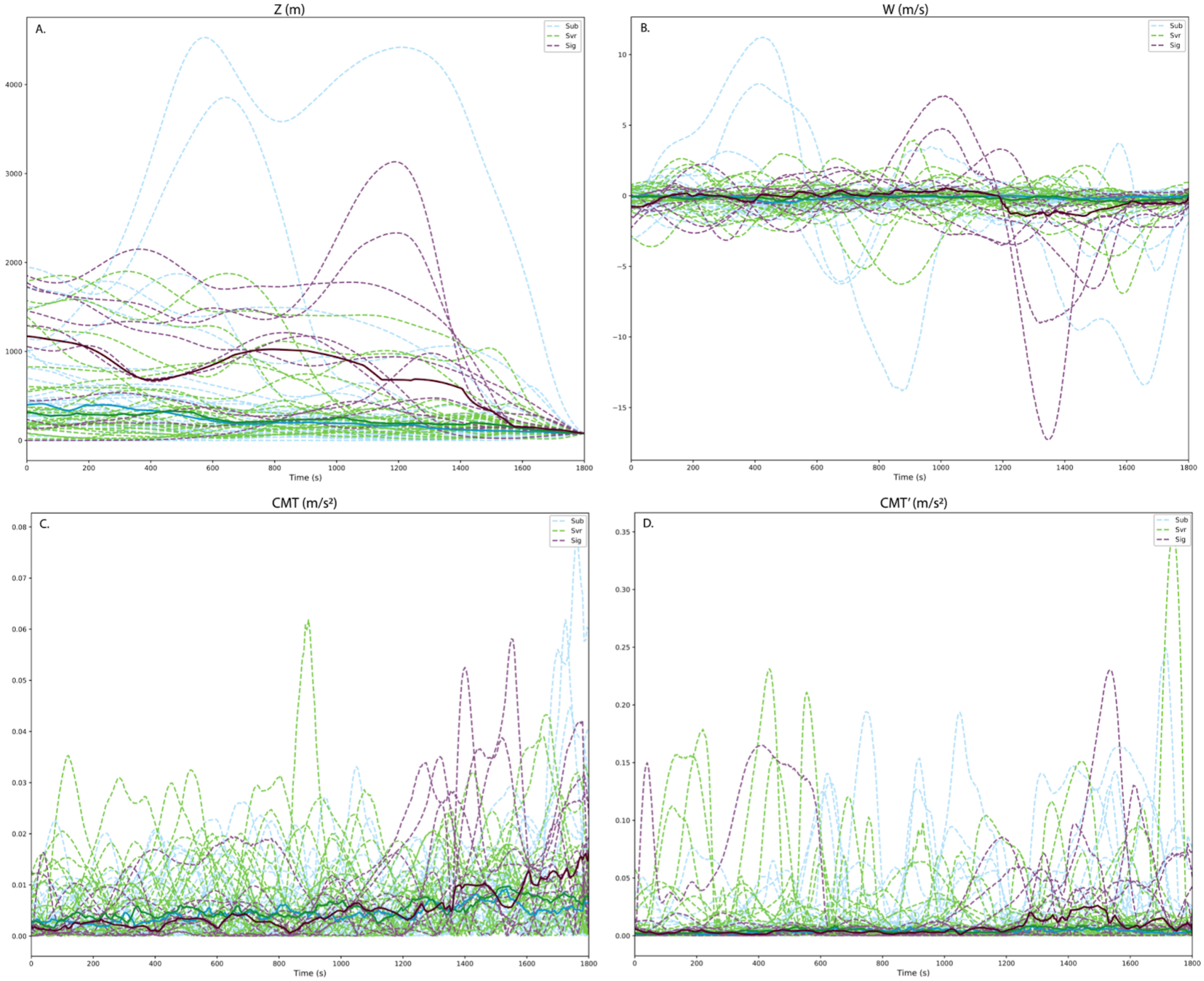

Figure 61. Change in a) height, b) vertical velocity, c) CMT′, and d) CMT_0 for the 29 sub-severe, 26 severe, and 10 significant severe trajectories at 0730 UTC for the 25-26 June MCS. Dashed lines are individual trajectories and the solid line is the median.

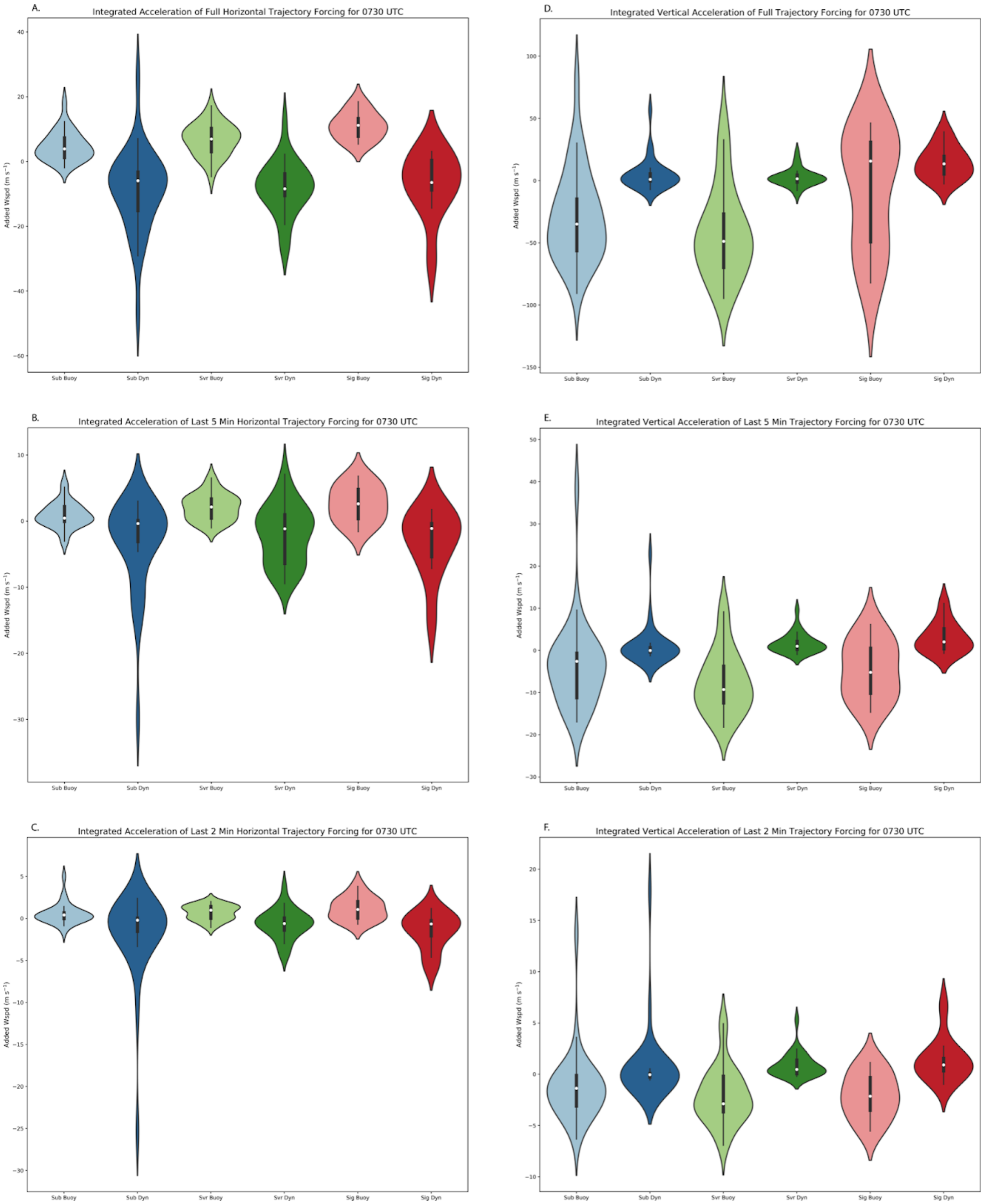
A. Integrated Acceleration of Full Horizontal Trajectory Forcing for 0730 UTC

B. Integrated Acceleration of Last 5 Min Horizontal Trajectory Forcing for 0730 UTC

C. Integrated Acceleration of Last 2 Min Horizontal Trajectory Forcing for 0730 UTC

D. Integrated Vertical Acceleration of Full Trajectory Forcing for 0730 UTC

E. Integrated Vertical Acceleration of Last 5 Min Trajectory Forcing for 0730 UTC

F. Integrated Vertical Acceleration of Last 2 Min Trajectory Forcing for 0730 UTC

Figure 62. The 0730 UTC integrated acceleration givestotal added wind speed from the buoyancy and dynamic forcing for a) the entire trajectory in the horizontal, b) the last 5 minutes of the trajectory in the horizontal, c) the last 2 minutes of the trajectory in the horizontal, d) the entire trajectory in the vertical, e) the last 5 minutes of the trajectory in the vertical, and f) the

last 2 minutes of the trajectory in the vertical. Sub-severe distributions are in blue, severe in green, and significant severe in red.

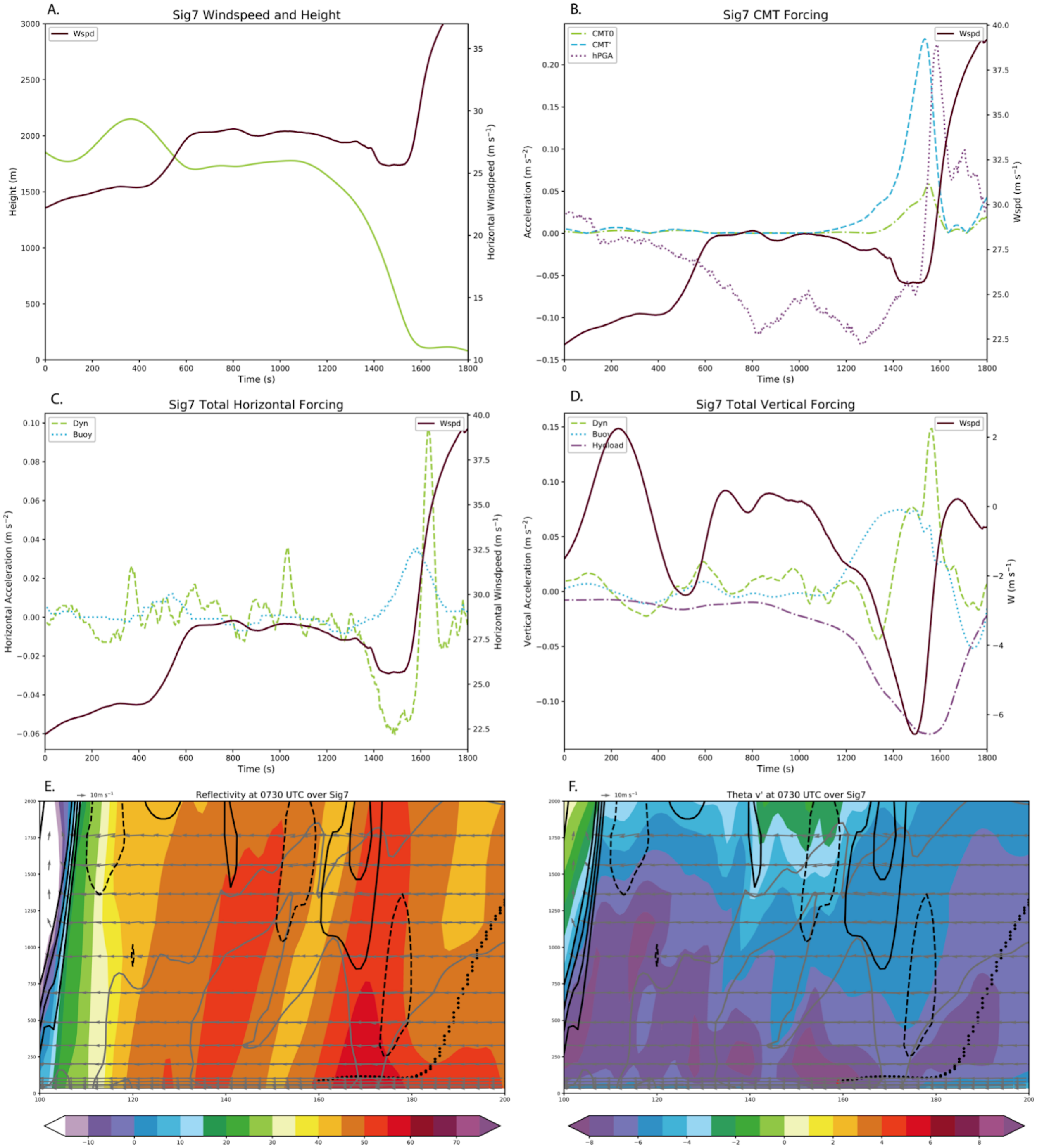

Figure 63. The sig7 trajectory at 0730 UTC a) height and wind speed, b) CMT and hPGA forcing with wind speed, c) horizontal dynamic and buoyancy forcing with wind speed, d) vertical dynamic and buoyancy forcing with w, e) reflectivity cross-section over sig7, and f) Θ_v' cross-section over sig7. Reflectivity and Θ_v' have solid (dashed) contours for updrafts (downdrafts) every 2 m s^{-1} (-2 m s^{-1}). Solid gray contours are for severe winds and significant severe winds.

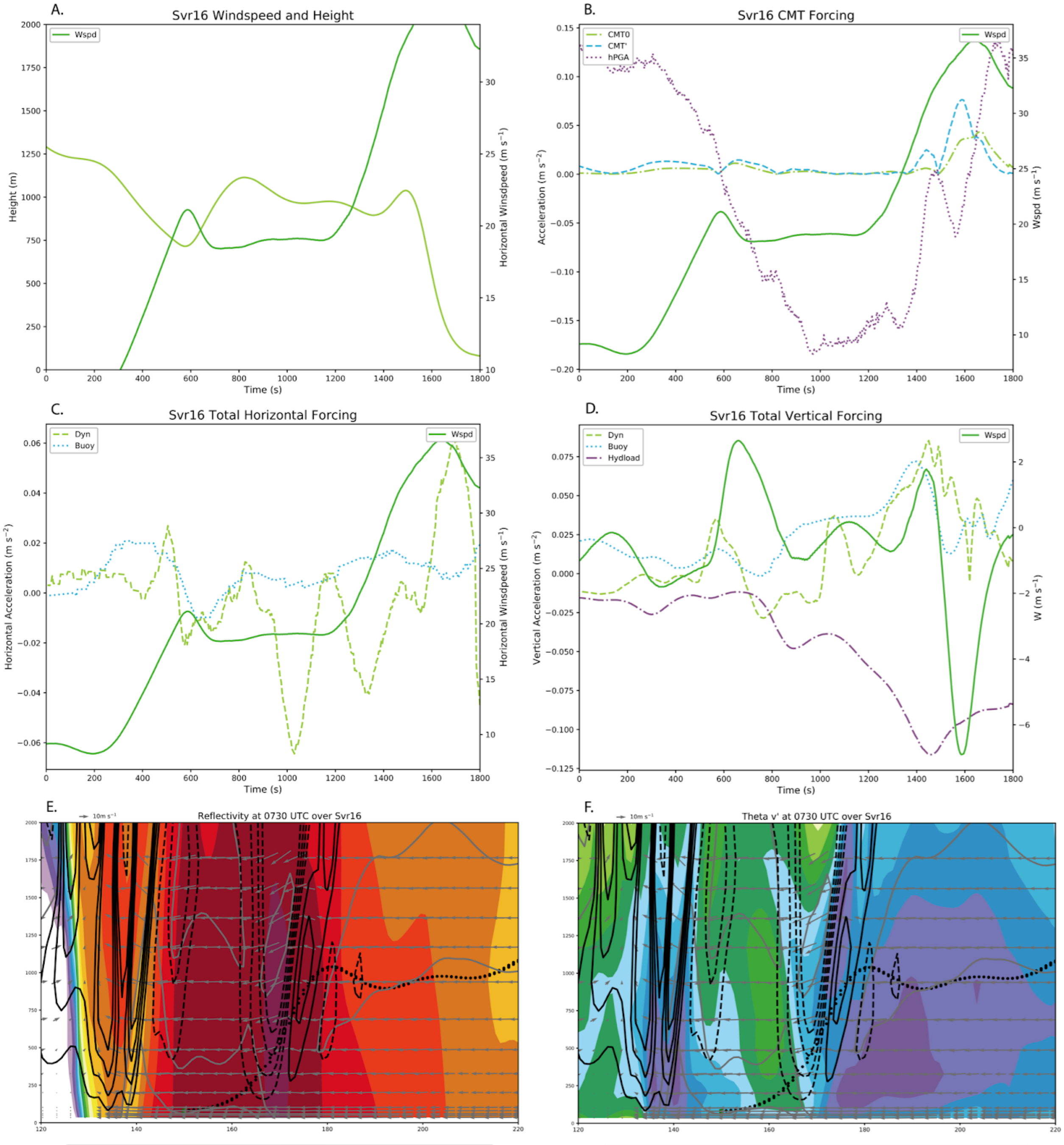

Figure 64. The svr16 trajectory at 0730 UTC a) height and wind speed, b) CMT and hPGA forcing with wind speed, c) horizontal dynamic and buoyancy forcing with wind speed, d) vertical dynamic and buoyancy forcing with w, e) reflectivity cross-section over svr16, and f) Θ_v' cross-section over svr16. Reflectivity and Θ_v' have solid (dashed) contours for updrafts (downdrafts) every 2 m s^{-1} (-2 m s^{-1}). Solid gray contours are for severe winds and significant severe winds.

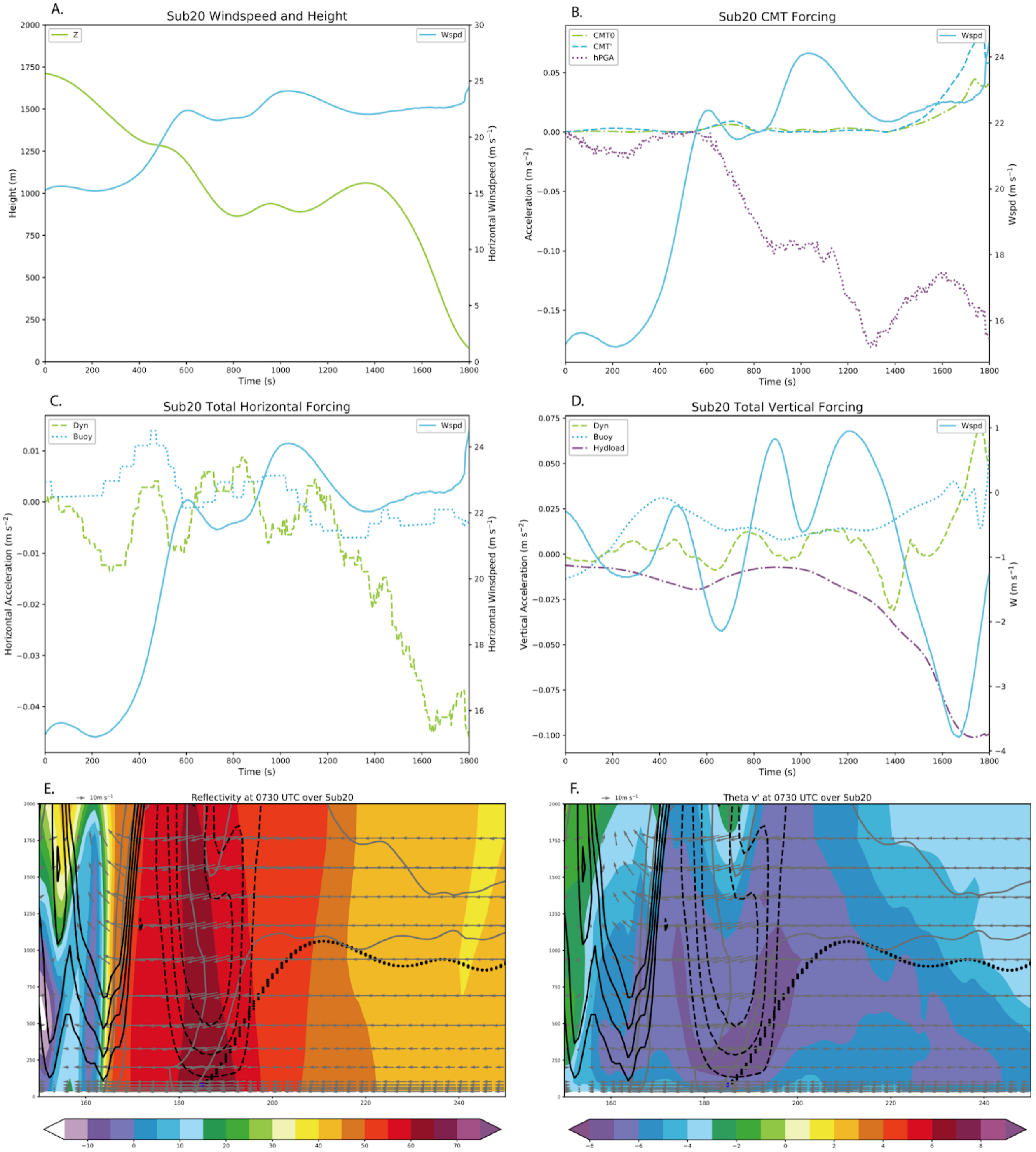

Figure 65. The sub20 trajectory at 0730 UTC a) height and wind speed, b) CMT and hPGA forcing with wind speed, c) horizontal dynamic and buoyancy forcing with wind speed, d) vertical dynamic and buoyancy forcing with w, e) reflectivity cross-section over sub20, and f) Θ_v' cross-section over sub20. Reflectivity and Θ_v' have solid (dashed) contours for updrafts (downdrafts) every 2 m s^{-1} (-2 m s^{-1}). Solid gray contours are for severe winds and significant severe winds.

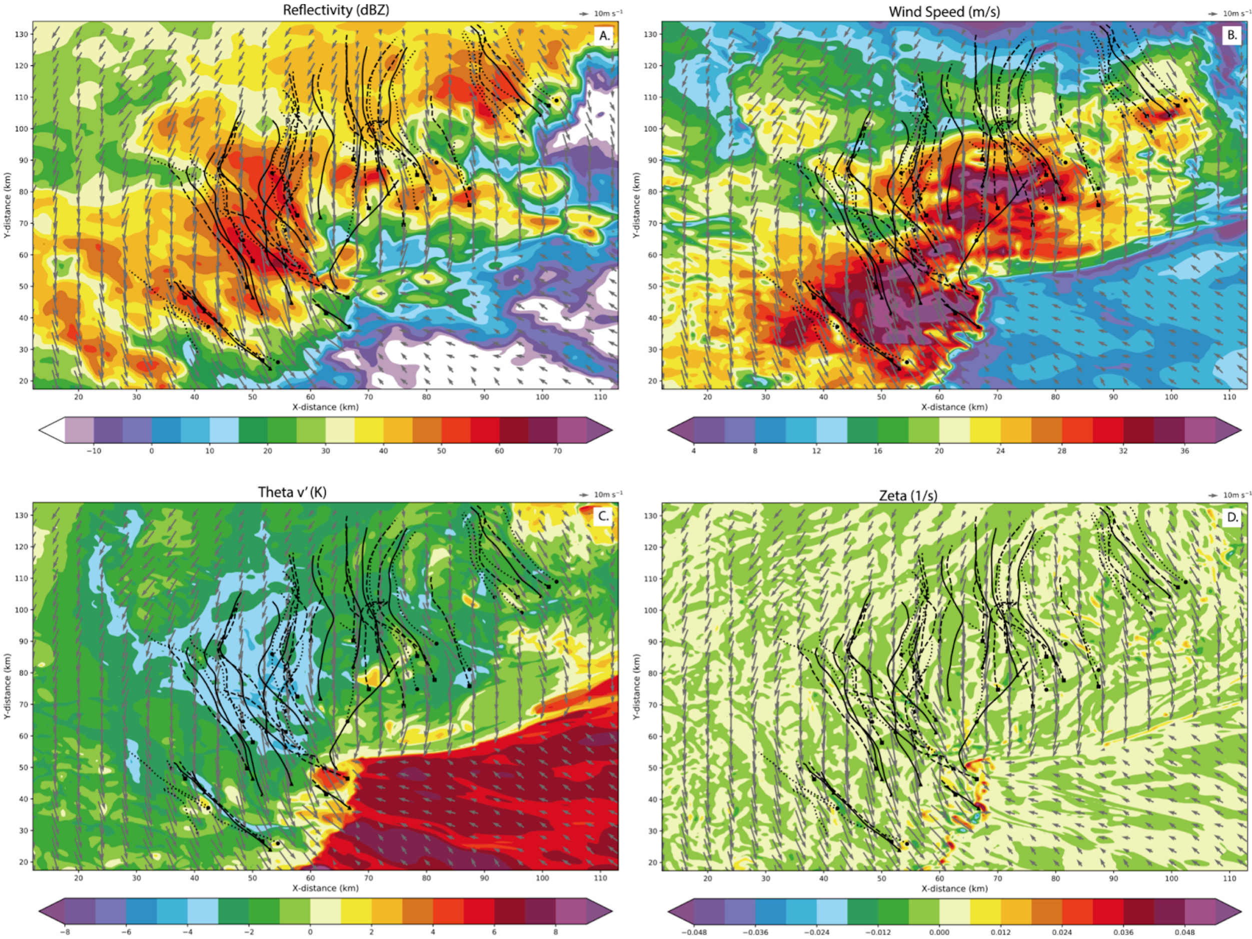

Figure 66. Horizontal plots of the 5-6 July MCS at 80 m at 0430 UTC of a) reflectivity, b) wind speed, c) Θ_v', and d) vertical vorticity with wind vectors. Severe (sub-severe) [significant severe] trajectories are indicated by dashed (dotted) [solid] lines and end in square (circle) [triangle] points.

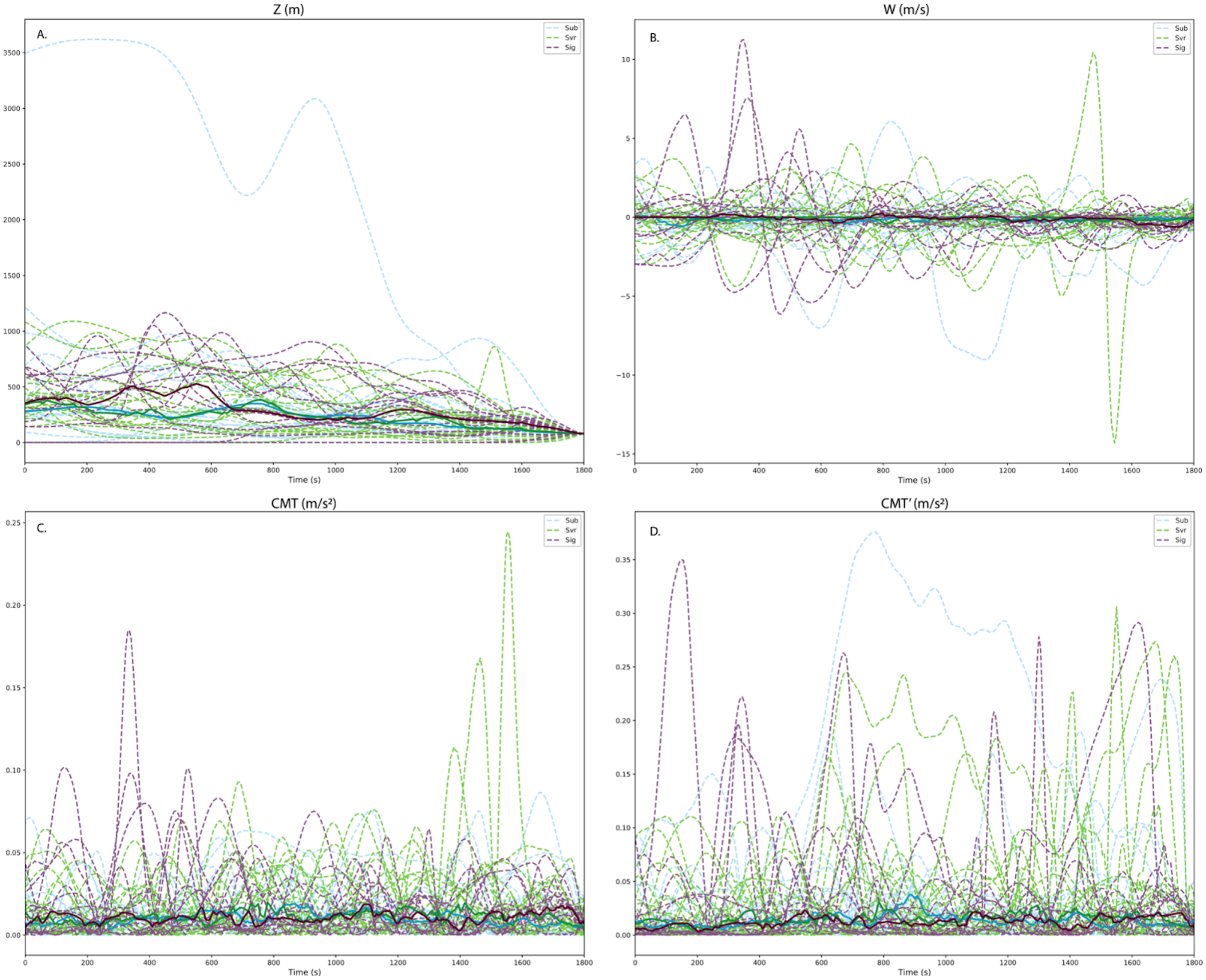

Figure 67. Change in a) height, b) vertical velocity, c) CMT′, and d) CMT_0 for the 18 sub-severe, 21 severe, and 14 significant severe trajectories at 0430 UTC for the 5-6 July MCS. Dashed lines are individual trajectories and the solid line is the median.

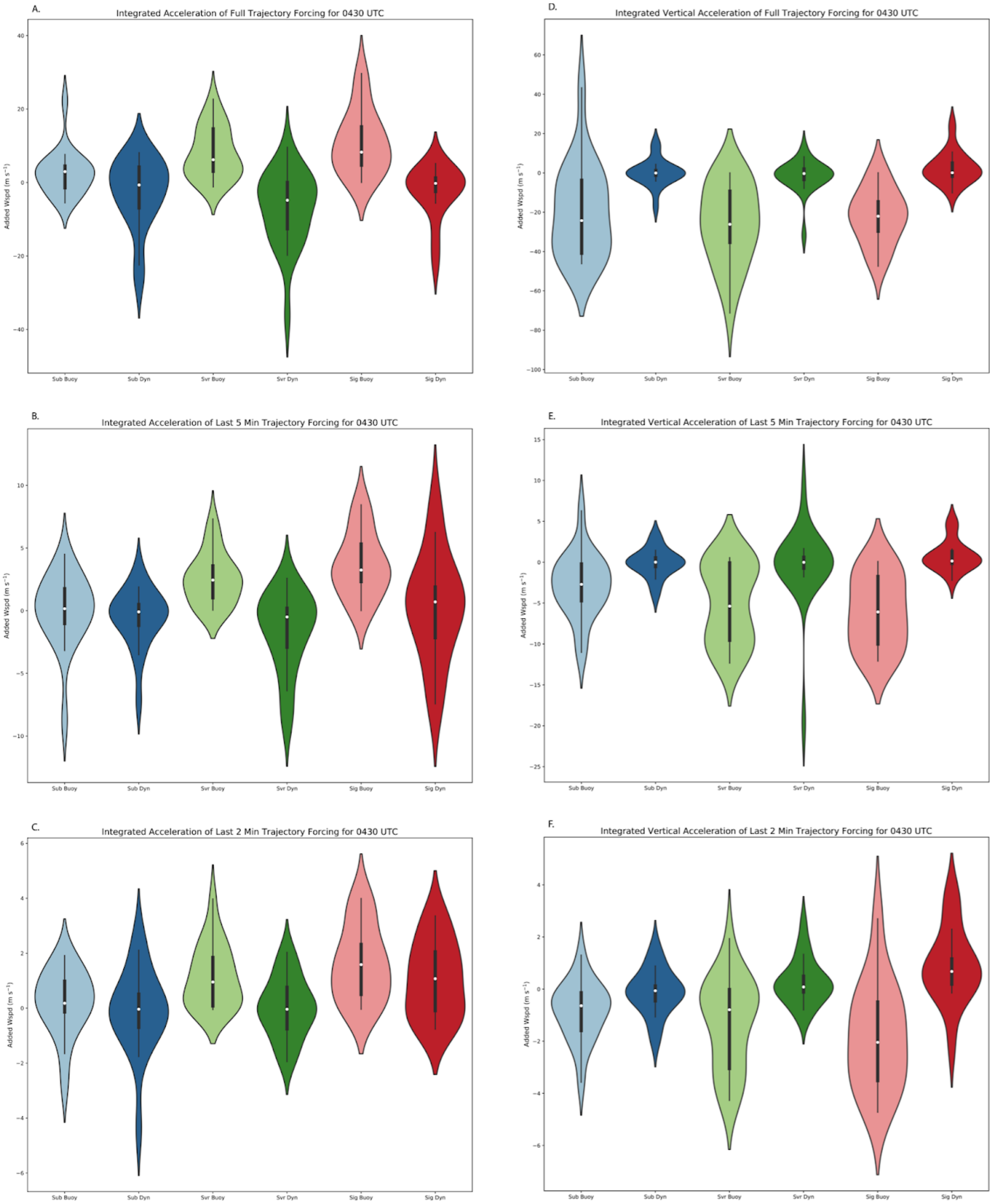

Figure 68. The 0430 UTC integrated acceleration givestotal added wind speed from the buoyancy and dynamic forcing for a) the entire trajectory in the horizontal, b) the last 5 minutes of the trajectory in the horizontal, c) the last 2 minutes of the trajectory in the horizontal, d) the entire trajectory in the vertical, e) the last 5 minutes of the trajectory in the vertical, and f) the

last 2 minutes of the trajectory in the vertical. Sub-severe distributions are in blue, severe in green, and significant severe in red.

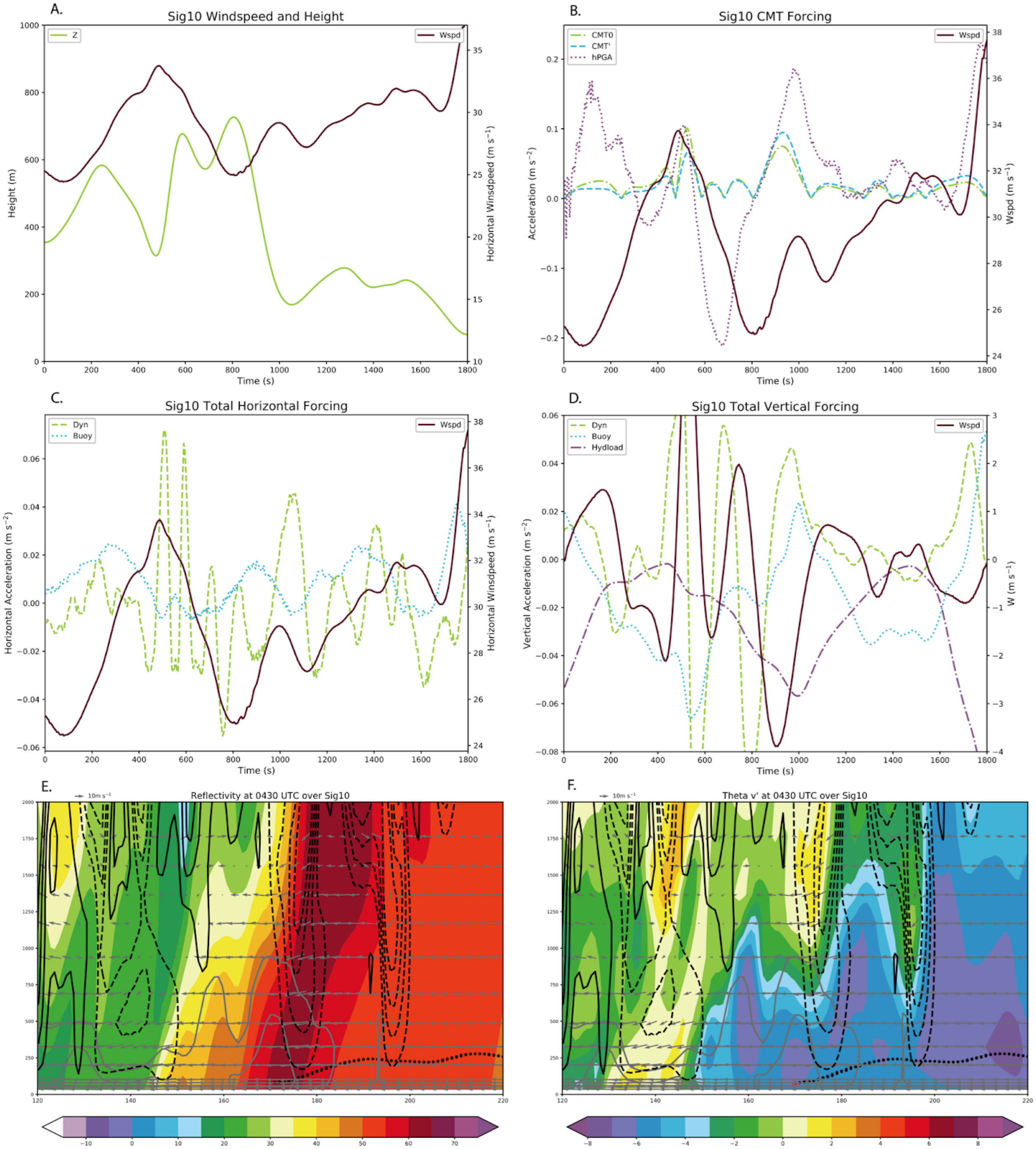

Figure 69. The sig10 trajectory at 0430 UTC a) height and wind speed, b) CMT and hPGA forcing with wind speed, c) horizontal dynamic and buoyancy forcing with wind speed, d) vertical dynamic and buoyancy forcing with w, e) reflectivity cross-section over sig10, and f) Θ_v' cross-section over sig10. Reflectivity and Θ_v' have solid (dashed) contours for updrafts

(downdrafts) every 2 m s^{-1} (-2 m s^{-1}). Solid gray contours are for severe winds and significant severe winds.

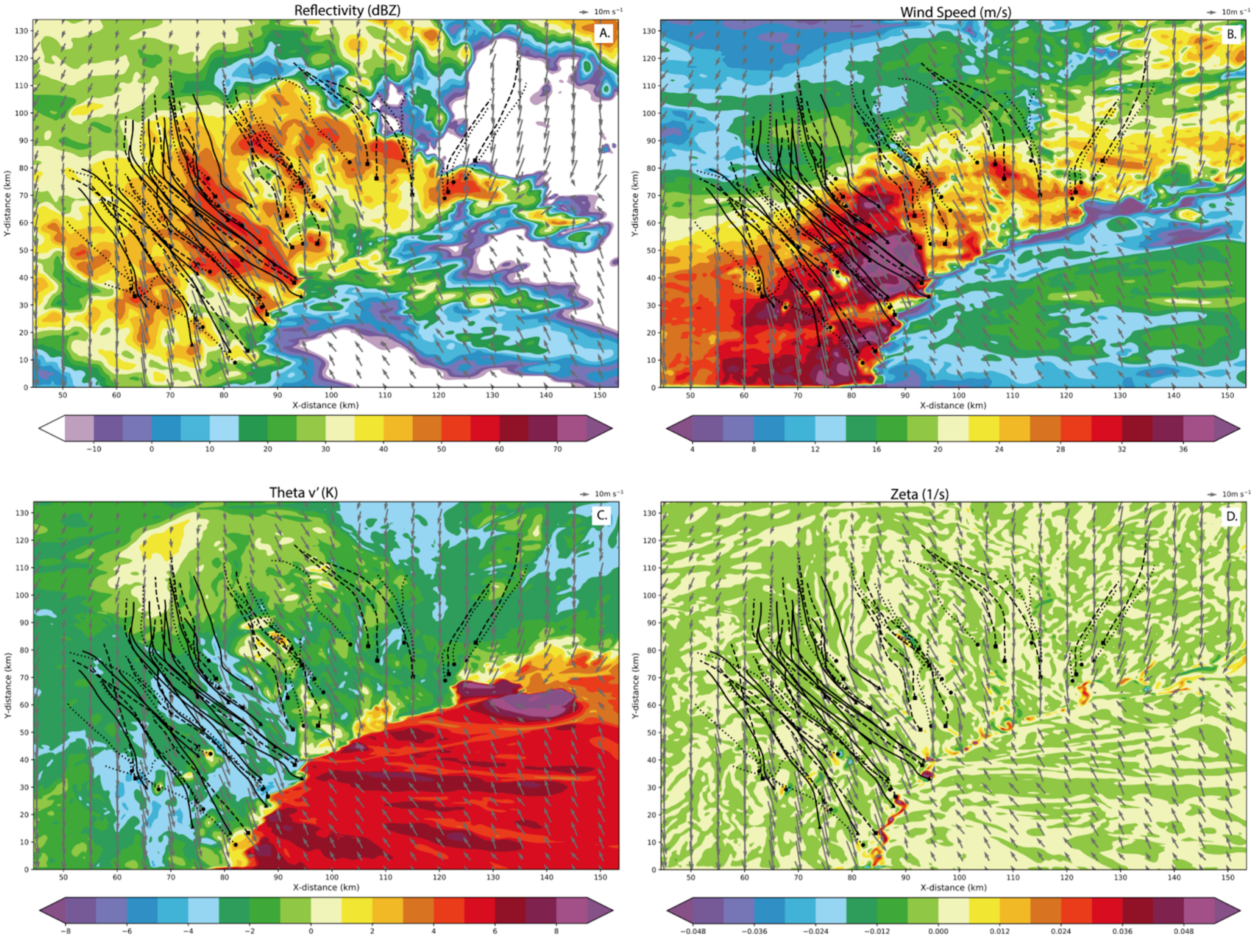

Figure 70. Horizontal plots of the 5-6 July MCS at 80 m at 0500 UTC of a) reflectivity, b) wind speed, c) Θ_v', and d) vertical vorticity with wind vectors. Severe (sub-severe) [significant severe] trajectories are indicated by dashed (dotted) [solid] lines and end in square (circle) [triangle] points.

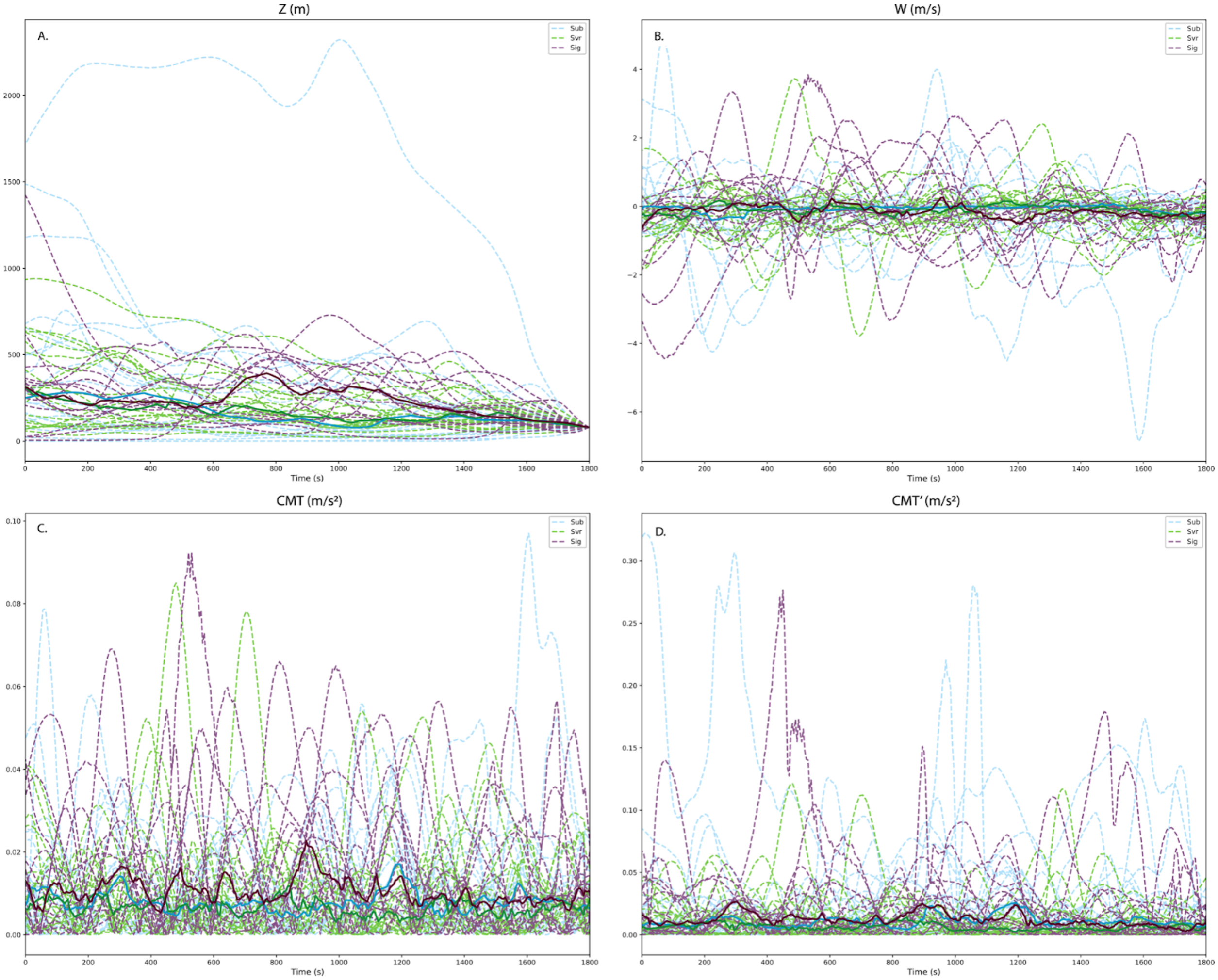

Figure 71. Change in a) height, b) vertical velocity, c) CMT′, and d) CMT_0 for the 20 sub-severe, 19 severe, and 14 significant severe trajectories at 0500 UTC for the 5-6 July MCS. Dashed lines are individual trajectories and the solid line is the median.

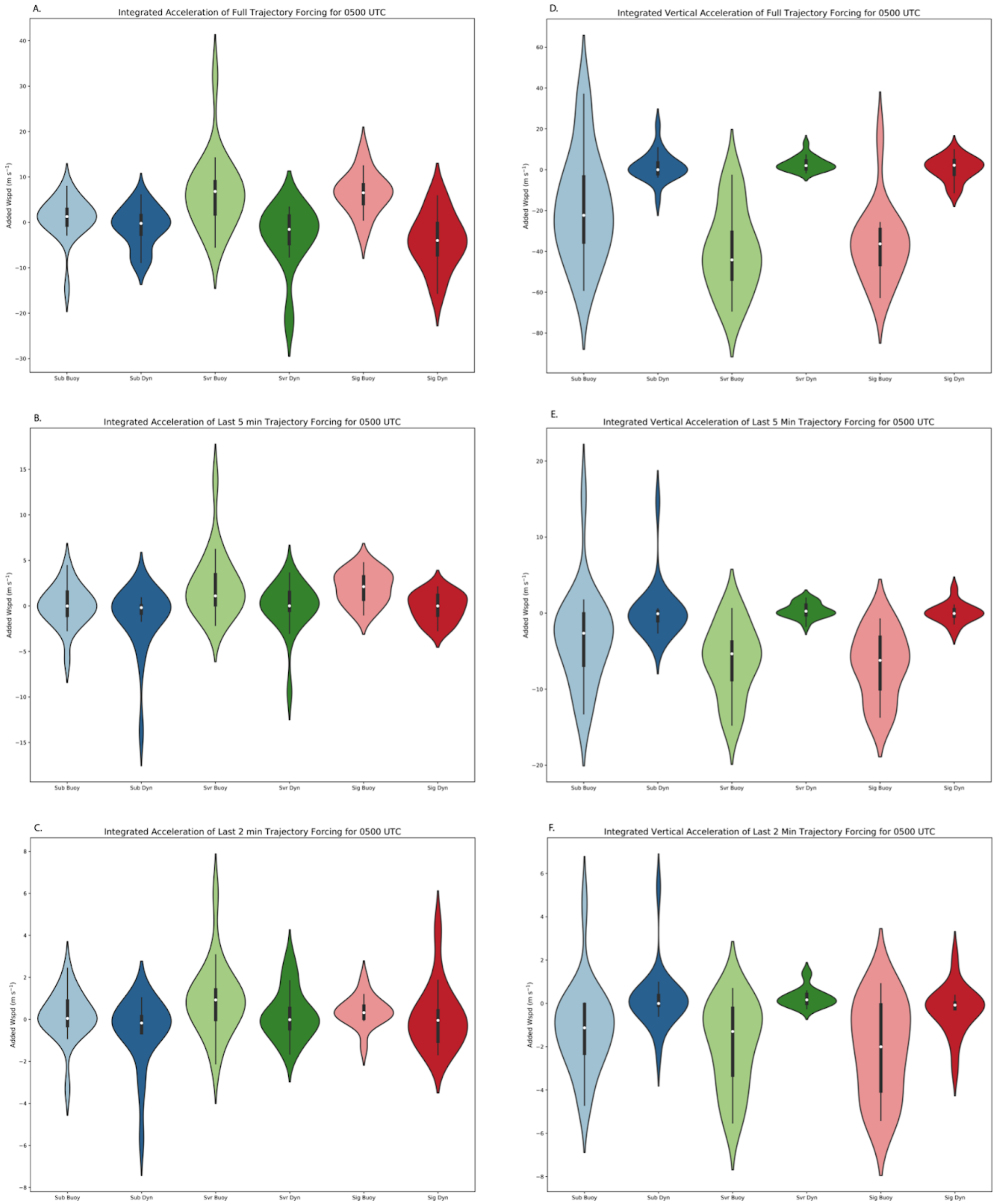

Figure 72. The 0500 UTC integrated acceleration givestotal added wind speed from the buoyancy and dynamic forcing for a) the entire trajectory in the horizontal, b) the last 5 minutes of the trajectory in the horizontal, c) the last 2 minutes of the trajectory in the horizontal, d) the entire trajectory in the vertical, e) the last 5 minutes of the trajectory in the vertical, and f) the

last 2 minutes of the trajectory in the vertical. Sub-severe distributions are in blue, severe in green, and significant severe in red.

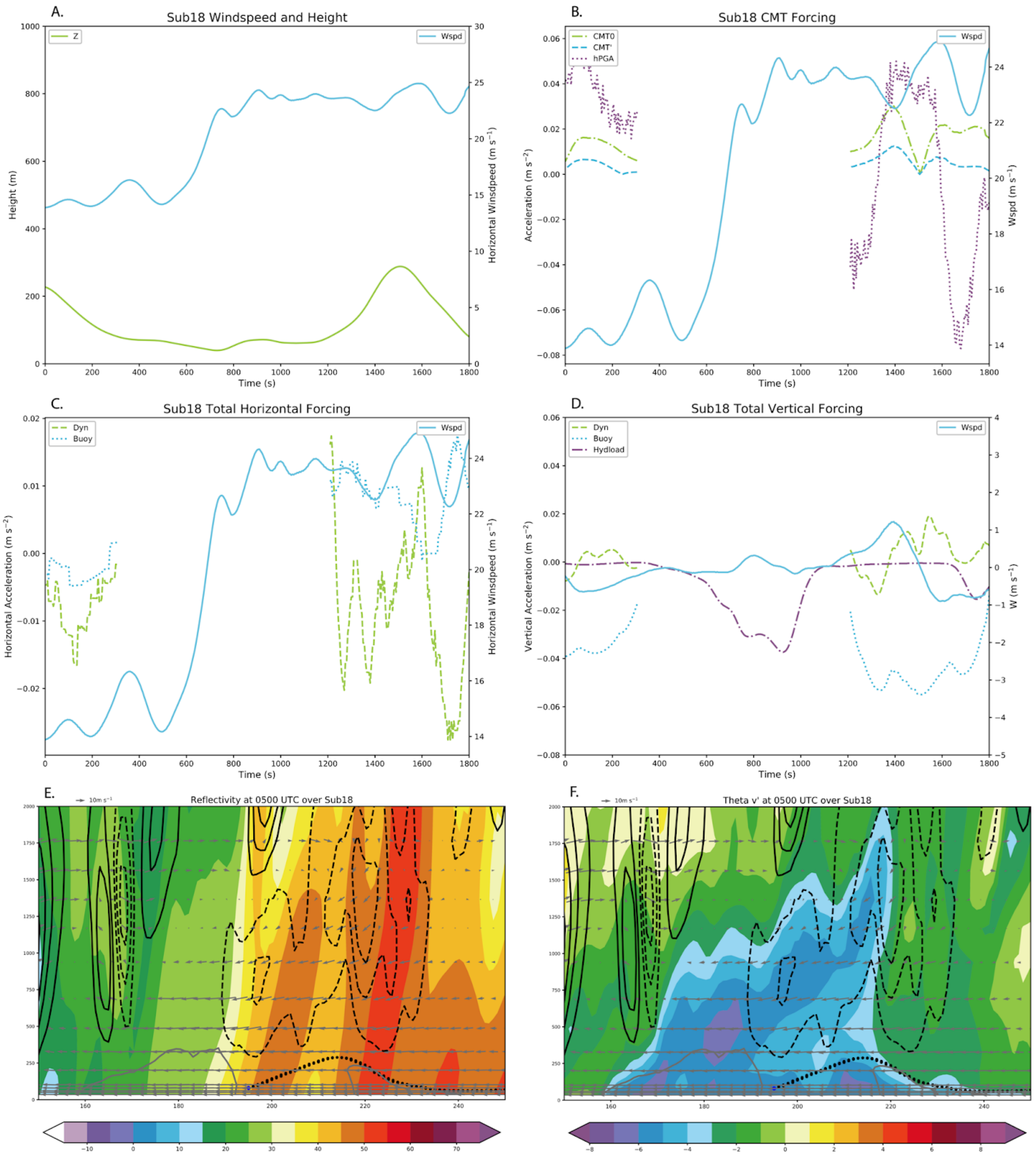

Figure 73. The sub18 trajectory at 0500 UTC a) height and wind speed, b) CMT and hPGA forcing with wind speed, c) horizontal dynamic and buoyancy forcing with wind speed, d) vertical dynamic and buoyancy forcing with w, e) reflectivity cross-section over sub18, and f) Θ_v' cross-section over sub18. Reflectivity and Θ_v' have solid (dashed) contours for updrafts (downdrafts) every 2 m s^{-1} (-2 m s^{-1}). Solid gray contours are for severe winds and significant severe winds.

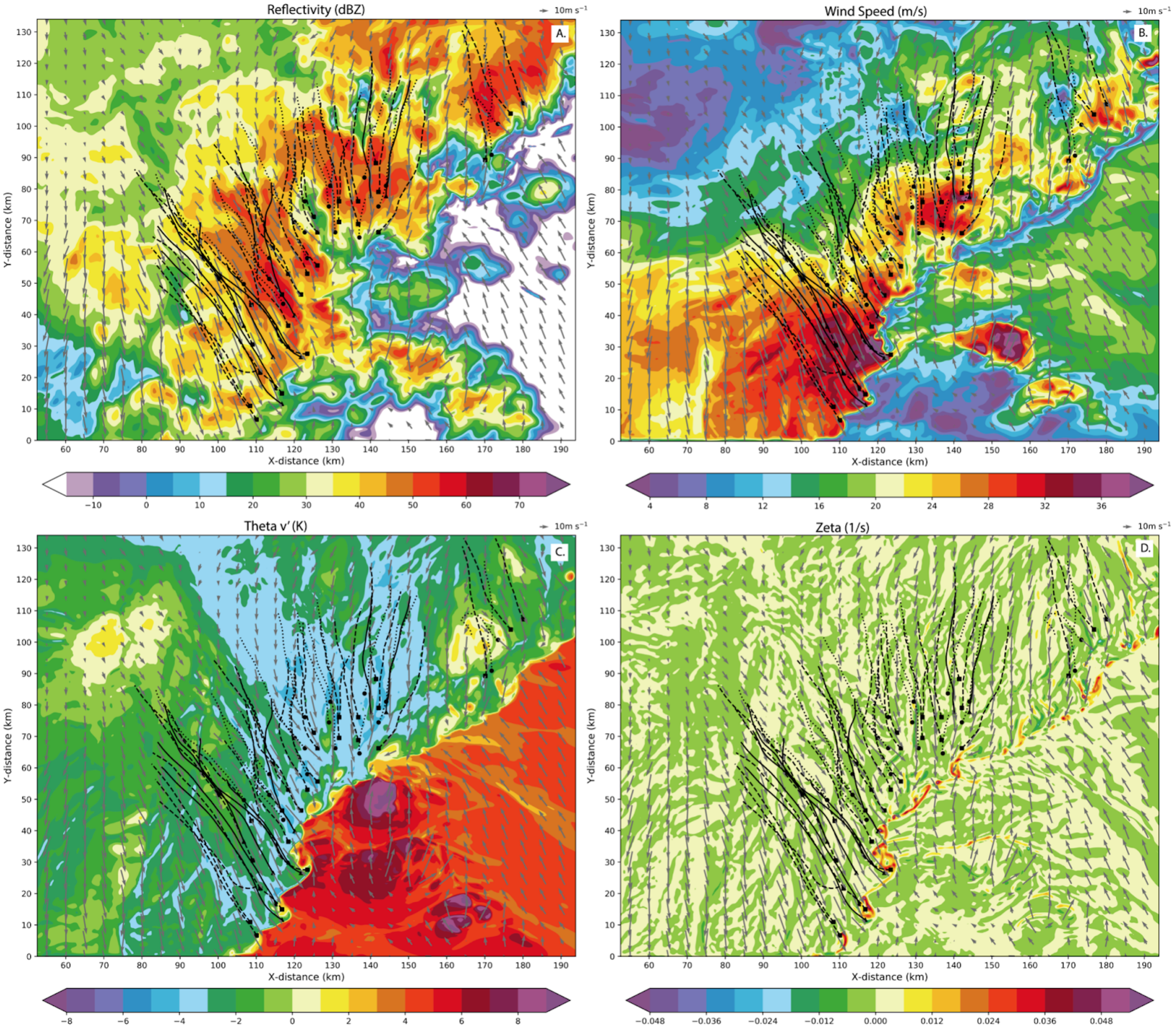

Figure 74. Horizontal plots of the 5-6 July MCS at 80 m at 0530 UTC of a) reflectivity, b) wind speed, c) Θ_v', and d) vertical vorticity with wind vectors. Severe (sub-severe) [significant severe] trajectories are indicated by dashed (dotted) [solid] lines and end in square (circle) [triangle] points.

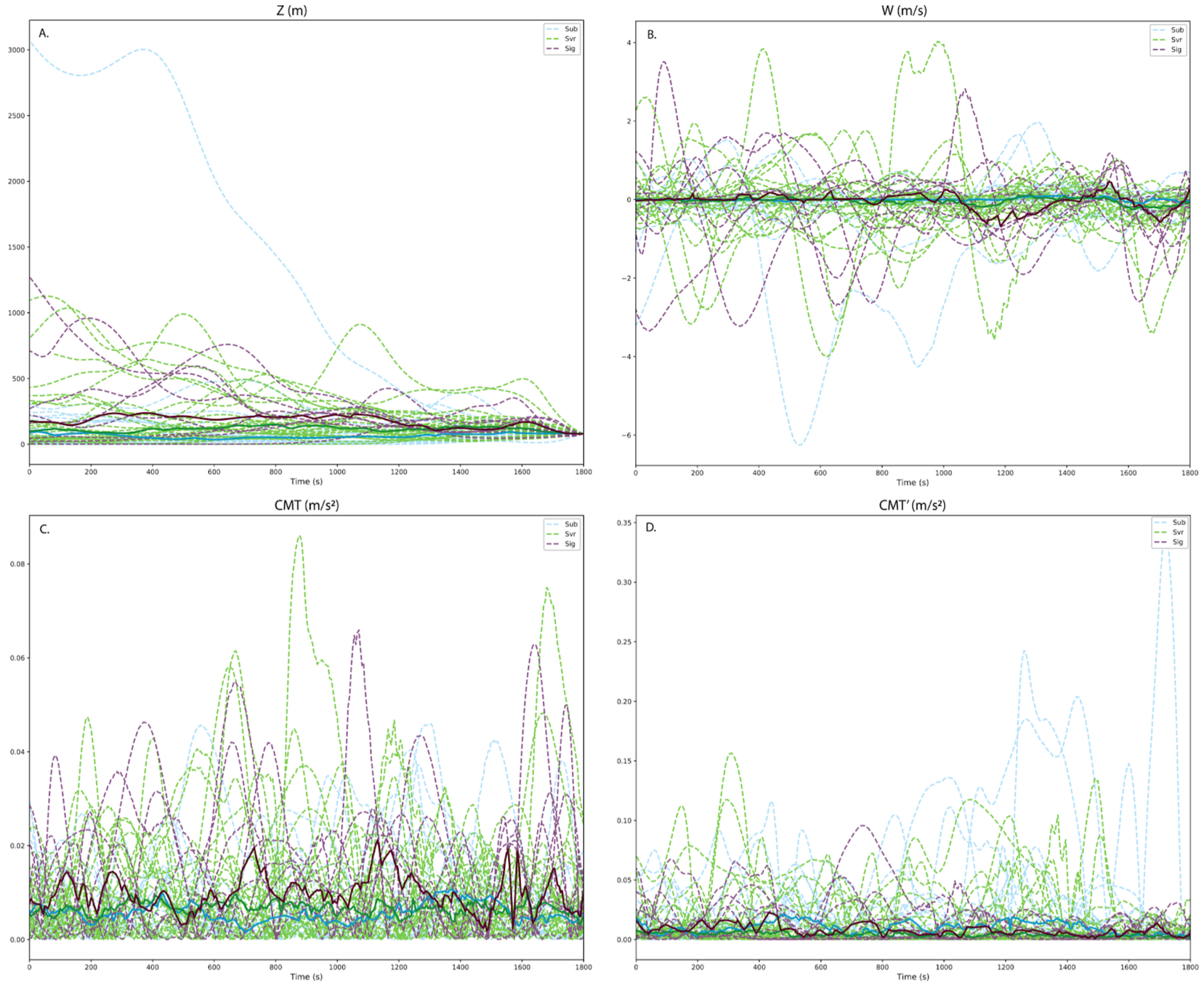

Figure 75. Change in a) height, b) vertical velocity, c) CMT′, and d) CMT_0 for the 17 sub-severe, 27 severe, and 9 significant severe trajectories at 0530 UTC for the 5-6 July MCS. Dashed lines are individual trajectories and the solid line is the median.

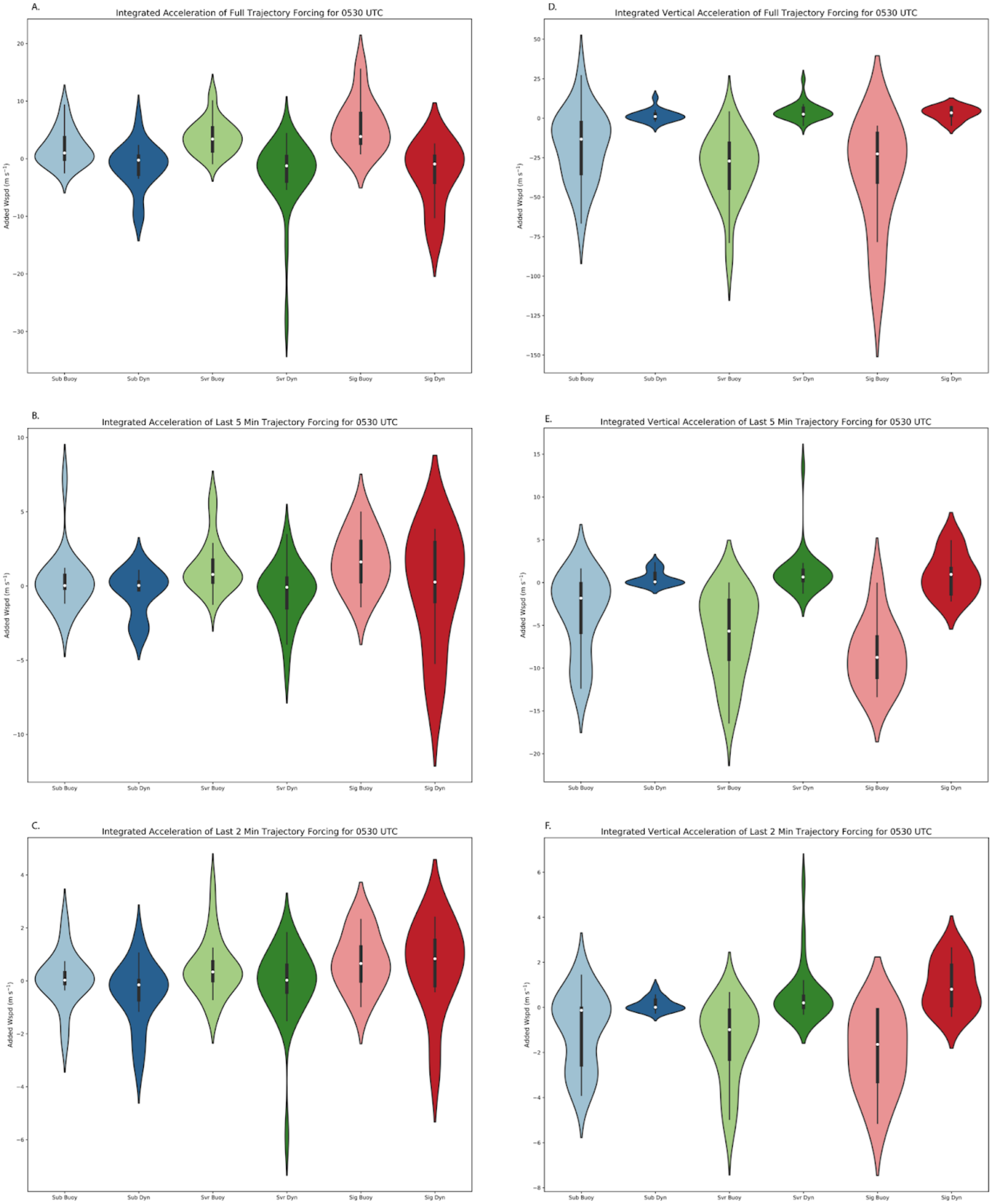

Figure 76. The 0530 UTC integrated acceleration givestotal added wind speed from the buoyancy and dynamic forcing for a) the entire trajectory in the horizontal, b) the last 5 minutes of the trajectory in the horizontal, c) the last 2 minutes of the trajectory in the horizontal, d) the entire trajectory in the vertical, e) the last 5 minutes of the trajectory in the vertical, and f) the

last 2 minutes of the trajectory in the vertical. Sub-severe distributions are in blue, severe in green, and significant severe in red.

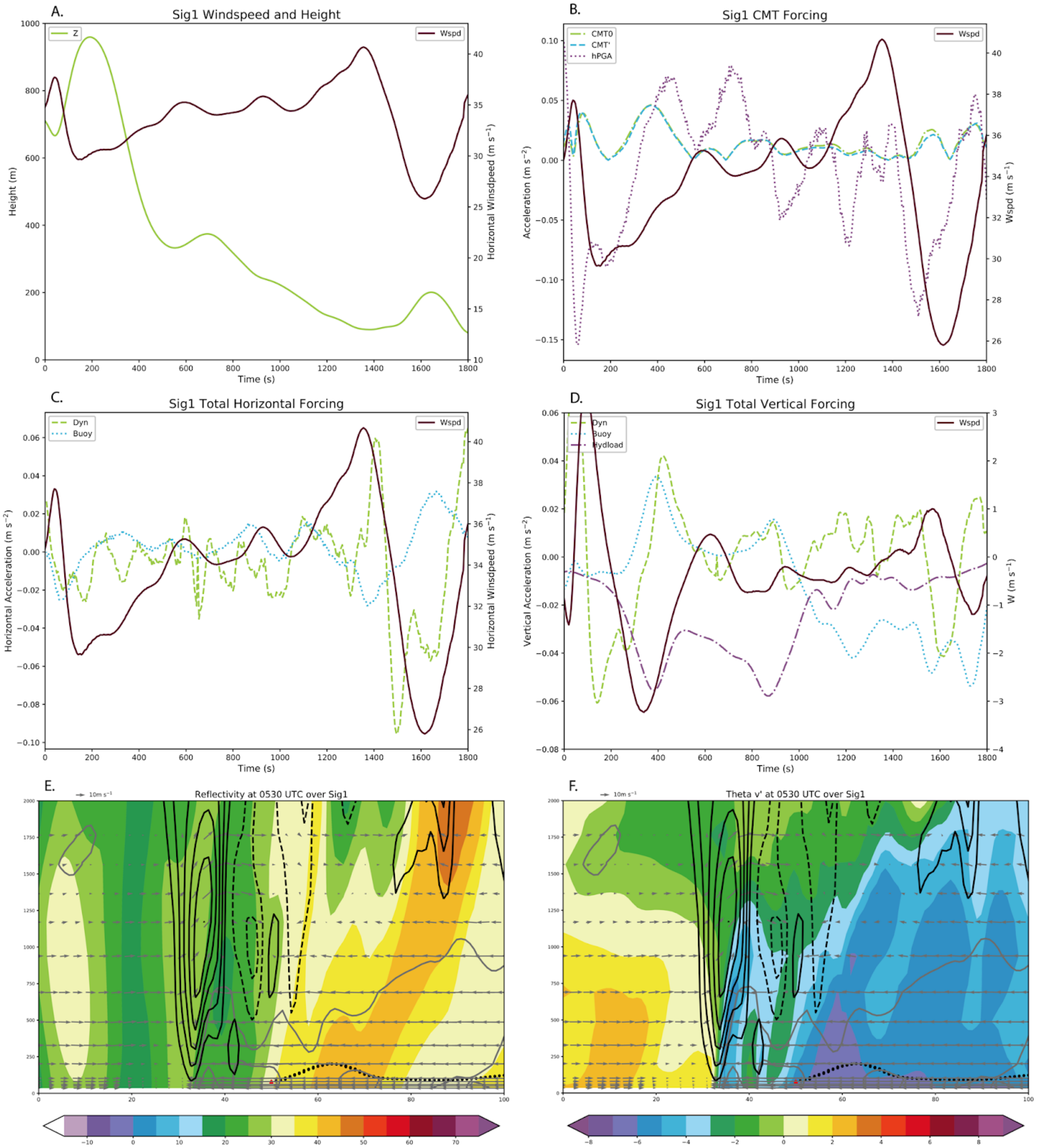

Figure 77. The sig1 trajectory at 0530 UTC a) height and wind speed, b) CMT and hPGA forcing with wind speed, c) horizontal dynamic and buoyancy forcing with wind speed, d) vertical dynamic and buoyancy forcing with w, e) reflectivity cross-section over sig1, and f) Θ_v' cross-section over sig1. Reflectivity and Θ_v' have solid (dashed) contours for updrafts (downdrafts) every 2 m s^{-1} (-2 m s^{-1}). Solid gray contours are for severe winds and significant severe winds.

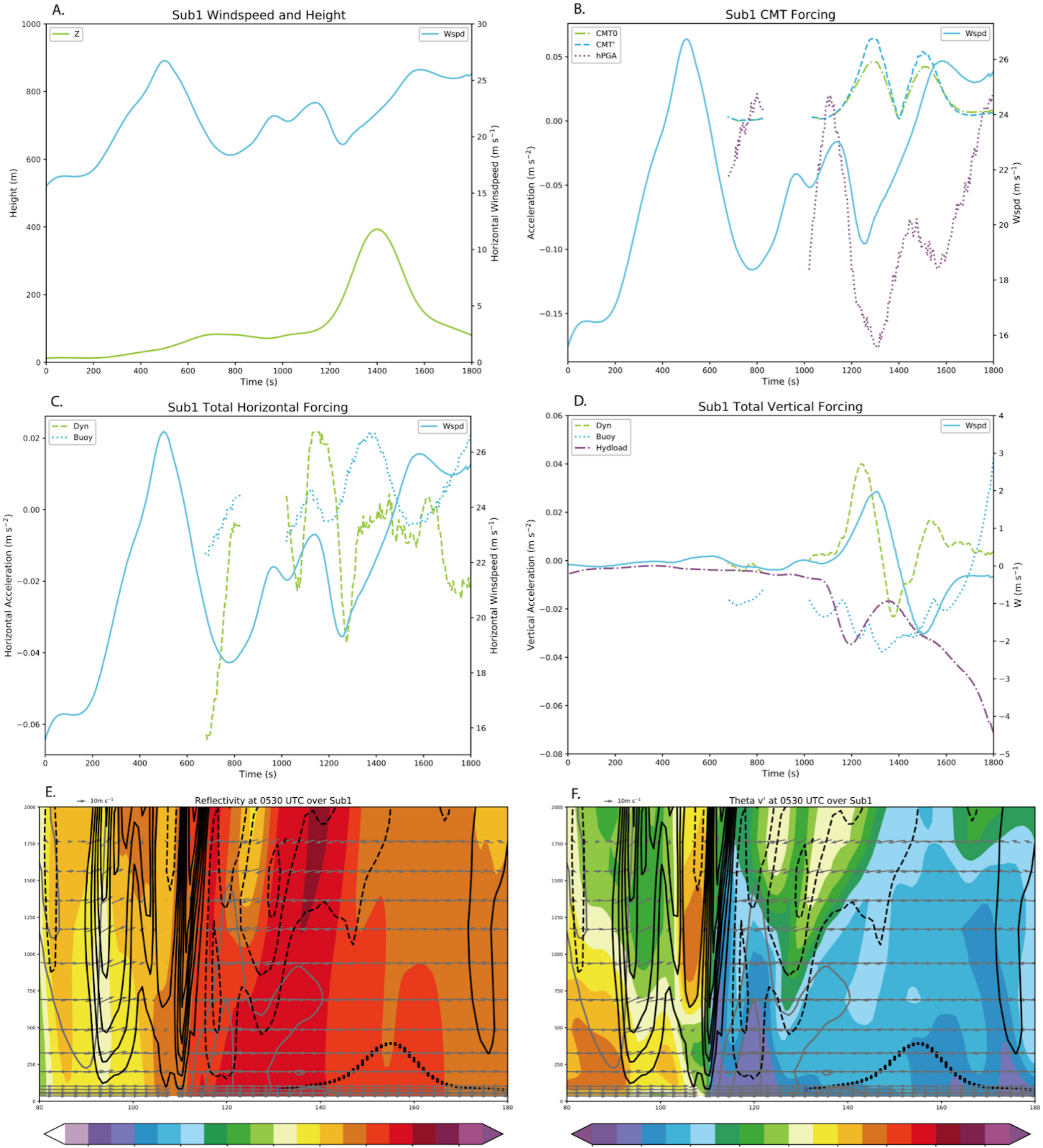

Figure 78. The sub1 trajectory at 0530 UTC a) height and wind speed, b) CMT and hPGA forcing with wind speed, c) horizontal dynamic and buoyancy forcing with wind speed, d) vertical dynamic and buoyancy forcing with w, e) reflectivity cross-section over sub1, and f) Θ_v' cross-section over sub1. Reflectivity and Θ_v' have solid (dashed) contours for updrafts (downdrafts) every 2 m s^{-1} (-2 m s^{-1}). Solid gray contours are for severe winds and significant severe winds.

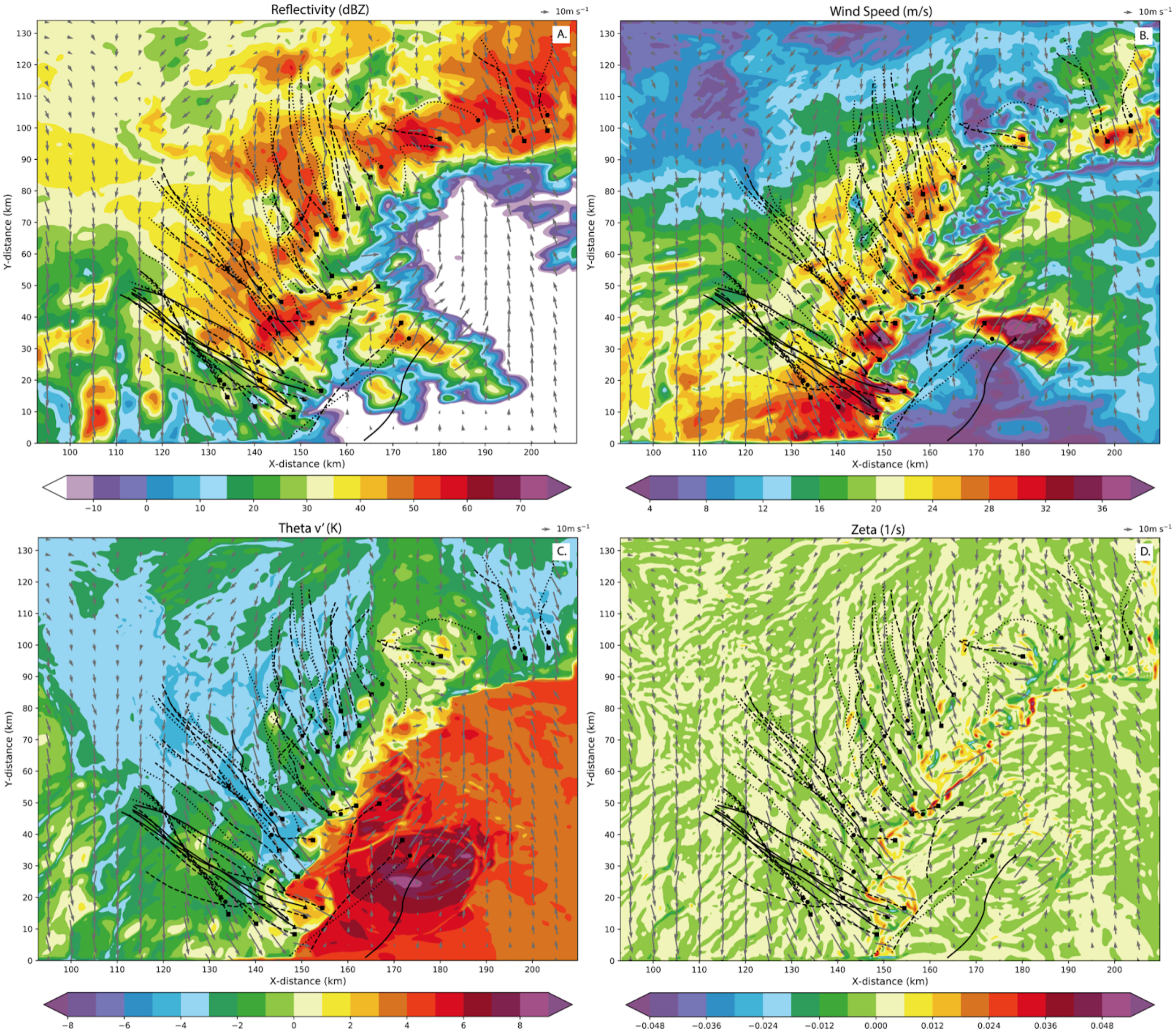

Figure 79. Horizontal plots of the 5-6 July MCS at 80 m at 0600 UTC of a) reflectivity, b) wind speed, c) Θ_v', and d) vertical vorticity with wind vectors. Severe (sub-severe) [significant severe] trajectories are indicated by dashed (dotted) [solid] lines and end in square (circle) [triangle] points.

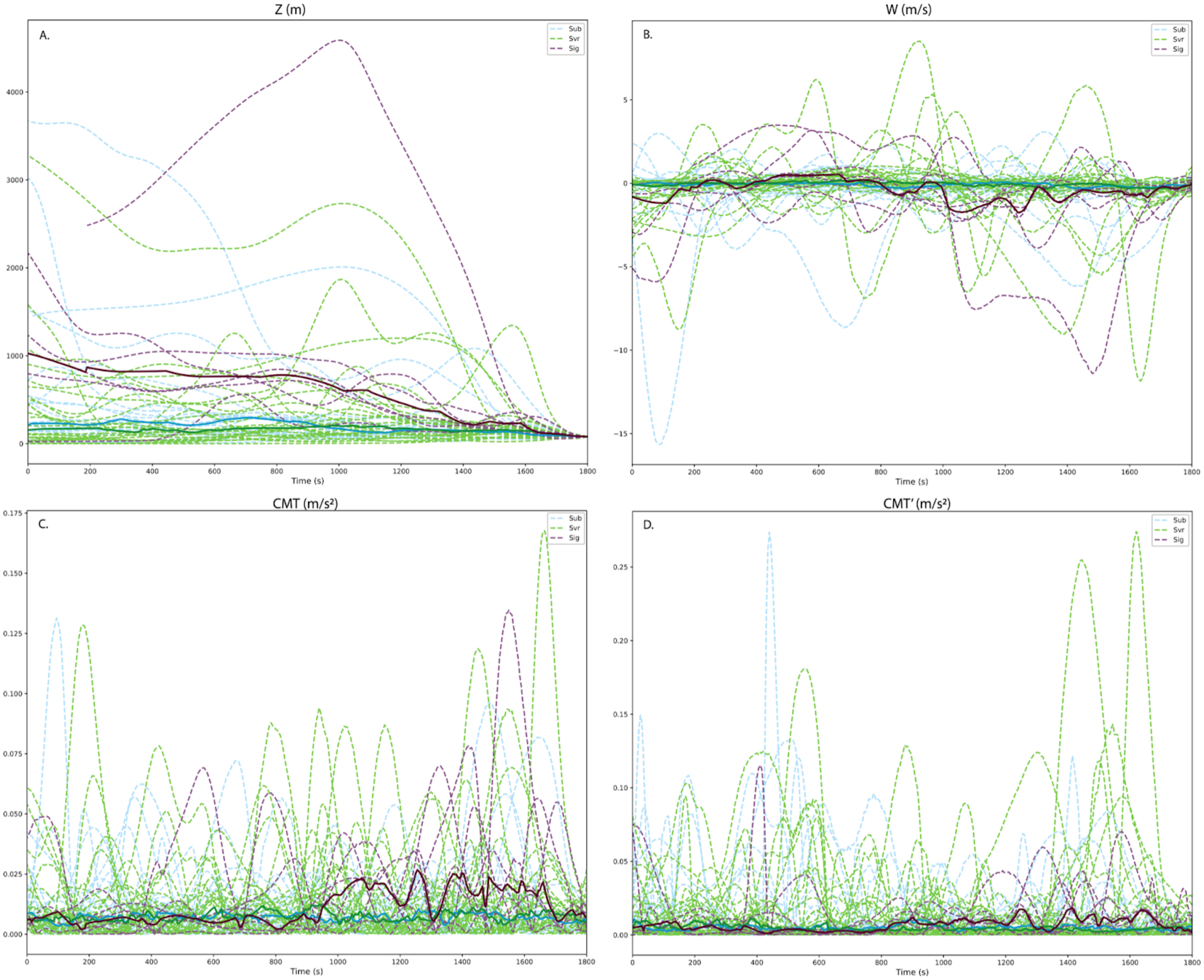

Figure 80. Change in a) height, b) vertical velocity, c) CMT′, and d) CMT_0 for the 20 sub-severe, 27 severe, and 6 significant severe trajectories at 0600 UTC for the 5-6 July MCS. Dashed lines are individual trajectories and the solid line is the median.

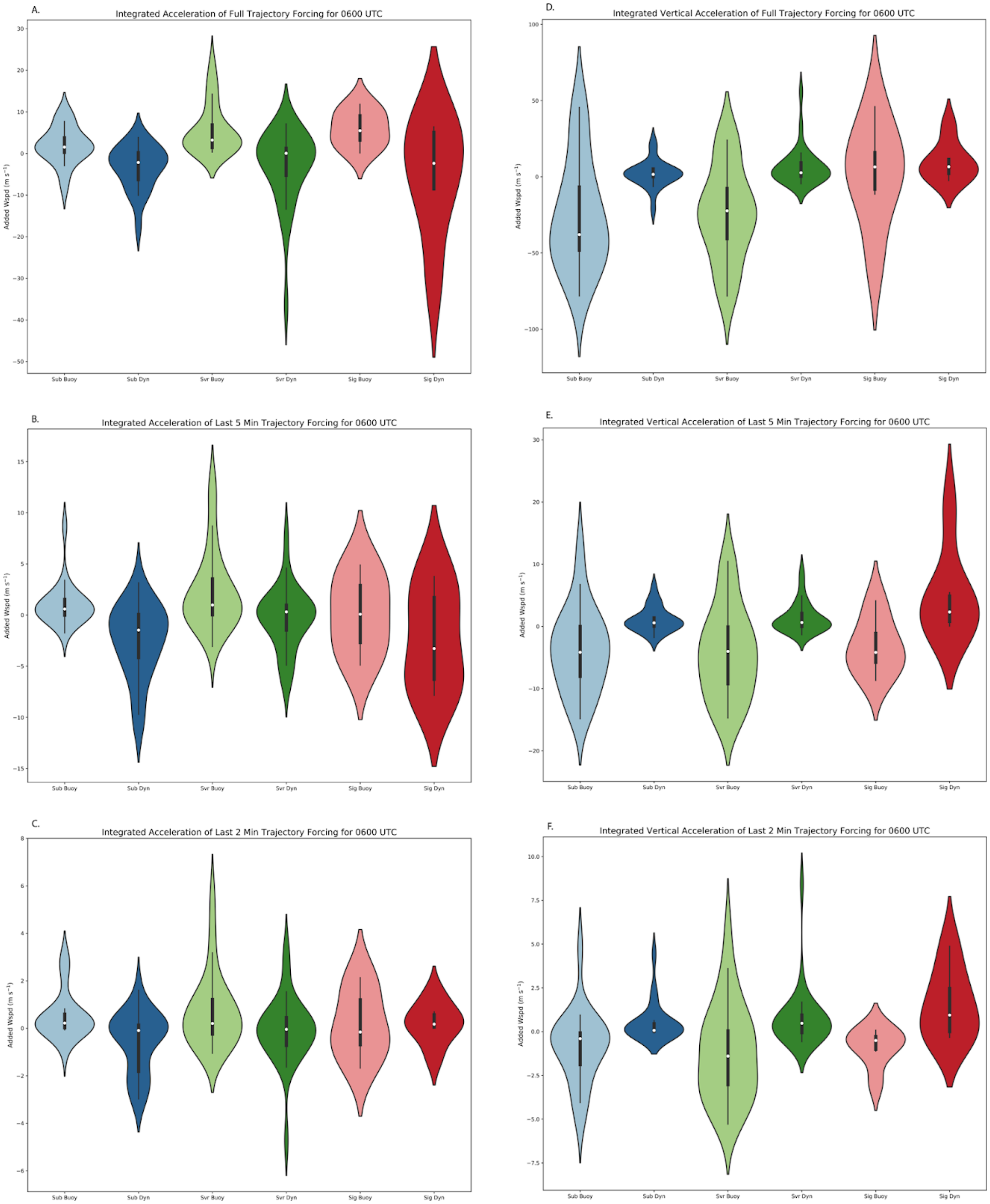

Figure 81. The 0600 UTC integrated acceleration givestotal added wind speed from the buoyancy and dynamic forcing for a) the entire trajectory in the horizontal, b) the last 5 minutes of the trajectory in the horizontal, c) the last 2 minutes of the trajectory in the horizontal, d) the entire trajectory in the vertical, e) the last 5 minutes of the trajectory in the vertical, and f) the

last 2 minutes of the trajectory in the vertical. Sub-severe distributions are in blue, severe in green, and significant severe in red.

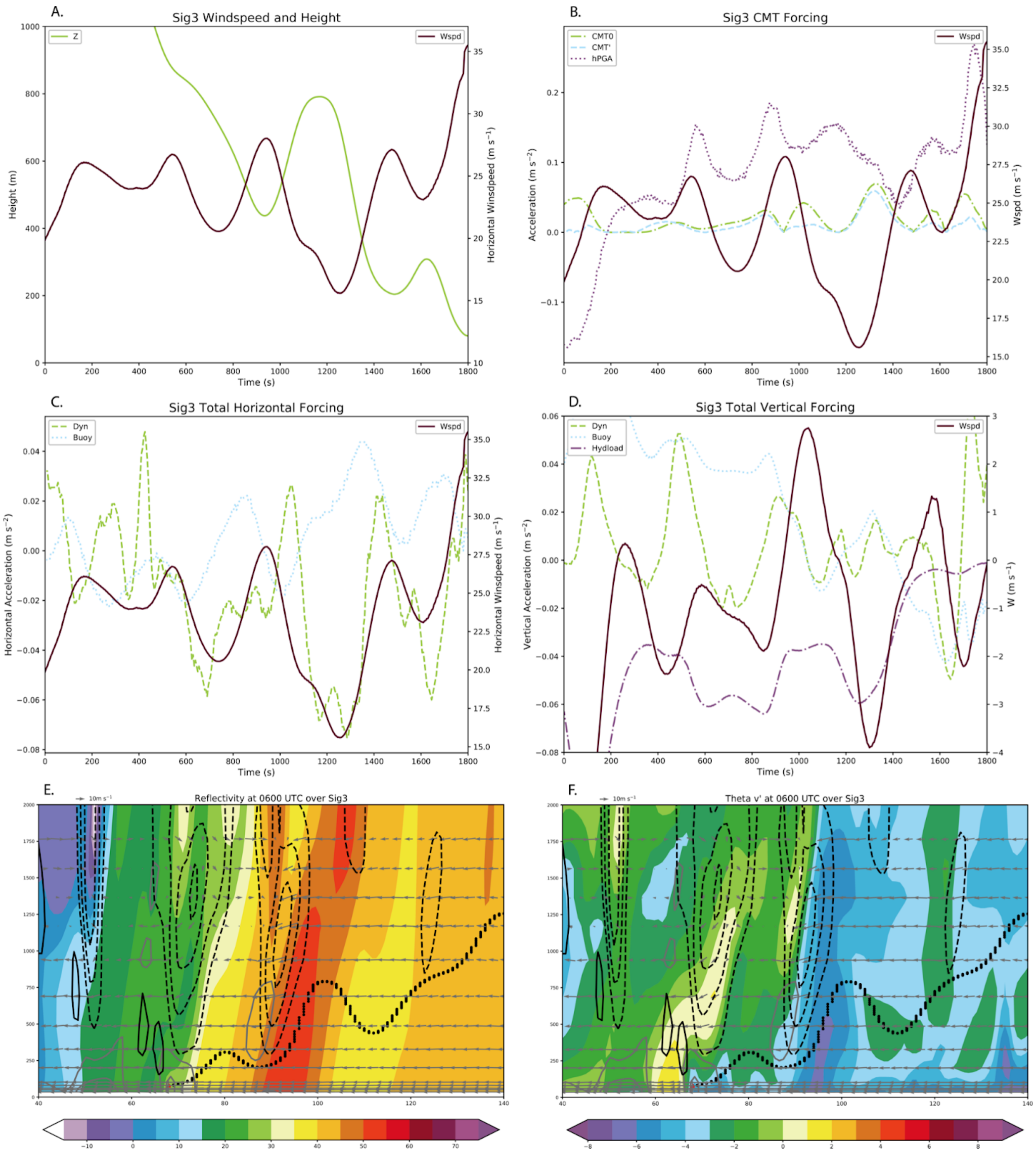

Figure 82. The sig3 trajectory at 0600 UTC a) height and wind speed, b) CMT and hPGA forcing with wind speed, c) horizontal dynamic and buoyancy forcing with wind speed, d) vertical dynamic and buoyancy forcing with w, e) reflectivity cross-section over sig3, and f) Θv′ cross-section over sig3. Reflectivity and Θv′ have solid (dashed) contours for updrafts (downdrafts) every 2 m s-1 (-2 m s-1). Solid gray contours are for severe winds and significant severe winds.

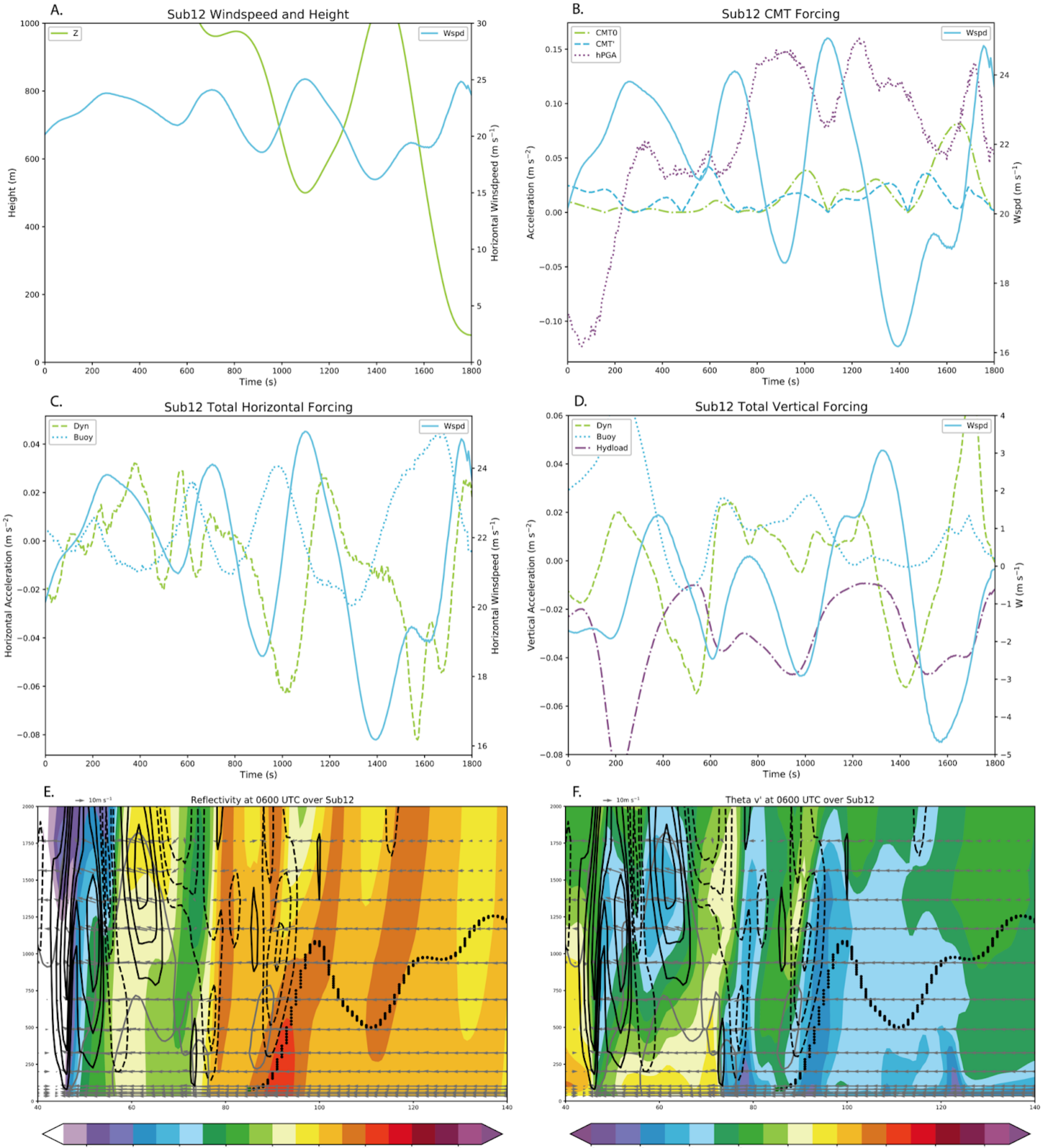

Figure 83. The sub12 trajectory at 0600 UTC a) height and wind speed, b) CMT and hPGA forcing with wind speed, c) horizontal dynamic and buoyancy forcing with wind speed, d) vertical dynamic and buoyancy forcing with w, e) reflectivity cross-section over sub12, and f) Θ_v' cross-section over sub12. Reflectivity and Θ_v' have solid (dashed) contours for updrafts (downdrafts) every 2 m s^{-1} (-2 m s^{-1}). Solid gray contours are for severe winds and significant severe winds.

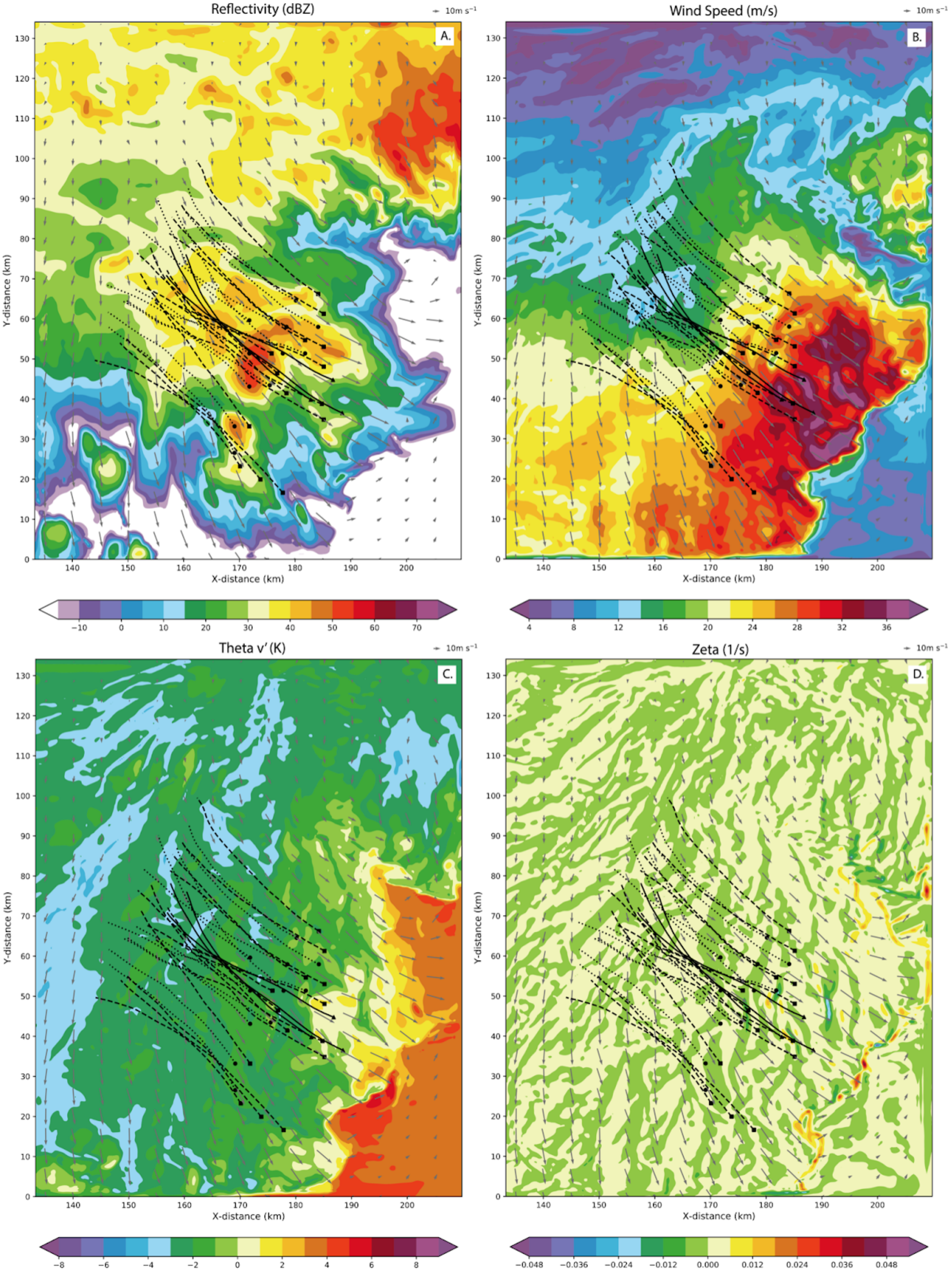
Reflectivity (dBZ)
Wind Speed (m/s)
Theta v' (K)
Zeta (1/s)
A.
B.
C.
D.
10m s⁻¹
Y-distance (km)
X-distance (km)
0
10
20
30
40
50
60
70
80
90
100
110
120
130
140
150
160
170
180
190
200
−10
0
10
20
30
40
50
60
70
4
8
12
16
20
24
28
32
36
−8
−6
−4
−2
0
2
4
6
8
−0.048
−0.036
−0.024
−0.012
0.000
0.012
0.024
0.036
0.048

Figure 84. Horizontal plots of the 5-6 July MCS at 80 m at 0630 UTC of a) reflectivity, b) wind speed, c) Θ_v', and d) vertical vorticity with wind vectors. Severe (sub-severe) [significant severe] trajectories are indicated by dashed (dotted) [solid] lines and end in square (circle) [triangle] points.

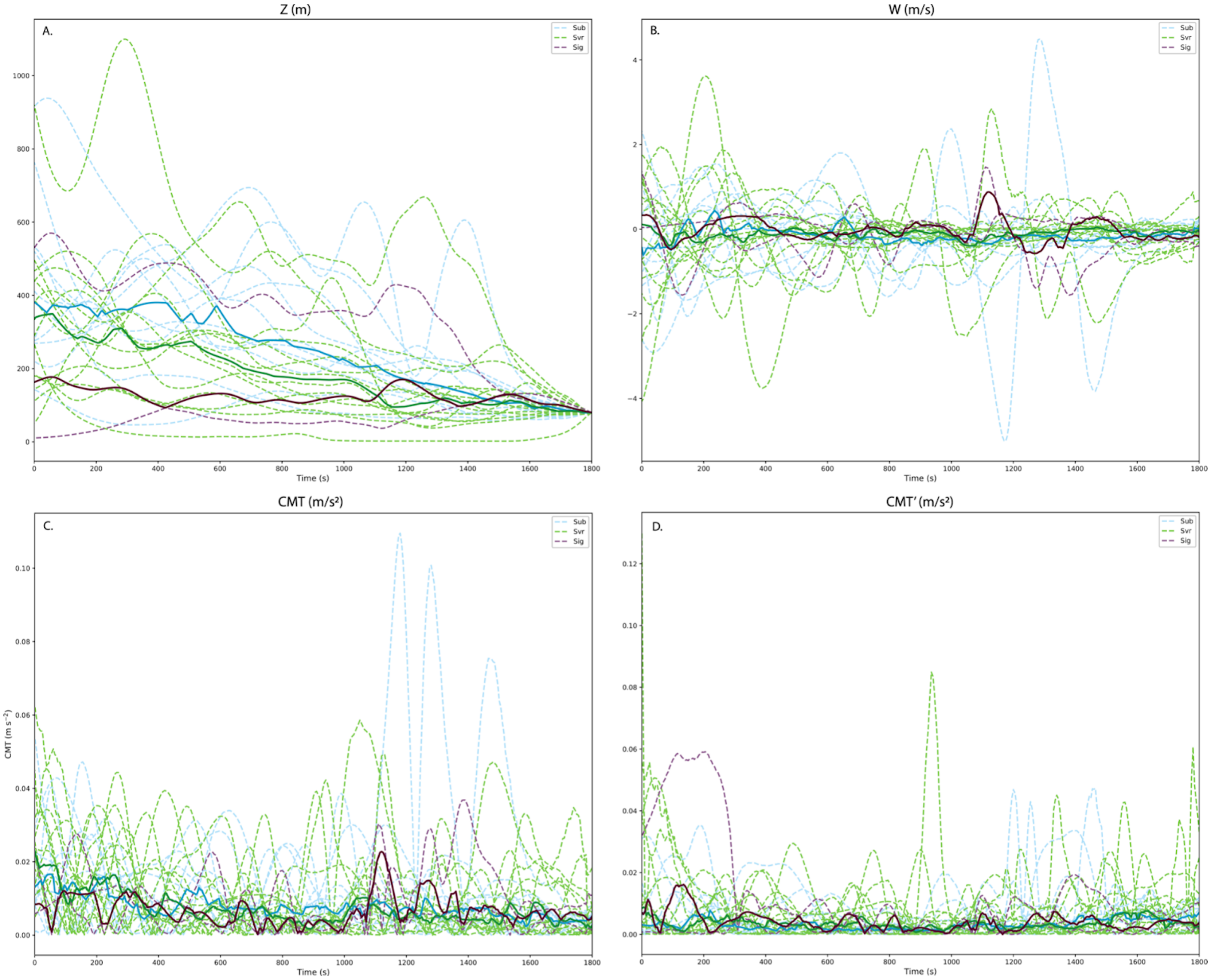

Figure 85. Change in a) height, b) vertical velocity, c) CMT′, and d) CMT_0 for the 11 sub-severe, 14 severe, and 3 significant severe trajectories at 0630 UTC for the 5-6 July MCS. Dashed lines are individual trajectories and the solid line is the median.

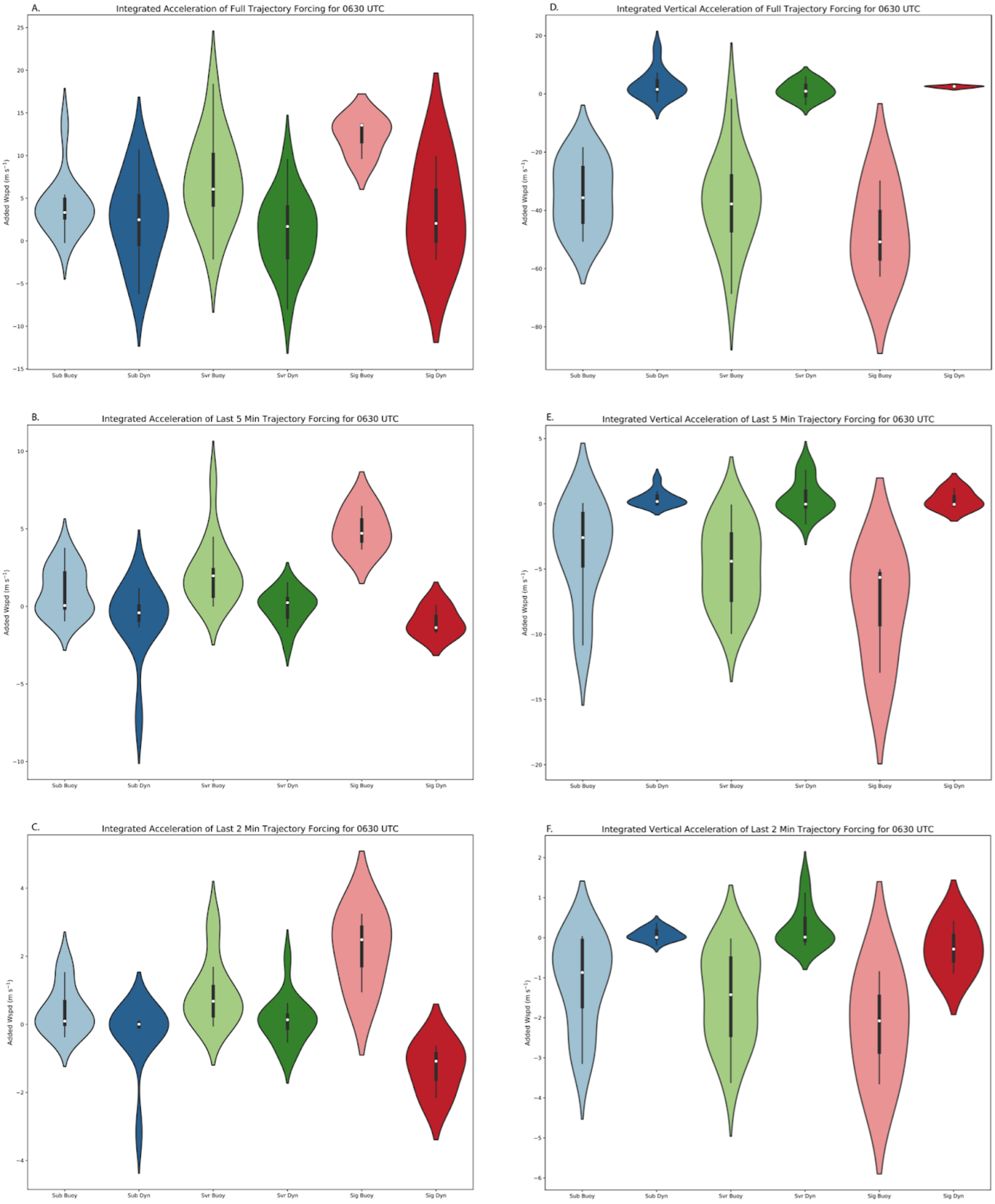

Figure 86. The 0630 UTC integrated acceleration givestotal added wind speed from the buoyancy and dynamic forcing for a) the entire trajectory in the horizontal, b) the last 5 minutes of the trajectory in the horizontal, c) the last 2 minutes of the trajectory in the horizontal, d) the entire trajectory in the vertical, e) the last 5 minutes of the trajectory in the vertical, and f) the

last 2 minutes of the trajectory in the vertical. Sub-severe distributions are in blue, severe in green, and significant severe in red.

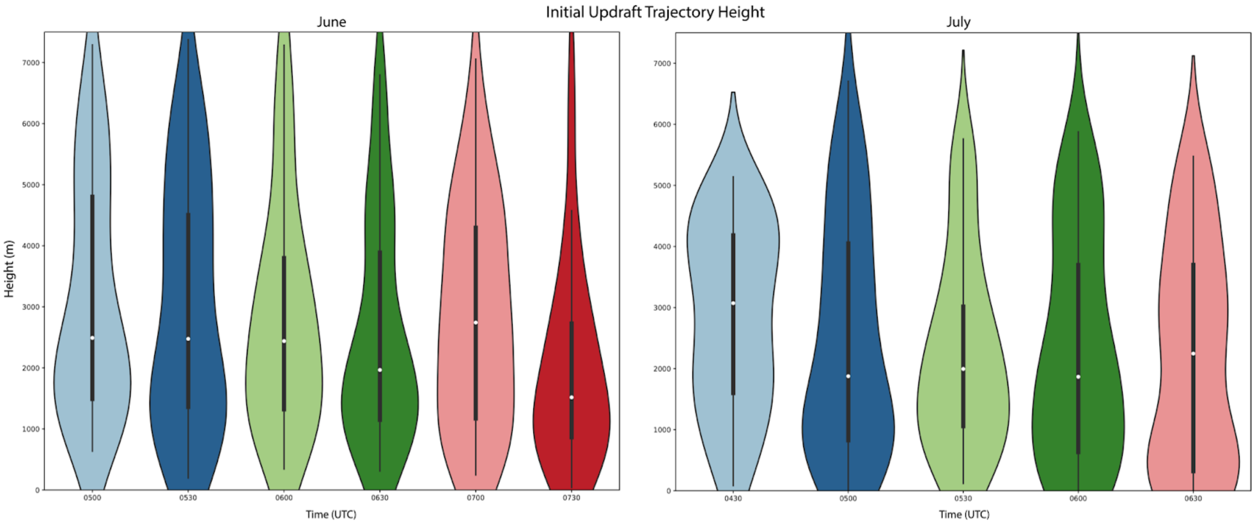

Figure 87. Distributions of 50 randomly selected updraft inflow trajectory initial height every 30 minutes for a) 25-26 June and b) 5-6 July. The median is denoted by the white circle.

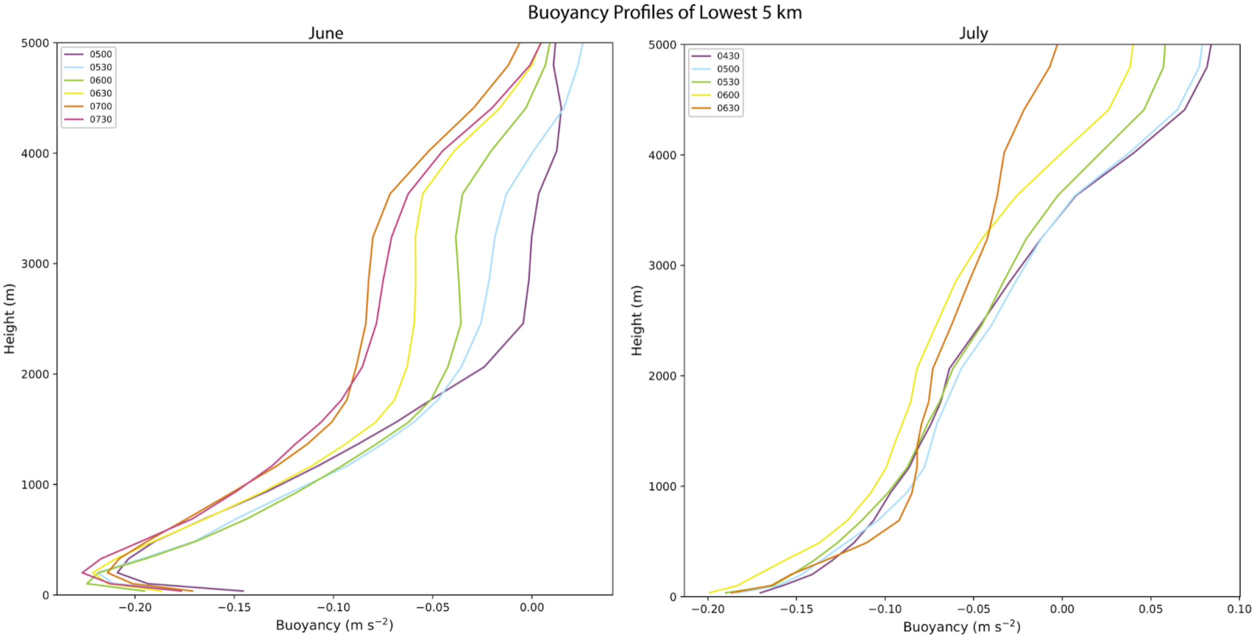

Figure 88. Vertical profiles of the buoyancy of the lowest 5 km every 30 minutes for a) 25-26 June and b) 5-6 July.